THÈSE

En vue de l'obtention du

DOCTORAT DE L'UNIVERSITÉ DE TOULOUSE

Délivré par :

Institut Supérieur de l'Aéronautique et de l'Espace

Présentée et soutenue par :
Karim ELAYOUBI

le mardi 11 juin 2019

Titre :

Study of communications channels for optical links through the atmosphere

Étude des chaînes de communication pour liaisons optiques à travers l'atmosphère

École doctorale et discipline ou spécialité :
ED GEET : Photonique et systèmes optoélectroniques

Unité de recherche :
Équipe d'accueil ISAE-ONERA OLIMPES

Directeur(s) de Thèse :

Mme Angélique RISSONS (directrice de thèse)
M. Jérôme LACAN (co-directeur de thèse)

Jury :

M. Christophe PEUCHERET Professeur ENSSAT - Président
Mme Angélique RISSONS Professeure ISAE-SUPAERO - Directrice de thèse
M. Ammar SHARAIHA Professeur ENIB - Rapporteur
Mme Christelle AUPETIT-BERTHELEMOT Professeure ENSIL - Rapporteur
M. Aniceto BELMONTE Professeur Technical University of Catalonia, BarcelonaTech
M. Jérôme LACAN Professeur ISAE-SUPAERO - Co-directeur de thèse
Mme Anne Laure BILLABERT Maître de Conférences CNAM

Abstract

Due to expected capacity bottlenecks of exploited microwave technologies, feeder links for data relay or broadband access systems will require the implementation of high capacity optical communication links between space and the ground. In this context, it is necessary to detail the investigation of the optical technologies and techniques that could enable the transmission of high data rates at optical frequencies through the Earth's atmosphere, with regard to all kinds of the atmospheric phenomena. In particular, the adverse effects of atmospheric turbulence fading are of special relevance to optical communication systems for ground-to-space uplink applications. Although previous studies and experiments have demonstrated the feasibility of such optical links at low data rate, research is still needed to identify technical solutions and strategies adapted to the specific constraints imposed to these high-speed links in order to ensure the required level of performance. Against this background, various test benches have been developed to characterize different modulations and detection techniques for optical communication systems prior to be incorporated in the conceptual design of future 1-Tb/s ground-space optical links. The expected performances of such experimental demonstration are derived based on simulation models taking into account the atmospheric turbulence effects, in order to prove the feasibility of reliable ground-to-space high date rate optical communication links. The main objective of this thesis is the investigation of the free space optical communication through the atmosphere under different turbulence regimes. Both simulation and experimental demonstrations of such communications are considered and the associated results are detailed.

Résumé

Les télécommunications optiques en espace libre pour les applications satellites deviennent une alternative aux communications radiofréquences pour les liens feeder (segment Satellite-Gateway) qui commencent à présenter une saturation en termes de bande passante avec une faible capacité des liaisons. Ces liaisons optiques présentent des avantages majeurs notamment une large bande passante disponible, l'insensibilité aux interférences ou encore l'absence de régulation (pas de coût lié à l'utilisation de telle ou telle bande de longueur d'onde a contrario de la RF). Elles sont envisagées pour les futurs systèmes satellitaires utilisant des satellites en orbites géostationnaires (GEO : Geostaionary Orbit) ou des orbites terrestres basses (LEO : Low Earth Orbit) afin d'augmenter la capacité des données transmises. L'architecture des terminaux (OGS et satellites) et la modulation optique utilisée sont déterminantes pour la robustesse d'une telle liaison aux effets induits par les couches de l'atmosphère. Bien que des expérimentations aient démontré la faisabilité de ce type de solution pour les télécommunications par satellites à des débits de l'ordre du Gb/s, des travaux de recherche sont encore nécessaires pour identifier les solutions techniques adaptées à ce nouveau médium de transmission et développer des émetteurs et récepteurs pouvant supporter des débits allant jusqu'à 1Tb/s. Les travaux menés au cours de cette thèse ont pour objectif de développer des architectures des liaisons optiques utilisant différents formats de modulation afin de maitriser le comportement des récepteurs après propagation atmosphérique (lien montant et lien descendant). Après avoir simulé la liaison avec un logiciel dédié à l'optique, un banc expérimental émulant le lien laser atmosphérique a été développé. Dans les deux cas, l'impact des effets atmosphériques a été pris en compte. La traversée des couches de l'atmosphère présente des variations brusques d'atténuation dues aux turbulences atmosphériques qui agissent directement sur l'indice de réfraction affectant l'amplitude et la phase du signal optique (on parle aussi des effets de scintillation). Il en résulte potentiellement des pertes de paquets d'informations. Différents scénarii de perturbations atmosphériques (Faible turbulences, Beam Wander, Fortes turbulences) ont été appliqués pour simuler numériquement chaque modèle de canal de communication. Le développement du banc ELLA (Emulateur Lien Laser Atmosphérique) a été réalisé pour émuler la traversée des couches atmosphériques et pour valider expérimentalement en laboratoire les différents scénarii simulés numériquement. Le taux d'erreur binaire (BER, Bit Error Rate) a été estimé avec et sans effet de fading induit par l'atmosphère dans différentes conditions de turbulences atmosphériques afin de déterminer les caractéristiques des liaisons optiques les plus robustes.

Contents:

CONTENTS

List of figures:

List of tables:

Chapter 1

1 Introduction and context

After a brief introduction on optical communications and their challenges, the objective of this chapter is to make a flashback on the communication history and the state of the art of free space optical communication. Then, we focus on satellite optical communication and especially on ground-to-space optical links. We start by presenting the actual radiofrequency (RF) limitations and detail the main advantages of optical communication links to overcome these limitations.

We describe the Geostationary Equatorial Orbit (GEO) and the Low Earth Orbit (LEO) used for ground-to-space optical communications. Finally, we detail the basics of space optical communication theory and we describe the different parts needed to connect the satellite to the ground station. The last part is dedicated to the thesis objectives and different directive lines that we follow to achieve them.

1.1   Introduction

After a brief introduction on optical communications and their challenges, the objective of this chapter is to make a flashback on the communication history and the state of the art of free space optical communication. Then, we focus on satellite optical communication and especially on ground-to-space optical links. We start by presenting the actual radiofrequency (RF) limitations and detail the main advantages of optical communication links to overcome these limitations.

We describe the Geostationary Equatorial Orbit (GEO) and the Low Earth Orbit (LEO) used for ground-to-space optical communications. Finally, we detail the basics of space optical communication theory and we describe the different parts needed to connect the satellite to the ground station. The last part is dedicated to the thesis objectives and different directive lines that we follow to achieve them.

1.2   Space optical communication and satellite systems

1.2.1   Radio frequencies and theirs limitations

Next generation high throughput satellite systems are expected to achieve up to 1 Tb/s data rate in order to reach the data rate requirements for Internet and telecommunication. The current RF communications present several limitations. The first one is the saturation of RF bandwidth allocated for the actual telecommunication technology. In fact, most satellites use the Ka band today, which has a total bandwidth of 3.5 GHz for both downlinks and uplinks, spread out around central frequencies of 20 GHz and 30 GHz. The second limitation is the relentless need for capacity which starts to overcome the capacity of the Ka band.

1.2.2   Geostationary orbit (GEO) and Low Earth orbit (LEO) for satellite systems

The geostationary orbit, often referred to as a geosynchronous equatorial orbit (GEO), is a circular geosynchronous orbit at around 36 000 km above Earth's equator and following the direction of Earth's rotation. This orbit is particularly interesting because the communication satellite can make a time-continuous cover of the same spot on earth. However, the long distance of transmission from the satellite to the ground leads to high latency and huge amount of electrical power consumption to satisfy a good signal to noise ratio (SNR) at the user receiver. In contrast, low earth orbits (LEO), which are around 2 000 km away from the Earth's ground, require less power for transmission but the coverage of the satellite scans the ground instead of being on a fixed area. This property involves the use of satellite constellations in order to have time-continuous coverage of a wide ground area.

Many laser communication links have been established which proves that this communication technology is a viable alternative to radio communication in space. The first space radio communication was Telstar 1 which was the first true space communication demonstration done on 1962. Equipped with a powerful transmitter and a receiver, it allowed to establish the first television American shows broadcasting for Europe and for European people (the first live transmission). In 1963, NASA sent the first satellite on the geostationary orbit, which orbit earth 35.900 km above the ground.

1.2.3   Feeder links and users links

The feeder link designates transmission of the data between the ground station and the satellite whereas the user link corresponds to the transmission of the data between the satellite and the user terminals. Both of them are bidirectional. When the link is established from the ground segment to the space segment we talk about uplink whereas the downlink designates the opposite direction. To complete the definitions the forward link corresponds to the communication from the ground station

to the users through the satellite whereas the return appellation is used for the opposite direction. Figure 1-1 details different scenarios of FSO communication between Optical Ground Station (OGS), GEO satellites and LEO satellites.
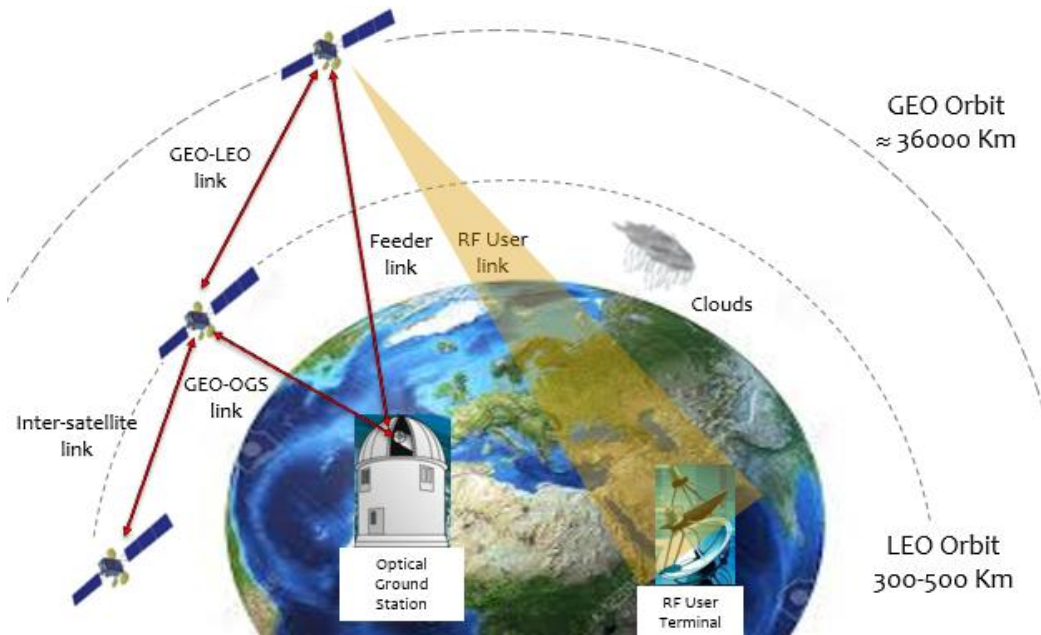
Figure 1-1: Free space optical network including both of LEO and GEO scenarios

1.2.4   Advantages of free space optical links

The advantages offered by optical communication systems for special applications are many compared with RF communications. Among these advantages are:

- **Huge modulation bandwidth:** the amount of information that we can transmit is directly related to the modulated carrier. A high carrier is expected to have wide available bandwidth around it. In RF and microwaves systems the allowable bandwidth can be up 4 GHz for example in the Ka-band (19 or 29 GHz). For optical communication, the allowable bandwidth is around 10 THz if we consider the commercially used C and L bands which is far away from the RF capacity of the Ka and Ku bands (10^3 times more)[1].

- **Low beam divergence**: typically, an optical beam presents a divergence between 10 and 100 μrad in contrast to RF waves for which the divergence is 1000 times bigger. In fact, the divergence is proportional to λ/D_R where λ is the carrier wavelength and D_R is the aperture diameter. As a conclusion, the beam spread offered by the optical carrier is narrower than for RF carriers. This also allows increasing the signal intensity received after propagation for a given emitted power.

$$\frac{\theta_{RF}}{\theta_{Optical}} \approx 1000$$
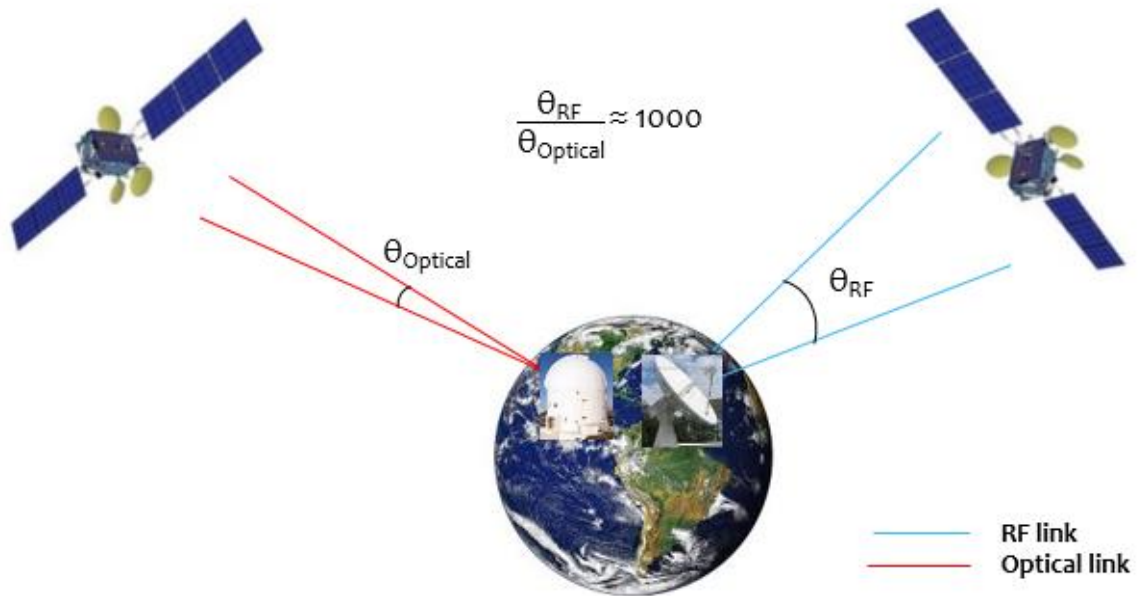
Figure 1-2 : Comparison of FSO and RF beam divergence between OGS and satellite

- **High security:** Optical beams have a low probability of being jammed or deflected thanks to their high directivity and low divergence. Any kind of interception is therefore very difficult due to the non-detectability of FSO communication by spectrum analyzers.

- **Small Size, Weight and Power (SWaP)**: optical payload can offer more than half of the masse and power consumption compared to RF systems (e.g., Cubesats or nanosatellites). Indeed, for a given transmitter power level, the optical intensity is greater at the receiver thanks to the narrow beam divergence, as we detailed before. Thus, the shorter wavelength of optical carrier permits to design smaller antennas than for RF system to achieve the same gain. Typically, the antenna size for the optical system is 30 cm while RF systems need an antenna size of 150 cm for a given gain. We present in Table 1-1 a comparison between optical and RF communication systems using 10 W and 50 W for optical and Ka band systems, respectively between LEO and GEO links [2].

	Optical	RF	System optical linear gain
GEO-LEO			
Antenna Diameter	10.2 cm	220 cm	21.6
Mass	65.3 kg	152.8 kg	2.3
Power	93.8 W	213.8 W	2.3
GEO-GEO			
Antenna Diameter	13.5 cm	210 cm	15.6
Mass	86.4 kg	145.8 kg	1.7
Power	124.2 W	204.2 W	1.6
LEO-LEO			
Antenna Diameter	3.6 cm	80 cm	22.2
Mass	23.0 kg	55.6 kg	2.4
Power	33.1 W	77.8 W	2.3

Table 1-1: Comparison of mass, power and antenna size for GEO and LEO links for FSO and RF [3]

Table 1-2 summarizes the main difference between free space optics (FSO) and RF technologies:

	FSO systems	RF systems
Data rate range/ Channel	100 Mbps to few Gbps	Less than 100 Mbps
Channel security	High	Low
SWaP	Low	High
Source of signal mitigation and degradation	Atmospheric turbulences, Clouds	User interferences, Multipath fading
Beam divergence	Low	Large

Table 1-2 : Properties of FSO and RF communication systems

We consider in Table 1-2 a communication scenario of one channel where the FSO's data rate can reach 1Tbps by using Wavelength Division Multiplexing technology (WDM).

- **Interferences:** RF communication suffers from interferences between adjacent carriers while the high directivity of optical communication prevents them. The International Telecommunication Union (ITU) regulates RF spectra to avoid interference problems. They did not define yet any restriction for frequency use and bandwidths in optical spectrum.

- **Wavelengths division multiplexing (WDM)**

Whereas conventional RF feeder links require tens of gateway station (RF ground stations), the total capacity can be linked through a single optical ground station using WDM techniques as known in terrestrial fiber communication. In order to compare the advantage of optical feeder links, Table 1-3 illustrates the required number of gateway stations as a function of the feeder link capacity.
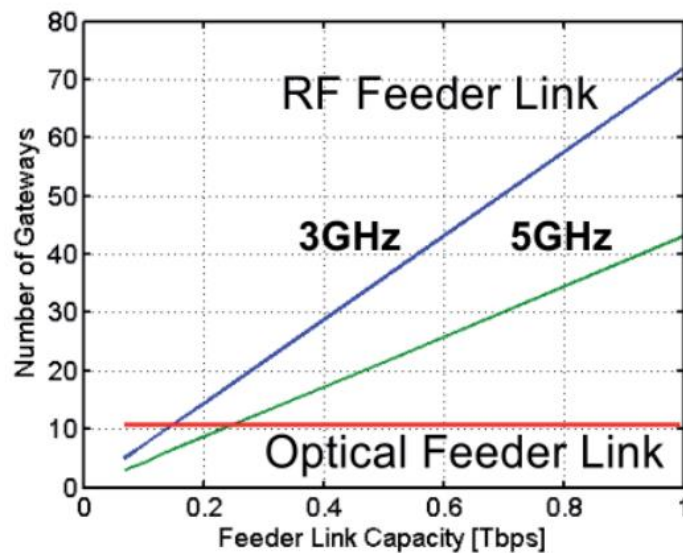
Figure 1-3: Number of gateways for RF feeder link technology versus optical feeder link [3]

From these curves, the optical feeder link can be achieved for different data rate using the same number of gateway stations. Only the number of channels multiplexed inside have to be changed and the complexity of the Optical Ground Station (OGS) need to be managed.

1.3   State of art of free space optical communication

1.3.1   Challenges of satellite optical communication

FSO technology uses atmospheric channel as a propagating medium whose properties are random function of time and space. Various unpredictable environmental factors, such as clouds, fog, snow, etc., cause strong attenuation and distortion in the optical signal and limit the link distance. The inter-satellite FSO links are less challenging because the atmosphere is not present on the transmission channel. That is why a commercial data relay service named EDRS (European Data Relay Satellite System) using FSO links is already deployed. However other factors, like pointing error or background noise contribute to limit the data rate today [4].

To offer significant potential to improve the FSO communication capacity, major issues need to be studied such as:

- Advanced optical modulation and optical communication architecture design to reach high data rate.
- Atmospheric random phenomena such as turbulence and clouds that strongly affect the propagation of the optical beam through the atmosphere.
- Atmospheric effect compensation using real-time optical correction systems such as adaptive optics or data correcting such as error correcting code.

Inter-satellite FSO links are not subject to weather conditions or cloud outages as the satellite orbits are far above the atmosphere. In this case, the major challenge is caused by the acquisition and tracking as two satellites move with different relative velocity. As inter-satellite or inter-orbital links have to cover larger distances, therefore the transmission scheme has to be power-efficient with good sensitivity at the receiver. Although, inter-satellite FSO links are not subject to atmospheric and weather limitations, they are limited by other challenges such as Point-Ahead-Angle (PPA), Doppler shift, acquisition and tracking, background radiation and satellite platform stability.

- **Point-Ahead-Angle (PAA):**

Due to the relative motion between the transmitter and the receiver terminals, the return signal is required to be offset from the beacon beam used for satellite location. This pointing offset is called PPA. It depends upon the relative velocity between the two satellites and is used to compensate the travel time over the long cross link distances. The PPA can be calculated from

$$\theta_{PPA} \approx 2\frac{V_{Sat} - V_{OGS}}{c}$$

where c is the velocity of light in vacuum, V_{Sat} and V_{OGS} are the satellite and OGS speeds transverse to the propagation link. For a GEO satellite, its speed can be given by

$$V_{Sat} = \omega_{Earth}(R_E + H_{GEO})$$

with $\omega_{Earth} = 2\pi/86400\,s = 73\mu rad.\,s^{-1}$, $R_E = 6400\,km$ and $H_{GEO} = 36000\,km$. When the satellite is on the zenith of the OGS (OGS located on the equator), $V_{OGS} = \omega_{Earth} * R_E$. Then if we consider $0 < V_{OGS} \leq \omega_{Earth} * R_E$, the PPA will be in the range

$$2\frac{\omega_{Earth} * H_{GEO}}{c} < \theta_{PPA} < 2\frac{\omega_{Earth} * (R_E + H_{GEO})}{c}$$

$$17.5\ \mu rad < \theta_{PPA} < 20.6\ \mu rad$$

Figure 1-4 illustrates the parameters used to estimate the PAA on the GEO scenario for a propagation time duration of δT:
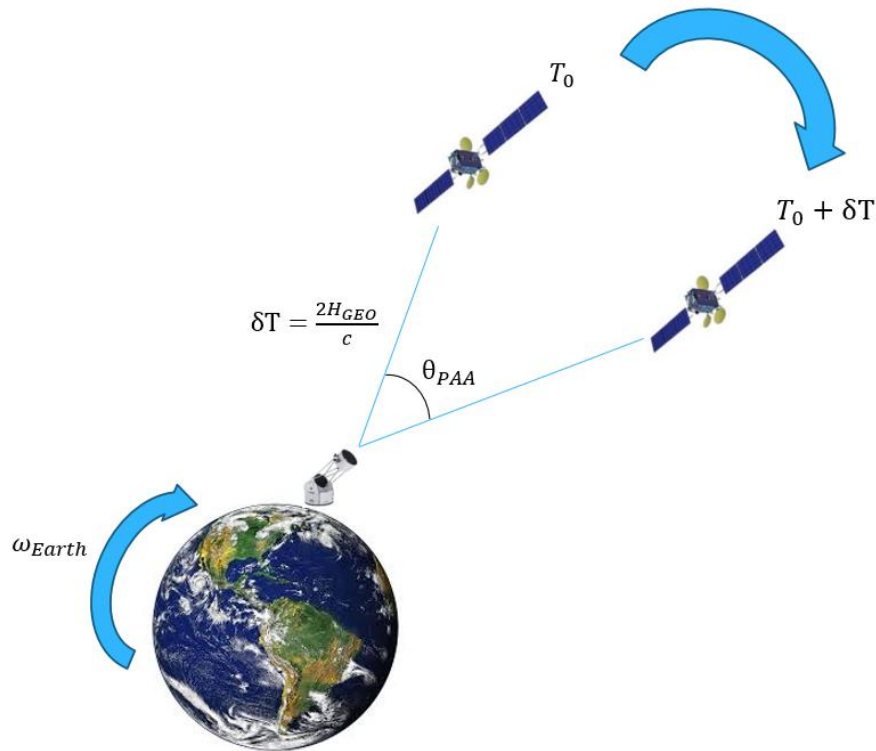
Figure 1-4: Point ahead angle (PPA) definition in the case of OGS to GEO communication

Considering the same calculation, the PAA effect is usually smaller than $0.3 \ \mu rad$ for links of ground to LEO satellite [5].

- **Doppler Shift:**

The change in frequency of received signals due to the relative movement between the source and the receiver leads to Doppler effects. This effect can happen in inter-satellite link or satellite to ground link. The Doppler shift to be compensated is up to $\pm 7.5 \ GHz$ around the frequency carrier ($\approx$ $193.1 \ THz$) for optical communication between LEO and GEO transmission [6].

- **Background noise sources**:

The noise sources for FSO links depend on the field of view of the telescope and the detection technique used on board the satellite (either optically pre-amplifier receiver or avalanche photodiode). Other background noise sources present around the satellite environment and consist on stellar and celestial radiation fluxes.

- **Amplification noises:**

For direct detection, the main noise sources are shot noise due to the signal detection process, optical noise due the Amplified Spontaneous Emission noise (ASE) or the beat noise between ASE and the optical signal.

1.3.2 Optical communication history

In 1794, Chappe's optical telegraph connected Paris to Lille and Paris to Brest via a network of semaphores conveying step and coded messages with a propagation speed of 35 km/h. However, the optical telegraph was quickly abandoned due to the advantages of electrical communication could experienced a rapid progression.

The photophone was developed in 1880 by Alexander Graham Bell. It is a telecommunication device that allows transmission of speech using a beam of light. It worked with light modulation induced by the deformation of a mirror under the effect of voice. The receiver uses a selenium cell whose resistance varied according to the light intensity received. Then the information can be recovered.

In the 1980s, the beginning of semiconductor lasers was an important point for optical communication. With their long lifespan and high efficiency, they allowed working with high signal-to-noise (SNR) ratios. Several years after, fibered lasers and fiber optic technology appeared and brought technological maturity and a solution to increase bandwidth demand. With 0.2 dB/km of attenuation using optical fiber, they allowed high speed and long-range transmission.

1.3.3 Optical feeder links

Optical feeder links are divided in two categories: uplinks and downlinks. If the satellite would have a regenerative payload (becoming a transceiver satellite), the optical feeder link could be transmitted on board the satellite thanks to optical modulation and coding. The optical modulation could then be chosen for the optical communication and a powerful error correction scheme could be applied in order to compensate the bit errors induced by the turbulence fading [3].

Uplink and downlink optical transmission channels are very different from each other because the turbulence part of the atmosphere is either crossed at the beginning of the transmission (uplink) or close to the end (downlink). This asymmetry brings very different effects and should be considered for the system design.

1.3.3.1 Optical uplinks

The receiver telescope is located on the satellite that can be considered as a point-receiver from the turbulence point-of-view. In these conditions, the receiver area is much smaller than the size of the arriving optical beam where both phase and intensity distortion are also smaller. Due to the size of the small receiver aperture, the received optical beam is not affected by the phase distortion and the only turbulence effect is the intensity fluctuation (called scintillation) that can be characterized by the scintillation index, defined as the normalized variance of the receiver intensity [7].

The beam wander is another atmospheric effect to be considered for uplinks optical communications. This effect acts on the propagation direction that is deviated by turbulence cells larger than the optical beam diameter. The strength of beam wander depends on the size of the optical beam and the turbulence cells which can cause a strong fading on the received optical signal. At the satellite level, the received is much bigger than the telescope size where only the optical power variation could disturbed the communication. The phase distortion effects are neglected in this case.

1.3.3.2 Optical downlinks

For the optical downlink, the receiver telescope is located on the OGS that is usually much bigger than the phase and intensity distortion [8]–[10]. A part of the received optical beam is collected and the phase distortion cannot be neglected as for uplinks communication. Thereby adaptive optics systems

are used to estimate the incoming wave-font and correct the phase distortion to optimize the single mode fiber coupling efficiency.

The next part presents the main free space optical demonstrations in both uplinks and downlinks scenarios.

1.3.3.3 Optical feeder link demonstrations

Currently, free-space optical communications through the atmosphere are still at the stage of demonstration and need to increase in maturation. During the past decade, many experimental programs have been studied and realized with satellite and payloads to investigate optical feeder links and to prove its possibility [11]. Here is a chronological summary of such demonstrations.

- **SILEX/ARTEMIS in 2001**. The European Space Agency (ESA) performed the world-first Semiconductor-laser Inter-satellite Link Experiment (SILEX) between its GEO data-relay satellite ARTEMIS and the Earth observation LEO satellite SPOT-4 [12]. It was a two-way link between satellites using a GaAlAs laser diode with Pulse Position Modulation (PPM) at 50 Mbps. The transmitter emitted a power of 60 mW at 800 nm and the detection part used an avalanche photodiode (APD) as well as a tracking system comprising of a tilting mirror and CCD matrices. After hundreds of laser communication links, they prove that, having pointing, acquisition and tracking requirements, laser communication technologies are a viable and good alternative to radio communication in space [13]. The achievements of the SILEX program were an important technology step because it successfully demonstrated for the first time in orbit. However, the optical technology developed for this program needed to be more mature to compete with radio communication technology.

  The first bidirectional optical link between ARTEMIS and the ESA's Optical Ground Station (OGS) located in Tenerife (Spain) at Observatorio Del Teide was established in November 2001 [14].

Figure 1-5 : ESA's optical ground station building in Tenerife

- **LOLA in 2006** : the Liaison Optique Laser Aéroportée (LOLA) experiment was a bidirectional link between the GEO satellite ARTEMIS and an airplane representative of the medium and high altitude [15]. The uplink had a 2 Mbps capacity modulated using a PPM while the downlink had a 50 Mbps using the On Off Keying (OOK) Modulation. This experiment was done as part of a French program by Astrium (now Airbus Defense & Space) and Thales with the aim to

characterize the propagation of light beam in the atmosphere and to validate the system performance capabilities of the link [16].

Figure 1-6 : The LOLA bidirectional link

- **TerraSAR-X in 2008.** The Laser Communication Terminal (LCT) on the German satellite TerraSAR-X, manufactured by Tesat Spacecom has performed a link with the German Space Agency's (DLR) OGS in Oberpfaffenhofen. The LCT is equipped with coherent Binary Phase Shift Keying (BPSK) transmission laser. During this demonstration, there were long periods of error less telecommunications intersected with peaks of error due to the scintillation of the laser beam under the atmospheric turbulence. Note that the U.S satellite NFIRE was equipped with another LCT to carry out experimental trials of inter-satellite links [17][18].

- **LLCD in 2013.** A broadband link between the ground and the lunar orbit was achieved with the Lunar Laser Communication Demonstrator (LLCD) [17]. Three stations were used in this demonstration: The OGS in Tenerife, the Optical Comm Telescope Lab of the JPL at Table Mountain and a specific terminal at White Sands (cf. Figure 1-7) with 4 emitters with a 15 cm diameter and 4 receivers with a 40 cm diameter [19]. The modulation used for this demonstration was the PPM with wavelengths around 1500 nm and achieved a 622 Mbps capacity for the downlink and 20 Mbps on the uplink.

Figure 1-7 : Lunar Laser Communications Ground Terminal in White Sands (NASA)

- **OPALS – 2014**. The Optical Payload for Lasercom Science (OPALS) is an experimental terminal developed by NASA Jet propulsion Laboratory to be used on the International Space Station (ISS). They achieved a video transfer from the ISS to JPS's Optical Communications Telescope Laboratory (OCTL) with 50 Mbps data rate at 1550 nm.

- **SOCRATES/SOTA – 2015.** The Small Optical Transponder (SOTA) terminal on the Japanese Space Optical Communications Research Advanced Technology Satellite (SOCRATES) was developed by the National Institute of Information and Communication Technology (NICT) for free space optical communication using microsatellites. This terminal has been used to establish link with the Observatoire de la Cote d'Azur (OCA) in France [20]. The demonstration was financed by the French space agency CNES with the participation of Airbus Defense & Space, Thales Alenia Space and ONERA (the French aerospace lab).

Table 1-3 summarizes the main characteristics of the previous optical communications including the near-future systems and programs such as Japan's Data Relay System (JDRS) program, China's first optical communication and Russia's Onboard Terminal of a laser Communication System.

Year	Program	Scenario	Link direction	Wavelength (Up/Down) (µm)	Data rate (Up/Down) (Mbps/Mbps)	Modulation (Up/Down)	Detection	Link range (Km)
1994	LCE (Japan)	GEO-OGS	Bidirectional	0.5 /0.8	1/1		Direct	≈ 38.000
1995	GOLD (USA)	GEO-OGS	Bidirectional	0.5 /0.8	1/1	PPM/PPM	Direct	≈ 38.000
2001	SILEX (Europe/ESA)	GEO-LEO GEO-OGS	Bidirectional	0.8 /0.8	50/50	PPM/OOK	Direct	≈ 38.000
2001	GeoLITE (USA)	GEO-OGS	Uplink	≈ 1.5	1000		Direct	≈ 38.000
2006	OICETS (Japan)	LEO-GEO LEO-OGS	Bidirectional	0.8	50	OOK	Direct	≈ 610
2008	LUCE (Japan)	GEO-LEO	Bidirectional	0.8/0.8	2/50	PPM/OOK	Direct	2.640
2011	TerraSAR-X (Europe/DLR)	GEO-LEO	Bidirectional	1.06/1.06	5600/5600	BPSK/BPSK	Coherent	≈ 45.000
2011	HY-2 (China)	OGS-LEO		1.5	504		Direct	
2011	BTLS (Russia)	ISS-OGS		1.5/0.85	125		Direct	<1.000
2013	LLCD (USA)	OGS-Moon	Bidirectional	1.55/1.55	622/20	PPM/PPM	Direct	≈385.000
2014	OPALS (USA)	ISS-OGS	Downlink	1.55	50	OOK	Direct	≈ 700
2014	EDRS (Europe/ESA)	GEO-LEO GEO-OGS	Bidirectional	1.06	1800	BPSK	Coherent	>45.000
2014	ALPHASAT (Europe/ESA)	OGS-GEO	Bidirectional	1.06/1.06	1800/1800	BPSK	Coherent	≈ 38.000
2014	SOCRATES (Japan)	OGS-LEO	Downlink	1.55	50	OOK	Direct	2.640
2015	SOTA (Japan)	LEO-OGS	Bidirectional	1.5/1.06	1 to 10	OOK	Direct	≈ 1.000
2018	LCRD (USA)	GEO-LEO GEO-OGS	Bidirectional	1.5	622/2.800	PPM/DPSK	Direct	≈ 38.000
2018	OSIRIS (v3) (Europe/DLR)	OGS-LEO	Downlink	1.5	10.000	OOK	Direct	
2018 2020	Optel-µ (Europe/RUAG)	Deep Space-OGS OGS-LEO	Bidirectional	1.5/1.06	2.000	OOK and PPM	Direct	400 to 900
2019	JDRS (Japan)	OGS-GEO	Uplink	1.5	1.800	DPSK	Direct	≈ 38.000

Table 1-3 : Overview of several past and planned OGS-Satellites optical links

NASA has continued and expanded its optical communication program since the success of Lunar Laser Communication Demonstration (LLCD) which we gave detail in previous table. NSAS's next related mission is the Laser Communication Relay Demonstration (LCRD) [21]. The LCRD program is scheduled to launch to GEO in June 2019 which will be a hosted payload on the US Air Force Research Lab (AFRL) Space Test Program's STPSat-6. In addition, it is designed to complete the Ka-band RF single access service on the next generation of NASA's near-Earth relays.

Figure 1-8 summarizes the planned next generation relay constellation in GEO in 2025. While the initial demonstration may use existing NASA optical ground stations, there are also plans to develop low-cost optical ground stations to support such rates.
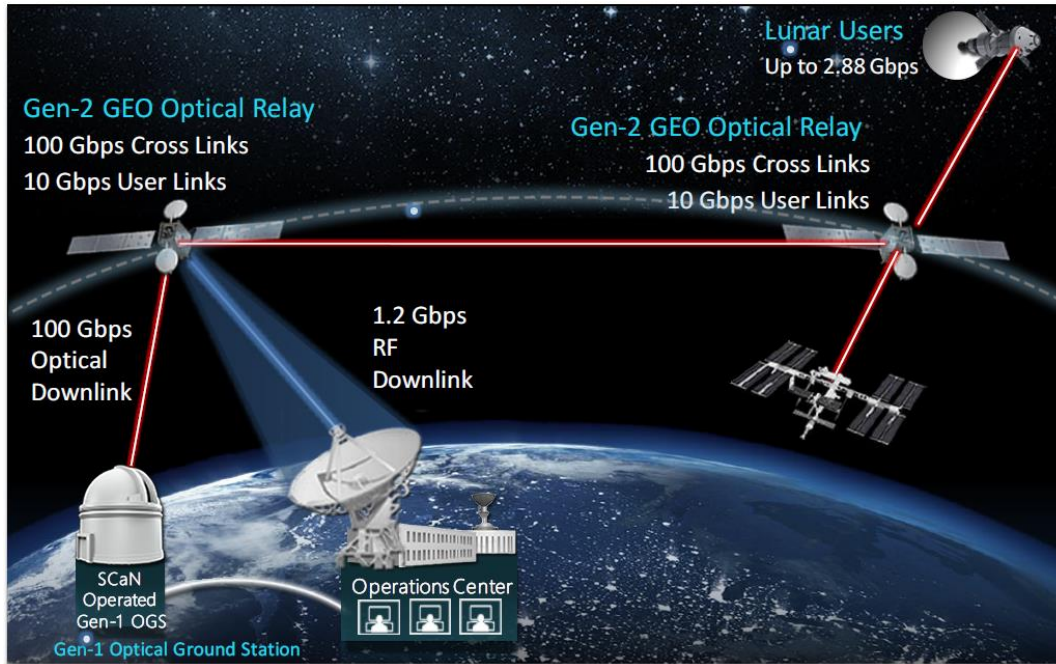
Figure 1-8: NASA's next generation relay constellation in GEO in 2025 [22]

In Japan, the first bi-directional laser communications demonstration using the Laser Communication Equipment on the ETS VI satellite was successfully performed by the communications Research Laboratory (CRL). The Japanese OICETS satellite was launched in August 2005 and the inter-orbit optical communication link experiment was successfully established [23], [24]. Figure 1-9 plots the data rate trend for space qualified laser communication missions as a function of launched year.
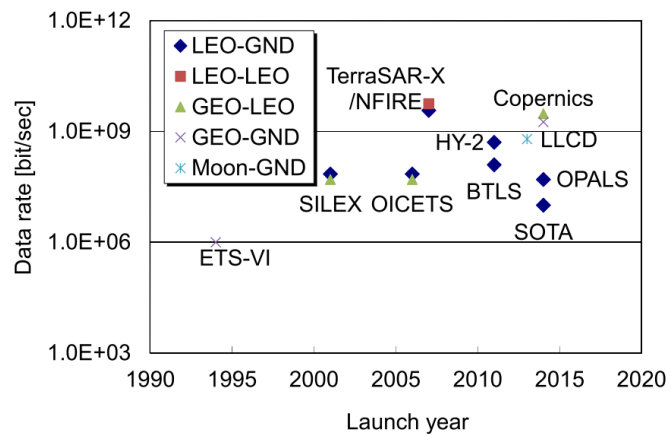
Figure 1-9: Data rate trend for FSO missions as a function of launch year [11]

As the figure shows, the maximum data rate has been increasing and two streams can be observed. One is for high speed communications on the order of several Gbps, for which the term *high data throughput* is used. The second stream is to moderate speed communication for which the term *low complexity* is used. The possible working areas within space laser communication and specific characteristic are discussed in the Consultative Committee for Space Data Systems (CCSDS) but all terms and directives have not yet been finalized [25].

1.3.3.4   Laboratory demonstration

The German Aerospace Center (DLR) in collaboration with Fraunhofer Heinrich Hertz Institute (HHI) have developed a Terabit-per-second Long-Range Free Space Optical Transmission test bench named the THRUST-Testbed dedicated to emulate GEO feeder link [26]. The testbed targets specifically the effect of the index-of-refraction turbulence (IRT) onto the Tbps DWDM signal beam in the uplink. Forty optical signals each carrying an OOK modulation with 43 Gbps data channel and based on Mach Zehnder Modulator (MZM) are multiplexed into one single mode fiber using DWDM technology. An EDFA amplifies the totality of these signals and the opto-mechanical assembly guides the beam towards the receiving terminal. At the receiver, a DWDM demultiplexer separates the different channel wavelengths which are detected using individual direct detection receiver [27].

For the propagation channel, two effects are emulated in the optical bench: scintillation and errors pointing. The scintillation is the result of self-interference process due to phase distortion produced by small scale index of refraction fluctuations. The pointing errors resulting from the beam wandering cause strong fading on the received signal. Thereby in FSO communication by satellites, pointing and tracking procedures that can minimize beam wandering are used.

The main objectives of this project is to demonstrate an optical communication through the atmosphere with a throughput over 1Tbps under realistic turbulence environment, to characterize the communication link with atmospheric turbulence and to minimize the turbulence impact in the received signal [26].

1.4   Link budget

The link budget is an accounting of all gain and losses that gives an indication of the overall performance of the link. It estimates the received optical power P_R as a function of the emitted optical power P_E, taking into account the losses in the atmospheric propagation. Two examples of uplink budget and downlink budget are detailed in order to illustrate different loss during atmospheric propagation. Most of the terms and quantities appearing in the uplink budget are the same as in the downlink case where only important ones are discussed. More details about link budgets are shown in the Optical Link Study Group: Final Report [28]. We have to emphasize that the link budget deals with average optical powers and does not take into account directly the quality of the signal that is the signal to noise ratio (SNR). Hence the link budget has to be completed by other specifications that give the required quality of the signal at the emission associated with sensitivity of the receiver.

1.4.1   Uplink scenario

The optical ground terminal has to transmit a powerful laser beacon for the pointing and tracking process that allows the space terminal to track it. In order to mitigate the effect of atmospheric turbulence, the beacon would be transmitted as an incoherent superposition of several beams (4 apertures for the Lunar Atmosphere and Dust Environment Explorer (LADEE) demonstration) emitted from corresponding separate sub-apertures from mutually incoherent sources. For the LADEE uplink demonstration, the link budget is illustrated in Table 1-4.

LINK BUDGET	
Tx Ave Power	**40.00 dBm**
Tx Antenna Gain	109.66 dBi
Tx Array Gain	6.02 dBi
Tx Transmission Loss	-3.34 dB
Tx Pointing Loss	-1.56 dB
EIRP	**120.78 dBW**
Isotropic Space Loss	-309.86 dB
Atmospheric Loss	-1.94 dB
Irradiance at rx aperture	**412.6E-09 W/m^2**
Rx Antenna Gain	106.77 dBi
Rx Array Gain	0.00 dB
Rx Transmission Loss	-4.81 dB
Rx Pointing Loss	-1.24 dB
Total Optical Path Loss	**-100.32 dB**
Ave Power at Rx Detector	**-60.32 dBm**
Req. Irradiance at rx aperture	63.0E-09 W/m^2
Link Margin (Irradiance)	**8.16 dB**

Table 1-4: Link budget of the LADEE demonstration illustrating an uplink scenario [28]

According to the link budget, the irradiance at the receiver aperture is higher than required irradiance in order to complete successfully the acquisition procedure. The dBi means decibels relative to an isotropic antenna. The link margin defined by the difference of the required irradiance and the received irradiance equals 8.16 dB. If we compare the average optical power sent and received, a difference of around 100 dB has to be noted that corresponds to the total optical path loss.

Under the same condition and for the same demonstration, a link budget of downlink scenario is illustrated in the next part.

1.4.2   Downlink scenario

If we consider broadband access scenario, bidirectional links are essential for getting the data coming from the users and for integrating acknowledgement and retransmission protocols such protocols cope with atmospheric disturbances. This aimed to prevent the loss of data during the redirection of the link to a second telescope if the first had to be totally obscured by clouds. An example of link budget of this protocols transmission is shown in Table 1-5.

LINK BUDGET

Tx Ave Power	**26.99 dBm**
Tx Photons / Pulse	1.25E+10
Tx Antenna Gain	106.77 dBi
Tx Transmission Loss	-4.82 dB
Tx Pointing Loss	-0.31 dB
Isotropic Space Loss	-309.86 dB
Atmospheric Loss	-1.44 dB
Rx Antenna Gain	118.18 dBi
Array Gain	6.02 dB
Rx Transmission Loss	-3.34 dB
Rx Pointing Loss	0.00 dB
Rx Fiber Coupling Loss	-3.57 dB
Total Optical Path Loss	**-92.38 dB**
Ave Power at Rx Detector	**-65.39 dBm**
Photons / Pulse at Rx Detector	**7.26E+00**
Required Photons / Pulse	3.74
Link Margin	**2.88 dB**

Table 1-5: Link budget of the LADEE demonstration illustrating a downlink scenario [28]

Comparing to the uplink, the link margin is smaller in the case of the down link due to the difference between the average sent power (40 dBm for uplink and 27 dBm for the downlink). Basically, the electrical power is limited on-board the satellite so the emitted power is constraint. In addition, the receiver antenna gain for the downlink is 12 dB more than the receiver antenna gain for the uplink due to the telescope size that is bigger on the case of downlink. Again, the weight and size of equipment are limited on-board whereas on-ground we are less constrained.

The next part is dedicated to the link performances assessment used to evaluate the strength of an optical communication link through the atmosphere.

1.5   Link performances assessment

This part is dedicated to introduce assessments that we will use to evaluate an optical link performance. The most important one is the Bit Error Rate (BER) that gives information about the average number of erroneous bits after its propagation through the atmosphere or a model of the atmosphere. For a given transmission setup, we can define the receiver sensitivity that corresponds to the mean received optical power to achieve the target BER (signal quality). This sensitivity level is then injected in the optical link budget for sizing the system. The link budget takes then into account the quality of the signal and not only average optical powers. The power fading is another important parameter that we will use to estimate the time duration corresponding to data that are lost due to an atmospheric induced burst of attenuation.

1.5.1   Bit Error Rate

One of the most used parameters to evaluate the performance, of a transmission is the BER. But, the important question for FSO communication system operated in the presence of turbulence is, how does optical turbulence affect the BER?

Due to the detection noise that is induced by optoelectronic devices and the small received optical power, there is a non-negligible probability to detect the wrong bit state. In the case of OOK modulation, there are two possibilities that can degrade the BER:

- The detection of one ''1'' while a ''0'' was transmitted
- The detection of one ''0'' while a ''1'' was transmitted

For each case, we define the error probability corresponding respectively to the probabilities to obtain ''1'' or ''0''. They will be noted $P(1|0)$ and $P(0|1)$.

The BER can be measured after reception as the rate between the erroneous bits and the total sent bits:

$$BER = \frac{Number\ of\ erroneous\ bits}{Total\ number\ of\ bits} \tag{1.1}$$

Assuming that the probability of sending ''0'' and ''1'' are respectively p_0 and p_1, the BER can be written as:

$$BER = p_0 P(1|0) + p_1 P(1|0) \tag{1.2}$$

On the case of Gaussian approximation and for an equiprobable source of data ($p_1 = p_0 = \frac{1}{2}$), the BER can be written using the complementary error function complementary ($erfc$):

$$BER = \frac{1}{2}[P(1|0) + P(1|0)] = \frac{1}{4}\left[erfc\left(\frac{I_1 - I_D}{\sigma_1}\right) + erfc\left(\frac{I_D - I_0}{\sigma_0}\right)\right] \tag{1.3}$$

Where I_1, I_0, σ_1 and σ_0 are respectively the mean levels and the standard deviations of distributions of '1' and '0' and I_D is chosen to verify $\frac{d(BER)}{dI_D} = 0$ and can be expressed as:

$$I_D = \frac{I_0\sigma_0 + I_1\sigma_0}{\sigma_0 + \sigma_1} \tag{1.4}$$

The Figure 1-10 shows an example of the detected signal including the detection threshold.
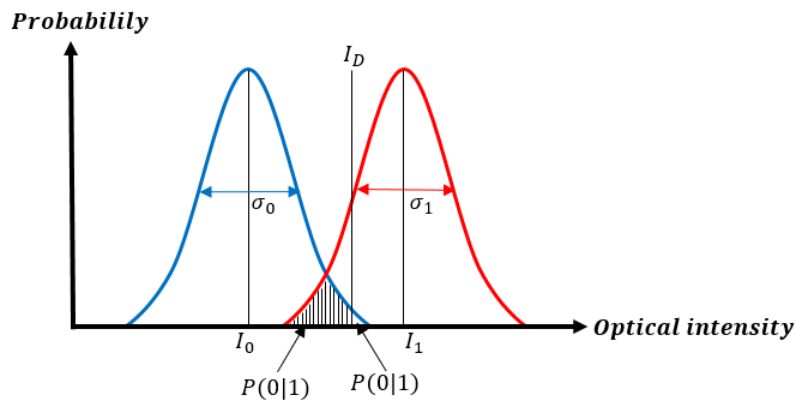
Figure 1-10: Illustration of the bit errors sources

By injecting (2) in (1), the BER becomes:

$$BER = \frac{1}{2} erfc\left(\frac{(I_1 - I_0)}{\sqrt{2}(\sigma_0 + \sigma_1)}\right) = \frac{1}{2} erfc\left(\frac{Q}{\sqrt{2}}\right) \approx \frac{1}{Q\sqrt{2\pi}} e^{-\left(\frac{Q^2}{2}\right)} \tag{1.5}$$

With

$$Q = \frac{(I_1 - I_0)}{(\sigma_0 + \sigma_1)} \tag{1.6}$$

In this manuscript, we will focus on the OOK and DPSK modulation and we will give the theoretical trends of BER.

Considering that the post-detection noise is dominant in the transmission and the noise distribution can be approximated as Gaussian. Assuming that both symbols have identical noise variance and are equally likely to be transmitted, the decision threshold level is set halfway between the symbols currents. The BER can therefore be expressed as a function of the Signal-to-Noise Ratio (SNR) as [29]:

$$BER_{OOK} = \frac{1}{2} erfc\left(\frac{1}{2\sqrt{2}}\sqrt{SNR}\right) \tag{1.7}$$

where $erfc(x)$ is the complementary error function given by $erfc(x) = \frac{2}{\sqrt{\pi}} \int_x^\infty e^{-t^2} dt$. By the same way and under ideal transmission condition, the BER of DPSK is given by:

$$BER_{DPSK} = \frac{1}{2} erfc\left(\frac{1}{\sqrt{2}}\sqrt{SNR}\right) \tag{1.8}$$

1.5.2 Entropy and mutual information

In probability theory and information theory, the mutual information (MI) of two random variables is a measure of the mutual dependence between the two variables. More specifically, it quantifies the amount of information obtained about one random variable through the other random variable. In addition, the mutual information is used to evaluate the channel capacity that corresponds to the maximum of mutual information. For OOK optical modulation, the received samples of both states of the modulation (0 and 1) follows an asymmetric Gaussian distribution around the mean value.

Assuming that the symbols emitted during successive intervals are statically independent and for a stochastic process for which the samples 0 and 1 are denoted by the random variables X and Y, the mutual information is given by $I(X;Y) = H(X) - H(X|Y)$ where $H(X)$ and $H(X|Y)$ are respectively the entropy and the conditional entropy [30]. The mutual information can be given by [31]:

$$I(X|Y) = \sum_{x \in \{0,1\}} \int p(x)p(y|x) \log\left(\frac{p(y|x)}{p(y)}\right) dy \tag{1.9}$$

For the error code correcting layer that could be used on the receiver to recover the lost data, the mutual information gives more information about the received data correlation than the BER [32]. An example will be detailed in section 4.5.

1.5.3 Receiver sensitivity

As a definition, the receiver sensitivity is the minimum value of average received power to achieve the specified BER value. Due to atmospheric effects, the optical power fluctuates and for low power value, the receiver does not receive enough power to decode the information. In FSO communication, the objective value of BER is 10^{-9}. Values between 10^{-3} and 10^{-9} could be improved by using an error code correcting in order to recover a part of erroneous data and improve the BER [33]. For value higher than 10^{-3}, the optical communication is considered totally lost and the received data are cannot be

exploitable. Table 1-6 gives ideal value of receiver sensitivity for optically preamplified OOK and the Differential Phase Shift Keying (DPSK) receivers for both NRZ and RZ pulses [34]. More information will be given in the next chapter.

	NRZ OOK	RZ OOK	RZ DPSK	NRZ DPSK
BER =10^{-6} sensitivity (ppb)	27 (-44.6 dBm)	60 (-41.1 dBm)	16 (-46.8 dBm)	19 (-46.1 dBm)
BER =10^{-9} sensitivity (ppb)	38 (-43.1 dBm)	35 (-43.7 dBm)	20 (-45.9 dBm)	30 (-44.1 dBm)

Table 1-6: Receiver sensitivity values for OOK and DPSK modulation for 10 Gb/s

The average optical power used to be given by photons per bit (ppb) or dBm. They are related by the following relation:

$$P_{ppb} = \frac{10^{\left(\frac{P_{dBm}-30}{10}\right)}}{h\nu R} \tag{1.10}$$

where P_{ppb} and P_{dBm} are respectively the average optical power expressed on ppb and dBm, R is the data rate communication, ν is the frequency of the light and h denotes the Planck's constant.

For 10 Gb/s transmissions, optically pre-amplified, single mode receiver architectures are the most practical as the components are widely available and near quantum limited sensitivities have been achieved [35]. The quantum limit power for an optically preamplified receiver at 10 Gb/s is around 38 photons per bit (ppb) for 10^{-9} of BER, which corresponds to -43 dBm. Several experiments were done to evaluate the receiver sensitivity and most of them give values between -40 dBm and -37 dBm at 10 Gb/s for a BER of 10^{-9} in [35] [34] [36] [37]. For receivers using APD photodetectors, the best sensitivity at 10 Gb/s achieved by Tzeng [38] equals -28.7 dBm.

The BER depends on both short-term errors resulting from electronic-circuit related noise and the turbulence induced long-term random breaks in communication data known as atmospheric signal fading. The short-term data losses can be partially recovered using various data coding techniques [33], [39][28] but the signal fading induced by atmospheric layers represents the main challenge faced by FSO communication systems through the atmosphere.

According to the state of the art of free space scenarios detailed in Table 1-3, the receiver sensitivities are summarized and plotted as a function of the communication data rate in Figure 1-11.
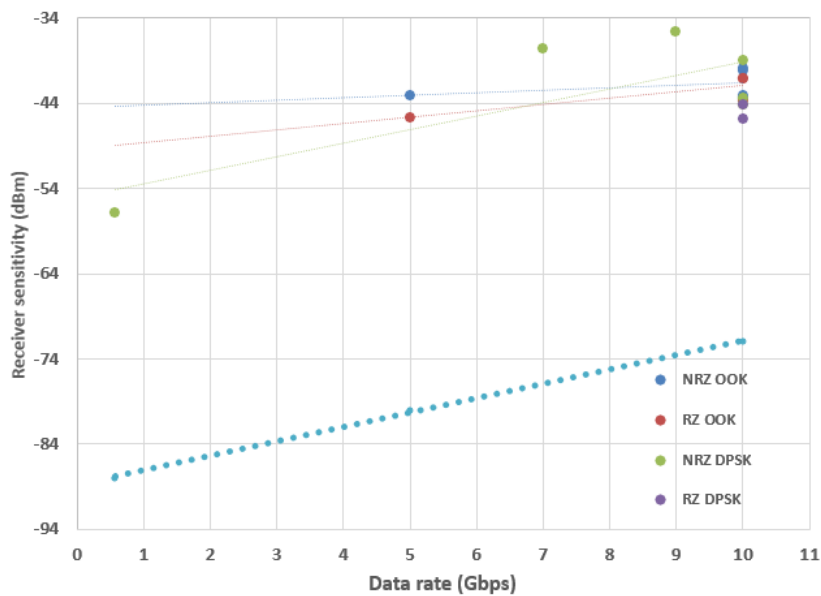
Figure 1-11: Receiver sensitivity for BER =10^{-9} for different optical modulation

1.5.4   Fade duration and compensation

The distortion caused by atmospheric scintillations are responsible for severe signal fading in FSO communication systems and therefore compromise link reliability. We define the fading time as the time duration that the average received optical power stays under the receiver sensitivity given by a target (we often take $BER = 10^{-9}$). In addition, the fading duration includes the required delay time to establish the link communication when the turbulence conditions decrease.
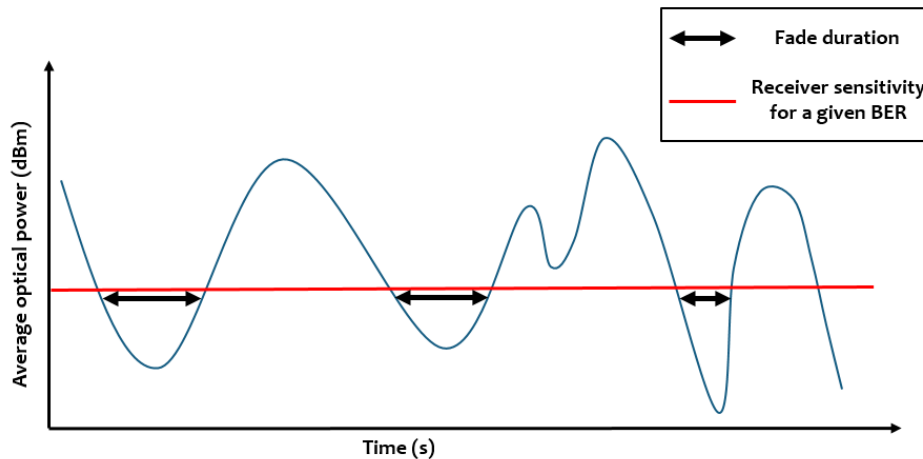
Figure 1-12: Illustration of the fading time for a given BER level (average optical power received after atmospheric propagation)

Under different levels of scintillation, there are different statistic models to describe the distribution of channel states. For weak turbulence condition, the most widely accepted model is lognormal turbulence model [41]. For moderate strong turbulence conditions, Gamma-Gamma turbulence models are often used [42].

1.5.4.1   Error correcting code

High data rate over a time-fading channel (atmospheric layers) can be successfully achieved thanks to forward error correction techniques [43] such as low-density parity-check (LDPC) codes and turbo codes that are at the heart of the latest standards for satellite communication. Fade duration in the order of tens of milliseconds can be compensated by a careful choice of the coding scheme. In order to limit the complexity, the redundancy can be split over two-stage codes: an inner code is intended to correct bit errors due to the channel noise, while an outer code is used to compensate losses due to fading noise.

1.5.4.2   Interleaving

Symbol time-interleaving is also mandatory to overcome errors bursts that are characteristic of FSO optical channel. An example is given by Figure 1-13 in which the error correcting codes assumed to be able to recover the information of 1 bit lost within a 4 bits words.
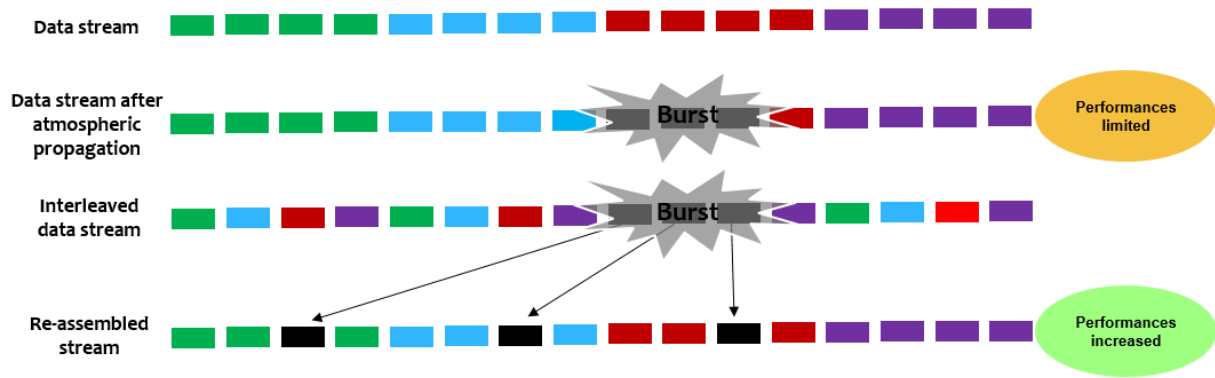
Figure 1-13 : Benefits of interleaving process on the case of burst causing a part of data stream losses.

In this example, the data stream to be sent is comprised of packets of 4 bits. Without the interleaving, the red packet loses 3 of the 4 bits and the error correcting code could not be able to recover the information. By applying the interleaving process, the 3 bits lost are distributed onto 3 different packets and the data recovering by FEC is possible. However, the interleaving process needs high memory sizes to mix the data stream before sending it to the channel.

1.5.5   Adaptive optics

The adaptive optics (AO) system is a servo system which modifies in real time the emitted wave front in order to pre-compensate or post-compensate the wave front deformation due to atmospheric turbulence. In addition, due to the Earth's rotation during the beam's propagation, the point-ahead angle (PAA) between the downlink and the uplink has to be considered and make the turbulences effects slightly different for the two paths [20], [33], [44]–[46].

As a result, these effects have to be taken into account for the AO system to ensure the right compensation for each case (uplink or downlink). Figure 11 shows the simplified principle of pre-compensation using adaptive optics in case of plane waves.
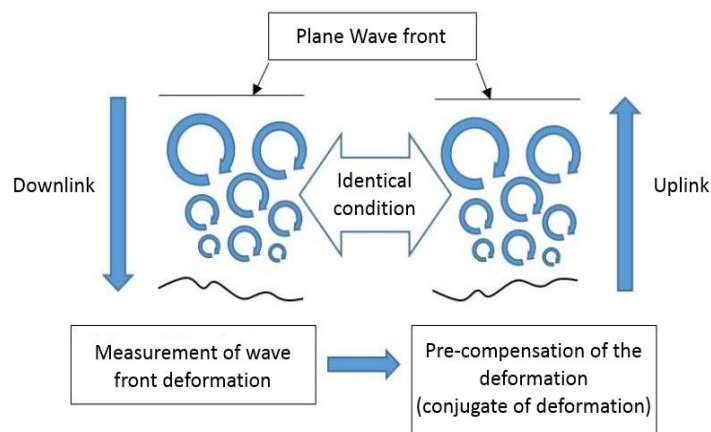
Figure 1-14: Adaptive optics correction in case of plane waves

The major objective for incorporation of adaptive optics systems into FSO communication is the active prevention of long-term data loss rather than data recovery. The challenge is the real-time control with very short time lock of the active components such as the wave-front sensor in order to make communication signal less likely.

1.5.6 Multiple aperture receivers

Various diversity techniques have been proposed in the literature to eliminate the influence of the atmospheric turbulence. The use of a multiple aperture with coherently superposed receiving systems presents an important potential to overcome atmospheric layers effects [47]. This technology is particularly interesting for downlink optical feeder because the beam size after the propagation which can reach more than hundreds meters for uplink (beam deviation over a long distance), reaches only tens of meters in the downlinks. Thereby, a multiple aperture system used on the ground (downlinks) can support such complex systems while the satellite cannot support it that can increase satellite weight.

In this configuration, the information signal is transmitted via a single aperture trough the atmosphere layers and then received by multiple apertures on the ground. Each aperture recovers the optical signal to be coupled in fiber respectively. An example is done by C. Lao [48] where a multiple aperture system is investigated using DPSK optical modulation. Its schematic view is given in Figure 1-15.
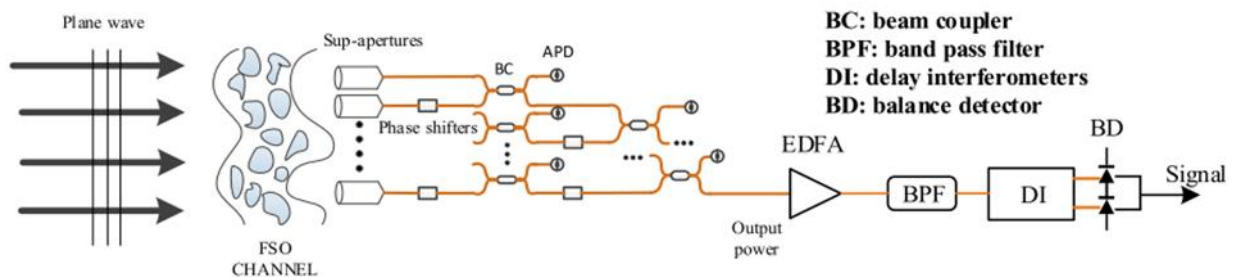
Figure 1-15: Schematic view of direct detection DPSK multiple aperture receiver system for the FSO downlink communication [48].

All branches in the receiver have to be sufficiently separated to guarantee that the turbulence effect in each sup-aperture is independent and identically distributed. C.Lao has also studied the influence of the number of aperture and coupling efficiency [48].The most advantage is that the required OSNR at the receiver present a benefit of 3 dB compared to single aperture.

To summarize, a multiple aperture technology could be an alternative to adaptive optics and especially when the number of apertures increased. Instead of using the deformable mirror, optical phase shifters are used, in a certain manner, to equalize the wavefront spatial phase distortions. Despite different benefits that this technology can bring, the optical system complexity is increased by increasing the number of needed components. (i.e. the system cost). The requirement for high speed loop control is not solved compared to the AO system.

1.5.7 Coupling efficiency into single mode fiber

There are two main types of optical receiver for space applications, the low complexity and the high complexity. The low complexity is based on APD. It takes advantage of the wide collection area of the APD and the complex fiber injection mechanism is banished. This receiver is simple and low cost but its data rate is limited by three main factors: the intrinsic sensitivity of the APD, the APD bandwidth, and the complexity to build a free space optical multiplexer with a huge number of channels. Regarding this limitation in terms of maximal reachable data rate, the high complexity receiver is preferred. It is based on low noise optical amplifier (LNOA) and PIN photodiode. The bandwidth of the PIN is widely greater than the APD and the overall sensitivity is improved compared to the low complexity receiver. However, the optical amplifier requires the injection of the light in the fiber. As the objective is to reuse

a maximum of the technologies developed for the terrestrial telecommunications, the majority of the components are single-mode. Hence the fiber injection mechanism is required to inject in a single mode fiber which increase the complexity of the system.

This mechanism makes the link between the free space pupil of the telescope and the fiber-guided part that begins typically with the optical amplifier. However, the atmospheric mitigations (introduced in 1.3.1) may strongly degrade the coupling efficiency of the incoming optical signal to the fiber.
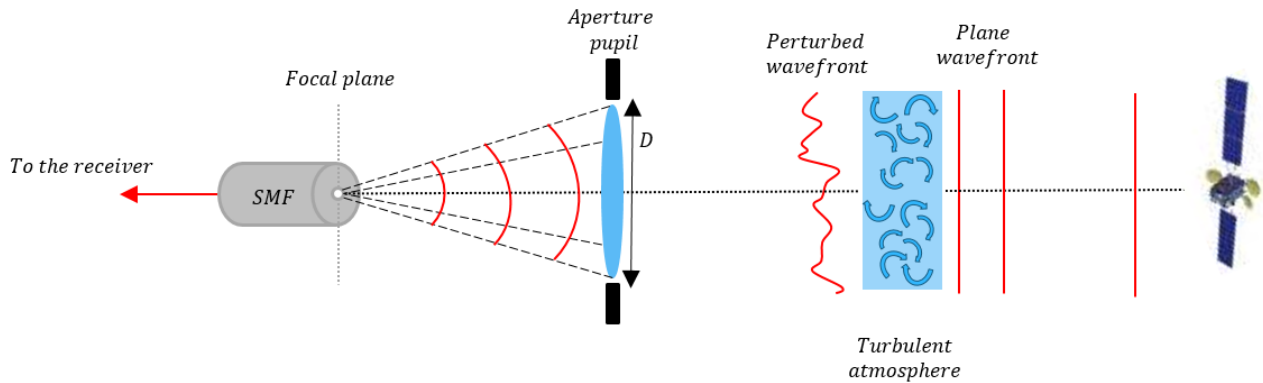
Figure 1-16: Illustration of a downlink optical wavefront through the turbulent atmosphere with the receiving aperture and the SMF

The complex amplitude of an electromagnetic field propagating through the atmosphere could be noted as:

$$\Psi(r,t) = A_0 e^{(\chi(r,t)+ j\phi(r,t))} \tag{1.11}$$

Where $\chi(r,t)$ corresponds to fluctuations induced by the atmospheric turbulences and, $\phi(r,t)$ represents the phase variation induced by the aberrations [49] and A_0 denotes the complex field amplitude without perturbation.

In the pupil plane, the coupling efficiency is given by:

$$\rho(t) = |\Omega(t)|^2 \tag{1.12}$$

Where $\Omega(t)$ the matching of the pupil with the SMF mode (considered as a Gaussian noted $M_0(r)$, given by [49]:

$$\Omega(t) = \frac{\iint P(r).\Psi(r,t).M_0^*(r)d^2r}{\left(\iint P(r).\Psi(r,t).\Psi^*(r,t)d^2r \iint P(r).M_0(r).M_0^*(r)d^2r\right)^{\frac{1}{2}}} \tag{1.13}$$

$P(r)$ denotes the pupil transmittance given by:

$$P(r) = \begin{cases} 1 & if\ 0 \leq \frac{2|r|}{D} \leq 1 \\ 0 & otherwise \end{cases} \tag{1.14}$$

S. Shaklan and F. Roddier [49] have calculated that ~80% of the power incident at the pupil can be coupled into the SMF placed on the axis in the focal plane. This efficiency injection decreases in the case of strong turbulences.

The coupling efficiency of the freely propagation optical field into an SMF is defined as the ratio of the average power coupled into the fiber to the average available power in the focal plane. It is given by:

$$\eta_f = \frac{\langle P_f \rangle}{\langle P_i \rangle} = \frac{\langle |\int E_B(x,y)F_B^*(x,y)dxdy|^2 \rangle}{\langle \int |E_B(x,y)|^2 dxdy \rangle} \tag{1.15}$$

where $E_B(x,y)$ is the distribution of the focused optical beam on the focal plane and $F_B(x,y)$ is the normalized fiber mode profile when the normalized frequency V of the SMF is in the range of $1.9 \leq V \leq 2.4$.

During the atmospheric propagation, the spatial coherence of the signal beam is degraded by atmospheric turbulence which limits the NMF coupling efficiency. The influence of turbulence on the coupling efficiency has been analyzed over various turbulence strength. The results detailed in [50] illustrates the SFM coupling efficiency drops from 81% without phase distortion to 10% in the case of strong turbulences. In addition, AO shows that it is inevitable to compensate the high-order aberrations in strong turbulence but in average turbulence condition the coupling efficiency maybe increased from 10 % to 46.1 % [50]. Figure 1-17 illustrates the effect of the lens parameters (diameter and focal distance ratio) on the coupling efficiency.
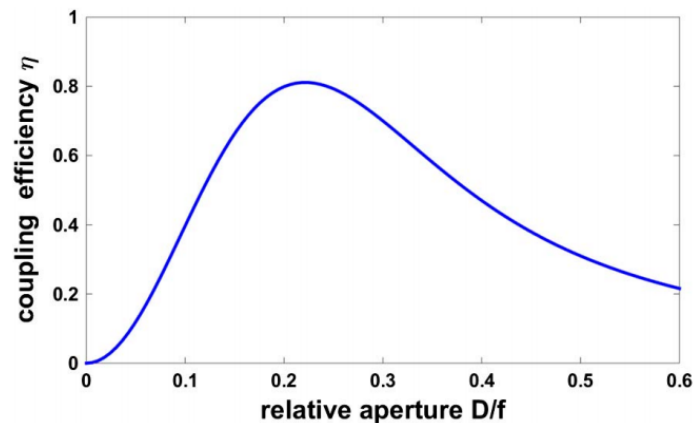
Figure 1-17: Relationship between coupling efficiency and the relative aperture of the coupling lens [50]

1.5.8   Coherent receiver systems

In order to increase the link performances after atmospheric turbulence, a coherent optical receiver may be used on the ELLA bench. In the coherent communication system, the transmitted information can be encoded in the complex electric field, including amplitude, phase and polarization. The coherent receiver measures these degrees of freedom by beating the received signal with a local oscillator (LO). Through the turbulence, the coherence of the signal can be reduced and the use of a single-element detector with uniform LO beam will produce mismatch of the amplitudes and phases of the fields. Thereby the detection by multiples apertures leads to reduce the probability of deep fades where detection efficiency have been studied [51].

As for the muti-aperture detectors, if the apertures are sufficiently separated, fades in different apertures of the coherent receiver can be considered statically independent. A. Belmonte and J. Kahn have demonstrated that using coherent arrays with a reasonably small number of hexagonal sub-apertures (around 20 apertures) increases the communications performance by several decibels [51].
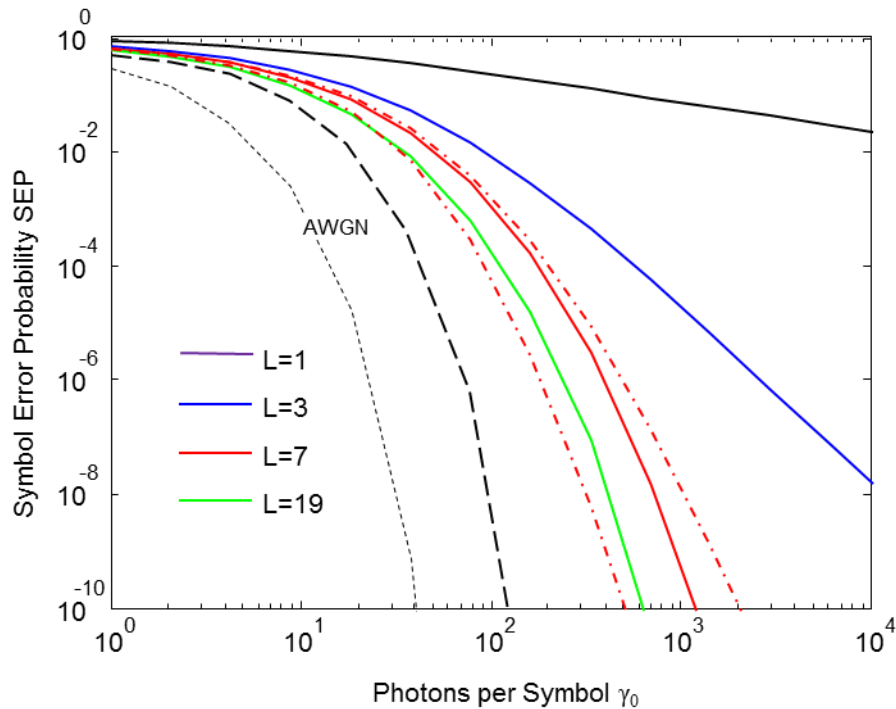
Figure 1-18: Symbol error probability (SEP) as a function of photon per symbol for different number of sub-aperture (L) using coherent receiver.

Figure 1-18 illustrates the evolution of the symbol error probability (SEP) for different number of sub-apertures. It can be remarked that the required photons per symbol to achieve the same SEP is higher when the number of sub-apertures is low. As a conclusion, when the multi-apertures is considered, the performance improves markedly.

The next part gives the structure of the thesis manuscript including the main objectives to be achieved and the steps followed.

1.6 Thesis objectives and structure

1.6.1 Thesis objectives

The global objectives of the work detailed in this dissertation is to study the free space optical communication architectures for ground-to-satellite and satellite-to-ground links. The first one is to study the main parameters of the transmitters and the receivers in order to improve the link performances for several optical modulations (NRZ OOK, RZ OOK, NRZ DPSK and RZ DPSK). These model performances will be estimated using the receiver sensitivity that depends directly on the receiver component parameters, the Bit Error Rate with given levels and the fading time due to the propagation through the atmospheric turbulence.

The next objective is to detail the atmospheric layers that the optical beam will cross and give a model taking into account the atmospheric effect on the communication link performances. Theoretical and simulation models are considered to provide the closest model to the realistic optical wave propagation in the atmosphere, obviously taking into account the model's complexity and the necessary time to estimate the atmospheric mitigations and fluctuations. As a result, this model will provide the time series describing the atmospheric propagation effects (low turbulences or high turbulences) that we can use for both simulation and experiment models.

Then, we will validate our simulation model on an optical bench designed to work for both OOK and DPSK modulation and able to multiplex up to 4 channels. A dynamic attenuator is used to consider the power variations using time series to emulate the atmospheric effects on the optical bench.

Finally, a development of a free space optical bench to build a more realistic low order turbulences atmospheric is developed. It includes a Digital Micro-Mirror (DMD) that it used to disturb the optical beam wavefront using Zernike polynomials. This experience presents several issues such as the optical alignment using lens and sensors areas. The single mode fiber injection to recover the disturbed optical beam is also considered before sending the optical signal to the receiver. The link performance could then be estimated.

This manuscript will include the previous objectives and the main results obtained with all needed details to understand the free space optical communication scenarios.

1.6.2   Thesis structure

This first chapter briefly underlined the state of the art of FSO communication through the atmosphere and the associated challenges. In addition, it includes the plan and the objectives of the thesis work.

In chapter 2, we detailed the fundamentals of the atmospheric propagation effects and the main concepts as well as the basics of optical wave propagation theory. The time series describing atmospheric propagation will be described by detailing the model used to generate it.

The chapter 3 is dedicated to the simulation of FSO communication chain using both of OOK and Differential Phase Shift Keying (DPSK) modulations. We will focus only on the communication chains using these modulations with different duty cycle in order to detail parametric effects of the link components on the communication performances and the receiver sensitivity. The data rate objective of our communication links is 10 Gbps for one optical channel and many channels will be multiplexed in order to raise the capacity link. The last part of this chapter is dedicated to compare the link performances with theoretical values.

Chapter 4 is dedicated to the experiment models developed to emulate an end-to-end FSO link emulating the atmospheric propagation. An optical fibered bench using both of OOK and DPSK modulations is implemented and described by illustrating its performances and detailing its limits. Two different ways to emulate the atmospheric turbulences are investigated and their associated components are added to the fibered bench in order to complete the FSO model. The last part gives the main experiment results achieved with the optical bench that are compared to the simulation results detailed in the previous chapter.

Finally, the last chapter summarized the work realized during this thesis and especially, the difficulties encountered to achieve the experimental models. The perspectives and recommended propositions of the ELLA bench are also detailed in order to perform the FSO activities developed at the IRT.

Thanks to the works coming from Camboullives's PhD study which a complete model was developed with different turbulence scenarios [52]–[54].

Chapter 2

2 System design for Feeder link optical communication

Free space optical communication through the atmosphere is becoming the main subject of satellite applications and recent field of research. Finding optimal transceivers and link architectures are under active investigation. In this chapter, we will describe the functionality and component of each part of the free space optical communication links. The modeling of On Off Keying (OOK) and Differential Phase Shift Keying (DPSK) communication subsystems is described and detailed. Except for studying each part for the link, the data rate chose for communication link is 10 Gbps. Then, we will extend the architectures to multichannel using a wavelength division multiplexing system (WDM) to increase the data rate up to 40 Gbps. The optimization of the system communication is investigated according to the communication standard recommendations for several system parameters.

2.1 Introduction

Free space optical communication through the atmosphere is becoming the main subject of satellite applications and recent field of research. Finding optimal transceivers and link architectures are under active investigation. In this chapter, we will describe the functionality and component of each part of the free space optical communication links. The modeling of On Off Keying (OOK) and Differential Phase Shift Keying (DPSK) communication subsystems is described and detailed. Except for studying each part for the link, the data rate chose for communication link is 10 Gbps. Then, we will extend the architectures to multichannel using a wavelength division multiplexing system (WDM) to increase the data rate up to 40 Gbps. The optimization of the system communication is investigated according to the communication standard recommendations for several system parameters.

2.2 Optical communications links subsystems

This section details the optical detection and modulation generations techniques studied in the framework of this thesis. For the detection, both of direct detection and balanced detection are described and used for given transmitters.

2.2.1 Optical modulations

The first optical modulation considered is the On Off Keying (OOK) optical modulation that is very mature on terrestrial fiber connection with hundreds Gbps of data rate. In addition, the (OOK) modulation is also used because the transmitter and the receiver hardware are relatively simple and fiber optic networks generally operate at high signal-to-noise (SNR) with small dynamic range requirements. Also known as binary amplitude shift keying, OOK is a form of intensity modulation (IM) which binary information represented by the presence or absence optical signal within symbol. Then, the receiver will convert this presence or absence to 1-bit or 0-bit logical decision according to the received symbol energy that compared with a predetermined threshold. For the FSO communication, and with the complexity of the atmosphere propagation part, the ground-to-satellite link was demonstrated with just tens Mbps data rate [1][2]. For this modulation, two formats are included in this modulation group: Non Return to Zero (NRZ) and Return to Zero (RZ).

The second optical modulation we will study is DPSK modulation. In a differential encoding scheme, each bit behaves as a phase reference for the next bit. In addition, the data is encoded on the binary phase changes between adjacent bits using differential precoding where a 1-bit is encoded onto a π phase shift whereas 0-bit corresponds to no phase change. As a comparison with OOK, the symbol spacing for DPSK increases by a factor of $\sqrt{2}$ with the same average optical power [56]. This advantages can be understood by comparing the constellations diagram of both modulations. In the case of OOK the difference between two symbols equals the signal energy, E_S, assuming NRZ pulse coding, an infinite extinction ratio and an average optical power of $\frac{1}{2}|0|^2 + \frac{1}{2}|E_S|^2 = \frac{1}{2}|E_S|^2$. For DPSK, both constellation points have the same signal energy but a differential phase of either Δɸ = 0 or Δɸ = π. By using the same average power calculation, we DPSK average power is the same as OOK: $\frac{1}{2}\left|\frac{\sqrt{2}}{2}E_S\right|^2 +$ $\frac{1}{2}\left|\frac{\sqrt{2}}{2}E_S\right|^2 = \frac{1}{2}|E_S|^2$. However, as the symbol distance is increased with a factor of $\sqrt{2}$ in a comparison to OOK modulation, the total intersymbol states power is two time more than OOK ($P_{OOK} = 2.P_{DPSK}$) which explains a 3 dB improvement of OSNR [57], $P_{OOK}(dB) = 3\ dB + P_{DPSK}(dB)$. This improvement

will be an important advantage for the receiver sensitivity which can insure the same performances level with less power in comparison with OOK.
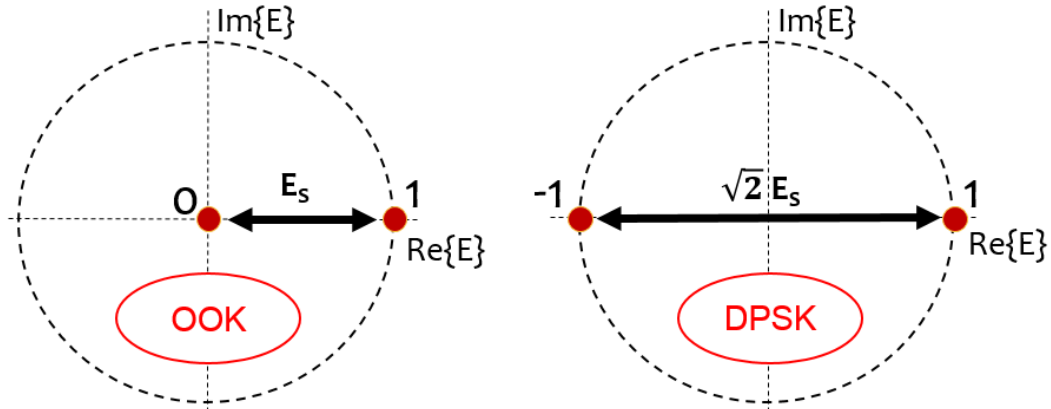
Figure 2-1: Diagram constellation for OOK and DPSK modulation having the same average power.

2.2.2   Optical windows and carriers

For our applications and because of the absorption at certain wavelengths by molecules existing in the atmosphere, there is a limited number of the emission windows we can use for optical communication through the atmosphere. The loss in the atmospheric channel is described by Beer's law [58].

The wavelength range of FSO communication system is chosen to have minimal absorption. Some typical values of atmospheric molecular absorption coefficients are given in table 1.

Wavelength range (nm)	Molecular Absorption (dB/Km)
550	0.13
690	0.01
850	0.41
1550	0.01

Table 2-1: Molecular absorption at typical wavelengths [4]

Majority of FSO systems are designed to operate in windows of 1520-1600 nm (C-band) because of the readily availability of the transmitter and detector components at these wavelengths. To generate an optical source with a constant amplitude, frequency and phase is impossible due to the spontaneous emission with random phase that are added to the output field.

Assuming that the instantaneous power of the optical field emitted by a continuous wavelength laser source is a stationary random process denoted $P_{CW}(t)$ with the average value is P_0, we can write the instantaneous laser output field and power [59] :

$$E_{cw}(t) = \mathcal{R}e\left(\sqrt{P_{cw}(t)}.\,e^{i\omega_0 t}.\,e^{-i\varphi(t)}\right) \; where \; \|E_{cw}(t)\|^2 = P_{cw}(t) \tag{2.1}$$

$$P_{cw}(t) = P_0 \left(1 + \frac{\widetilde{P(t)}}{P_0}\right) \; with \; \widetilde{P(t)} = \langle\, P_{cw}(t)\rangle \tag{2.2}$$

Where $\frac{\tilde{P}}{P_0}$ is the power ratio corresponding to power fluctuation due to noise such as Relative Intensity Noise (RIN), phase noise and Amplified Spontaneous Emission noise (ASE) that have to be considered to increase the FSO communication link performances.
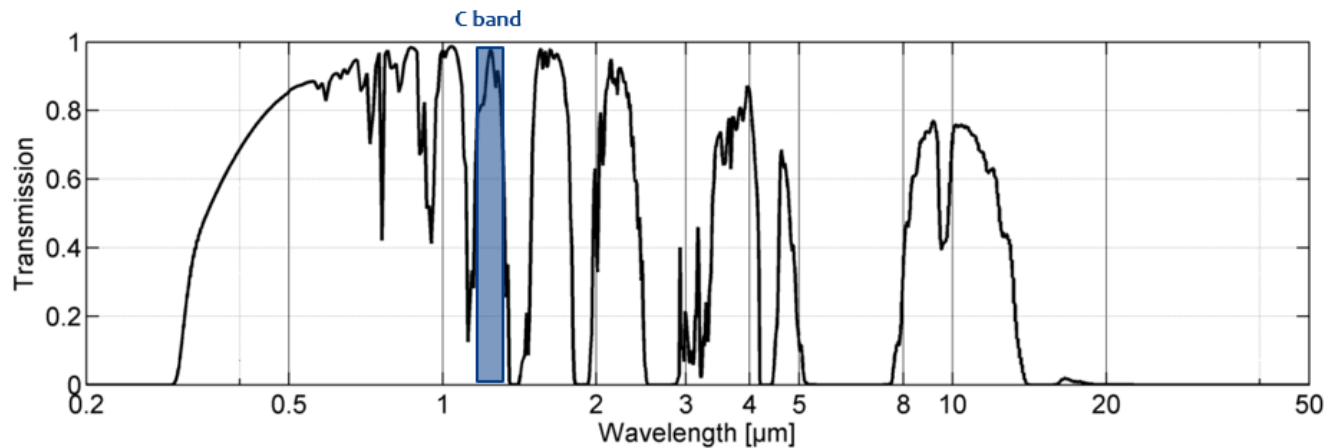
Figure 2-2: Atmospheric transmission as a function of communication wavelength [60]

2.2.3   Noise sources

The relative intensity noise (RIN) describes the instability in the power level of a laser source that can be generated from the cavity vibration, fluctuation in the laser gain medium or from transferred intensity noise from a pump source (EDFA). Hence, when the SNR is limited by the RIN, it does not depend on laser power. For FSO optical communication, the RIN can be generated on-board as other various noise sources (thermal noise, dark noise, shot noise, …) that leads to increase the BER of the communication link.

The RIN is calculated in the electrical domain after many calibrations of the detector. For a typical device its value is around $-110\,dB/Hz$ where the low RIN value could verify $RIN < -160\,dB/Hz$ [61].

The next part is dedicated to introduce OOK optical modulation link where different components and their main parameters are described.

2.2.4   OOK communication link

2.2.4.1   NRZ OOK Transmitter

OOK optical modulation is realized by switching the output of laser ON or OFF according to the information to be transmitted. The transmitter structure NRZ OOK modulation is depicted in Figure 2-3. For the data generation, a Pseudo Random Binary Sequence (PRBS) is used to drive the optical modulator through a driver amplifier in order to adjust the data level and insure the right transcription from RF domain to optical domain.
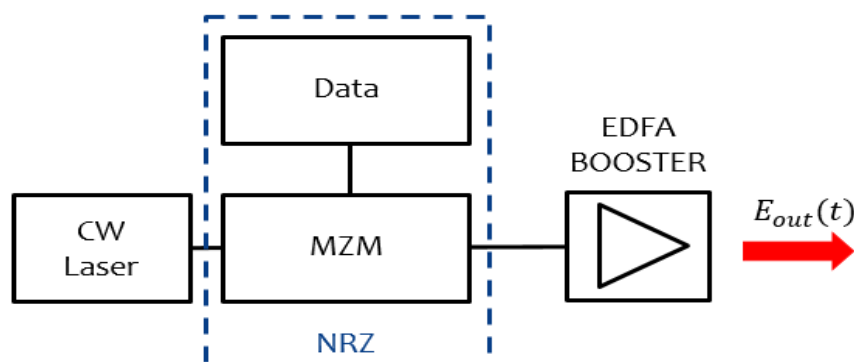
Figure 2-3: Transmitter structure for NRZ OOK modulation

2.2.4.1.1   Mach Zehnder modulator

Mach-Zehnder Modulators are used for external modulation which offer the possibility of modulating both of intensity and phase with wide-band characteristics. A simplified scheme of the MZM modulator is shown in Figure 2-4:

$V_1(t)$

$E_{in}(t)$ $E_{out}(t)$

$V_2(t)$
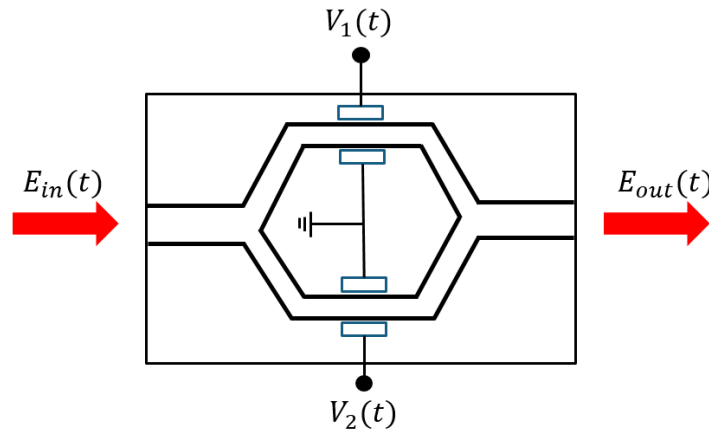
Figure 2-4: schematic view of a MZM waveguides

This modulation is obtained by switching the laser source between ON and OFF and achieved by modulating the output of the laser using a MZM. In addition, the modulator is biased at 50% of transmission that is known as quadrature point. In this configuration, the data electrical signal will switch between the maximum and the minimum to ensure the electro-optic conversion. It consists in splitting the input optical signal into two parts reacting as a 50/50 coupler. The two signal paths make up the two interferometer's arms. To create the intensity modulation, two voltages, denoted $V_1(t)$ and $V_2(t)$ are applied to both of arms, equipped with phase shifters, to introduce the phase difference. Finally, both arms are recombined into an output waveguide. The optical field ''transfer function'' T_E of an MZM intensity modulator driven by denoted $V_1(t)$ and $V_2(t)$ can be expressed as:

$$T_E\big(V_1(t), V_2(t)\big) = \frac{E_{out}(t)}{E_{in}(t)} = \frac{1}{2}\big(e^{i\varphi(V_1)} + e^{i[\varphi(V_2)+\varphi_0]}\big) \tag{2.3}$$

where φ_0 is an additional constant phase shift in one of the arms, $\varphi(V_1)$ and $\varphi(V_2)$ are the optical signal phase of both arms that can be expressed as:

$$\varphi(V_1) = \varphi_1(t) = \frac{V_1(t)}{V_\pi}\pi \quad and \quad \varphi(V_2) = \varphi_2(t) = \frac{V_2(t)}{V_\pi}\pi \tag{2.4}$$

V_π is the required voltage to obtain a phase shift of π in each arm, making the modulator switching from the maximum to the minimum of signal transmission. For the NRZ OOK modulation, the data electrical signal is generated using a pseudo-random bit sequence (PRBS) which corresponds to both $V_1(t)$ and $V_2(t)$ to insure the amplitude modulation. The optical spectrum and eye diagram of the NRZ OOK transmitter with R data rate is given in Figure 2-5:
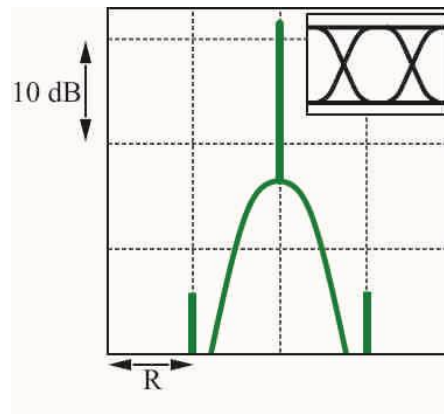
Figure 2-5: Optical spectrum of NRZ OOK transmitter for R Gbps (top left: eye diagram)

The optical spectrum for optical communication is an important characteristic of any modulation format to be employed to raise communication data rate using a Dense Wavelength Division Multiplexed (DWDM) systems. Most information of the communication performances could be extracted from the optical spectrum such as the optical filter required for low distortion and crosstalk or channel spacing necessary to be used for multiplexed system. In the NRZ OOK optical spectrum, the spectrum has a strong component on the frequency corresponding to the optical carrier and the associated lobe contains more 90% of optical power. Figure 2-6 illustrates the obtained NRZ OOK optical signal.
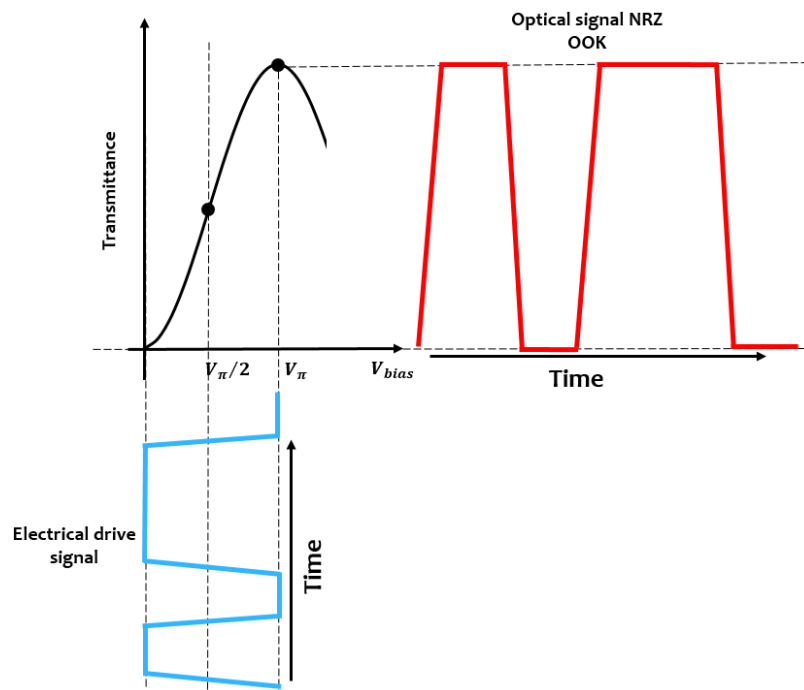
Figure 2-6: Generation of the NRZ OOK optical signal

2.2.4.1.2   Pulse carver and duty cycle

For the RZ OOK, a second MZM is used at the output of the first one named Pulse Carver that can manage the duty cycle of pulses (Figure 2-3).
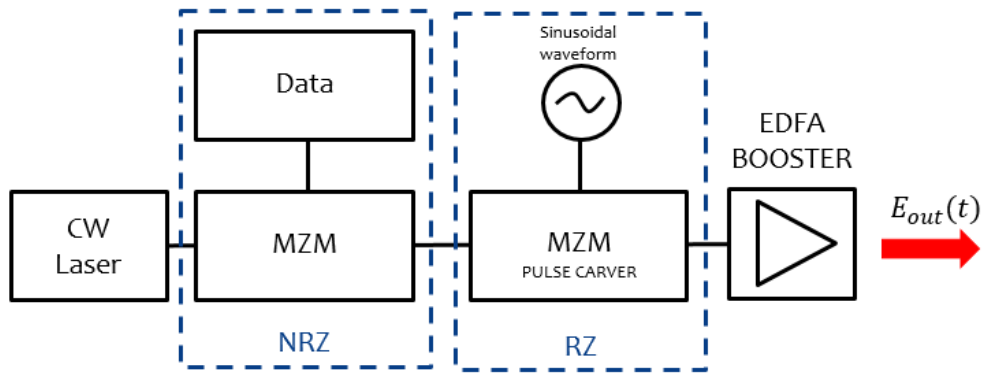
Figure 2-7 : Transmitter structure for RZ OOK modulation

Previously, the benefits of RZ formats were often overlooked because the generation requires two MZM modulators. Fortunately, in recent years, it has been demonstrated that RZ pulses can have superior performances over NRZ where nonlinearities are present [33]. In addition, RZ formats has greater tolerance to polarization variation during the propagation [34].

We assume throughput this dissertation that RZ formats are generated by driving the pulse carver by a sinusoidal drive waveform. We define the pulse duty cycle with, T_{FWHM}/T_S where T_{FWHM} is time duration of the Full-Width measured at Half-Maximum intensity and T_S is the symbol duration. This ratio depends on the drive waveform amplitude and three duty cycles values will be studied that are 33%, 50% and 67%. Here are the three ways that the pulse carver needs to be derived (Figure 2-4):

- For 33% duty cycle: The bias point must be at the maximum of transmission and driven with a sinusoid signal with an amplitude of $2V_\pi$ and a frequency $R/2$
- For 50% duty cycle: The pulse carver is biased in the quadrature point with R electrical signal frequency with a peak to peak amplitude of $V\pi$
- For 67% duty cycle: In this case, the pulse carver must be biased in the middle of two maxima with $R/2$ electrical signal frequency with amplitude of $2V_\pi$.
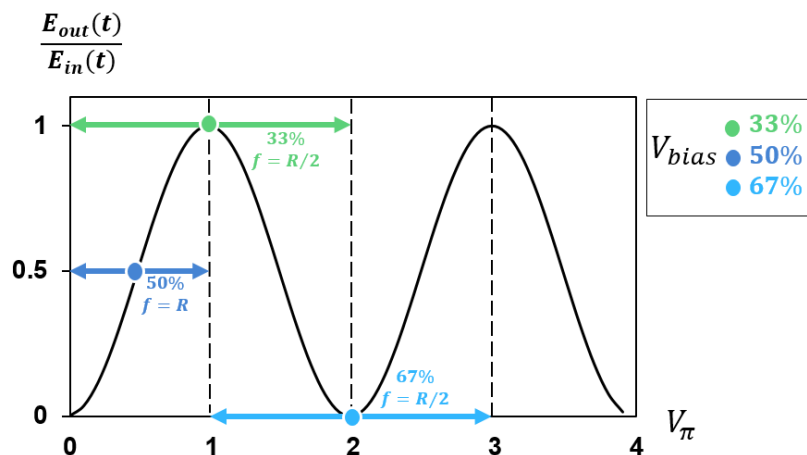
Figure 2-8: Different ways to drive the pulse carver in order to generate RZ pulses

For 33 % RZ OOK, the optical spectrum and eye diagram is shown in Figure 2-8:
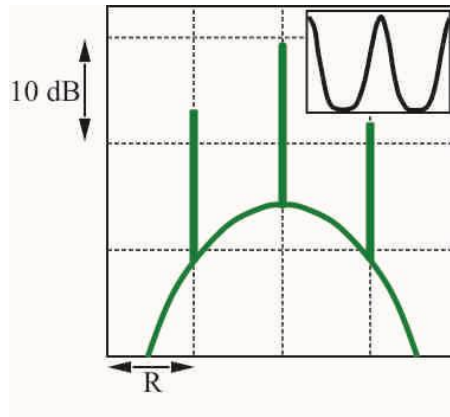
Figure 2-9: Optical spectrum of 33% RZ OOK transmitter @ R Gbps (top left: eye diagram)

The primary advantage of reducing the duty cycle is the higher peak power in a time duration which is less than the bit time making pulses more strong for the confinement. As a result, short duty cycle permits to increase the receiver sensitivity due to its low InterSymbol Interferences (ISI) between adjacent bits.
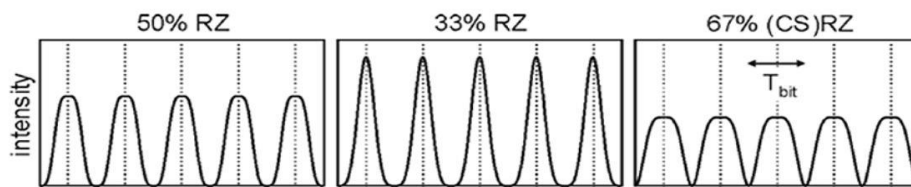
Figure 2-10: Theoretical RZ pulses for 33%, 50% and 67% [62]

For the short duty cycles, most of bit energy is focused on the middle of the bit time. On the frequency domain, it corresponds to having a large central optical lobe containing up to 90% of bit energy. The table 2 summarizes the effect of the RZ pulses on the optical spectrum.

Duty Cycle	33%	50%	67%	100% (NRZ)
Optical spectra				
Principal lobe width	47 GHz	33 GHz	26 GHz	20 GHz
Secondary lobe width	***	14 GHz	12 GHz	10 GHz

Table 2-2: the effect of reducing the duty cycle on the optical spectrum @ 10 Gb/s

2.2.4.1.3   Booster amplifier

The most common type of optical amplifier are Erbium doped fiber amplifiers (EDFA). They are constructed by doping a single mode fiber with Erbium (Er^{3+}) ions and pumping the fiber with one or more pump lasers. The wavelength of the pump signal is either around 980 nm or 1480 nm. The typical gain of an EDFA can be around 40 dB and the output power depends on the number of pump lasers and their respective pump powers. In addition, their gain over bandwidth is managed to be flat output spectrum in order to ensure uniform amplification that is necessary for WDM channels [57].

The Figure 2-11 illustrates energy level diagram of an EDFA with both of 980 nm and 1480 nm pumping scheme. The principle of amplification, in the case of 980 nm pumping, consists on exciting Erbium ions from the fundamental state E_1 to the excited state E_3 thanks to the pumping laser. However, the excited state is not stable and Erbium ions are soon dropped to the metastable state E_2 waiting for the population inversion conditions. This transition is named relaxation [63] that can be non-radiative (from E_3 to E_2) or radiative as the spontaneous emission (from E_2 to E_1) . When an optical signal of c-band wavelength passes through this doped fiber, particles in the metastable state are transited to the fundamental level via stimulated radiation and generate photons identical to the photons of the incident signal. In the case of 1480 pumping, the difference from 980 nm pumping remains on avoiding the excited state and simulated radiation of Erbium ions still identical then 980 nm pumping between the metastable state and the fundamental.
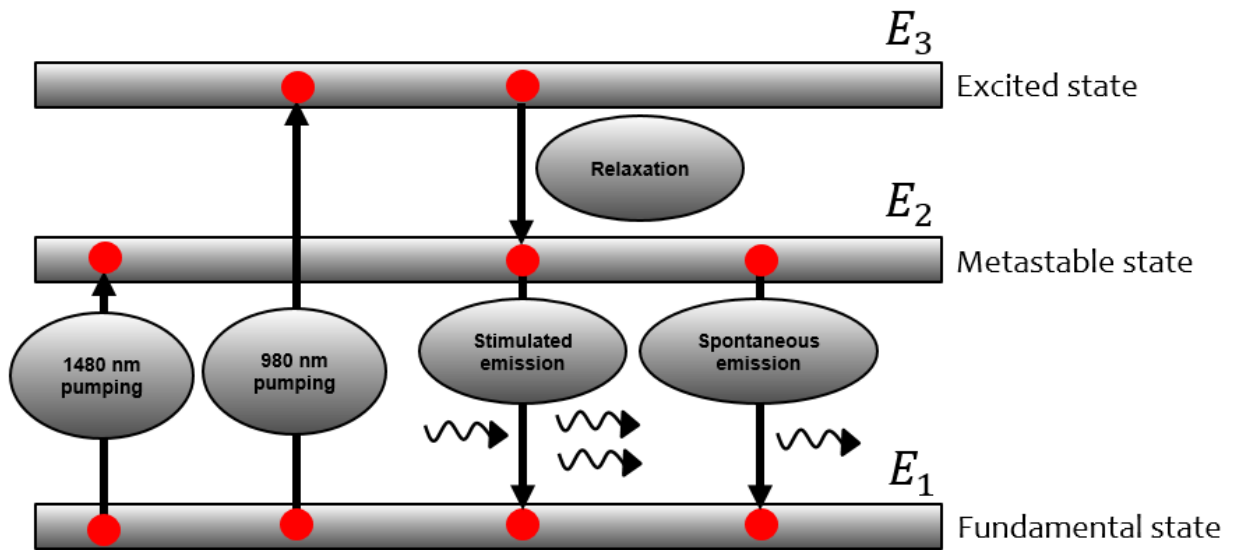
Figure 2-11: Energy level diagram of an EDFA for 980 nm and 1480 nm pumping.

The optical signal amplification gain G of an EDFA is given here after:

$$G(dB) = 10.\,log_{10}(P_{out}/P_{in}) \tag{2.5}$$

The most important parameter to qualify an amplifier performance is the noise figure F_n that depends on the signal-to-noise (SNR) ratio at the input and the output on the EDFA. The SNR serves as a measure of the quality of the signal and noise levels in the photocurrent of a photodetector placed in the signal path. Therefore, the SNR can be calculated in terms of the received signal photocurrent, i_{sig} and the variance of received photocurrent noise, σ_n^2 [64][65].
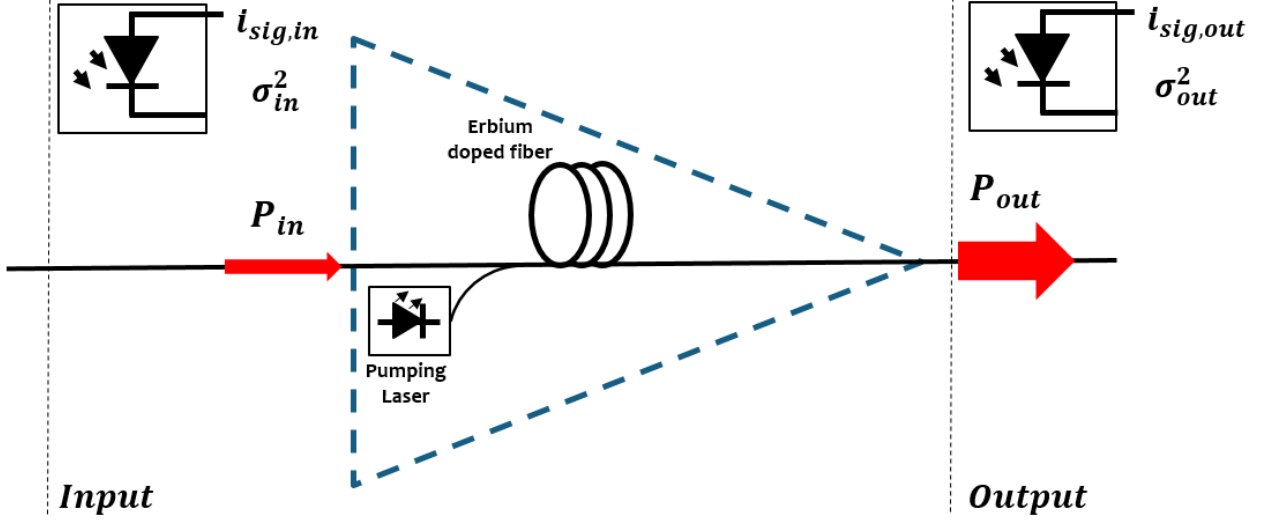
Figure 2-12: EDFA's components and main parameters

$$SNR = \frac{\langle i_{sig} \rangle^2}{\sigma_n^2} \text{ and } F_n = \frac{SNR_{in}}{SNR_{out}} \tag{2.6}$$

The received photocurrent noise concerns all noise generated before the estimation. Assuming the only noise at the input of the EDFA is the shot noise and defined to be shot noise limited. For the EDFA output and because of the amplified spontaneous emission (ASE) on the amplifier, we consider that the shot noise and the signal-to-ASE beat noise predominate over ASE-ASE beat noise. Consequently, SNR_{in} and SNR_{out} by [57][66]

$$SNR_{in} = \frac{\langle i_{sig,in} \rangle^2}{\sigma_{shot,in}^2} = \frac{\Re^2 P_{in}^2}{\sigma_{shot,in}^2} = \frac{\eta P_{in}}{2h\nu B_e} \tag{2.7}$$

$$SNR_{out} = \frac{\langle i_{sig,out} \rangle^2}{\sigma_{shot,in}^2} = \frac{\Re^2 G^2 P_{in}^2}{\sigma_{shot,out}^2 + \sigma_{sig-ASE}^2} = \frac{\Re^2 G^2 P_{in}^2}{2q\Re G P_{in} B_e + 4\Re^2 G P_{in} N_0 B_e} \tag{2.8}$$

Where $\Re$ is photodetector responsivity given by $\Re = \eta.\,q/h\nu$, η is the photodetector quantum efficiency, $N_0 = n_{sp}(G-1)h\nu$ is the single side ASE power spectral density, where n_{sp} is the inversion coefficient and B_e is the baseband bandwidth of the noise. As a conclusion, the noise figure becomes [67][68]:

$$F_n = \frac{SNR_{in}}{SNR_{out}} = 2n_{sp}\left(1 - \frac{1}{G}\right) + \frac{1}{G} \tag{2.9}$$

The noise figure expression can be divided in two part, the first depending on the signal-to-noise beat noise and the second depending on the shot noise.

$$F_{n,sig-ASE} = 2n_{sp}\left(1 - \frac{1}{G}\right) \text{ and } F_{n,shot} = \frac{1}{G} \tag{2.10}$$

The typical value of EDFA's noise figure is between 3.5 dB and 9 dB [63] and it equals 4 dB for Low Noise Optical Amplifier (LNOA).

After describing all OOK transmitter components and their functionalities, we will describe now the needed passive and active components used to decode the OOK modulated signal.

2.2.4.2 Pre-amplified optical receiver for OOK modulation

The general principle used for the receiver to decode the OOK modulation is based on two different parts: pre-amplication part using a Low Noise Optical Amplifier (LNOA) and detection part based on PIN photodetector. Optical and electrical filters are also used to perform the optical signal after the atmospheric propagation. The Figure 2-13 shows the direct detection receiver with a pre-amplification part.
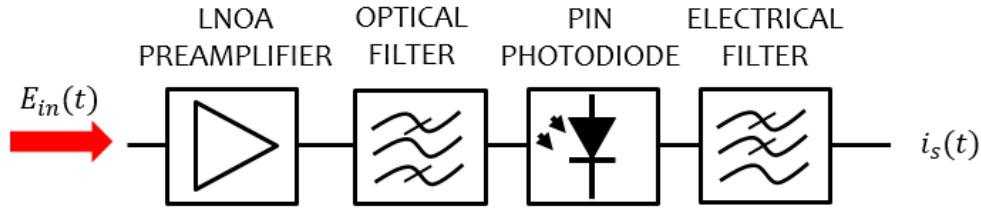
Figure 2-13: Préamplified optical receiver for direct detection

2.2.4.2.1 Pre-amplification

After atmospheric propagation of the optical beam, the signal is attenuated and when it arrives to the receiver, the noise level could be higher than the optical signal. For this reason, the use of LNOA on the first stage of receiver is important in order to amplify the signal before detection. The EDFA uses the same technology as an ordinary EDFA (described on 2.2.4.1.3) and the noise figure is given by the same equation

$$F_n = 2n_{sp}\left(1 - \frac{1}{G}\right) + \frac{1}{G} \tag{2.11}$$

The ideal linear value of noise figure for an EDFA equals 2 (corresponding to 3 dB) and it's obtained in the case of $n_{sp} = 1$ and for high gain value ($G \gg 1$).

2.2.4.2.2 Optical filtering

In various analyses of optically preamplified receivers, the optical filter had therefore been assumed to let the data pass undistorted [66][69]. In addition, the use of pass-band optical filter lead to suppress the potential accumulation of background noise and ASE noise [14][15]. The optical filter also makes the amplifier more stable by increasing the threshold of lasing at the ASE peak and can perform the pulse-shaping with removing out of band the ASE contribution that competes with the signal for gain [59]. They are based on interference, diffraction, or absorption and can have a fixed bandwidth value or tunable value. The choice of the technology filter depends on the application and the system design using optical filters. For preamplified optical receivers, the used passband filters are Fabry-Pérot Filter (FPF) and Fiber Bragg grating (FBG). The FBG is combined with a circulator to convert FBG's bandstop characteristics into passband characteristics [72]. The optical passbands of FPF and FBG filters under Lorentzian approximation are given by [70]

$$B_O^{FPF}(f) = \frac{1}{1 \quad + \quad i\frac{2f}{B_{FWHM}}} \tag{2.12}$$

$$B_O^{FBG}(f) = \frac{-i\kappa \sin[\beta(f)L_g]}{\tanh(\kappa L_g)\beta(f)\cos[\beta(f)L_g] - i2\pi\left(\frac{f}{v_g}\right)\cos(\beta(f)L_g)} \tag{2.13}$$

Where B_{FWHM} denotes the filter's full width at half maximum of transmission (or 3-dB bandwidth), κ is the grating coupling's coefficient, $\beta(f) = \sqrt{(2\pi f/v_g)^2 - \kappa^2}$ is the grating coupling coefficient, v_g is the group velocity and L_g is the grating length.

The value of FBG filer is designed to have the desired passband by adjusting L_g and κ.

2.2.4.2.3 Photo-detection

The main role of photodetectors is to convert the optical signal into photoelectric waveform and recover the data transmitted through the FSO and amplified by the LNOA. The requirements of photodetectors for embedded system are compact size, high efficiency, good reliability and small massive area that are met by photodetectors made from semiconductors materials. For FSO systems, the most used photodetectors are PIN photodiodes and avalanche photodiodes (APD) [73].

The PIN photodiodes have a layer of undoped semiconductor material, made by intrinsic material, between the p an n doped regions. When the optical signal arrives on the PIN photodetectors, most of incoming photons are absorbed is the intrinsic region that generate charge carriers which contribute to the photocurrent.

The responsivity $\Re$ is one of the most important parameters characterizing the quality of the PIN and is defined as the ration between the produced current and the received optical power. It is given A/W and its value depend on the quantum efficiency and the wavelength to be detected. The best commercialized PIN guarantee the responsivity values between $0.7\,A/W$ and $0.85\,A/W$ which depends on the wavelength and the PIN substrate. In addition, when we use PIN on the receiver, it has been demonstrated [34], [37], [70], [71] that better receiver sensitivity is achieved with the preamplified receivers using PIN compared to APD receivers. The responsivity is given by

$$\Re = \frac{\eta.q}{h\nu} \tag{2.14}$$

Where q denotes the electron charge in Coulomb and η is the quantum efficiency corresponding to the number of the photo-carriers generated per incident photon, noted $h\nu$ in joule.

The output photo-current is proportional to the photodiode responsivity and the amplitude field square, as we can show in the equation below:

$$i_{out} \propto \Re.E_s(t).E_s^*(t)$$
$$\propto \Re.\left(As(t)e^{(i\varphi_s)}\right)\left(A_s^*(t)e^{(-i\varphi_s)}\right) \tag{2.15}$$
$$\propto \Re.|As(t)|^2 \propto \Re.P_{in}$$

where $E_s(t)$ denotes the field of the optical signal, $As(t)$ is the complex amplitude of the optical signal, φ_s represents its phase and $\Re$ represents the responsivity of the photodetector.

The second type of photodetectors is APD photodiodes. It's designed differently from PIN by including an additional layer multiply the number of generated electron-hole. The main role of the second layer is to amplify the produced photocurrent. Moreover, the performance of an APD is characterized by its multiplication factor given by

$$i_{out} = M.i_s = M.\Re.P_{in} \tag{2.16}$$

For this reason, the use of a preamplification process is not necessary and makes the APD photodetectors more sensitive. Otherwise a PIN photodiode followed by an electronic amplifier could provide a good sensitivity and may be advantageous over an APD because of its low cost.

Therefore, all information about the polarization or phase are lost and the only exploitable information is the signal amplitude which is enough for OOK modulation.

2.2.4.2.4 Electrical filtering

After the optical filter and the PIN photodetector, the electrical signal can go through a low-pass filter in order to perform the detected signal. An electrical preamplification part may be used before the electrical filtering to ensure the required SNR level of the photo-detected signal. The impulse response of the entire electronics is denoted $h(t)$ and verifies $\int_{-\infty}^{+\infty} h(t)\, dt = 1$.

In the frame of this work, the electrical filter is assumed to have a fifth-order Bessel characteristics that is used in optical receivers, even at data rates in tens of gigabit-per-second regime thanks to its little overshoot [70]. The transfer function of the fifth-order Bessel filter is given by:

$$H_{BF}(f) = \frac{945}{if^5 + 15f^4 - 105if^3 - 420f^2 + 945if + 945} \tag{2.17}$$

Other type of electrical filters may be used presenting lower performance than of the fifth-order Bessel filter such as the first order RC low-pass or the first order Gaussian low-passer.

2.2.4.3 Noise sources on the direct detection receiver

In this part, we will detail noises generated when the amplification process is taking place for pre-amplified optical receiver. We now investigate the impact of the booster ASE on the signal-to-noise ratio (SNR) in an optically preamplified receiver. As we introduced previously, the received signal passes the EDFA, the optical band-pass and then the PIN photodetector. The induced current from the detected optical power is proportional to the amplification gain and the responsivity of the photodetector. Assuming that the ASE is a circularly symmetric complex stochastic process and using standard semi-classical method described in [74][71], The total noises variance can be written as:

$$\sigma_{Total}^2 = \sigma_{Thermal}^2 + \sigma_{Shot-ASE}^2 + \sigma_{ASE-ASE}^2 + \sigma_{ASE-sig}^2 + \sigma_{Dark}^2 + \sigma_{Shot-sig}^2 + \sigma_{RIN}^2 + \sigma_{Background}^2 \tag{2.18}$$

The next table details the expression of each noise contribution:

Noise contribution variance		Expression
Thermal noise	$\sigma_{Thermal}^2$	$(4.k_B.B_E.F_n)/R_L$
Shot − ASE beat noise	$\sigma_{Shot-ASE}^2$	$2.q.\Re.G.S_{ASE}.B_0.B_E$
ASE − ASE beat noise	$\sigma_{ASE-ASE}^2$	$4.\Re^2.G.P_{in}.S_{ASE}.B_0$
ASE − Signal beat noise	$\sigma_{ASE-sig}^2$	$2.\Re.S_{ASE}^2.B_0.B_E$
Shot − Signal beat noise	$\sigma_{Shot-sig}^2$	$2.q.R.G.P_{in}.B_E$
Relative intensity noise	σ_{RIN}^2	$2.R^2.P_{in}^2.RIN.B_0$
Backgound noise	$\sigma_{Background}^2$	$R^2.\alpha^2.\ P_{in}^2$
Dark noise	σ_{Dark}^2	$2.q.i_d.B_E$

Table 2-3: Noise contributions generated at the optically amplified receiver

Where k_B is the Boltzmann constant, B_E is the electrical filter bandwidth in GHz, F_n is the noise figure of the optical amplifier in dB, R_L is the load resistance in Ohm, B_0 is the optical filter bandwidth in

GHz, S_{ASE} is the power spectral density, q is the elementary charge and i_d is the dark current of the PIN photodiode in Ampère and RIN is the relative intensity noise given by Hz^{-1}.

The shot noise is generated in two ways: photons from optical signal and photons from ASE. This is why we have to take into account both of signal and ASE beat noises. The last three noises used to be neglected and many models include it in order to have a complete noise model. The background noise corresponds to photons coming from sources around the satellites i.e. light diffusion. We consider in this approximation that the parameter α corresponds to the percentage of the received optical power.

These noise contributions are studied in order to distinguish the dominant noise for different amplification gain and different receiver input power. The components parameters are set to the commercial values and the noise contributions are plotted as a function of the amplification gain and the received average optical power. These results are shown in Figure 2-14 and Figure 2-15:
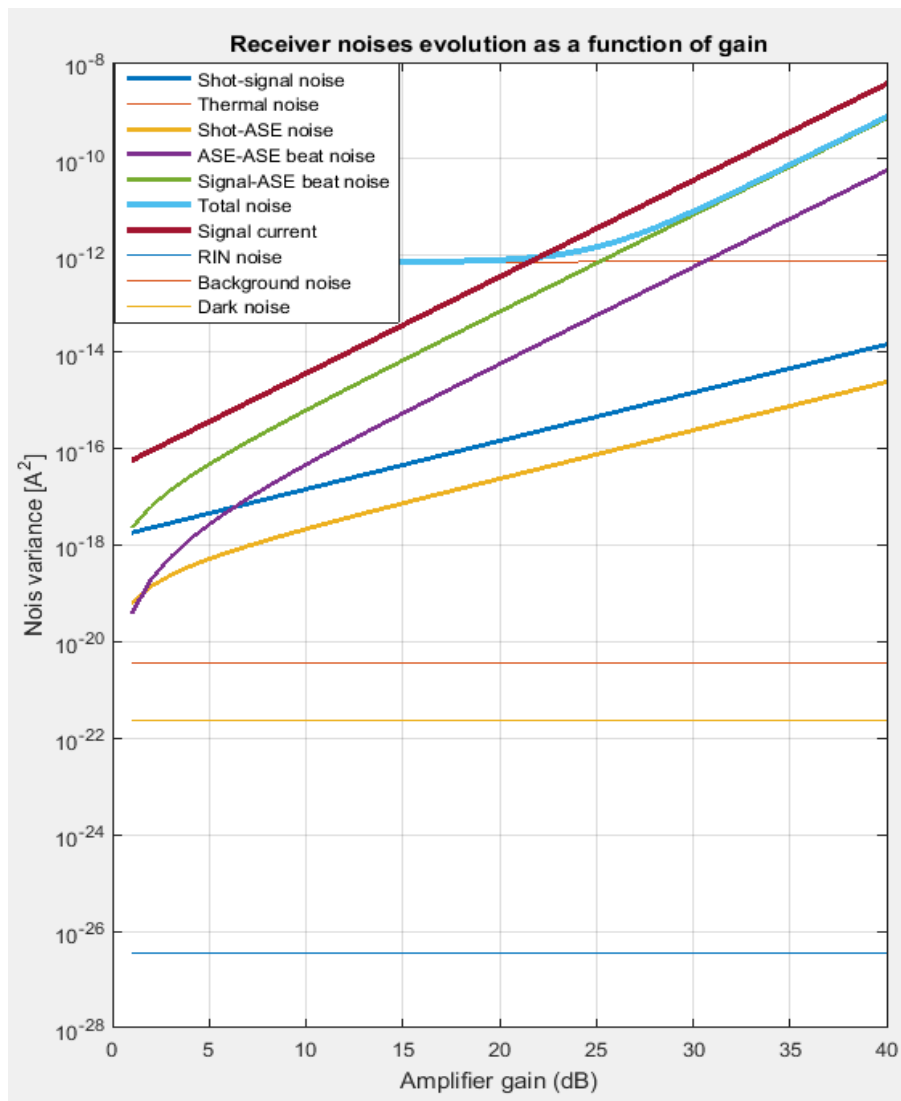
Figure 2-14: Variation of signal power and each noise variation as a function of amplifier gain

It is shown that the total noise dominates the signal optical current when the gain is less than 22 dB. Up to this limit, the thermal noise becomes the dominate noise where its value is approximately equal to the total noise. Beyond 22dB gain, the noise contributions are less important than the optical current. In such receiver parameters, an amplification gain more than 22 dB is necessary to insure an

optical communication link with less detected errors (low BER). Figure 2-15 summarizes the optical power at the receiver effect in each noise contributions.
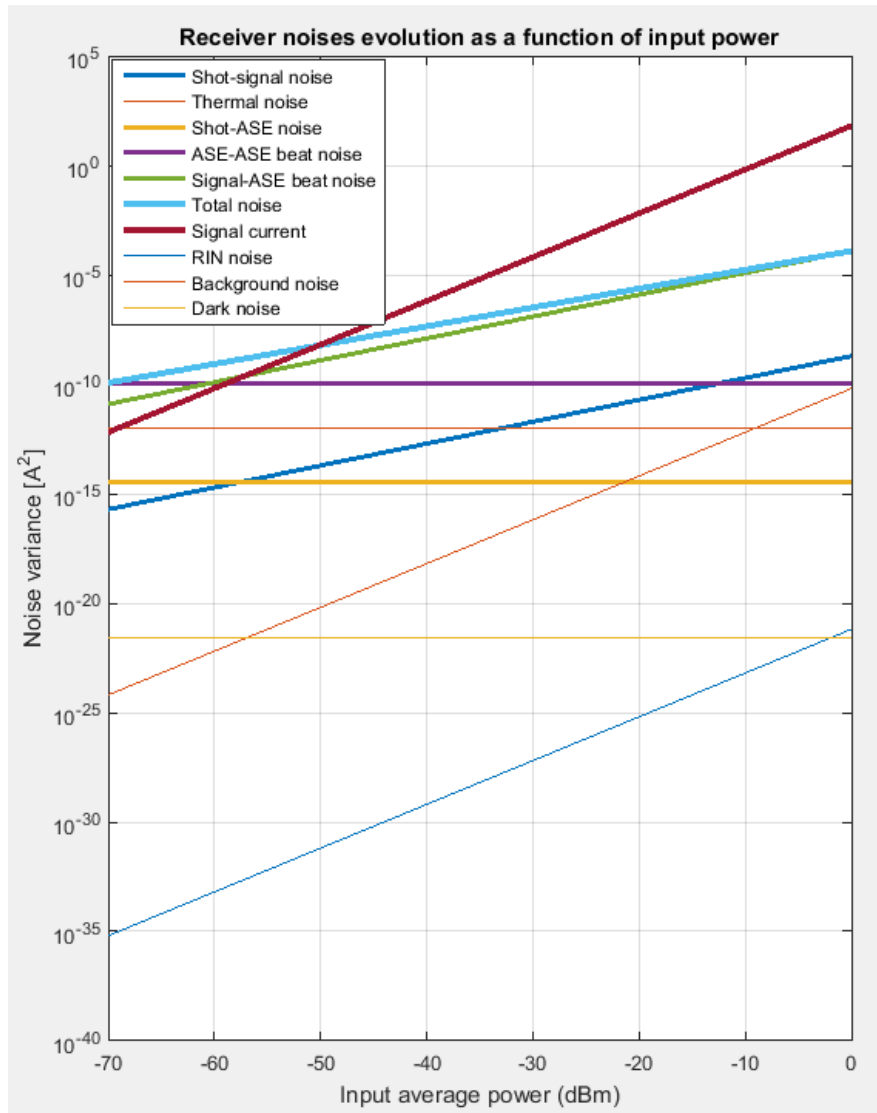
Figure 2-15: Variation of signal current and each noise variation as a function of the input optical power

By the same way, a received optical power threshold between the noise domination and the optical power domination. This threshold equals -50 dBm which means that if the received average optical power is under this value, the noise dominates the optical signal and the communication link is totally cut (or presenting high BER). In addition, the RIN and background noises could be neglected comparing other noise contributions.

These comparisons allow to target the dominant noise from both gain effect and optical power effect where a compromise has to be considered to optimize the optical receiver performance and guarantee the optical communication.

The next part is dedicated to introduce to the DPSK optical modulation link where different components and their main parameters are described.

2.2.5   DPSK communication link

2.2.5.1   DPSK transmitter

The transmitter is based on the same structure employed in OOK systems with the only difference of a pre-coding step in the original data sequence. In addition, the optical power appears in each bit since the information is carried in the phase. The main component that we need to generate a DPSK optical modulation on the transmitter part is a differential coder that we will detail here after.
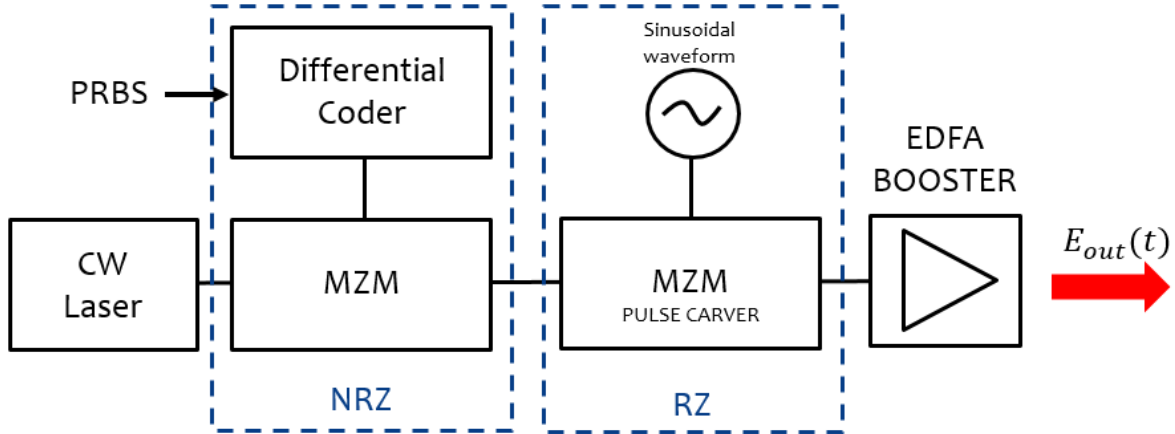
The pulse carver can also be used for the DPSK optical signal in order to modify the duty cycle and generating RZ DPSK modulations. It acts only on the optical power and conserving the data information in the differential phase. The same duty cycles values described on the section 2.2.4.1.2 are generated the same way are considered and evaluated.

2.2.5.1.1   Differential coder

As we introduced briefly previously, DPSK modulation uses the phase of the preceding bit as relative phase reference. Furthermore, the electrical data signal is encoded before modulation to realize the required correlation between consecutives bits and to avoid propagation errors that may occur by differential decoding at the receiver. The coding process is given by the following rule using the XNOR logic operation:

$$c(t) = \overline{m(t) \oplus c(t - T_b)} \tag{2.19}$$

where $c(t)$ is the coded information, $m(t)$ is the state of the bit to be transmitted and $c\,(t - T_b)$ the previous encoded bit. Then, the produced binary sequence $c(t)$, after the differential coder drives the modulator, where phase shift is applied when $(t) = 1$, and no phase shift if $c(t) = 0$. The Figure 2-16 illustrate an example of differential coding of bits sequence:

Data sequence	0	1	1	0	0	1	0
XNOR (0 ref)	1	1	1	0	1	1	0
Phase shift	π	0	π	π	0	π	π
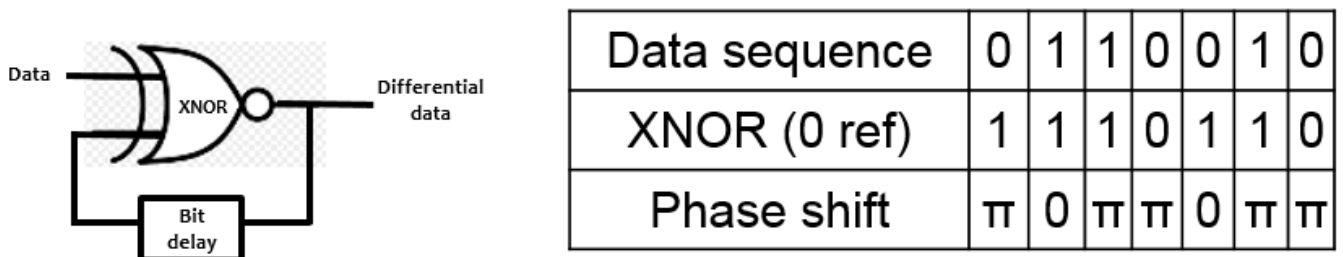
Figure 2-16: Differential coder (left) and data sequence coded (right)

As a comparison, we can write the electrical field in case of OOK and DPSK as:

$$E_{OOK}(t) = m(t)E_0 \cos(\omega_0.t) \qquad\qquad E_{DPSK}(t) = E_0 \cos(\omega_0.t + c(t).\pi) \qquad (2.20)$$

Another method to make a differential data coding could be an alternative to the electrical method. The data stream can be directly encoded on the PRBS generator. Thereby, using this method, a differential encoder device can be avoided.

2.2.5.1.2   Optical modulators

The MZM is biased in the minimum of the transmission and the electrical driving voltage has a peak-to-peak voltage with an amplitude of 2Vπ. The modulator therefore switches between two adjacent crest points, which encodes the 180° phase jumps. This is visible in the NRZ-DPSK output signal, which shows characteristic intensity dips when the modulator switches between maxima. The produced optical signal spend most of time on the high state except when the information data signal switches characterized by fast transitions to the low level. Figure 2-17 shows the necessary parameters of the electrical drive signal and the way to drive the MZM in order to insure the DPSK modulation.
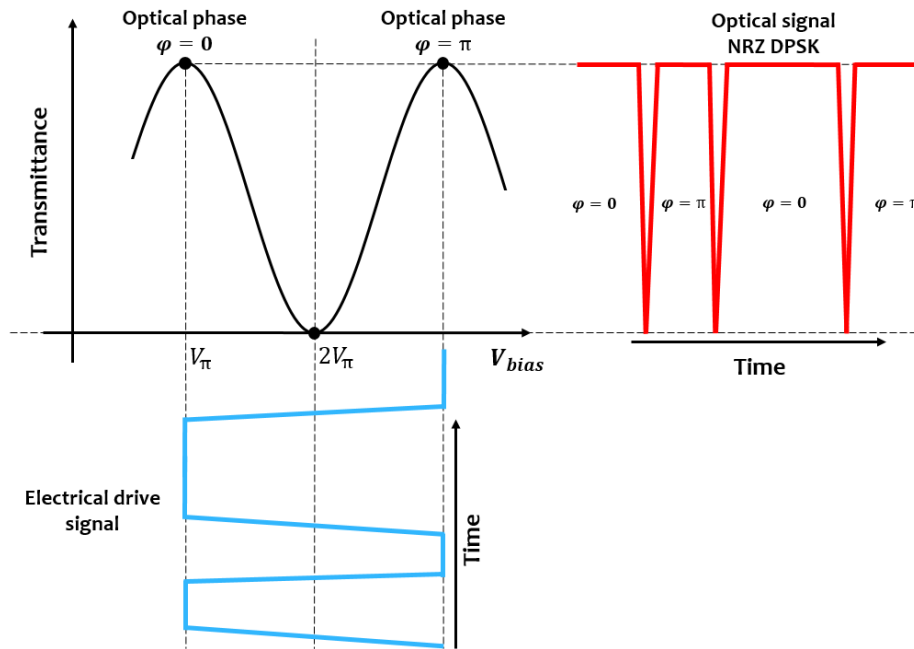
Figure 2-17: Generation of the NRZ DPSK optical signal including the signal phase variation

By using the same process as OOK, to implement the RZ DPSK, the pulse carver is added to NRZ DPSK to obtain RZ pulses with conserving the data encoded on the phase.

After describing all DPSK transmitter components and their functionalities, we will describe now the needed components to decode the DPSK modulated data.

2.2.5.2   Pre-amplified optical receiver for DPSK modulation

For the same reason as the preamplified receiver for OOK modulation described on the section 2.2.4.2.1, the use of an LNOA after the atmospheric propagation leads to amplify the optical signal and limits the cumulative noise amplification before decoding the DPSK modulation.

2.2.5.2.1   Delay line interferometer

To be able to decode the information contained on the signal phase, the receiver needs a Delay Line Interferometer (DLI) based on two-beam interference. It is composed on a 50/50 optical coupler to split the amplified optical signal on two parts in which one beam is time-delayed to the other by a desired interval. The time delay required to decode DPSK modulation equals to 1-bit time delay $T_b = 1/R$ with R is data rate. Then both signals are recombined to interfere each other and produce constructive and destructive interferences. The Figure 2-18 shows the DLI principle and the produced optical spectrums.
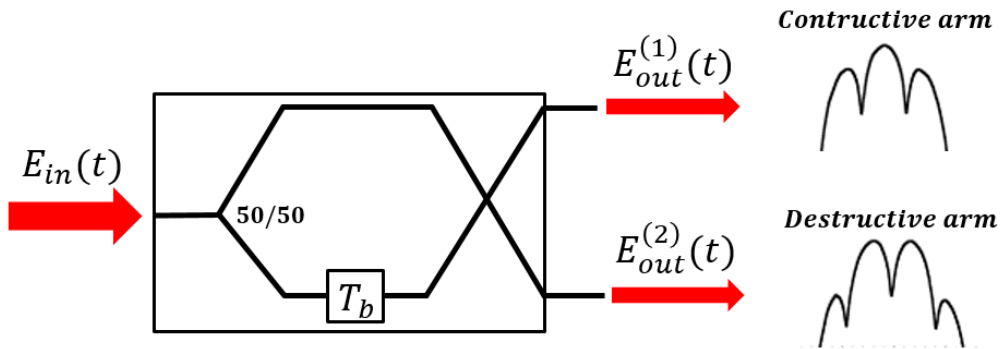
Figure 2-18: Delay Line Interferometer and spectrum state

The transfer function of each arm can be written on the equations (6) and (7) [75]:

$$H_1(f) = TF\left(\frac{E_{out}^{(1)}(t)}{E_{in}(t)}\right) = \left(\frac{e^{-i2\pi fT_b}+1}{2}\right) \ , \ |H_1(f)|^2 \propto \cos^2(\pi fT_b) \tag{2.21}$$

$$H_2(f) = TF\left(\frac{E_{out}^{(2)}(t)}{E_{in}(t)}\right) = \left(\frac{e^{-i2\pi fT_b}-1}{2}\right) \ , \ |H_2(f)|^2 \propto \sin^2(\pi fT_b) \tag{2.22}$$

Both of the constructive and destructive output ports of the DLI carry the fully information of the DPSK modulation. Therefore, detecting either only one of the output could be sufficient (known with *single-ended detection*) but if we want to obtain the 3-dB improvement of the DPSK over OOK modulation, both arms signals have to be simultaneously detected [57]. This is known as balanced detection that will be described in the next part.

2.2.5.2.2   Balanced detection

The balanced detection (or balanced photo-receiver) uses two PIN photodiodes followed by a differential amplifier.
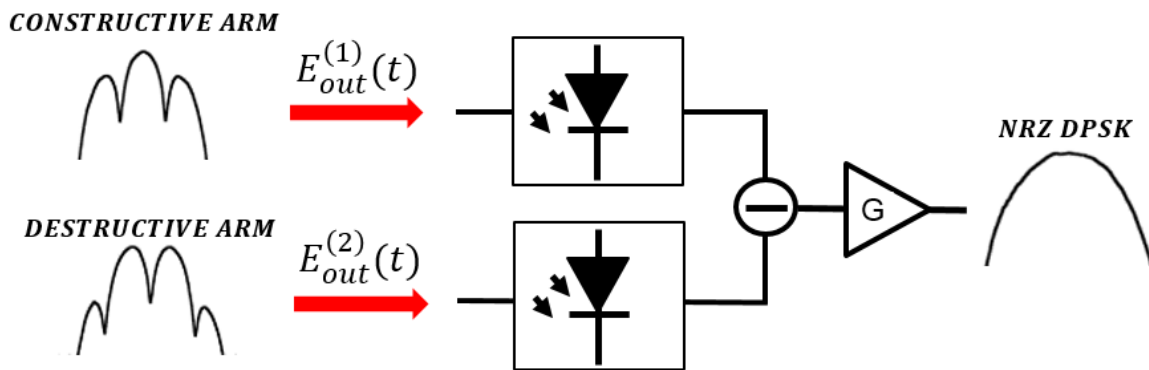
Figure 2-19: Balanced photo-detector used for DPSK optical modulation

The performances of both the OOK and DPSK modulations link architectures are affected by several phenomena inherent to their components.

2.3 Communication channel through the atmosphere

After describing the optical architectures used for FSO optical communication for satellites applications, this part is dedicated to describe the atmosphere and the optical beam properties during the atmospheric propagation.

2.3.1 Atmospheric layers

FSO technologies use atmospheric channel as a propagating area whose properties are random function of space and time. As a result, the optical beam suffers from a random phenomenon that is depending on weather, geographical location and in high altitude from the ground. Various unpredictable factors like clouds, snow and rain cause strong attenuation in the optical signal and limit the capacity communication.

The atmosphere extends to several hundred kilometers above the ground level. One of subdivisions of the atmosphere based on the average temperature variation is shown in Figure 2-20. When a laser beam propagates through atmosphere, it undergoes power loss on the first kilometers from the ground because most of earth's atmospheric mass and particles are located in the lower layers.
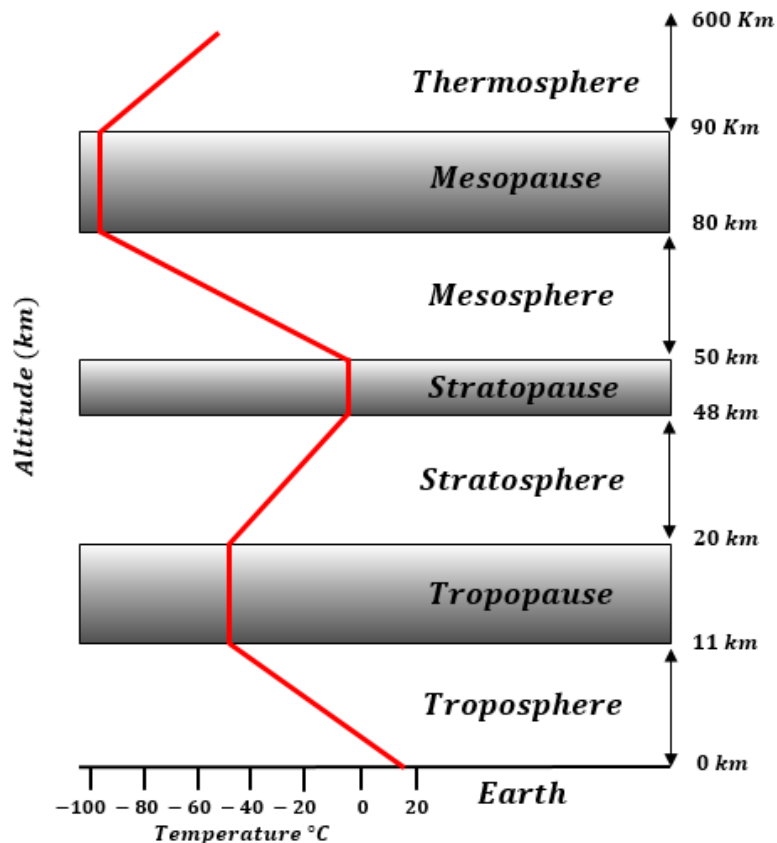
Figure 2-20: Diagram depicting various atmospheric layers and air temperature [76]

2.3.2 Atmospheric mitigations

The three primary atmospheric process that affect optical wave propagation is FSO communication are absorption, scattering and optical turbulence qualified by refractive index fluctuations.

Absorption:

The absorption occurs when a photon of radiation is absorbed by the atmospheric molecules that converts photons into kinetic energy or re-radiates it. This energy is a strong function of the wavelength of incoming photons, where the most severe absorption occurs at ultra-wave wavelengths (under 200 nm) due to O_2 and O_3 molecules, while the absorption is very low at visible wavelengths.

Scattering:

Similar to absorption, light scattering is also depending on the wavelengths. However, there is no loss energy during the process. All particles that are small in comparison with wavelength of radiation will produce the Rayleigh scattering (or molecular scattering). In addition, Rayleigh scattering is quite pronounced while scattering for wavelengths greater than 3 μm is non-existent. Another scattering type exists for particles comparable in size to the wavelength radiation named Mie Scattering (or aerosol scattering). Unlike Rayleigh scattering which has a symmetrical angular distribution, this type of scattering is more concentrated in the forward direction.

Molecular absorption and scattering effects are often combined and can be described by a single attenuation coefficient α which can be written as

$$\alpha(\lambda) = \alpha_A(\lambda) + \alpha_S(\lambda) \qquad (2.23)$$

where α_A and α_S are the coefficient parameters describing molecular absorption and scattering respectively. By defining attenuation coefficient, we can define the transmission of laser radiation noted τ for a propagation distance of L that is related to attenuation coefficient by

$$\tau = e^{\left[\frac{-\alpha(\lambda)}{L}\right]} \qquad (2.24)$$

Both absorption and scattering are deterministic effects that are quite well known and can be predicted based on a variety of conditions.

Refraction:

In regards to atmospheric turbulence, it is produced by temperature variations manifested as refractive index fluctuations. The refractive index is a function of atmospheric pressure, humidity and temperature. For optical and infrared wavelengths, it is detailed on [77] and given by

$$n(\vec{r}, t) = 1 + \frac{1}{T(\vec{r}, t)} \left(\alpha_d(\lambda) P_d(\vec{r}, t) + \alpha_w(\lambda) P_w(\vec{r}, t) \right) \qquad (2.25)$$

where $r(x, y, z)$ and t are the spatial and temporal coordinates, $P_d(r, t)$ is the partial pressure of the dry air, $P_w(r, t)$ is the partial pressure of water vapor, $\alpha_d(\lambda)$ and $\alpha_w(\lambda)$ are respectively function of wavelengths characterizing the dry air and water vapor. $T(r, t)$ is the atmospheric temperature. This relation shows that the refractive index is a random function, created by wind and temperature gradient.

All these fluctuations have important consequences on FSO applications such as optical communication, astronomical imaging or radars using lasers. The next part is dedicated to detail statistical study of their effects.

2.3.3   Statistical properties of atmospheric mitigations

To characterize the atmospheric turbulence for optical applications, we study the fluctuations of the refractive index introduced previously. The first theoretical works related to the statistic description of atmospheric turbulence were those of Kolmogorov and his theory [78]. His model predicts that some initial energy was injected within large eddies and that this intrinsic energy transmitted to smaller eddies until the energy is dissipated. This process is known as the energy cascade theory. The Figure 2-21 shows the energy transfer between different sizes of eddies. In other words, His works allowed to derive the distribution law for the relative amount of turbulence at various scale sizes in the region that is referred to as the inertial subrange.
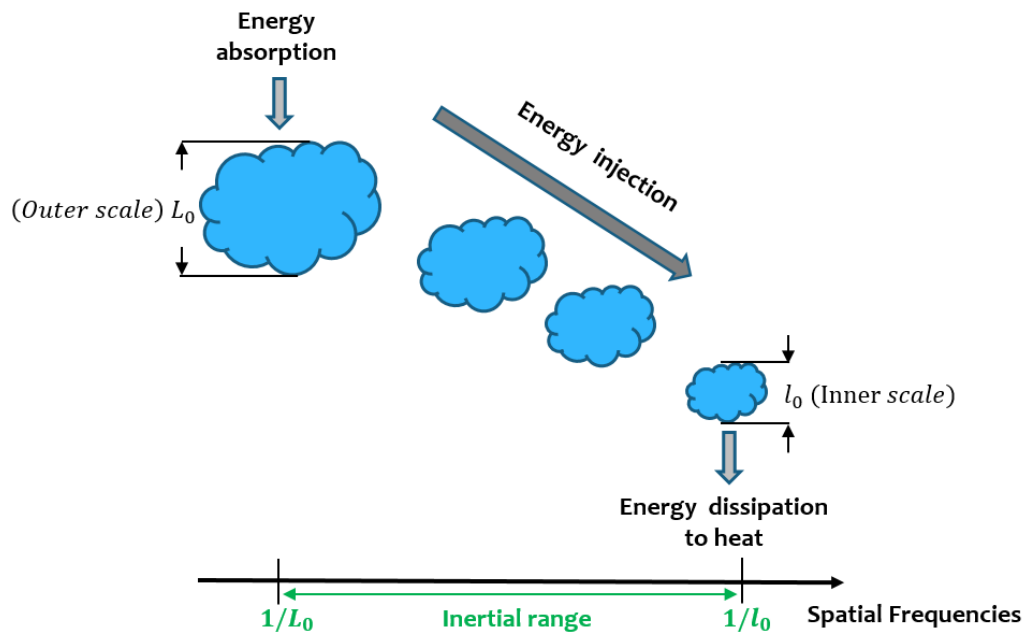
Figure 2-21: Illustration of the energy cascade process and division turbulent eddies in the atmosphere. The Kinetic energy is transmitted from larger heated masses to smaller.

In this figure, the inertial range can be defined as the range appearing between the spatial frequencies $1/L_0$ and $1/l_0$. It defines the range of spatial frequencies in which the atmospheric turbulence can be statically modeled. Both of L_0 and l_0 lengths define respectively the inner scale and the outer scale.

The inner scale defines an estimation of the smallest distances over which fluctuations in the atmosphere are correlated and bellow this distance, we consider that the kinetic energy is totally dissipated. In addition, the inner scale is depending on the density of the atmosphere and it can reach the centimeter in the tropopause layer.

For the outer scale, it is an estimation of the largest distance over which fluctuations in the atmosphere are correlated. In addition, it is conditioned by the strength of the phenomena at the origin of air masses such as the scale of the ground temperature variations, humidity and topography [79].

The introduction of the theory and vocabularies are used to define functions describing the atmospheric turbulence such as the structure function and power spectra density.

2.3.3.1   Structure function of the refractive index

The structure function describes the correlation between the relative indexes in two deferent points separated by the distance of $\vec{d}$. If we consider that the turbulence regime is both temporally and

spatially stationary, and $l_0 < |\vec{d}| < L_0$, the variance of the difference of refractive indexes between the two points, according to Kolmogorov and Obukhov [79], is given by

$$\Delta_{\boldsymbol{n}}(\vec{d}, t) = \langle |n(\vec{r} + \vec{d}, t) - n(\vec{r}, t)|^2 \rangle = C_n^2(h) d^{\frac{2}{3}} \tag{2.26}$$

where the operator $< ->$ represents the statistical average and $C_n^2(h)$ is the index of refractions structure parameter which indicates the strength of the turbulence in function of altitude. This parameter will be more detailed after. The validity domain of structure function is limited by the inner scale and outer scale.

Besides, the structure function is used to define one important parameter to qualify the atmospheric turbulence that is the Fried parameter. It is defined as an equivalent aperture diameter setting the telescope resolution limit in the presence of turbulence. For a plane wave and in the case of Kolmogorov spectrum, the Fried parameter is given by [80]:

$$r_0 = [0.42 k_0^2 \int C_n^2(z) dz]^{-\frac{3}{5}} \tag{2.27}$$

The spatial coherence function B_Ψ of the complex field quantifies the loss in spatial coherence and is given by:

$$B_\Psi = \langle \Psi(\vec{r}, t) \Psi(\vec{r} + \vec{\rho}, t)^* \rangle \tag{2.28}$$

Assuming that refractive index fluctuations are stationary, Yura's works has shown [81]:

$$B_\Psi = e^{-\left(\frac{\rho}{\rho_0}\right)^{\frac{5}{3}}}, \ l_0 \ll \rho \ll L_0 \tag{2.29}$$

Where ρ is the amplitude of $\vec{\rho}$ and ρ_0 is the coherence length of the field. The quantity ρ_0 can be taken as a measurement of the transverse-coherence length of the wave. It means that the oscillations of the wave at points separated by a large (small) distance compared to ρ_0 are mutually incoherent (coherent). The coherence length is given by [81]:

$$\rho_0 = [1.45 k_0^2 \int C_n^2(z) dz]^{-\frac{3}{5}} \tag{2.30}$$

By combining both of equations (22) and (24), the Fried parameter and the coherence length are related by:

$$r_0 \approx 2.11 \rho_0 \tag{2.31}$$

2.3.3.2   *Power spectra density of the refractive index*

The structure function of the refractive index is used to characterize the random process of atmospheric turbulence and it's also used to define the power spectra density. The spectral density, or Kolmogorov's spectrum, is defined in the inertial domain by [78]

$$W_{\Delta n}(f) = 0.033(2\pi)^{-\frac{2}{3}} C_n^2(h) f^{-\frac{11}{3}}, \ \frac{1}{L_0} < f < \frac{1}{l_0} \tag{2.32}$$

where f is the spatial frequency given in m^{-1}. This spectra have a power density saturation when $f < \frac{1}{L_0}$ and with a frequency cutting at $f = \frac{1}{l_0}$. Von Karman proposed a general representative for whole range spatial frequencies ($0 \leq f < \infty$) that is given by [78]

$$W_{\Delta n}(f) = 0.033(2\pi)^{-\frac{2}{3}}C_n^2(h)(\frac{1}{L_0^2}+f^2)^{-\frac{11}{6}}e^{-\left(\frac{2\pi l_0}{5.91}f\right)^2} \quad , \quad 0 \le f < \infty \qquad (2.33)$$

The Figure 2-22 illustrates the modified Von Karman spectrum for different values of inner and outer scales and for $C_n^2(h) = 1$.
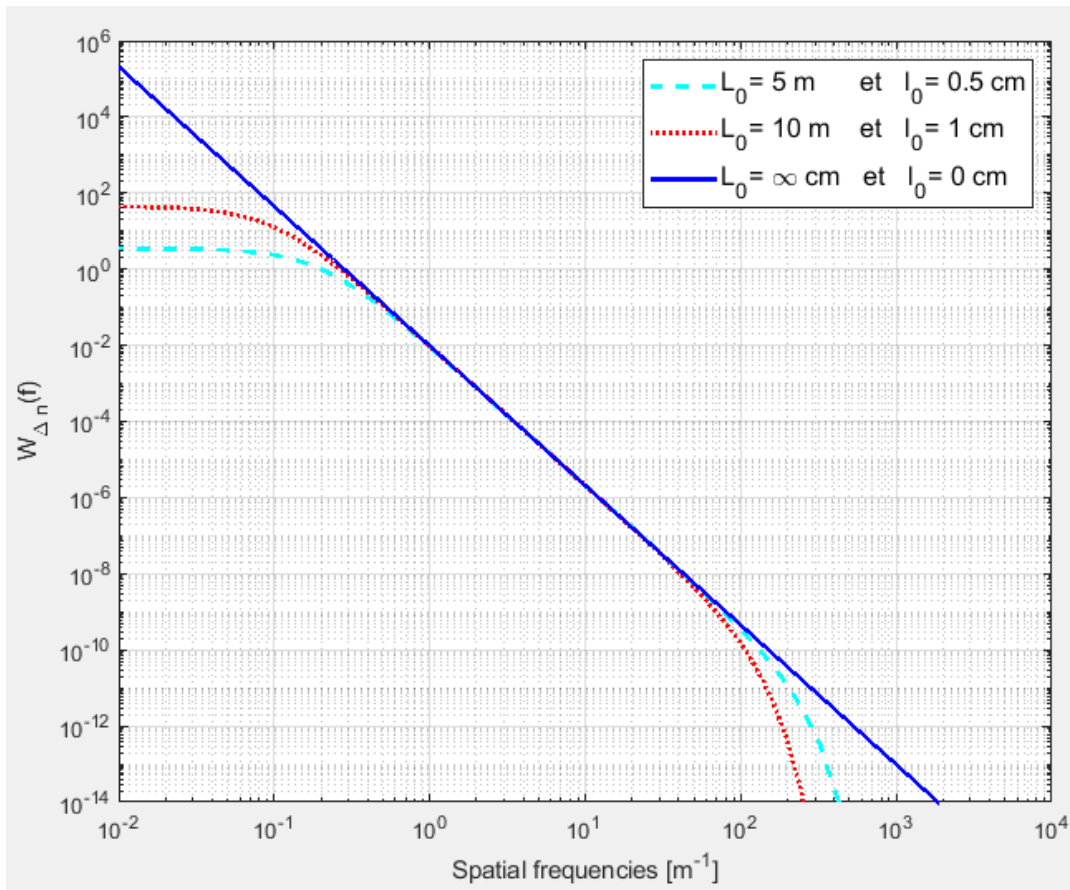
Figure 2-22: Power spectral density of refractive index fluctuations for $C_n^2(h)$ = 1 and different values of inner scale and outer scale.

According to the effect of inner scale and outer scale, shown in Figure 2-22, the Von Karman model ensures that the power spectral density is given without any singularity. In addition, it gives a prediction of high values of inner scale and low values of outer scale (ideal scale).

2.3.3.3   Refractive index structure constant profile

The air temperature fluctuations cause local refractive index variations which are neither constant nor homogeneous along the propagation line of sight. In addition, these refractive index fluctuations are characterized with their power spectral density. The variability of the refractive index is estimated by the refractive index structure parameters C_n^2 which corresponds to the variance of the refractive index between two points separated by one meter and can also characterize the turbulence strength. When the vertical path is considered, as in a feeder link scenario, the C_n^2 parameter is mainly affected by temperature changes along the different layers within the Earth's atmosphere. Consequently, it becomes a function of the height h above the ground level and the widespread C_n^2 profile model is the Hufnagel-Valley profile [46] defined by :

$$C_n^2(h) = 0.00594\left(\frac{v}{27}\right)^2 * (10^{-5}h)^{10} * e^{\frac{-h}{1000}} + 2.7 * 10^{-16} + C_g * e^{\frac{-h}{100}} \ [m^{-2/3}] \qquad (2.34)$$

where the typical value of C_g is $C_g = 5.4 * 10^{-14} m^{-2/3}$ corresponding to the refractive index structure parameter at the ground level, h is the altitude and $v = 21\,m/s$ is the root-mean-squared wind speed. These values corresponding to a strong turbulence case for 1550 nm wavelength communication [33], [46]. Throughput all this manuscript, this C_n^2 profile model is considered [79].

2.3.4 Optical beam propagation theory

After detailing different mitigations on the previous part, the interest now is to describe their effects on the optical propagation beam. While optical propagation through atmospheric turbulences, the optical wave will fluctuate in amplitude and phase because of the refractive index variations. **The description of these fluctuations relies on the analytic resolution of the Helmholtz propagation equation including paraxial approximation that we develop in this part.**

2.3.4.1 *Optical propagation: Helmholtz equation*

As any other electro-magnetic wave propagation in dielectric conditions, the optical propagated wave follows Maxwell's laws. Assuming that the optical wave is an electromagnetic wave, the turbulent atmosphere is isotropic and the characteristic evolution time of refractive index fluctuations is smaller than the optical wave period $2\pi/\omega$, the optical field, denoted $\vec{E}(\vec{r}, t)$, obeys to Helmholtz's propagation equation:

$$\nabla^2 \vec{E}(\vec{r}) + k_0^2 n(\vec{r})^2 \vec{E}(\vec{r}) + 2\nabla\left(\vec{E}(\vec{r}) . \nabla\big(\log(n(\vec{r}))\big)\right) = 0 \qquad (2.35)$$

Where $\vec{r}$ represent the coordinate of the studied point in space, $n(\vec{r}, t)$ is the refractive index on the same point, $k_0 = 2\pi/\lambda$ is the wave number of the beam propagation through vacuum and $\nabla^2 = \Delta = \frac{\partial^2}{\partial x^2} + \frac{\partial^2}{\partial y^2} + \frac{\partial^2}{\partial z^2}$ denotes the Laplacian. The last term, $2\nabla\left(\vec{E}(\vec{r}) . \nabla\big(\log(n(\vec{r}))\big)\right)$, is related to the variations of polarization of the wave and can be neglected for low wavelength values which is the case of 1550 nm [82]. Hence, the equation (25) is simplified and can be written as:

$$\nabla^2 \vec{E}(\vec{r}) + k_0^2 n(\vec{r})^2 \vec{E}(\vec{r}) = 0 \qquad (2.36)$$

2.3.4.2 *Paraxial approximation*

Assuming that the optical beam is propagating along the $\vec{z}$ axis. In solving the Helmholtz equation the parabolic methods has the advantage to represent the optical propagation under turbulence conditions. The amplitude of the scalar field can be written:

$$E(\vec{r}) = A_0 \Psi(\vec{r}) e^{ikz} \qquad (2.37)$$

where $\Psi(\vec{r})$ is the complex amplitude of the wave representing the deviation from the perfectly plane wave. By injecting equation (2.37) in equation (2.36) we obtain a new equation with $\Psi(\vec{r})$ as the unknown variable:

$$\nabla^2 \Psi(\vec{r}) + 2i\langle n(\vec{r})\rangle k_0 \frac{\partial \Psi(\vec{r})}{\partial z} + k_0\big((n(\vec{r})^2 - \langle n(\vec{r})\rangle^2)\big)\Psi(\vec{r}) = 0 \qquad (2.38)$$

We denote $\langle n(\vec{r}, t)\rangle$ the temporal average of the refractive index characterizing the propagation medium. The paraxial approximation consists in assuming that the scale of spatial fluctuations of $\Psi(\vec{r})$ is small compared to the wavelength and we can consider that $\left|\frac{\partial^2 \Psi}{\partial z^2}\right| \ll \left|k\frac{\partial \Psi}{\partial z}\right|$. This approximation remains true as long as the diffraction effects affecting $\Psi(\vec{r})$ vary slowly in propagation direction. In addition, the refraction index fluctuations can be written as $n(\vec{r}, t) = \langle n(\vec{r}, t)\rangle + N$ where N are

fluctuations of refractive index around the mean value that we consider $N \ll 1$. Hence, we can write, according to Taylor

$$n(\vec{r})^2 \approx \langle n(\vec{r}) \rangle^2 + 2N\langle n(\vec{r}) \rangle \tag{2.39}$$

Finally, under all these condition, the (28) becomes:

$$\frac{\partial^2 \Psi(\vec{r})}{\partial x^2} + \frac{\partial^2 \Psi(\vec{r})}{\partial y^2} + 2i\langle n(\vec{r}) \rangle k_0 \frac{\partial \Psi(\vec{r})}{\partial z} + 2k_0 \langle n(\vec{r}) \rangle N\Psi(\vec{r}) = 0 \tag{2.40}$$

2.3.4.3 Analytical solution: Rytov approximation

For the analytic resolution of the Helmholtz propagation equation, we need to consider many simplification. Two approaches based on weak fluctuations regime have been developed and called Rytov approximation and Born approximation [83][53][79]. The Rytov approximation considers that the perturbation is multiplicative to the unperturbed field while the Born approximation considers it as additive [84]. We will recall here after the treatment related only to the Rytov approximation because it gives closer results to the experimental analysis.

The amplitude of the field of a monochromatic optical wave can be written:

$$E(\vec{r}) = e^{\psi_0(\vec{r})} \tag{2.41}$$

During the atmospheric propagation, it is affected by random fluctuations of the refractive index and it can be written under Rytov approximation:

$$E(\vec{r}) = e^{\psi_0(\vec{r}) + \psi(\vec{r})} \tag{2.42}$$

where can be developed as $\psi(\vec{r}) = \psi_0 + \psi_1(\vec{r}) + \psi_2(\vec{r}) + \cdots$.

Applying this new amplitude field to the equation (26), we obtain

$$\nabla^2(\psi_0(\vec{r}) + \psi_1(\vec{r}) + \cdots) + \left(\nabla(\psi_0(\vec{r}) + \psi_1(\vec{r}) + \cdots)\right)^2 + k_0^2 n(\vec{r})^2 = 0 \tag{2.43}$$

In addition, the unperturbed field follows Helmholtz's equation

$$\nabla^2\psi_0(\vec{r}) + \left(\nabla\psi_0(\vec{r})\right)^2 + k_0^2\langle n(\vec{r}) \rangle^2 = 0 \tag{2.44}$$

In the Rytov method, only the first order is taken into account and higher levels are neglected and we can write $\psi(\vec{r}) = \psi_0 + \psi_1(\vec{r})$. In order to simplify, we consider that $\langle n(\vec{r}) \rangle = 1$ and we can express $\langle n(\vec{r}) \rangle^2$ defined on the equation (28), at the first order, as $\langle n(\vec{r}) \rangle^2 = 1 + 2N$. The equation (33) becomes:

$$\nabla^2\left(\psi_1(\vec{r})\right) + \nabla\psi_1(\vec{r})(\nabla\psi_1(\vec{r}) + 2\nabla\psi_0(\vec{r})) + 2Nk_0^2 = 0 \tag{2.45}$$

In the weak turbulence condition, Rytov approximation assumes $|\nabla\psi_1(\vec{r})| \ll |\nabla\psi_0(\vec{r})|$ and the equation (33) becomes:

$$\nabla^2\left(\psi_1(\vec{r})\right) + 2\nabla\psi_1(\vec{r})\nabla\psi_0(\vec{r}) + 2Nk_0^2 = 0 \tag{2.46}$$

Which has a solution [79]:

$$\psi_1(\vec{r}) = \frac{k^2}{2\pi E_0(\vec{r})} \int d\vec{r'} N(\vec{r'}) E_0(\vec{r}) \frac{e^{ik|\vec{r}-\vec{r'}|}}{|\vec{r}-\vec{r'}|} \tag{2.47}$$

2.3.4.4   Statistic properties of the field

In the Rytov approximation framework, the perturbation $\psi_1(\vec{r})$ can be decomposed as:

$$\psi_1(\vec{r}) = \chi(\vec{r}) + i\varphi(\vec{r}) \tag{2.48}$$

where $\chi(\vec{r})$ and $\varphi(\vec{r})$ are respectively the log-amplitude and the phase of the field. By applying the paraxial approximation to the equation (35), $\chi(\vec{r})$ and $\varphi(\vec{r})$ can be written as [79], [82] :

$$\chi = \frac{k^2}{2\pi} \int_0^L \frac{dh}{L-h} \int_{-\infty}^{+\infty} d\rho' \, n_1(\rho', h) \cos\left(k \frac{|\rho-\rho'|^2}{2(L-h)}\right) \tag{2.49}$$

$$\varphi = \frac{k^2}{2\pi} \int_0^L \frac{dh}{L-h} \int_{-\infty}^{+\infty} d\rho' \, n_1(\rho', h) \sin\left(k \frac{|\rho-\rho'|^2}{2(L-h)}\right) \tag{2.50}$$

2.3.4.5   Power spectral densities

According to the equation (34) and the phase-screens decomposition of turbulent volume given in [79], the power spectral densities of χ and φ are given for a propagation distance of L by:

$$W_\chi(f) = k^2 \int_0^L W_{\Delta n} \sin^2(\pi h \lambda f^2) dh \tag{2.51}$$

$$W_\varphi(f) = k^2 \int_0^L W_{\Delta n} \cos^2(\pi h \lambda f^2) dh \tag{2.52}$$

where $W_{\Delta n}$ is Power spectra density of the refractive index given by equation (23) and h is the propagation distance between $h = 0$ and $h = L$.

2.3.4.6   Probability density function

In the weak atmospheric turbulence case, χ and φ is the sum of random independent and centered Gaussian variables. For φ, it obeys a Gaussian probability density function centered in 0 with a full width at half maximum of $2\sqrt{2log(2\sigma_\varphi)}$ [85]. On the other hand, χ permits to calculate the optical wave irradiance (depending on the optical intensity) that is a parameter of greater interest in the regime of strong turbulence. It is be calculated as:

$$I = \Psi(\vec{r})\Psi(\vec{r})^* = I_0 e^{2\chi} \tag{2.53}$$

Therefore, the irradiance follows a log-normal probability law and the probability density of I is given by [85]:

$$P(I) = \frac{1}{\sqrt{2\pi}I\sigma_\chi} e^{-\left[\frac{\left(\log\left(\frac{I}{I_0}\right)-2\langle\chi\rangle\right)^2}{8\sigma_\chi^2}\right]}, I > 0 \tag{2.54}$$

The useful variable is the scintillation index noted σ_I^2 calculated as the normalized variance of the field intensity. It is related to the variance of the log-amplitude as follows:

$$\sigma_I^2 = \frac{\langle I^2 \rangle}{\langle I \rangle^2} - 1 = e^{4\sigma_\chi^2} - 1 \tag{2.55}$$

Being on the weak condition fluctuations and with an expansion on the first order, the equation (42) becomes:

$$\sigma_I^2 = 4\sigma_\chi^2 \tag{2.56}$$

To conclude the analytical study, the Rytov approximation leads to simplify the model characterization of the optical field propagation and simplifying its properties and deformations. For strong fluctuations condition, there is no analytic solution to the Helmholtz equation. We limited the presented work to plane wave but the same calculation can be done for spherical and Gaussian waves detailed in [79].

However, it is important to understand that this analytic characterization includes many approximations that can be more difficult to take into account in practice and in strong condition of atmospheric turbulence.

2.3.5 Modal decomposition of turbulent phase

2.3.5.1 Properties of turbulent phase

Turbulence effects on the phase perturbation can be described using a modal description. Several bases exist and the most commonly used one is the Zernike polynomials[86], [87]. In this part, a review of the Zernike polynomials and the statistical laws are described in part.

2.3.5.2 Zernike polynomials

The Zernike polynomials noted $Z_i(r, \theta)$ define an orthogonal basis on the unit circle and are generally used to describe the wavefront perturbation in terms of optical aberrations. In addition, they have the advantage to constitute an orthonormal basis over a circular pupil surface. Each polynomial has an analytic expression that is the product of radial function $R_n^m(r)$ and azimuthal $\phi_n^m(\theta)$ function where m and n are the radial and azimuthal degrees. They are given by [87]:

$$Z_i(\vec{r}, \theta) = R_n^m(\vec{r})\phi_n^m(\theta) \tag{2.57}$$

with

$$R_n^m(r) = \sum_{k=0}^{\frac{n-m}{2}} \frac{(-1)^k (n-k)!}{k!\left(\frac{n+m}{2}-k\right)!\left(\frac{n-m}{2}-k\right)!} r^{n-2k}, \ n \geq |m| \tag{2.58}$$

and

$$\phi_n^m(\theta) = \begin{cases} \sqrt{n+1} & if \ m = 0 \\ \sqrt{2(n+1)}\cos(m\theta) & if \ m \neq 0 \ and \ i \ even \\ \sqrt{2(n+1)}\sin(m\theta) & if \ m \neq 0 \ and \ i \ odd \end{cases} \tag{2.59}$$

The azimuthal value m takes values going from $-n$ to n verifying that $(n-m)$ is even. The first 15 Zernike polynomials are shown in the Figure 2-23 based on Noll's concept [86].

To model the perturbed waferont, the Zernike polynomials is complete and the pertubated phase can be decomposed using the Zernike polynomials:

$$\varphi(\vec{r}) = \sum_{i=1}^{\infty} a_i Z_i(\vec{r}) \tag{2.60}$$

where a_i are coefficients corresponding to the orthonormal basis formed by $Z_i(\vec{r}, \theta)$ and given by:

$$a_i = \frac{1}{\Sigma} \int_0^{\Sigma} \varphi\left(\vec{r'}\right) Z_i\left(\vec{r'}\right) d\vec{r'} \tag{2.61}$$

where Σ is the surface unit.

These coefficients describe a total statistical characterization of the turbulent phase thanks to Zernike polynomials. Therefore, Noll's [86] provides the results of the variances for the coefficients of each Zernike polynomials that is equal to the sum of the variances of every polynomial coefficient:

$$\sigma_\varphi^2 = \frac{1}{\Sigma} \int_0^\Sigma \langle \varphi\left(\vec{r'}\right)\rangle \, d\vec{r'} = \sum_{i=1}^\infty \langle a_i^2 \rangle \tag{2.62}$$

Finally, an expression for the variance of the turbulent phase, over a circular pupil diameter D, without the variance of the piston term (the coefficient a_k is associated only to the kth) is given by:

$$\sum_{i=2}^\infty \langle a_i^2 \rangle \cong 1.03 \left(\frac{D}{r_0}\right)^{\frac{5}{3}} \tag{2.63}$$
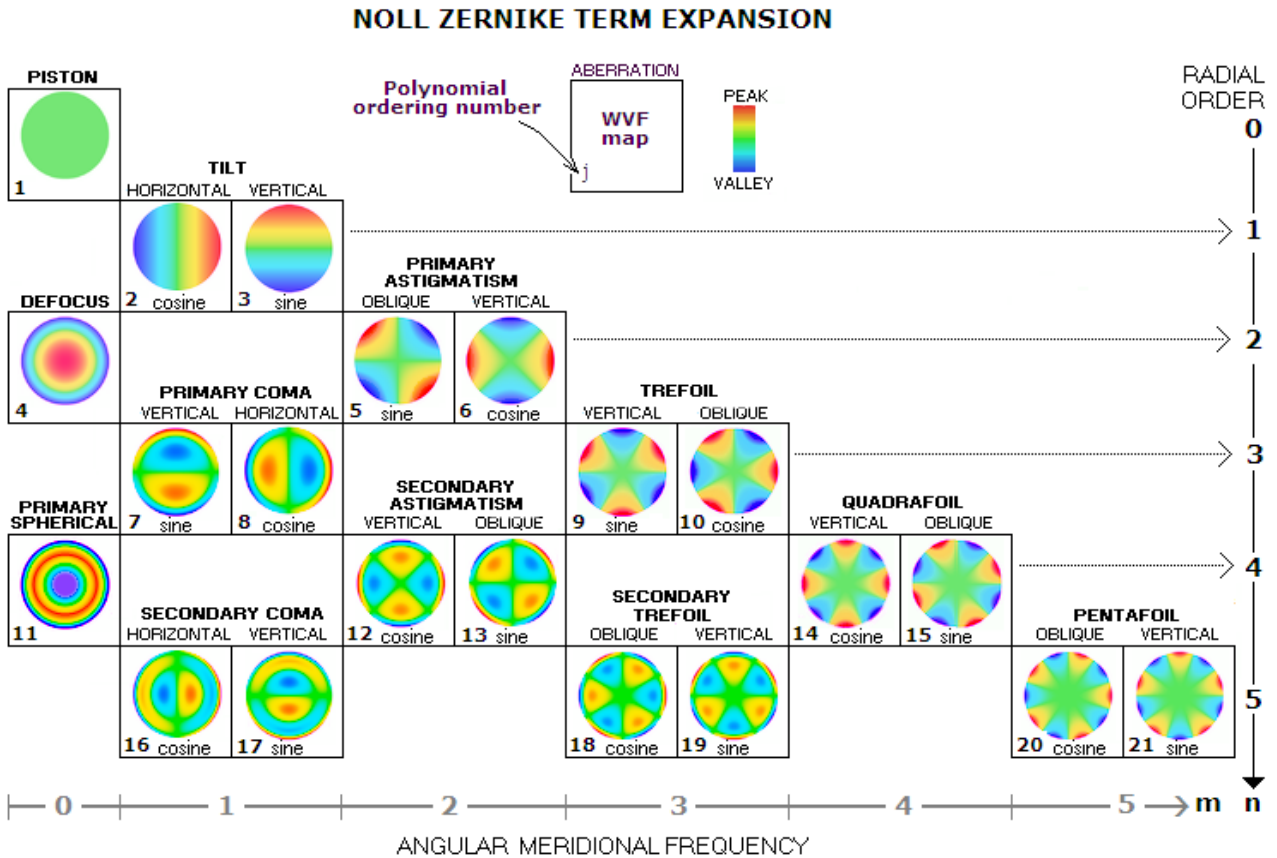
Figure 2-23: The first 21 Zernike polynomials ordered by increasing vertically by radial degree and horizontally by azimuthal degree [88]*.*

More information about Noll's index and classical names of each polynomials order are given in Appendix 6 of the manuscript.

2.3.6   Atmospheric turbulence on the Gaussian beam waves

The Gaussian optical beam have a characteristic radial intensity profile that expands laterally during their propagation. Gaussian beams are one of solutions to the electromagnetic wave equation under paraxial condition, as we used previously to describe the atmospheric effects.

2.3.6.1   *Gaussian beam properties*

The free space propagation of a single mode laser beam can be modeled as the lowest order Gaussian beam wave noted TEM_{00}.

Assuming that the optical source is located at $z = 0$ and the wave is propagating in the vacuum along $\vec{z}$, the field distribution of this fundamental mode is given by [85]

$$E_0(r,z) = \frac{w_0}{w(z)} e^{-\left(\frac{\rho^2}{w(z)^2}\right)} e^{-\left(\frac{ik_0\rho^2}{2R(z)}\right)} e^{\left(ikz - i\tan^{-1}\left(\frac{z}{Z_R}\right)\right)} \tag{2.64}$$

where $w(z)$ is the spot size of the beam at the maximum of amplitude down by a factor $1/e$, w_0 is its minimal radius size called the waist size and Z_R is the Rayleigh distance. Both of $w(z)$ and Z_R are related by

$$w(z) = \sqrt{w_0^2 \left(1 + \left(\frac{z - z_0}{Z_R}\right)^2\right)} \tag{2.65}$$

$R(z)$ is the curvature radius given by

$$R(z) = (z - z_0)\left(1 + \left(\frac{Z_R}{z - z_0}\right)^2\right) \tag{2.66}$$

The term $\tan^{-1}\left(\frac{z}{Z_R}\right)$ describes the phase shift for a z distance propagation (beam divergence) corresponding to the angle between the asymptotes and the propagation axis. For an optical wave, the divergence is typically small and the half angle divergence can be written as:

$$\theta_D \approx \frac{\lambda}{\pi w_0} \tag{2.67}$$

Thus, the form of the fundamental Gaussian beam is uniquely determined once the minimum spot size and its location are specified. The Figure 2-24 shows an example of Gaussian beam:
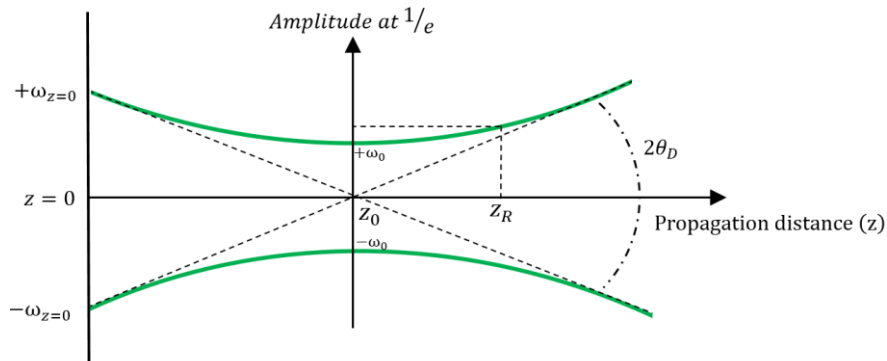
Figure 2-24: Propagation of a convergent Gaussian beam in vacuum with positive curvature

The classical models used for describing the propagation of optical radiation are plane and spherical waves. The most important part of the scientific literature devoted to optical propagation in atmospheric turbulence has been focused on the scintillation phenomenon [89].

2.3.6.2 Scintillation effects

As we introduced previously, the optical beam suffers from atmospheric turbulences acting on the refractive index along the propagation path. These index variations have a significant impact on the detected irradiance. In this part is focused on effects observed on a ground to satellite path (uplink) where most of atmospheric effects are located on first kilometers of propagation. In addition, the effects on the beam depends also on the turbulent size eddies and the optical beam properties such as the beam radius and beam divergence.

The main effects is the beam wander that it consists on the beam deviation from the original direction. It results from turbulent eddies that the size is larger than the beam radius. The optical beam is then refracted causing an important irradiance variations arriving to the satellite and the loss of ground to

satellite communication link. This phenomena is most important for the long distance communication (ground-to-GEO) because the beam deviation radius becomes important unlike to short distance. The Figure 2-25 illustrates the beam wander effect.
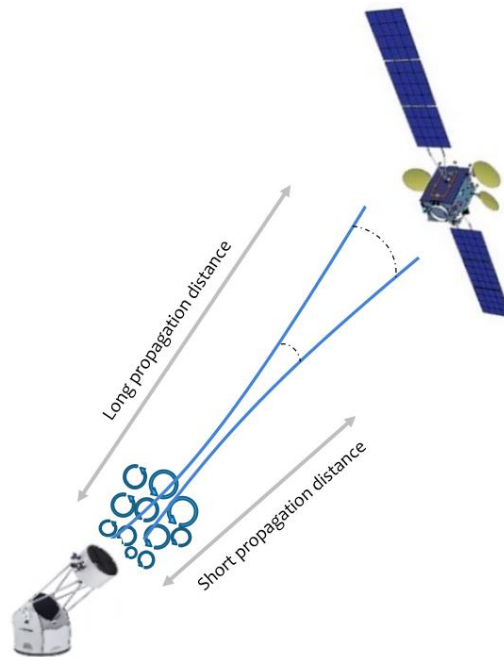
Figure 2-25: Beam wander effect for two different propagation distances through turbulent eddies

Another effect exists during these atmospheric propagation and it is called beam spreading that corresponds to an energy spreading. It consists on the widening of the beam size that is larger than atmospheric diffraction. In addition, the beam spreading appears when turbulent eddies are smaller than the beam size and it doesn't have any effect on the beam's direction.

Fante [90] introduces three variables to describe irradiance fluctuations arriving to the satellite. The first one is the short-term beam radius noted r_s corresponding to the radius of the beam spot observed with a very short exposure and caused by small eddies. The beam is then deflected by a distance of r_c that is a measure of the beam displacement at satellite altitude due to the beam wander effects (large eddies). The last variable is a long-term beam radius r_L corresponding to the beam radius with an exposure much large than time intervals between two deflections of the beam. The Figure 2-26 shows a comparison of these parameters in front the satellite. These three parameters can be linked by:

$$\langle r_L^2 \rangle = \langle r_s^2 \rangle + \langle r_c^2 \rangle \tag{2.68}$$

Analytical expressions have been given for the mean square of these variables. For r_L, it can be expressed by terms corresponding to the beam propagation through the vacuum and both of beam wander and beam spreading.

$$\langle r_L^2 \rangle = \left(\frac{L\lambda}{\pi \omega_0} \right)^2 + \omega_0^2 + 8.8 \left(\frac{L\lambda}{\pi r_0} \right)^2 \tag{2.69}$$

The beam wander is given by:

$$\langle r_c^2 \rangle = \frac{18.2 L^2}{k_0^2 r_0^{\frac{5}{3}} \omega_0^{\frac{1}{3}}} \tag{2.70}$$

Finally the short-term beam spread is given by subtracting $\langle r_C^2 \rangle$ from $\langle r_L^2 \rangle$.

$$\langle r_S^2 \rangle = \langle r_L^2 \rangle - \langle r_C^2 \rangle = \left(\frac{L\lambda}{\pi\omega_0} \right)^2 + \omega_0^2 + 8.8 \left(\frac{L\lambda}{\pi r_0} \right)^2 - \frac{18.2L^2}{k_0^2 r_0^{\frac{5}{3}} \omega_0^{\frac{1}{3}}} \tag{2.71}$$

Depending on the size of waist at the emission, the atmospheric effects differ and three different regime can be shown. They will be detailed in the next part.
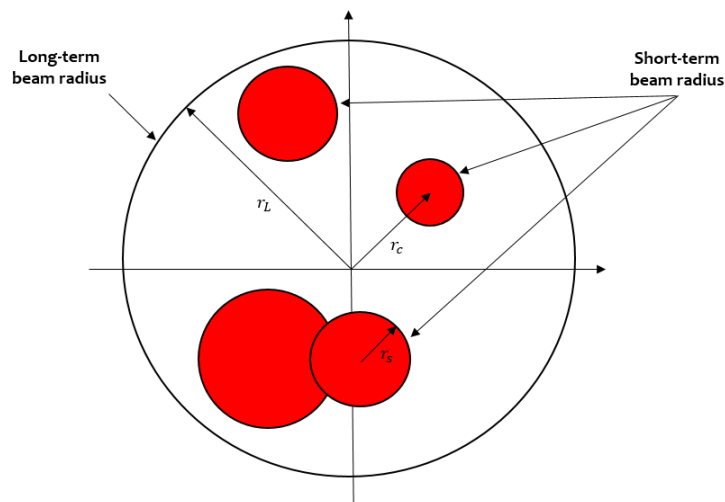
Figure 2-26: Comparison of Fante parameters on the satellite plane after atmospheric propagation

Both of beam wander effect and beam spreading effect contribute to the fading effect during the propagation and an appropriate model taking into account these fluctuations will be described in the next part.

2.3.6.3   Low Order Turbulence (LOT) model

We derive in this section the irradiance statistics of a Gaussian beam propagation through distributed atmospheric turbulence assuming two condition: multiple scattering effects are neglected and the transverse spectral content of the random turbulence is limited only to linear and quadrature phase terms (Tip/Tilt, Defocus and Astigmatism shown in Figure 2-23). This model is called Low Order Turbulence model (LOT). According to Baker [83], the LOT consists on integrating turbulence in a single phase screen placed at the transmitter prior to the propagation. This condition is valid for Ground-to-Satellite link where turbulence is in the near field while the satellite is in the far field. The phase screen can be under these conditions as [83]:

$$\Phi_{LOT} = k_0 \left[\theta_x x + \theta_y y + \Delta\kappa \frac{1}{2} \left((x^2 + y^2)^{\frac{1}{2}} w_0^2 \right) + c_5 \frac{1}{2} (x^2 - y^2) + c_5 xy \right] \tag{2.72}$$

where $\theta_{\{x,y\}}$ corresponds to the angular Tip/Tilt in radians, $\Delta\kappa$ corresponds to the defocus curvature and $c_{\{5,6\}}$ is the astigmatism curvature term in $[m^{-1}]$.

The normalized irradiance of a Gaussian beam propagating through atmospheric turbulence over a distance L is given by:

$$I(x, y, L) = \frac{2}{\pi\omega_x\omega_y} e^{\left(-\frac{2}{\omega_x^2}[(x-\delta_x)]\cos(\omega) + [(y-\delta_y)\sin(\omega)]^2 \right)} e^{\left(-\frac{2}{\omega_y^2}[(x-\delta_x)]\sin(\omega) - [(y-\delta_y)\cos(\omega)]^2 \right)} \tag{2.73}$$

The beam wander is quantified by the irradiance centroid displacement components, δ_x and δ_y , and beam breathing and beam distortion are quantified by the partial beam radii ω_x and ω_y. ω is the astigmatism parameter. These parameters are given by, respectively:

$$\delta_{\{x,y\}} = L\theta_{\{x,y\}} \tag{2.74}$$

$$\omega_{\{x,y\}} = w_0 \sqrt{\left[1 + L\left(\Delta\kappa \pm \sqrt{c_5^2 + c_6^2}\right)\right]^2 + \left(\frac{2L}{kw_0^2}\right)^2} \tag{2.75}$$

$$\omega = \frac{1}{2}\arg(c_5 + ic_6) \tag{2.76}$$

The central limit theorem ensures that the five turbulence coefficient $(\theta_x, \theta_y, \Delta\kappa, c_5$ and $c_6)$ representing the turbulence distribution are zero-mean Gaussian-distributed random variables [83]. Assuming Noll's phase variance [86], the LOT model neglects the following phase screen variance :

$$\sigma_{\delta\phi}(j > 6) = 0.065 \left(\frac{d_0}{r_0}\right)^{\frac{5}{3}} \tag{2.77}$$

The phase variation where j is the number of Zernike polynomial corresponding to all higher order than astigmatism (Figure 20), r_0 is the fried parameter and $d_0 = 2w_0$.

For the model that we will use to emulate atmospheric turbulence, we will consider that statistical equivalent between LOT and all order model is achieved when their ratio is less than 0.1.

 The phase screen and the beam size will satisfy:

$$\sigma_{\delta\phi}(j > 6) \leq \left(\frac{2\pi}{10}\right)^2 \quad and \quad w_0 \leq 1.5r_0 \tag{2.78}$$

In order to determine the validity range of the model, Baker [83] proposes two parameters to define the region of interest in which turbulence is located in the near field. These parameters are the Fresnel numbers of the initial beam at two different distances, $L \; and \; z_\tau$ and they are given by

$$N_{\{L,z_\tau\}} = \frac{\pi w_0^2}{\lambda\{L,z_\tau\}} \tag{2.79}$$

z_τ gives an estimation of the centroid of the turbulence strength on the propagation path. It is given by:

$$z_\tau = \frac{\int_0^L z C_n^2(z)dz}{\int_0^L C_n^2(z)dz} \tag{2.80}$$

According to Baker, the bounds of validity region are given by two conditions: the satellite is in the far field ($N_L < 1$) and the turbulence is located near the emitter ($N_{z_\tau} \gg 1$).

To summary, these hypothesis impose a minimum waist for the validity of the LOT model and three different turbulent regimes can be distinguishable. A-R. Camboullives has detailed these work during his thesis work [53][52].

2.3.6.4 Different turbulence regimes

Weak perturbation régime $w_0 < r_0$

The scintillation index for a laser may be divided in two parts, the on-axis scintillation measured on the optical axis and the second part takes into account the dependence of scintillation of the distance from the optical axis. The irradiance variation can be expressed by:

$$\sigma_I^2(r, L) = \sigma_I^2(0, L) + \sigma_{I,r}^2(r, L) \tag{2.81}$$

We demonstrate that the irradiance fluctuations due to the scintillation follows a log-normal probability density function. This law can expressed using the log-amplitude as:

$$\langle \chi \rangle = -\sigma_\chi^2 = -\frac{1}{4}\ln\left(1 + \sigma_I^2(0, L)\right) \tag{2.82}$$

The power density function of the irradiance can therefore be estimated to describe the weak perturbation case.

Beam wander regime $w_0 \approx r_0$

For the high beam size at the emission, the scintillation theory developed form Rytov approximation and numerical wave simulation illustrate divergences [89]. When the waist size is approximately equal to the Fried parameter, the scintillation is dominated by turbulence induced by the beam wander effect and for this reason, the regime is called beam wander regime. Considering the log-amplitude fluctuations noted I_S and beam wander effect, noted I_{BW}, the instantaneous irradiance is given by:

$$I(0,0, L) = I_S . I_{BW} \tag{2.83}$$

To question now is how to consider the scintillation on the beam wander regime. Two different approaches are done in the literature describing the junction of both scintillation and beam wander.

The first method, proposed by Andrews [7], considers that only the on-axis scintillation should be taken into account and the irradiance can be written as:

$$I(0,0, L) = e^{[2\chi(0,0)]} e^{\left[-2\frac{\delta_x^2 + \delta_y^2}{w_{ST}^2(L)}\right]} \tag{2.84}$$

where $w_{ST}^2(L) = \langle r_s^2 \rangle$ is the short term beam waist and (δ_x, δ_y) are the position of the centroid of the beam resulting from beam wander effect. From the equation (65), the scintillation index variance square can be written as:

$$\sigma_I^2 = \sigma_S^2(0,0, L) + \sigma_{BW}^2(L) \tag{2.85}$$

We will only focus on the beam wander part that is given by [91]

$$\sigma_{BW}^2(L) = \frac{4\alpha^2}{1 + 4\alpha} \text{ with } \alpha = \langle r_c^2 \rangle / \langle r_s^2 \rangle \tag{2.86}$$

The probability density function of the irradiance fluctuations induced by beam wander follows a modified beta distribution and can be written as [92]:

$$P_{I_{BW}}(I) = \frac{1}{2\alpha I_0}\left(\frac{I}{I_0}\right)^{\frac{1}{2\alpha}-1} \tag{2.87}$$

Assuming that the scintillation irradiance is normalized and $\langle I \rangle = I_0 = 1$. The equation (69) becomes:

$$P_{I_{BW}}(I) = \frac{1}{2\alpha}(I)^{\frac{1}{2\alpha}-1} \tag{2.88}$$

The second method considers that the log-amplitude scintillation is determined as a function of beam wander. This method is proposed by Dios [89] and the normalized on-axis instantaneous irradiance, given by the first method by equation (66), becomes:

$$I(0,0,L) = e^{[2\chi(\delta_x,\delta_y)]}e^{\left[-2\frac{\delta_x^2+\delta_y^2}{w_{ST}^2(L)}\right]}$$
(2.89)

Compared to the case where only the on-axis scintillation is taken into account, the equation becomes:

$$\sigma_\chi^2 = \frac{1}{4}\ln\left(1 + \sigma_{I,Gb}^2(\delta_x,\delta_y,L)\right)$$
(2.90)

where

$$\sigma_{I,Gb}^2(\delta_x,\delta_y,L) = \left(\sigma_I^2(0,L) + \sigma_{I,r}^2(\delta_x,\delta_y,L)\right)\langle I(\delta_x,\delta_y,L)\rangle^2$$
(2.91)

and

$$\langle I(\delta_x,\delta_y,L)\rangle^2 = e^{\left[-2\frac{\delta_x^2+\delta_y^2}{w_{LT}^2(L)}\right]}$$
(2.92)

where $w_{LT}^2(L) = \langle r_s^2 \rangle$ is the long term beam waist. Therefore, this regime described a log-amplitude depending on the centroid displacement (δ_x, δ_y).

Strong turbulence régime $w_0 > r_0$

When the emitted waist size ω_0 is very large than Fried parameter, the atmospheric effects corresponds to strong perturbations which leads to loss of special coherence of the beam during its propagation. Habash [42] have proposed a distribution called Gamma-Gamma distribution to describe irradiance fluctuations in strong perturbation case. The model assumes that the irradiance fluctuations resulting from small eddies, noted I_x, are modulated by irradiance fluctuations resulting from large eddies, noted I_y. Assuming that I_x and I_y are statistically independent and follows a Gamma distribution, the total irradiance has a Gamma-Gamma probability density function and can be written as:

$$P(I) = \frac{2(\alpha\beta)^{\frac{\alpha+\beta}{2}}}{\Gamma(\alpha)\Gamma(\beta)}I^{\frac{\alpha+\beta}{2}-1}K_{\alpha-\beta}(2\sqrt{\alpha\beta I}), I > 0$$
(2.93)

where K_p is a modified Bessel function Bessel function of p order, α and β are respectively the number of small and large eddies, detailed is [93], and Γ represents the Euler-Gamma function defined by:

$$\Gamma(s) = \int_0^\infty xe^{-x}x^{s-1}dx$$
(2.94)

The associated distribution can be written as:

$$\sigma_{pe}^2 = \langle r_c^2 \rangle\left[1 - \left(\frac{\pi^2 w_0^2/r_0^2}{1+\pi^2 w_0^2/r_0^2}\right)^{\frac{1}{6}}\right]$$
(2.95)

This distribution expression permits to compare the Gamma distribution and log-normal distribution which fits well with experimental results when the turbulence's strength increases [93]. However, it results from an empiric fitting and not from analytic description. An example of atmospheric turbulence effects is illustrated on the astronomical observation in [94]

2.4   Conclusion

In this chapter, we illustrates many optical architectures of the emitter and receiver used for FSO satellite communications. Both of OOK and DPSK needed components are studied and described on the aim to improve their performances. In addition, we presented the different mathematical descriptions of irradiance fluctuations resulting from the atmospheric turbulence. The atmospheric propagation model based on LOT will be simulated and its results will be used for simulation FSO communication link that we will develop in the next chapter.

Chapter 3

3 Simulation of free space optical communication through the atmosphere

---

This chapter is dedicated to detail the optical link implemented and simulated using VPItransmissionMaker[TM]. For each modulation format, several simulation results are given such as eye diagram, optical spectra, BER curves versus received optical power (ROP), etc. in order to investigate the effects of some parameters on the transmission performances of the link. For validating the link performances, the sensitivity, i.e. BER curves versus ROP, are plotted for different scenarios and compared with the state of the art.

3.1   Introduction

This chapter is dedicated to detail the optical link implemented and simulated using VPItransmissionMaker™. For each modulation format, several simulation results are given such as eye diagram, optical spectra, BER curves versus received optical power (ROP), etc. in order to investigate the effects of some parameters on the transmission performances of the link. For validating the link performances, the sensitivity, i.e. BER curves versus ROP, are plotted for different scenarios and compared with the state of the art.

The atmospheric propagation model that is used to emulate the atmospheric effects is a Low Order Turbulences (LOT) model considering Tip/Tilt, astigmatism and defocused of the optical beam during its propagation. It is capable to model the wavefront pre-compensation that can be done on the ground, before emitting the optical beam to the satellite, thanks to adaptive optics loop in order to reduce atmospheric impairments. The fading time induced by atmospheric channel is simulated in several turbulences scenarios (weak, strong and beam wander) and its effects are analyzed versus optical modulation (OOK vs DPSK) and the duty cycle of pulse shaping.

We also implemented a WDM optical link with two channels in the C-band in order to consider the crosstalk effect and show the system performances with this additional noise.

3.2   Simulation of free space optical communication

3.2.1   OOK communication link

Despite advantages of FSO for feeder link application, atmospheric layers have a strong effect on the link performances. This part is focused on the simulation of optical link in the absence of atmospheric effects for illustrating the intrinsic link performances. Then, the FSO part of the simulator will be included using time series of LOT model. Figure 3-1 illustrates a general view of the OOK communication link.
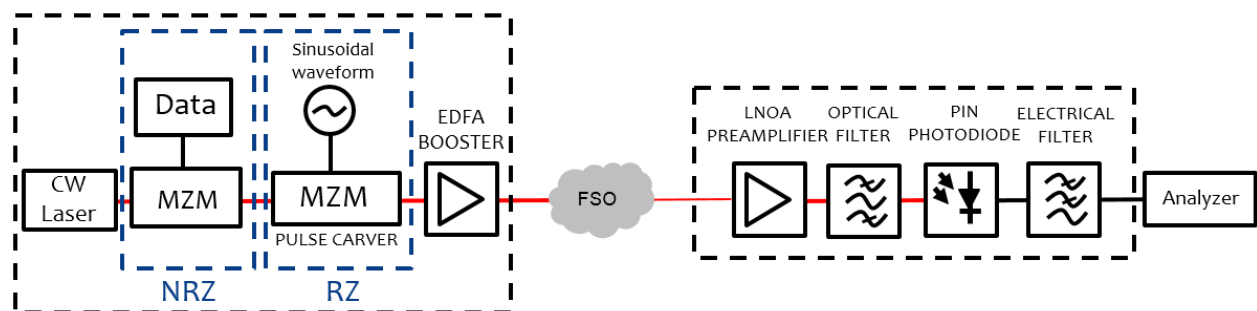
Figure 3-1: Transceiver designed under VPItransmissionMaker™ for both NRZ OOK and RZ OOK signal generation and preamplified direct detection receiver

3.2.1.1   Optical links parts

This optical link is known as an Intensity Modulation with Direct Detection receiver (IMDD). The OOK transmitter is made up using a CW laser and a MZM intensity modulation driven by the electrical data signal. The data stream is a Pseudo –Random Binary Sequence (PRBS) of $2^{31} - 1$ bits with data rate of 10 Gb/s. Other global parameters are given in Table 3-1. To convert this sequence on an electrical signal and to be on the closest experimental condition, an NRZ electrical coder is used with a raised-cosine shape with 22ps rise/fall time and total jitter duration (peak to peack) of 1.1 ps. The optical carrier is taken on the C-band (1550 nm) at 193.1 THz. The Table 3-1 and Figure 3-2 illustrate the global parameters of the link and the generated OOK optical signal with its eye diagram.

Simulation parameters	
Data rate	10 Gb/s
Sample per symbol	16 Samples
Number of simulated bits	2^{16} bits
Sample rate	160 GS/s
Time window	6.55 ms

Table 3-1: Global simulation parameters
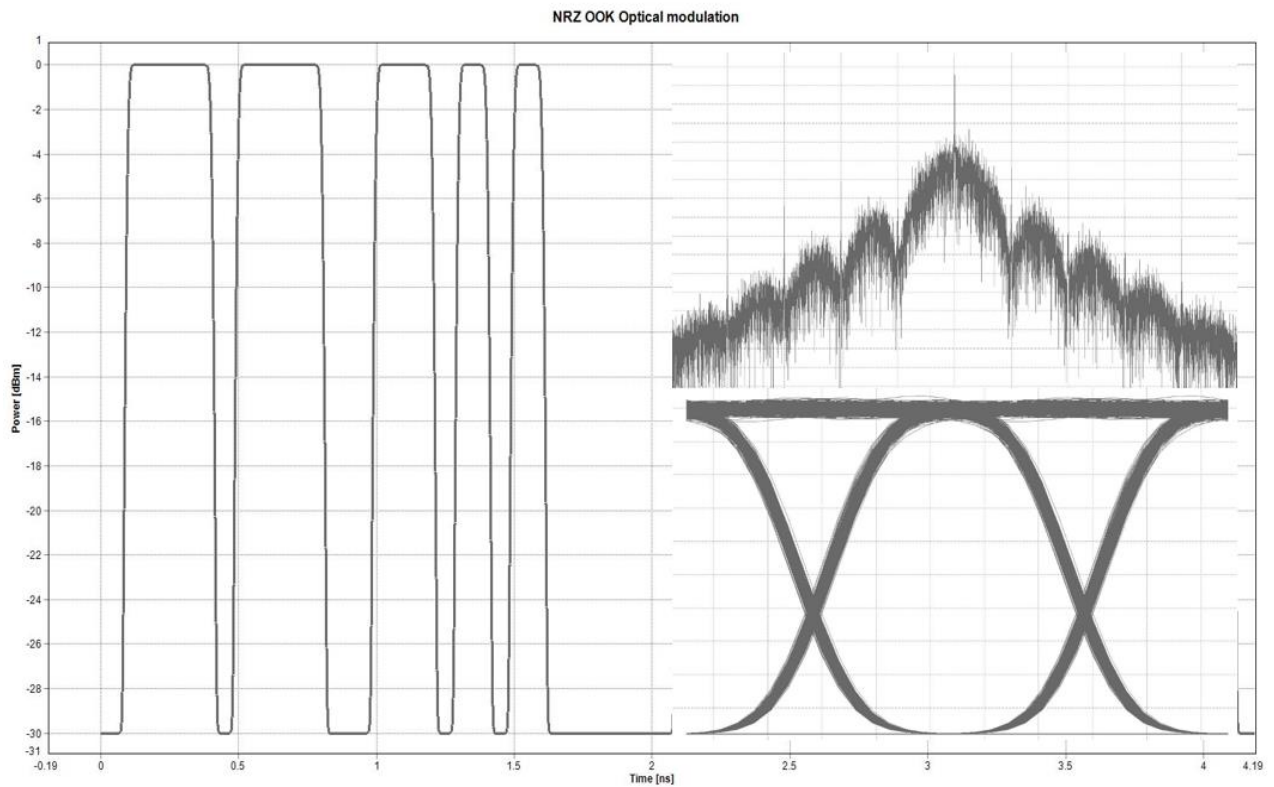
Figure 3-2: NRZ OOK optical signal (left) with eye diagram (down right) and optical spectrum (top right)

For the RZ, a second MZM is cascaded to the first one in order reduce the duty cycle. According to the bias voltage and the amplitude of the data signal, the duty cycle changes (cf. 2.2.4.1.2). We will only focus on the 50% RZ optical modulation in order to illustrate the effect of reducing cycle. Figure 3-3 shows 50% RZ OOK optical signal with associated optical spectrum and eye diagram.
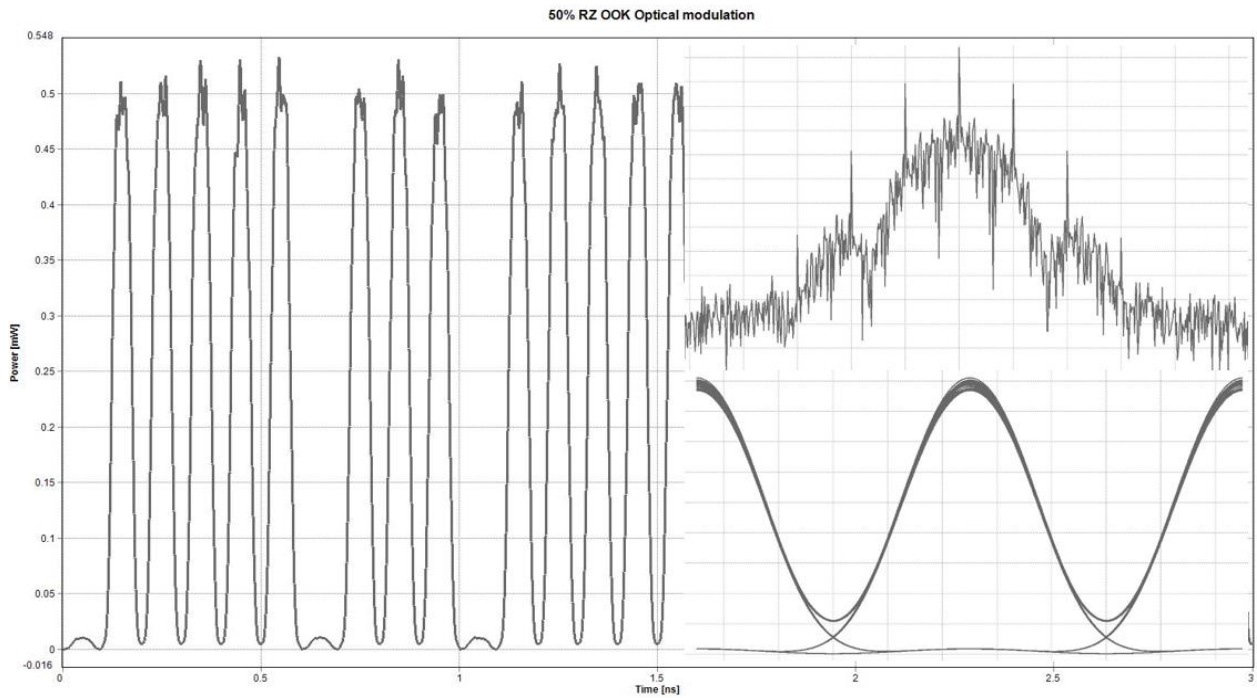
Figure 3-3: RZ OOK optical signal (left) with eye diagram (down right) and optical spectrum (top right)

An optical booster is used after the transmitter in order to compensate the losses due to the propagation through the atmosphere. The receiver is a preamplified optical receiver based on PIN photodetector. Table 3-2 summarizes the used parameters of the main devices.

To estimate the link performance without atmospheric conditions, the transmitter is connected to the receiver using a variable optical attenuator to modify the power level reaching at the input of the receiver and to estimate data transmission for different power level. In this way the attenuation has a fixed value over the total simulated time span.

Transmitter		Receiver	
Wavelength communication	1550 nm	EDFA Preamplifier	
CW Laser		Gain	20 dB
Linewidth	10 MHz	Noise figure	5 dB
RIN	-150 dB/Hz	Optical filter	
Data generation		Type	Gaussian
Rise/fall time type	Raised-cosine	Filer order	1
Rise/fall time duration	22 ps	Bandwidth	Optimized
Jitter duration	1.1 ps	Photodiode	
MZM		Responsivity	0.9 A/W
Extinction ration	30 dB	Dark current	0 nA
Insertion loss	4 dB	Thermal noise	$10\ pA/(Hz)^{0.5}$
Bias transmission	50%	Electrical filter	
Booster amplifier		Type	Low-pass Bessel 5th order
Gain	20 dB		
Noise figure	6 dB	Bandwidth	Optimized

Table 3-2: Transmitter and receiver parameters used for OOK link communication

81

To be able to make a comparison between simulation performances and experimental results, all simulation parameters are chosen to match with components that will be used on the optical bench for experimental validation.

- **BER calculation**

In well-designed FSO systems, BER performance is limited by the noise and the jitter that may cause errors on the link. One question raised by statistical BER estimation is how many bits must be transmitted through the system for a reliable result. The required number of bits to accomplish it depends on the required confidence level and the required BER threshold. The confidence level is defined as the percentage of test that the system's true BER value is less than the specified BER (with an ideal value of 100%) and for $BER = 1.10^{-9}$ with the level confidence of 95%, the required number of bits to be received is given by [95]:

$$N_{Bits} = \frac{-ln(1-CL)}{BER} \approx \frac{3}{BER} \approx 3.10^9 \; bits \qquad (3.1)$$

For data rate of $R = 10$ Gbps, the accumulation time is defined as:

$$T_{Accumulation} = R.N_{Bits} = 3s \qquad (3.2)$$

This approximation will be used for the whole dissertation work.

3.2.1.2 Link performances

After generating the OOK optical signal, the variable optical attenuator is used on the aim to get the link performances for different received optical power. The attenuation value is shifted by 1 dB and the BER is estimated as described before for each iteration. Figure 3-4 shows the BER variation for different average optical power. The sensitivity of the link is defined as the mean optical power at the input of the receiver required to satisfy a target BER. The chosen value for BER is 10^{-9} which characterizes a so called error-free transmission.

- **BER curves at three data rates**
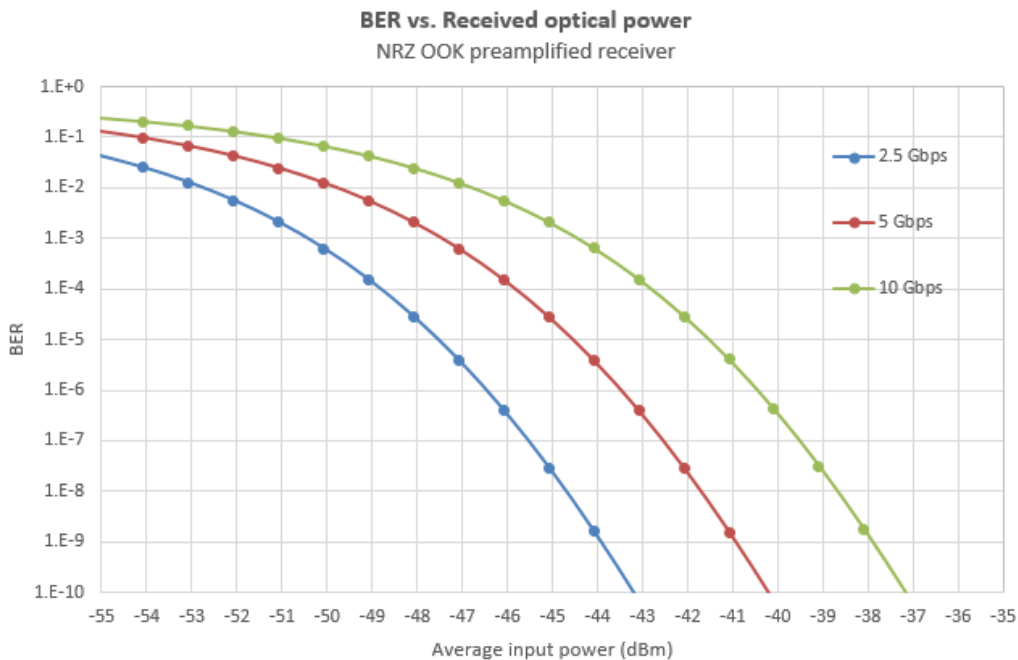
Figure 3-4: BER estimated for NRZ OOK link with preamplified receiver for three data rate values

We remark that when the data rate value is doubled, the power penalty between curves equals 3dB which matched well with the theory. We achieved a sensitivity of around-38 dBm for 10 Gb/s that is in the interval of state of art values. This value changes highly $(\pm 2\ dBm)$ by modifying any optical parameter such as optical bandwidth, electrical bandwidth, thermal noise or filtering types (this will be presented after).

- **Duty cycle effect**

For duty cycles are tested with the OOK optical link in order to illustrate its effects on the sensitivity of the link. Figure 3-5 depicts the BER curves simulated for duty cycles that are 33%, 50%, 67% and 100%. A duty cycle of 100% corresponds to NRZ modulation.
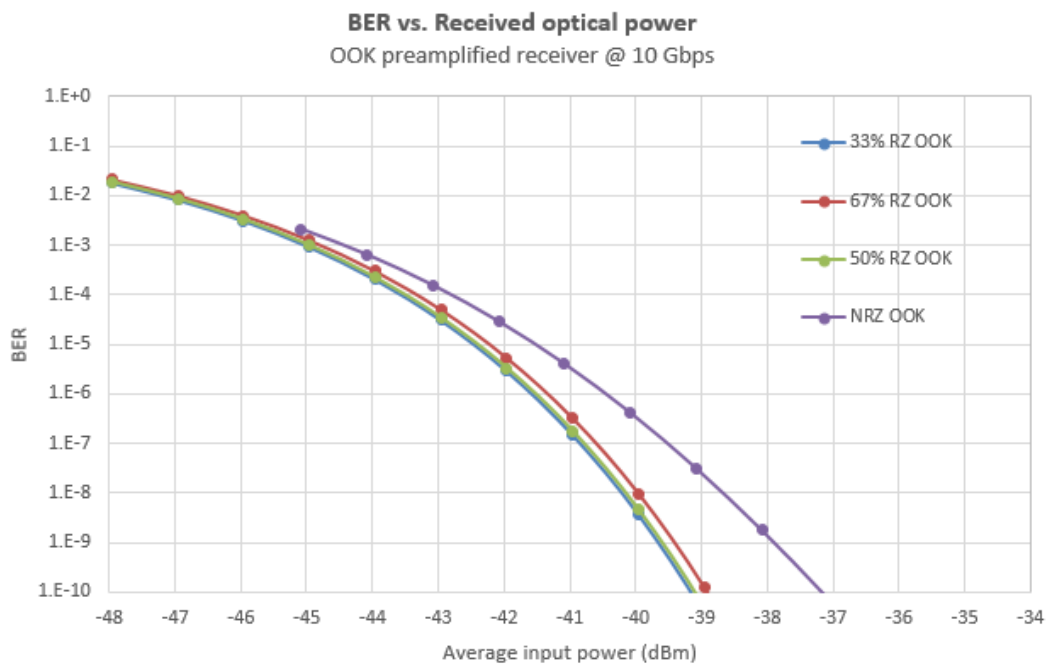
Figure 3-5: BER estimated for NRZ OOK link with preamplified receiver for different duty cycles @ 10 Gbps

We remark in these curves that reducing the duty cycle permit to increase the sensitivity of the receiver due to the energy concentration on the middle of the bit time. These short pulses allow to increase the robustness of the link and to get high sensitivities. Furthermore, we note that for 33%, 50% and 67% RZ OOK modulations, the sensitivity gain obtained by reducing the duty cycle is very low. This is due to the accumulation noise effects (rise/fall times, total jitter and optical amplifier noise). Hence, the decision time for short cycle to estimate the BER value, seems to be more difficult to adjust compared to NRZ OOK modulation where the optical signal spend more time at high level. This can explain the low difference between RZ BER curves. Figure 3-6 illustrates the duty cycle effect on the receiver sensitivity.
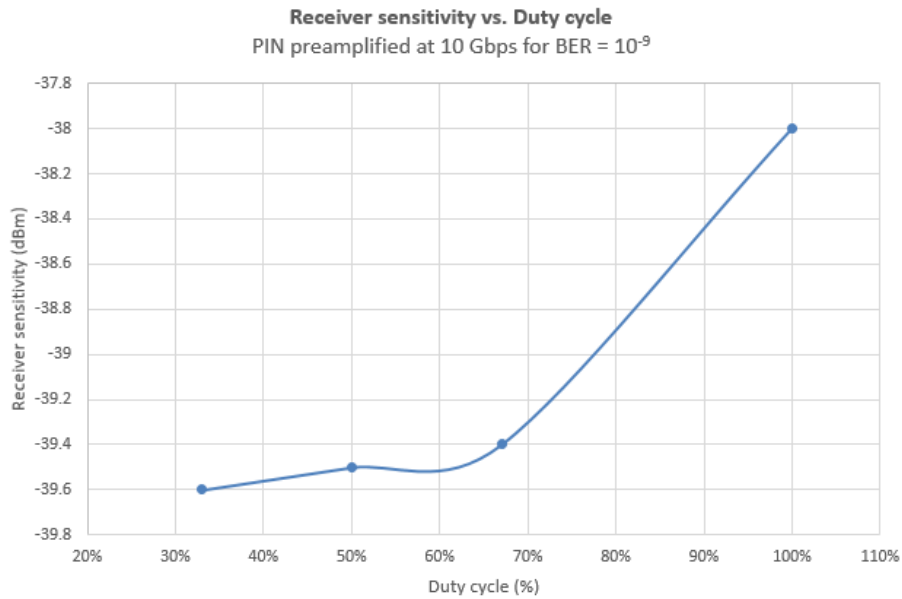
Figure 3-6: Receiver sensitivity vs. duty cycle for preamplified PIN receiver and a target of BER = 10^{-9}

As it can be remarked here, reducing the duty cycle aims at improving the link sensitivity up to 1.6 dB for 33% RZ. This is because all the energy of the bit is putted into a small fraction of the bit time leading to a better SNR at the receiver.

- **Receiver with avalanche photodetector (APD)**

The optical receiver based on an APD photodetector don't need any preamplification stage to amplify the optical signal after the propagation, thanks to it internal multiplication factor to amplify receiver photons numbers. Since theh EDFA is not required, we do not need to inject in single mode fiber. The signal can either stay in free space or be injected in multi-mode fiber. Both are compatible with the APD. Thus the APD receiver allows reducing the system complexity and power consupmtion but at the expense of a lower sensitivity and data rate limited by the APD bandwidth. Figure 3-7 illustrates the BER curves with an APD receiver.
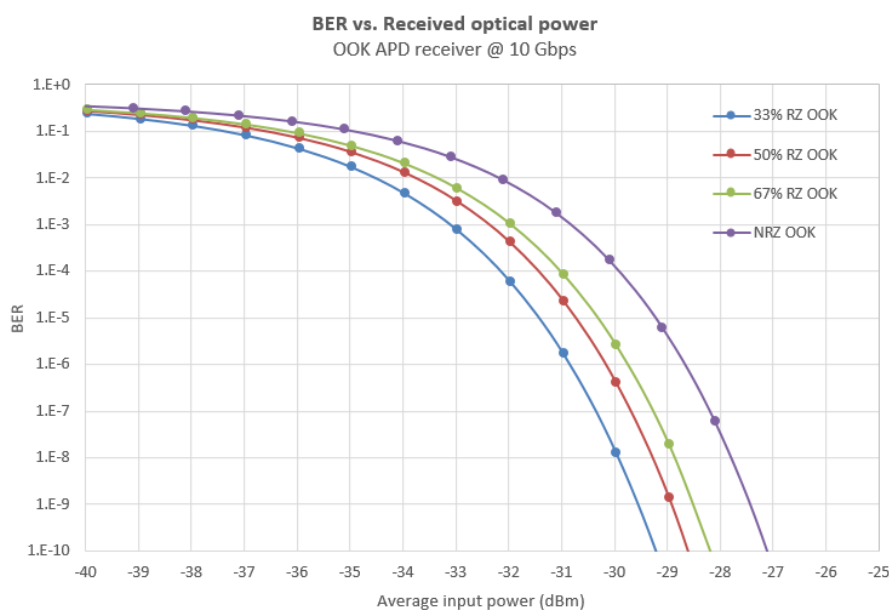
Figure 3-7: BER estimated for NRZ OOK link with avalanche photodetector (APD) as a receiver for different duty cycles

Contrary to the preamplified receiver, the improvement of the sensitivity by reducing the duty cycle is more important in the case of APD. The improvement can reach 2 dB between NRZ OOK and 33% RZ OOK modulation. For 10 Gb/s, the receiver sensitivity at $BER = 10^{-9}$ equals -27.5 dBm for a state of art value of -28.7 dBm. Figure 3-8 illustrates the duty cycle effect on the receiver sensitivity.

Receiver sensitivity vs. Duty cycle
APD receiver at 10 Gbps for BER = 10^{-9}
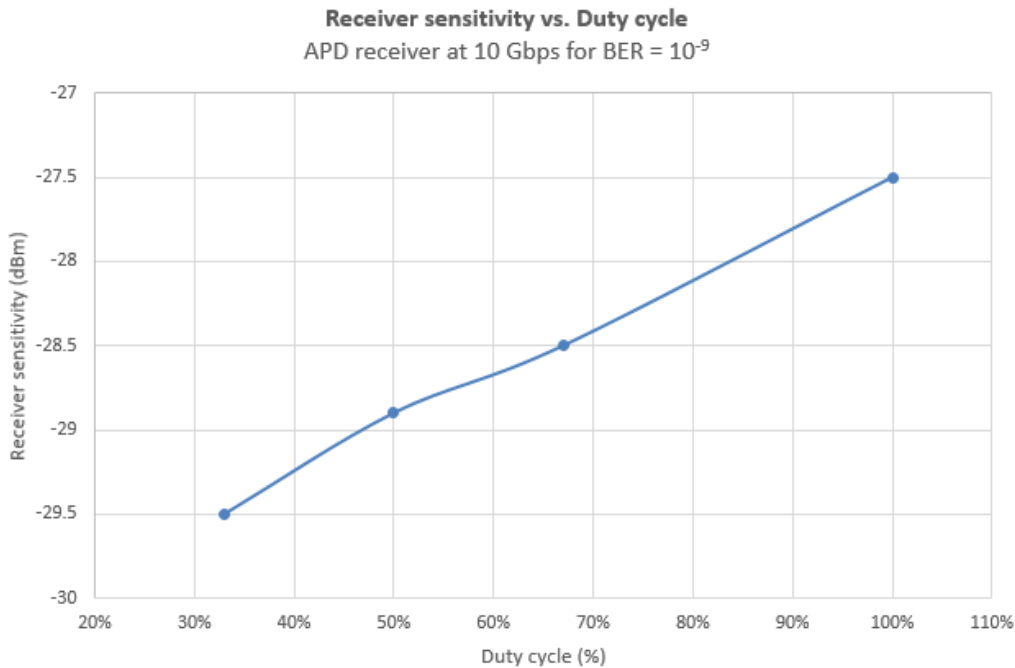
Figure 3-8: Receiver sensitivity vs. duty cycle for APD receiver

3.2.1.3   Main parameters effects

During the simulation process, we remarked that some model parameters act strongly on the link performances, and especially the model constituting the receiver. In this part, the optical and electrical filters bandwidths are studied in order to illustrate their effect on the BER estimation. The study is done for OOK optical link at 10 Gb/s with global parameters shown in Table 3-1. Previous duty cycle are also studied and the bandwidth values are compared with theoretical values [37] shown in Table 3-3.

	NRZ OOK	RZ OOK
Electrical bandwidth	0.75R	2R
Optical bandwidth	1.3R	2.5R

Table 3-3: State of the art values of optical and electrical bandwidth [2]

- **Optical bandwidth**

Firstly, the electrical bandwidth is fixed at the theoretical value. The electrical bandwidth is also varied for different duty cycles. This step allows having approximatively values of the optical bandwidths corresponding to the optimum of the sensitivity (shown in legend of Figure 3-9). Then the receiver sensitivity at $BER = 10^{-9}$ is estimated for each duty cycle and plotted in Figure 3-9.
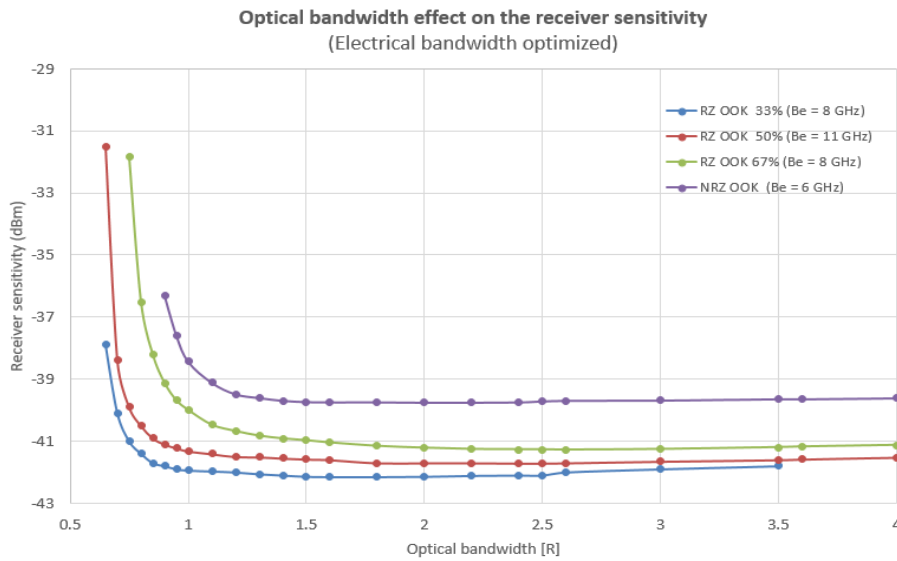
Figure 3-9: Optical bandwidth effect on the receiver sensitivity for different duty cycles

As we introduced briefly, the main objective of the optical filter is to reduce the amount of ASE reaching the detector to get reduced ASE-ASE beat noise. For RZ pulses, narrow-band optical filters lead to reduce the signal energy while for NRZ pulses they significantly increase the ISI. Thus, the tread-offs have to be made between the power going through the filter and the noise level to be filtered. Figure 3-9 shows a curve order that the smaller duty cycle is, the better receiver sensitivity become. In addition, for higher optical bandwidth (from 2R to 4R), the improvement could be neglected for BER at 10^{-9} and the best value of the optical bandwidth can be taken, for all duty cycles, between 1.2R and 1.5R. For the study of the electrical bandwidth effect, the optical bandwidth is set at the optimum value and the receiver sensitivity is plotted versus electrical bandwidth.

- **Electrical bandwidth**

In the same way, the optical bandwidth is fixed to the optimized value found in the previous optical filtering optimization and the electrical bandwidth values are varied. Receiver sensitivity is plotted in Figure 3-10.
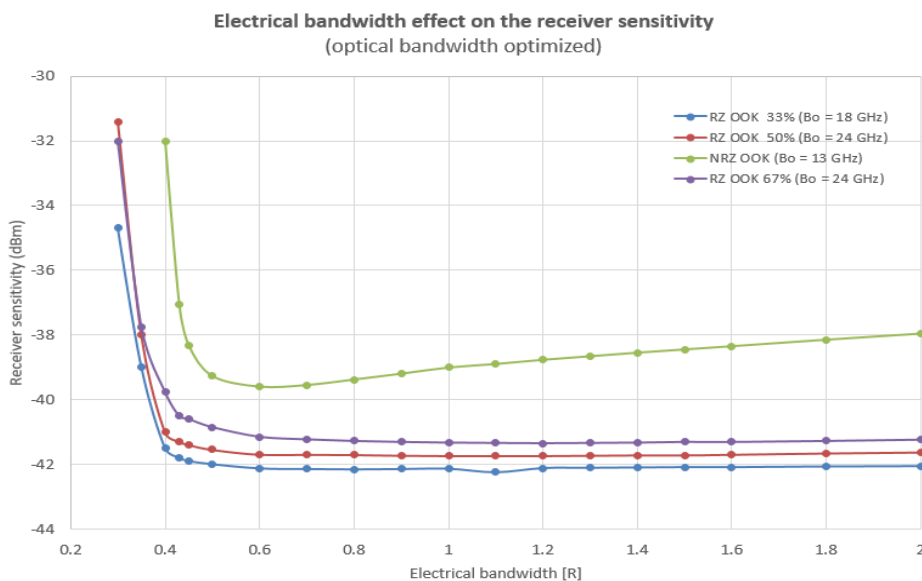
Figure 3-10: Electrical bandwidth effect on the receiver sensitivity for different duty cycles

For NRZ pulses, the receiver sensitivity shows an optimum around 0.6*R. This is consistent with respect of the theory. Low values of electrical bandwidth introduce ISI that degrade the BER. High values of electrical bandwidth are unable to filter enough noise which increases the BER. In contrary to NRZ, receiver sensitivity for RZ pulses seems to be unchanged for high electrical bandwidth values (similar effect as the optical bandwidth). Table 3-4 summarized optimum values of receiver sensitivity for OOK communication link.

Data rate	33%	50%	67%	NRZ
10 Gbps	-39.5 dBm	-39.6 dBm	-39.3 dBm	-38 dBm
5 Gbps	-41.5 dBm	-31.6 dBm	-41.3 dBm	-41 dBm
2.5 Gbps	-44.5 dBm	-44.6 dBm	-44.3 dBm	-44 dBm

Table 3-4: Summary of receiver sensitivities at BER=10^{-9} for different duty cycle and different data rate.

The next part is dedicated to the DPSK link where the optimized parameters are used to estimate the BER of the link and the receiver sensitivity.

3.2.2   DPSK communication link

As for OOK communication link, DPSK communication is studied in this part in order to optimize different tradeoffs (Noises, Receiver sensitivity, filtering) and give final performance of the link. Figure 3-11 illustrate a general view of the DPSK communication link.
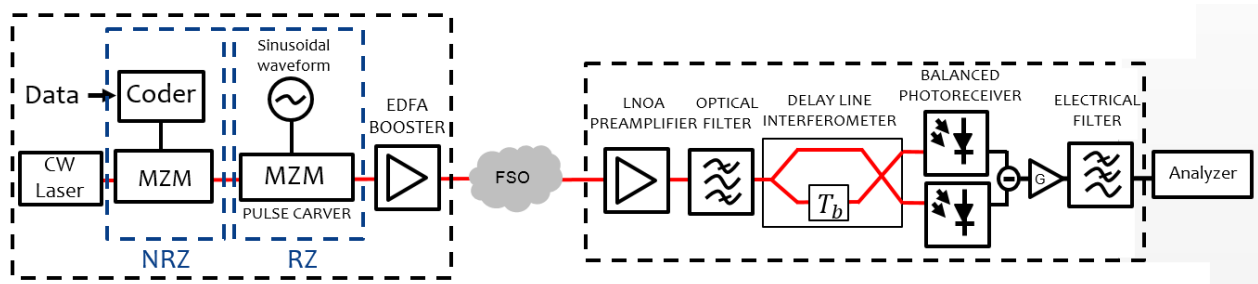
Figure 3-11: Transceiver designed under VPItransmissionMaker™ for both NRZ DPSK and RZ DPSK signal generation and preamplified receiver based on balanced photoreceiver and delay line interferometer

3.2.2.1   Optical transmitter

For the same optical carrier, a differential coder is used in order to convert the PRBS on differential PRBS where the data is coded the phase difference between successive bits. The optical modulator is biased on minimum of transmission with a modulation amplitude of $2V_\pi$ (c.f chapter2). With an optical analyzer, the optical signal can be shown with the associated optical spectrum and it eye diagram (Figure 3-12). The optical power is mostly on the ''1'' position and when differential data switches, the signal power presents a short transit to ''0'' before coming back the state ''1''. This transition can be also shown on the phase variation where the phase value changes for each transition of the optical power.
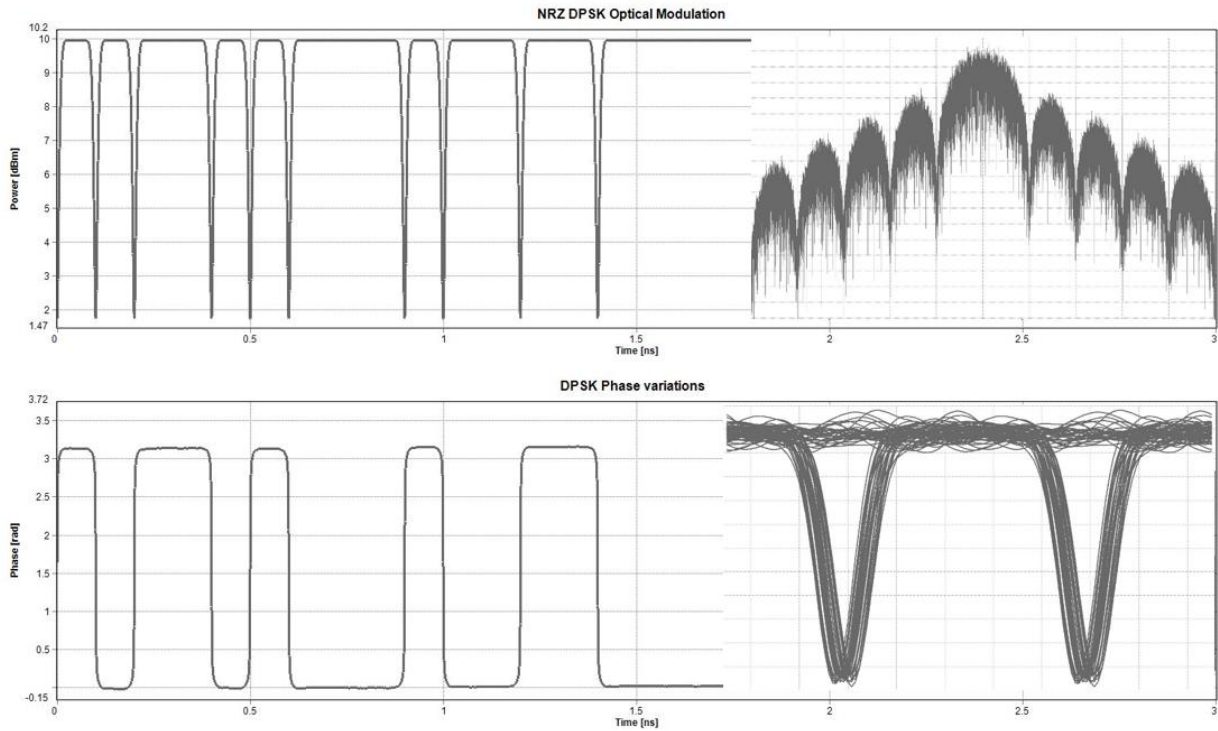
Figure 3-12: NRZ DPSK optical signal (left top) and phase variation (left down) with eye diagram (down right) and optical spectrum (top right)

To generate an RZ DPSK optical signal, the second modulator is biased in order to generate 50% RZ pulses. For the phase variation, there is no difference from NRZ DPSK and the optical signal present bits stream of ''1'' state with the desired duty cycle (it looks like a 50% RZ OOK with a data stream of one). The level of jitter is improved comparing to NRZ DPSK in order to decrease the loss level added by the second modulator. Figure 3-13 illustrate the 50% RZ DPSK optical signal with the associated optical spectrum and it eye diagram.
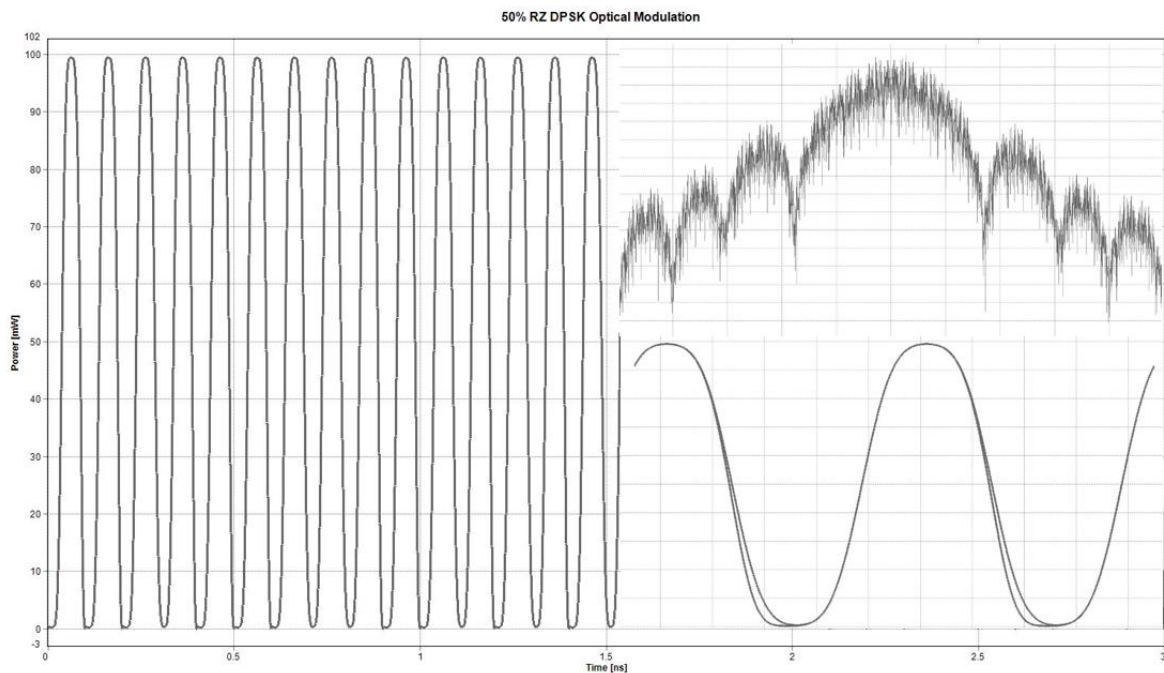
Figure 3-13: RZ DPSK optical signal (left) with eye diagram (down right) and optical spectrum (top right)

We can remark the jitter reduction effect on the eye diagram where the total transition time is lower than NRZ DPSK eye diagram. For the optical spectrum, the global characterization are identical for NRZ and RZ pulses except the size of RZ lobes that larger than NRZ lobes.

To estimate the link performance without atmospheric conditions, the transmitter is connected to the receiver using a variable optical attenuator to modify the power level arriving at the input of the receiver and to estimate data transmission for different power level.

3.2.2.2   Link performances

The DPSK link is set and simulated in order to estimate its performances on the absence of atmospheric turbulence. As the study done for OOK link concerning main parameters effects, DPSK link parameters are optimized and Figure 3-14 shows the BER curves for different duty cycles.
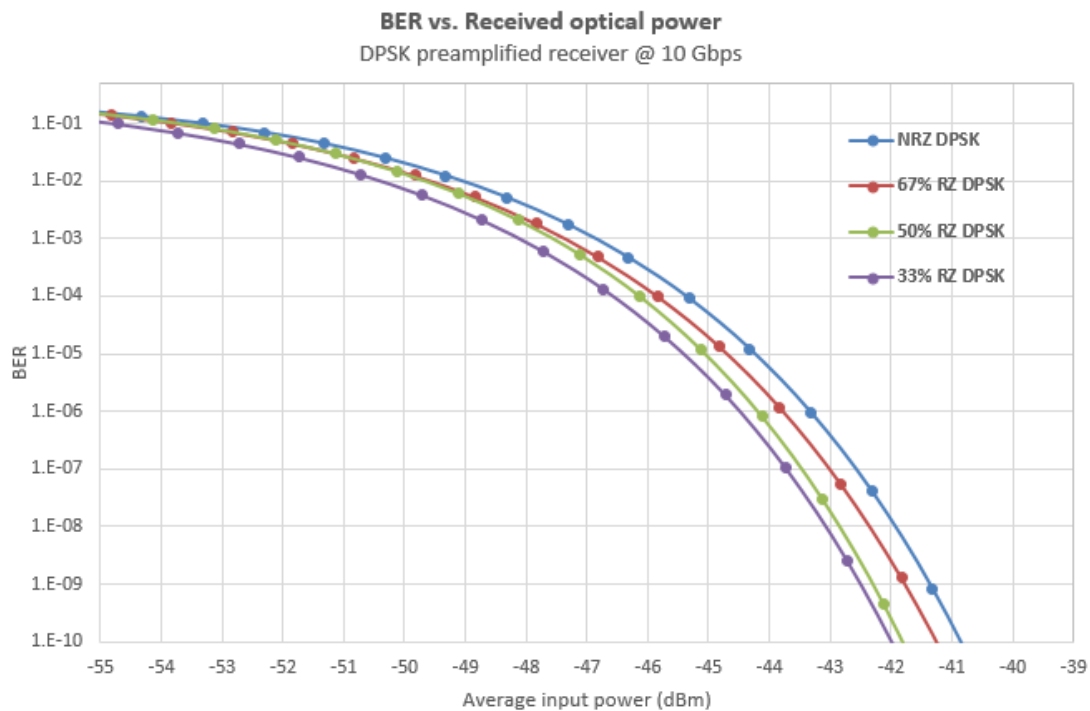
Figure 3-14: BER estimated for DPSK link for different duty cycles

The short duty cycles present an improvement of the receiver performance effect for the DPSK links. The NRZ DPSK shows an optical sensitivity of -41.2 dBm that corresponds to the state of the art value, of equivalent system [34]. In addition, for high value of the BER (10^{-2}or more), 50% and 67% BER curves intersect which means that no sensitivity gain is allowed.

The study of such system needs tradeoffs between all system parameters in order to achieve a given performance level. To be able to make a comparison with the experimental emulation links, all parameters are set to be the closest possible value to physical components that will be used on the optical bench. [96].

3.2.2.3   Summary of links performances

Table 3-5 illustrates the summary of link performances for both OOK and DPSK modulations and two different duty cycles (NRZ and 50%RZ). These values permits to achieve à $BER = 10^{-9}$ (objective of such applications) and atmospheric effects will be considered in the next level.

10 $Gbps$	NRZ OOK		50% RZ OOK		NRZ DPSK	50% RZ DPSK
	PIN	APD	PIN	APD		
Sensitivity at BER $= 10^{-9}$ (dBm)	-38	-27.5	-39.5	-28.8	-41.2	-42.3
Sensitivity at BER $= 10^{-3}$ (dBm)	-44.3	-30.8	-45	-32.2	-46.8	-47.5

Table 3-5: Summary of receiver sensitivities for both OOK and DPSK links and two different BER levels

Considering a BER at 10^{-9} which is considered as error free transmission, we can draw the following conclusions:

- NRZ OOK with APD has the lowest sensitivity but also the lowest complexity
- NRZ DPSK using balanced photo receiver with the EDFA has the highest sensitivity (not considering RZ variants) but also the highest complexity
- 50% RZ modulation allows increasing the sensitivity by roughly 1 dB comparing to NRZ
- PIN with EDFA receiver allows increasing the sensitivity by roughly 10 dB comparing to APD

So the optimal transmission chain to select will result in a trade-off between complexity and performances. Different markets will probably lead to different chosen solution.

On the next part, the propagation channel will be used to include atmospheric effects and to have an end-to-end FSO communication with more realistic conditions.

3.2.3 Atmospheric channel model

The atmospheric model for the uplink that we will use on the optical links simulated is an LOT. This model, detailed on 2.3.6.3 assumes that the turbulences can be integrated in a single phase screen placed at the transmitter prior to propagation. As a result, the effects of the propagation through all atmospheric layers are neglected inside the turbulent eddies. It has been demonstrated [52] that the LOT model is not fully accurate due to its lack of modeling the propagation of an optical beam through multiple phase screen but the advantage is its lowest complexity and simulation time

The phase screen, reminded in 2.3.6.3, is constructed as a linear combination of tip/tilt, defocus and astigmatism noted ϕ_{LOT}. Comparing to multiple phase screen propagation method where Zernike polynomial coefficients are estimated for each layer, the LOT coefficients are estimated over the whole turbulence volume in one screen phase. To illustrate the effects of the propagation of an uplink transmission through atmospheric layers, Camboullives compared in his PhD [54] the LOT model with 2-Layers Wave Optics (2L-WO). The conclusion is that the LOT model taking into account only a linear combination of tip/tilt, defocus and astigmatism, associated with only a two layers propagation are sufficient to describe the beam deformations resulting from atmospheric turbulence. Camboullives proposed a method to improve and expand the propagation in order to take into account the tracking and obtain time series of irradiance fluctuations for a given pointing ahead angle. This model is called WPLOT (With Propagation Low Order of Turbulence). Table 3-6 gives more information about these different models.

Model	Phase Screen Distribution	Propagation Method
LOT	*One phase screen obtained* *Linear combination of tip/tilt, defocus and astigmatism* *Placed at the transmitter*	*Analytic propagation of Gaussian beam*
2L-WO	*Two phase screens* *Linear combination of tip/tilt, defocus and astigmatism* *One at the ground layer and the one at 10 km*	*Fresnel propagation between the phase screens* *up to the satellite*
WPLOT	*Multiple phase screens* *Linear combination of tip/tilt, defocus and astigmatism* *Distributed along the propagation path*	*Analytic propagation of defocus effects* *(optical beam moving in front of the satellite)*

Table 3-6: Comparison of atmospheric propagation models

We will focus here on the average power fluctuation reaching the receiver telescope after emulating an atmospheric propagation with different turbulence strength. The next part is dedicated to the time series that can be generated with the WPLOT.

3.2.3.1   Time series

As an output of WPLOT model, time series are vectors of a given duration and resolution describing the impact on short term average optical power of the effects of the atmospheric channel. To describe different atmospheric effects where the fluctuations frequency is around $1\ kHz$, some parameters and approximation have to be taken into account.

The WPLOT can generate time series with different lengths but the computation time can be long (90 min for 1s times series and more than 2 days for 10s time series). For this raison, we will choose a time duration of 2s with 4000 samples/s which corresponds to 4 times the fluctuation frequency of the atmosphere). In addition, they are generated randomly even if compilation are done on the same conditions. Table 3-7 summarizes the main parameters used to emulate atmospheric effects with WPLOT.

Link parameter	value
Fried parameter r_0	$8.27\ cm$
Pointing telescope diameter	$16\ cm$
Tracking telescope diameter	$16\ cm$
Point-ahead angle PPA	$18.5\ \mu rad$
Delay before AO correction	$4\ ms$
Atmospheric profile	$Hufnagel - Valley\ 5/7$
Wind profile	$Bufton$
Elevation angle	90°
Beam waist	*Depend on the turbulence strenght*
Time duration	$2s$
Sample rate	$4000\ Samples/s$

Table 3-7: Global parameter used to emulate the WPLOT model

We will vary the beam waist to switch between weak turbulences regime, beam wander regime and strong turbulences regime according to a fixed Fried parameter value. The fading time is estimated in each case for times series of 2s with 4000 samples/s. Next figures illustrate the simulated time series due to LOT atmospheric turbulence in three cases. Each figure gives short term power fluctuations at the input of the satellite after atmospheric propagation for both after pre-compensation case and before pre-compensation case. These power fluctuations are generated around the power sensitivity of each optical receiver (-38dBm for OOK receiver and -41.2 dBm for DPSK receiver).

According to the value of Fried parameter of 8.27 cm, the optical beam size values that are chosen in order to have different turbulence cases over the same atmospheric propagation mode are presented in the Table 3-8

	Fried parameter	Beam size
Weak turbulences regime $\omega_0 < r_0$	8.27 cm	4 cm
Beam wander regime $\omega_0 \approx r_0$	8.27 cm	8 cm
Strong turbulences Regime $\omega_0 < r_0$	8.27 cm	16 cm

Table 3-8: The optical beam size considered to model of atmospheric turbulences

Here after, the time series generated in different cases are given where the pre-compensation by the adaptive optics is illustrated.

- **Low turbulences case**
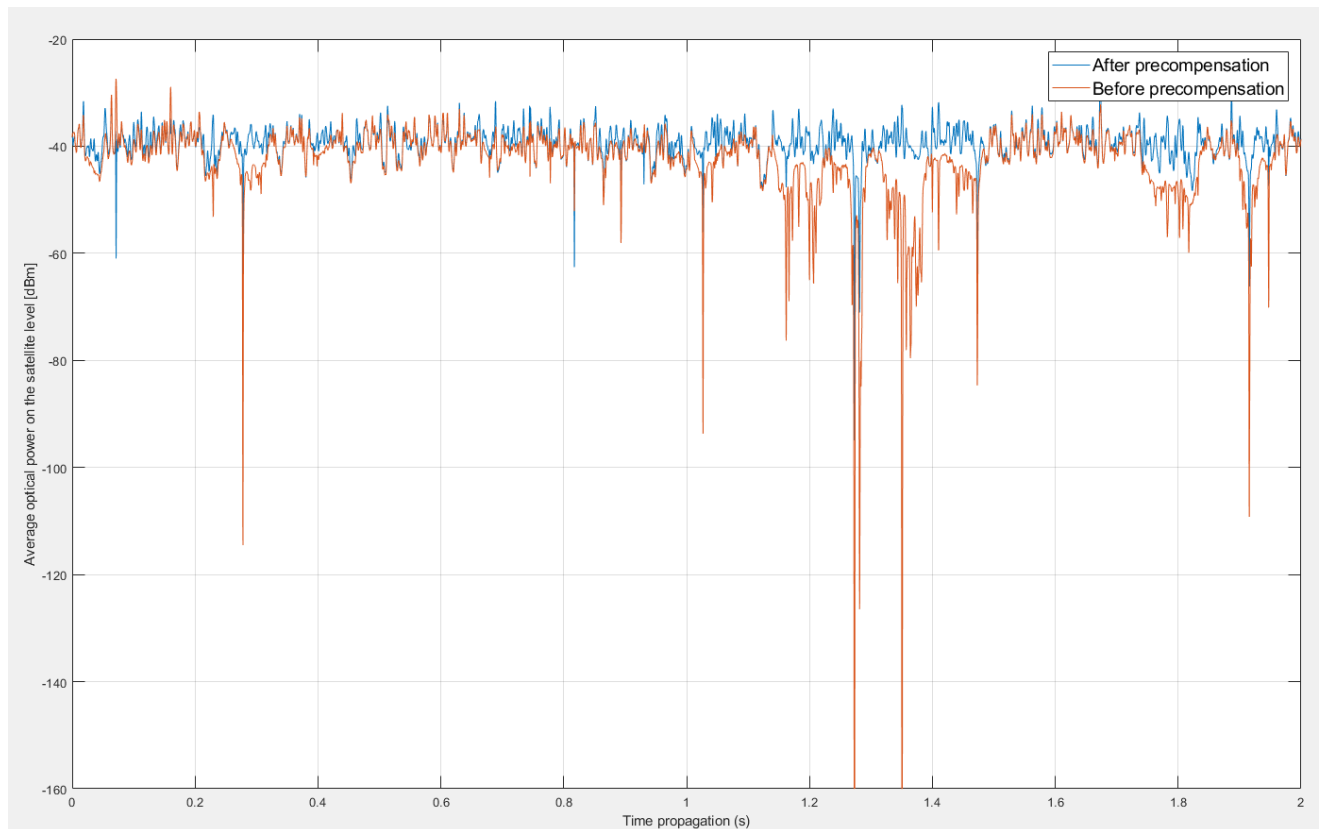
Figure 3-15: Times series of 2s with 4000 Samples/s generated with WPLOT on the case of low atmospheric turbulences (w_0 = 4 cm & r_0 = 8.27 cm) for both after pre-compensation case and before pre-compensation case

For low turbulences, power fluctuations without pre-compensation present very short time duration with huge power fading except around 1.4s and 1.8s where the duration time equals 0.1s. After pre-compensation process, it can be remarked that the average power is less fluctuating and the previous fading duration time becomes less important. Consequently, the fluctuation effects can be shown on the fading estimation.

The beam waist is now changed to be nearly equal to Fried parameter. The beam wander regime is then considered.

- **Beam wander regime**
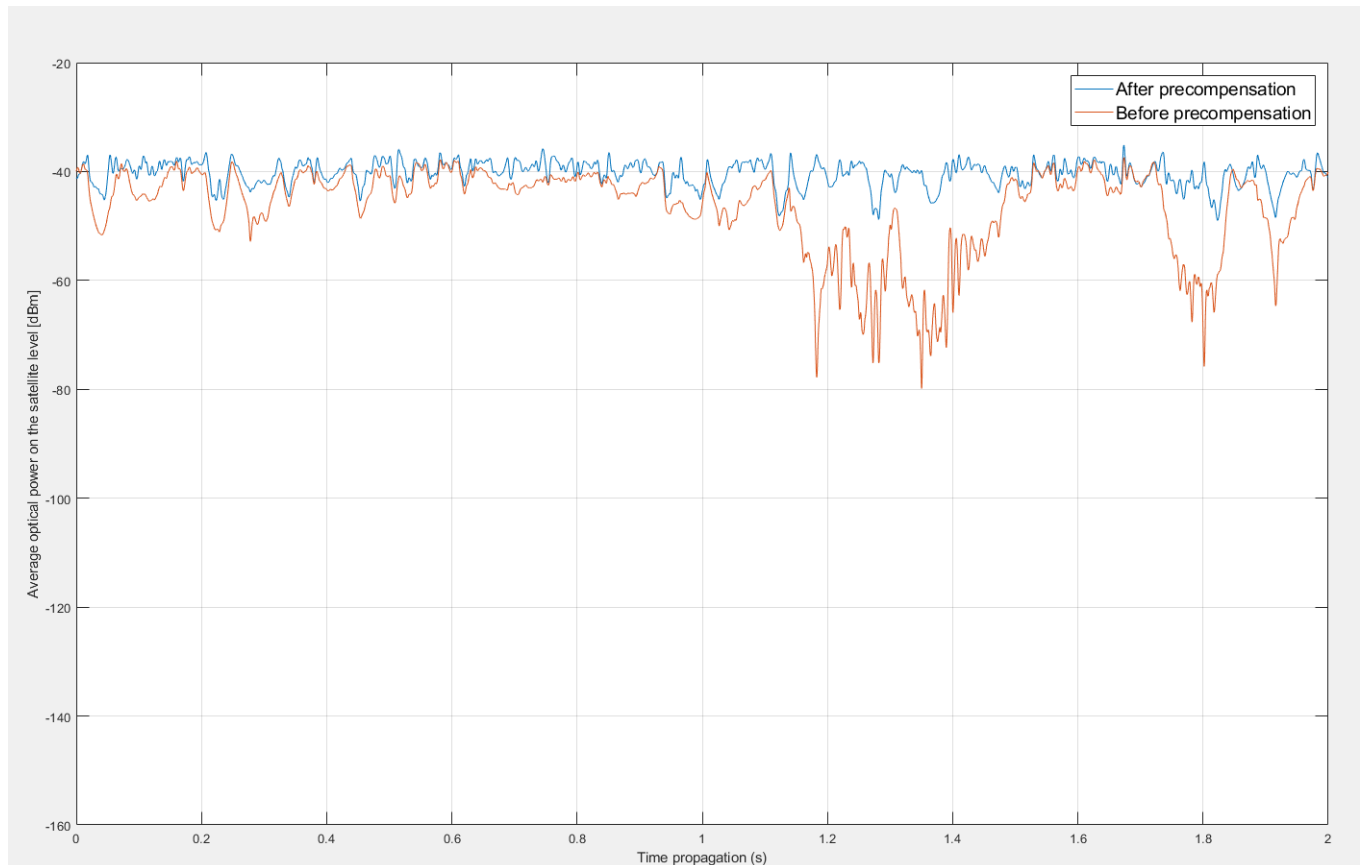
Figure 3-16: Times series of 2s with 4000 Samples/s generated with WPLOT on the case of beam wander regime (w₀ = 8 cm & r₀ = 8.27 cm) for both after pre-compensation case and before pre-compensation case

By comparing the beam wander regime to low turbulences, it can be shown that the power fluctuates at low instantaneous power levels (between 1.2s, 1.4s and 1.8s). The total average power receiver during 2s is less than the low turbulence case. The power fading are also reduced compared to the previous studied regime. If we predict the case of strong turbulences, this average power could be less with long time duration at low instantaneous power.

- **Strong turbulences**
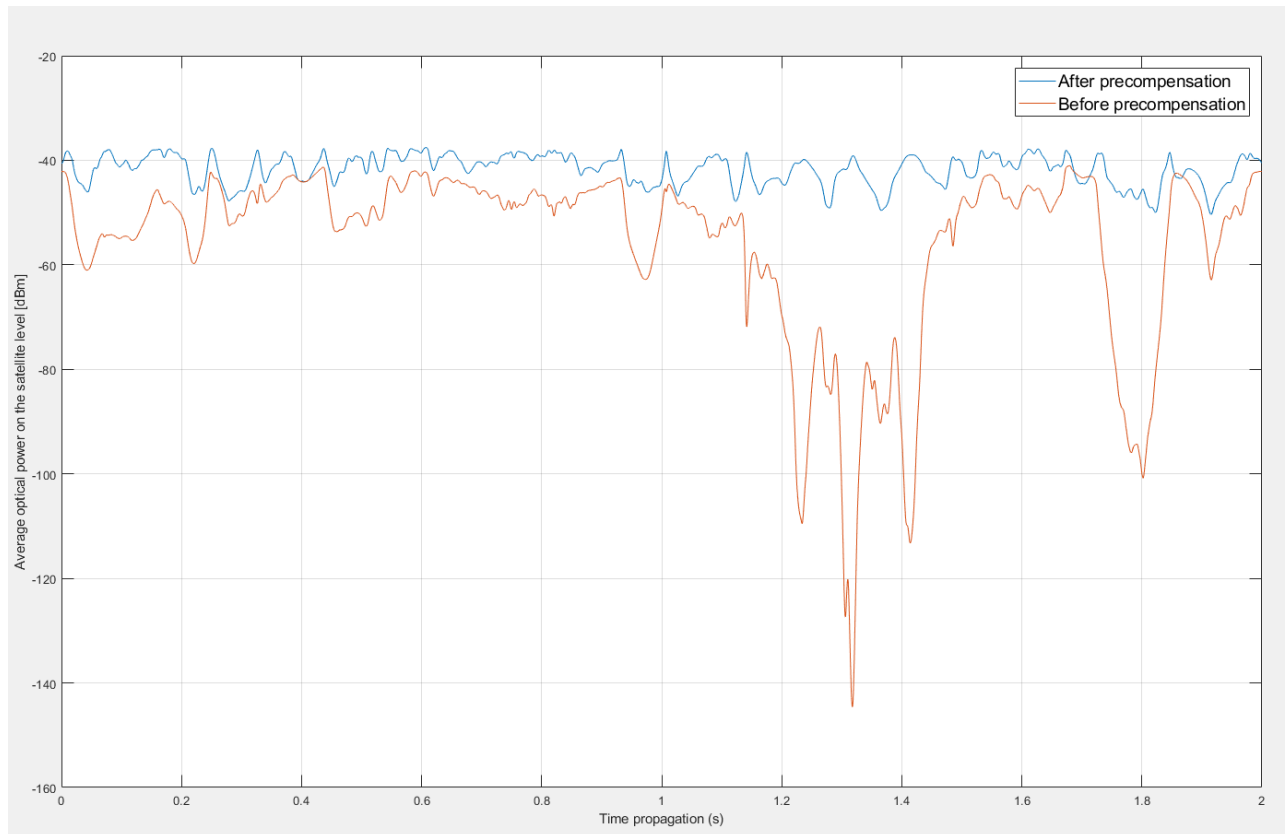
Figure 3-17: Times series of 2s with 4000 Samples/s generated with WPLOT on the case of strong
(w₀ = 16 cm & r₀ = 8.27 cm) for both after pre-compensation case and before pre-compensation case

This case illustrates very low optical power reaching -140 dBm with total absence of the signal for more than 0.1s of propagation. The fading estimation is more important and may be in some case equal to 100% for all the time series.

The fading time (the time during which the power is below the sensitivity of the optical transmission chain) is estimated for both OOK and DPSK communication in these three cases. Table 3-9 summaries the cases studied in this manuscript. We denote by AO the pre-compensation using AO.

	OOK communication link		DPSK communication link	
	NRZ	RZ	NRZ	RZ
Weak turbulences regime $\omega_0 < r_0$	Before AO	Before AO	Before AO	Before AO
	After AO	After AO	After AO	After AO
Beam wander regime $\omega_0 \approx r_0$	Before AO	Before AO	Before AO	Before AO
	After AO	After AO	After AO	After AO
Strong turbulences Regime $\omega_0 < r_0$	Before AO	Before AO	Before AO	Before AO
	After AO	After AO	After AO	After AO

Table 3-9: FSO communication link cases (Red: high turbulence, Orange: beam wander effect, Green: low turbulence)

Results will be given for two BER values $BER = 10^{-9}$ (considered as error free transmission) and $BER = 10^{-3}$ (considered the used of error code correction for giving finally error free transmission).

3.2.3.2   Weak turbulences regime

The beam waist is set at 4 cm to be on the weak turbulences regime. In the following table, the values in percentages describes the total time duration where the average optical power is under link sensitivity.

OOK DPSK	Without pre-compensation			With pre-compensation		
	Average power (dBm)	Fading time (%)		Average power (dBm)	Fading time (%)	
Duty cycle		NRZ	50%RZ		NRZ	50%RZ
Power threshold @ BER = 10⁻³	-42.7 -45.9	23.71% 28.36%	20.76% 23.71%	-39.5 -42.7	4.65% 6.61%	3.33% 4.65%
Power threshold @ BER = 10⁻⁹		89.31% 86.21%	70.30% 75.95%		86.21% 72.14%	45.89% 54.66%

Table 3-10: Fading time estimation over 2s atmospheric propagation on the weak turbulence regime for OOK and DPSK

For both OOK and DPSK, the average power is improved by $3\ dB$ on the case of pre-compensation. It means that the pre-compensation of atmospheric effects aims to focus more the optical beam on the receiver sensor and reduces the amplitude of moving. The fading time over 2s time series is also improved, from 28.36 % to 6.61 % for NRZ DPSK at BER = 10⁻³ and from 23.70 % to 4.65 % for NRZ OOK at BER = 10⁻⁹.

Now, we will increase the turbulence strength by choosing the beam size equaling the Fried parameter.

3.2.3.3   Beam wander regime

The beam waist is set at 8 cm to be in the beam wander regime.

OOK DPSK	Without pre-compensation			With pre-compensation		
	Average power (dBm)	Fading time (%)		Average power (dBm)	Fading time (%)	
Duty cycle		NRZ	50%RZ		NRZ	50%RZ
Power threshold @ BER = 10⁻³	-46.5 -49.7	44.38% 49.76%	40.93% 44.38%	-40.3 -43.5	6.88% 9.69%	4.43% 6.88%
Power threshold @ BER = 10⁻⁹		99.83% 99.83%	92.50% 95.65%		89.20% 89.20%	58.96% 67.01%

Table 3-11: Fading time estimation over 2s atmospheric propagation on the beam wander turbulence regime for OOK and DPSK

In the beam wander case, the improvement can reach $\sim 6\ dB$ after pre-compensation for both OOK and DPSK optical link. However, the fading time over the 2s of atmospheric propagation moves from 72.14 % to 89.20 % on the case of DPSK optical link and after pre-compensation.

The next case illustrates the worst case of atmospheric turbulence where the optical beam size equals two times the Fried parameter

3.2.3.4   Strong turbulences regime

The beam waist is set at 16 cm to be in the strong turbulences regime.

OOK DPSK	Without pre-compensation			With pre-compensation		
	Average power (dBm)	Fading time (%)		Average power (dBm)	Fading time (%)	
Duty cycle		NRZ	50%RZ		NRZ	50%RZ
Power threshold @ BER = 10^{-3}	-56	83.36% 88.40%	80.01% 83.36%	-41.8	22.20% 28.04%	16.39% 22.20%
Power threshold @ BER = 10^{-9}	-59.2	100% 100%	100% 100%	-44.9	98.44% 98.44%	75.11% 81.40%

Table 3-12: Fading time estimation over 2s atmospheric propagation on the strong turbulence regime for OOK and DPSK

This case (the worst case of turbulence) presents big fading up to 100%. It means that the average optical power received on the satellite is still under the link sensitivity for BER = 10^{-9} for both OOK and DPSK. The emission power has to be increased in order to allow the transmission in this atmospheric regime. The gain of the AO pre-compensation on the average power is more important on the strong turbulence case (15 dB) but the fading duration are still important for both threshold.

3.2.3.5   Summary of fading statistics

This part illustrates the benefit of the pre-compensation process and how it leads to improve the fading for both thresholds of BER. To make a well comparison between different turbulence cases, Figure 3-18 illustrates average power variation in each case.
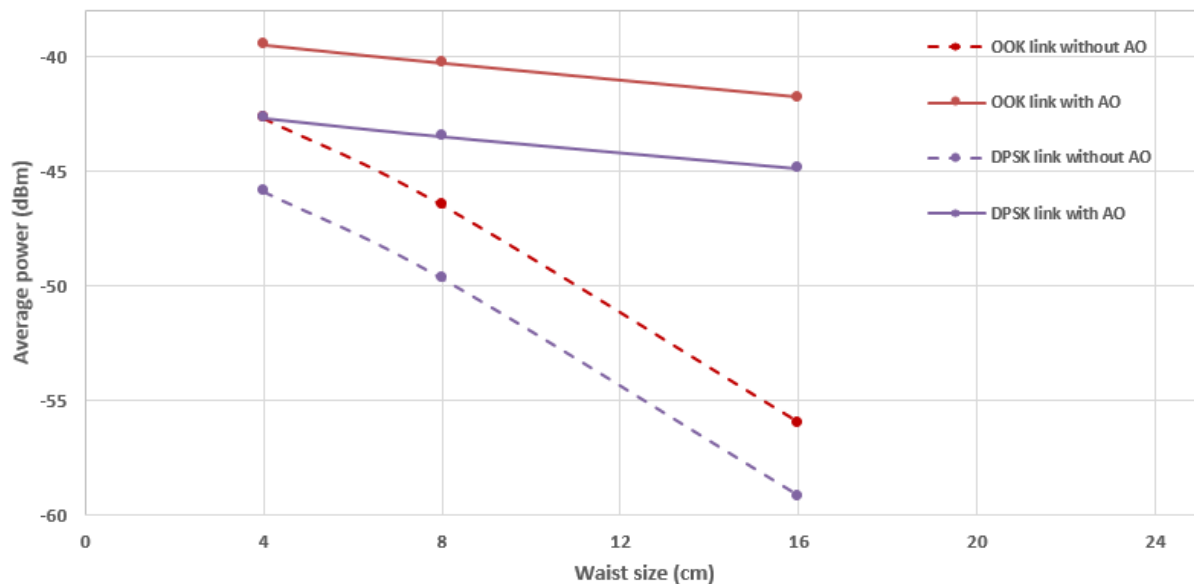
Figure 3-18: Average optical power received after propagation for different turbulence scenarios (given by the beam size)

The improvement in average received optical power due to the AO pre-compensation increases when the turbulent regime is increased relatively to the beam diameter. In addition, one can note that, for the weak turbulence, OOK link without AO and DPSK link with AO show the same received power due to their different receiver sensitivity. Hence, for the same performance, the optical link to be considered could be the OOK link because of its low complexity of transceiver architectures. In

addition, the way that the received power decreases on the case of without AO is higher than with AO in both of OOK and DPSK links. The communication stay strong when the turbulence become strength.

An improvement of 15 dB have to be noted on the case of high turbulences thanks to the AO pre-compensation.

If we focus now on the fading optimization, Figure 3-19 illustrates fading time evolution where the values can achieve 88%. With the pre-compensation, the worst fading time value is less than 30% for strong turbulences. In addition, we can remark also that the OOK link presents low values than DPSK links with and without AO.
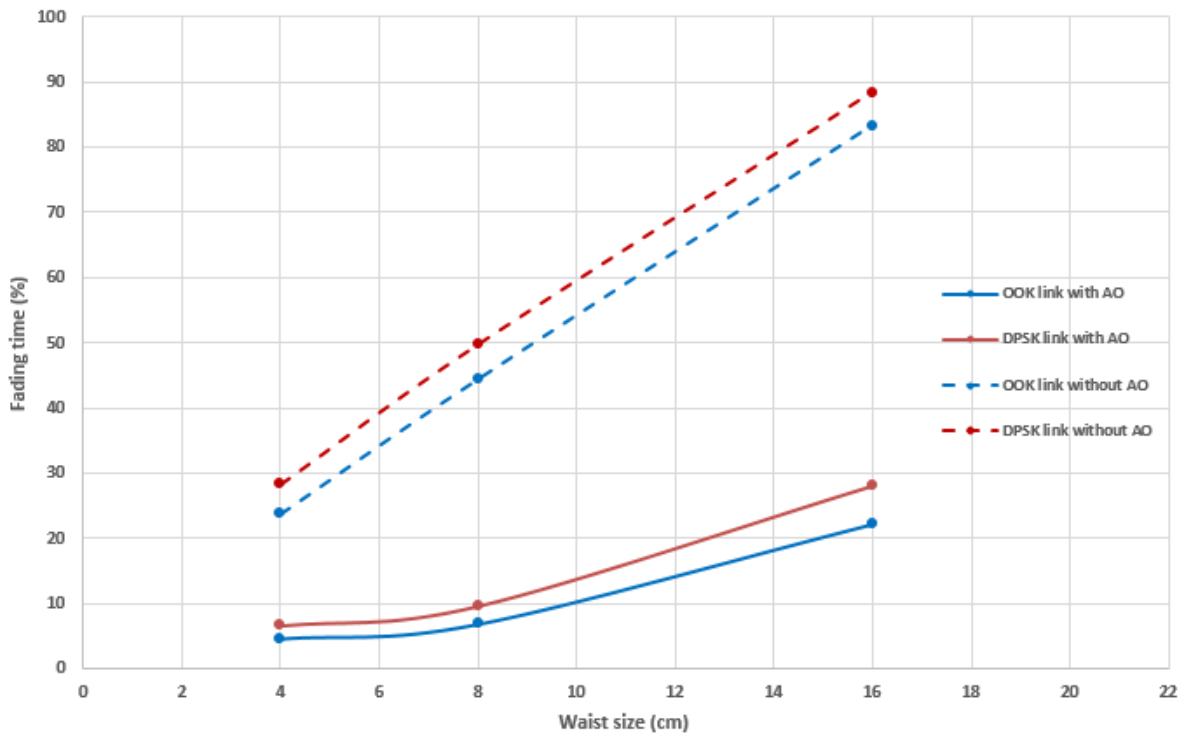
Figure 3-19: Fading time estimation over 2s atmospheric propagation vs. turbulence strength (given by the beam size) (both of NRZ OOK and NRZ DPSK links for BER at 10^{-3})

The receiver threshold is set to the sensitivity corresponding to 10^{-3} of BER. The required received power is low in this case and for this reason, we achieved a very low fading time values (less than 10%). In addition, all curves tend to the 0% fading for lowest value of the beam size. The Figure 3-20 illustrates the same curves but with receiver threshold corresponding to the 10^{-9} of BER.
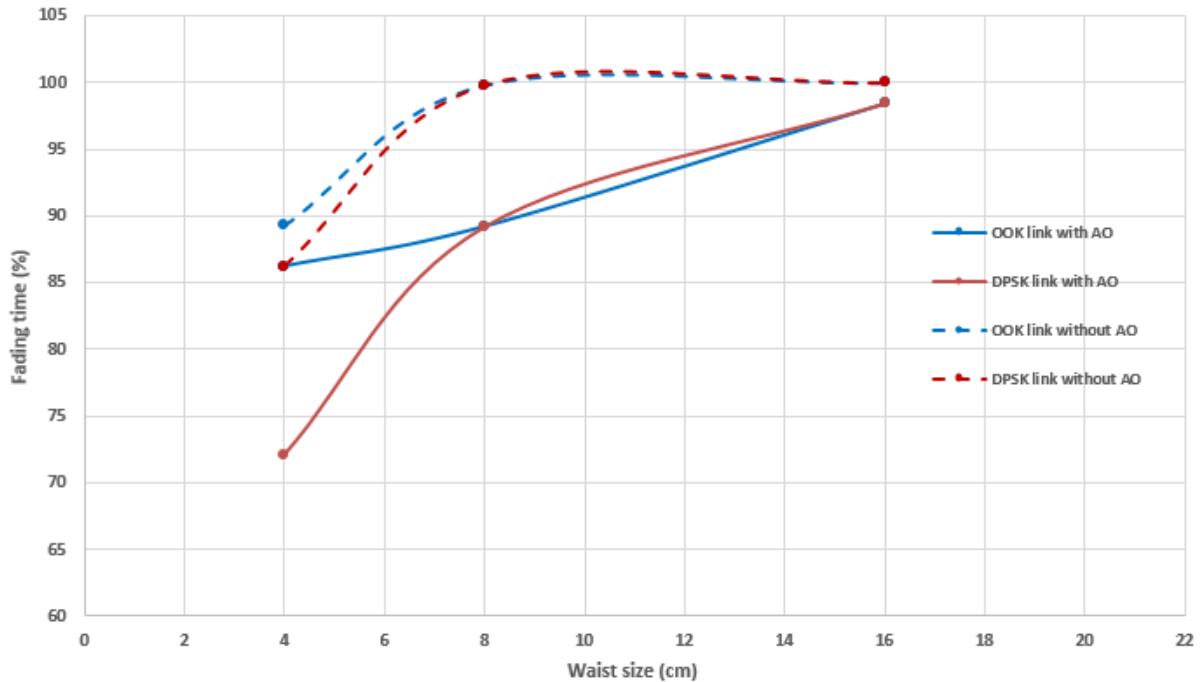
Figure 3-20: Fading time estimation over 2s atmospheric propagation vs. turbulence strength (given by the beam size) (both of NRZ OOK and NRZ DPSK links at 10^{-9})

We remark that all fading time values are located between 70% and 100% and the best value is achieved for DPSK link with AO. In addition, all curves tend to the maximum of the fading (100%) when the beam size rises.

3.2.3.6   Validity of the model

The French aerospace laboratory ONERA has developed a computer code called PILOT (Propagation and Imaging, Laser and Optics, through Turbulence) in order simulate the propagation of an optical beam through random media [97]. TURANDOT is based on the phase screen algorithm generated by PILOT dedicated to study situations which cannot be described with analytical approaches (scintillation saturation regime, temporal evolution and laser beam propagation). The advantage of this atmospheric propagation emulator is the ability to consider all type of waves-forms (spherical, plane, or truncated Gaussian beams) [97]. TURANDOT, using higher order of Zernike polynomials, has been validated in downlink case with experimental data from Optical Inter-orbit Communications Engineering Test Satellite [97].

A.R. CAMBOULIVES has compared the WPLOT performances with TURANDOT emulator which provides a description of the irradiance fluctuations in presence of Tip/Tilt correction and under different strength of turbulences. In addition, the WPLOT is much faster than TURANDOT against the small range of its employability. An example of probability density function (PDF) comparison between both of models is shown in Figure 3-21 [52]–[54]. A detailed description of the used function in WPLOT emulator is given in appendix 8.
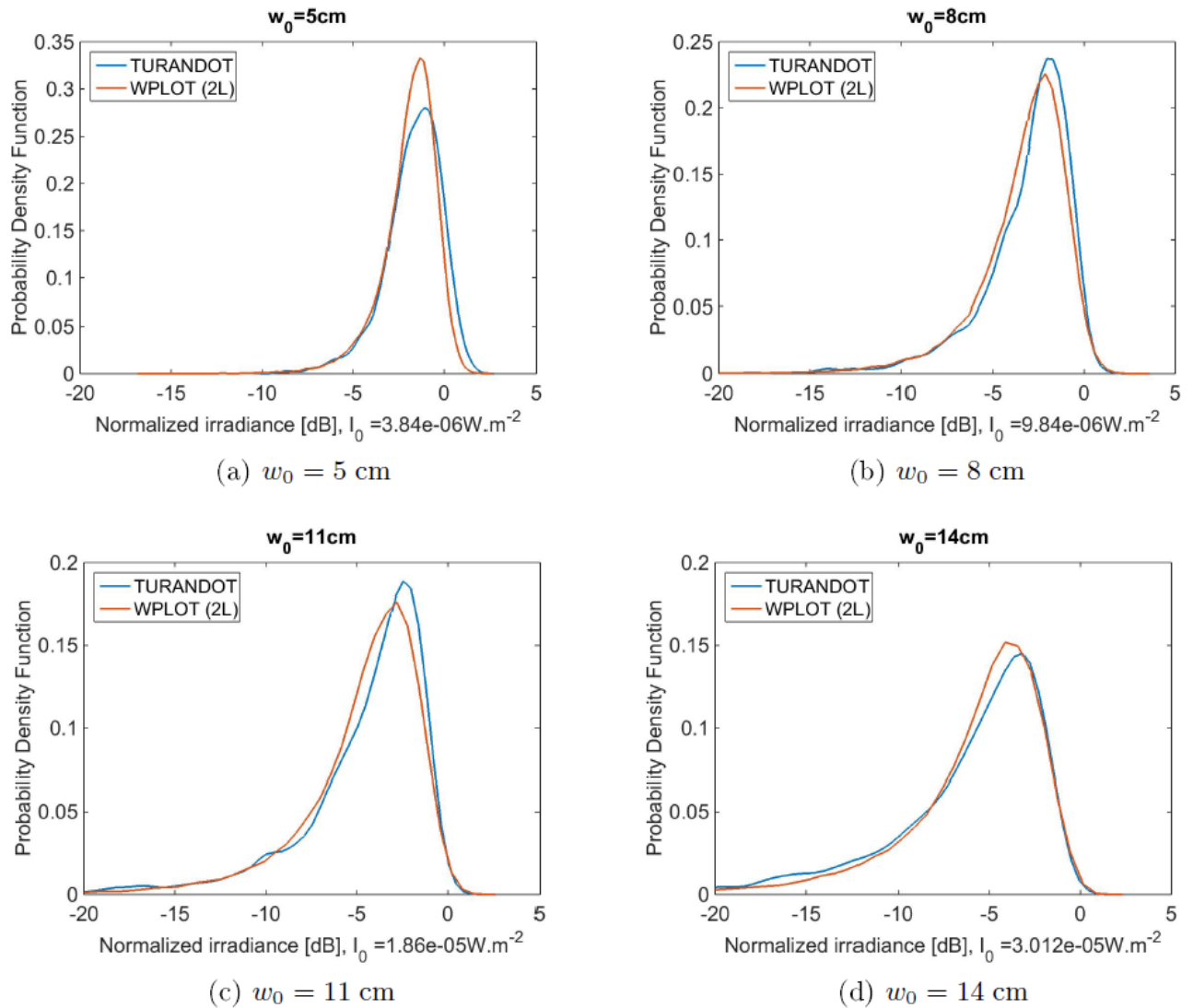
Figure 3-21: Probability density function comparison between TURANDOT and the WPLOT model using stronger atmospheric profile without tracking [54]*.*

The PDFs obtained with WPLOT and TURANDOT are very close which confirms the physical representativeness of the irradiance fluctuations obtained with WPLOT.

It has been observed that the WPLOT fits with TURANDOT model in the case of Hufnagel-Valley 5/7 atmospheric profile on the case of without pre-compensation (cf. 2.3.3). When the pre-compensation is considered, the results still good with by presenting a difference of 1 dB in the loss induced by turbulences. However, the irradiance fluctuation resulting from higher Zernike polynomials order are not taking into account in the WPLOT model. This is why the WPLOT is faster than TORANDO (not considering higher order of Zernike polynomials) [54].

3.2.4   Conclusion

In this chapter, we studied the simulation of the optical links using both of OOK and DPSK modulations for illustrating the effect of the main link parameters on the communication link performances. Our simulation studies and results have allowed us to understand the complexity of the link and to optimize both of transmitter and receiver to achieve an acceptable receiver level. In addition, the communication links are developed to be as close as possible to the realistic ground to satellite communication.

Then, the optical links are used with the time series in order to evaluate the receiver robustness versus different turbulences conditions (low turbulences, beam wander regime and strong turbulences). The fading time is also estimated in different cases for giving detailed statistic of each case where the best fading time value achieved is 3.33% over 2s time series of atmospheric propagation. The same time series will be used on the next chapter for the experimental part where an optical bench is developed to emulate an optical feeder uplink.

Chapter 4

4 Optical test benches emulating optical feeder link

After giving results and performances of the simulation model using both of OOK and DPSK links, the optical bench is described in this chapter and components performance are also given for 10 Gbps link communication. The main objective here is to design the hardware part of the FSO feeder link emulator. All assessments and setups are detailed in this chapter. A second optical test bench is also developed to complete the times series where the phase deformation of the optical beam is considered. A *Digital Micro-mirror Device* (DMD) device is used to disturb the optical spot sent from the transmitter before recovering it by a single mode fiber. In order to rise the data rate, a WDM system able to work up to 4 channels is considered and an example of two channels at 10 Gbps each one is explored.

4.1 Introduction

After giving results and performances of the simulation model using both of OOK and DPSK links, the optical bench is described in this chapter and components performance are also given for 10 Gbps link communication. The main objective here is to design the hardware part of the FSO feeder link emulator. All assessments and setups are detailed in this chapter. A second optical test bench is also developed to complete the times series where the phase deformation of the optical beam is considered. A *Digital Micro-mirror Device* (DMD) device is used to disturb the optical spot sent from the transmitter before recovering it by a single mode fiber. In order to raise the data rate, a DWDM system able to work up to 4 channels is considered and an example of two channels at 10 Gbps each one is explored. Both of the benches will be denoted as:

- **Optical fibred bench**: the bench is named (Emulateur de Lien Laser à travers l'Atmosphère) ELLA and used to emulate the feeder uplink/downlink depending on the used scenario which the deformation concerns only the power fluctuation.
- **FSO test bench:** The fibred bench may be completed by phase deformation component in order to model both of power and phase fluctuations. This part of the bench Phase Optic Emulator (POEM)

4.2 End-to-end fibred optical bench

The experiment set up permits to realize end-to-end fibred optical links with different optical modulations (NRZ OOK, NRZ DPSK, RZ OOK and RZ DPSK). It is composed of three main parts: transmitter, propagation channel and receiver. For the transmitter, two optical modulators are used on the transmitter part in order to be used in different configuration (one modulator to convert data signal in the optical carrier and the second as a pulse carver to manage the duty cycle). In addition, two continuous wave lasers, where the laser wavelength is tunable by controlling the temperature cavity, are set up on the transmitter part in order to be used for multiplexing two channels. The wavelengths can be then adjusted to the multiplexer (on the transmitter) and to the demultiplexer (on the receiver) wavelengths channels with channel spacing of 50 GHz that we use on the bench as optical filters. Wavelengths channels of MUX/DEMUX are shown in Table 4-1.

Number of channel	Wavelength central channel (nm)
1	1552.94 nm
2	1553.34 nm
3	1553.74 nm
4	1554.15 nm

Table 4-1: Value of wavelength channels of the multiplexer and the demultiplexer used on the optical bench (on the transmitter and the receiver)

The first laser is set to 1552.94 nm to be connected to the channel 1 of the multiplexer and the same wavelength is used for all configurations using single-channel.

The receiver part is composed on 3 different photo-receivers (PIN, APD and balanced photo-receiver). In addition, an LNOA is used at the input of this part to amplify the optical signal after going through the FSO part where the optical signal is attenuated two ways (static and dynamic). Hence, we can switch between configurations by connecting the desirable component (PIN or APD for OOK modulation) thanks to many optical couplers to make the bench more ergonomic.
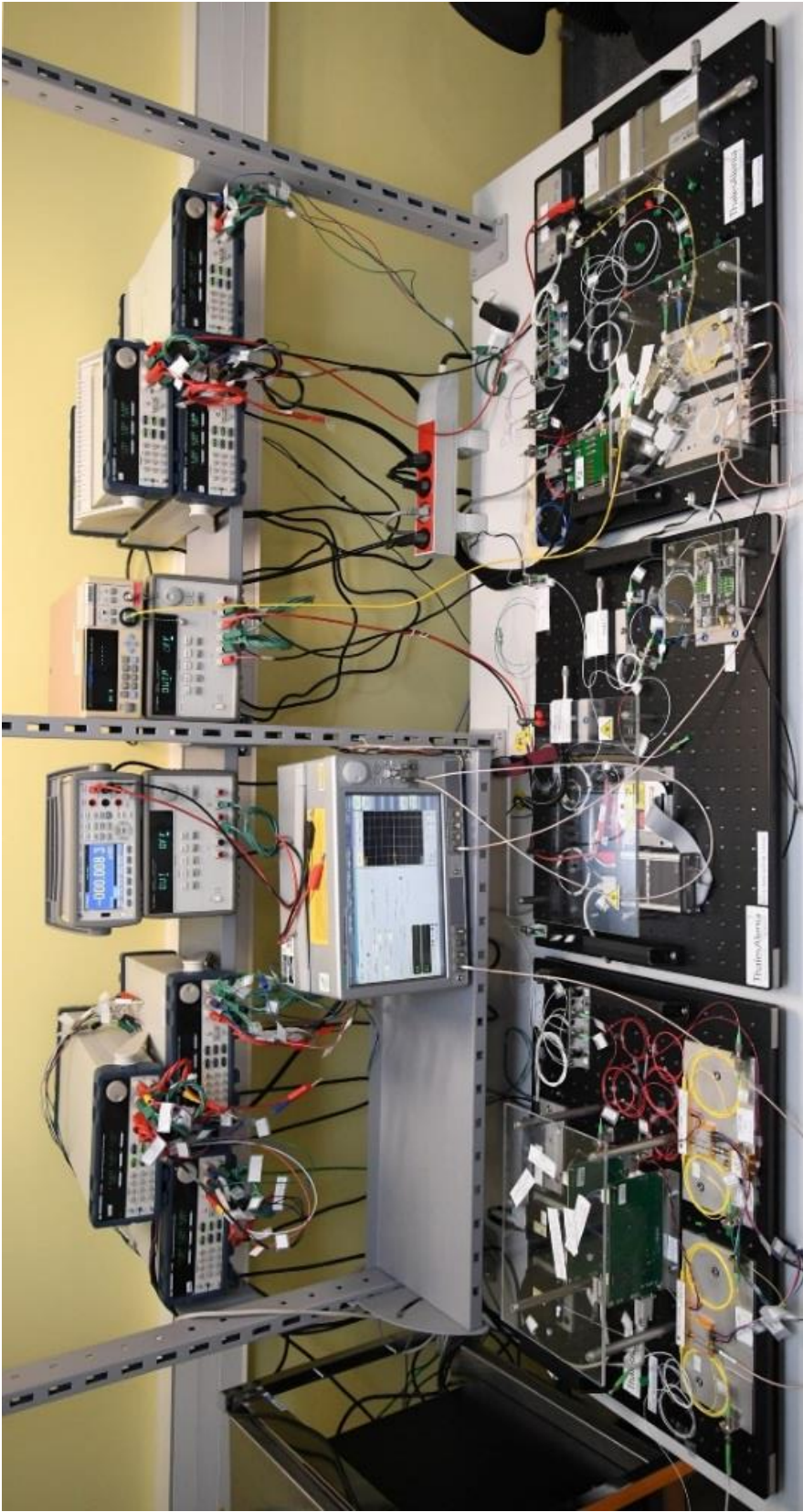
Figure 4-1: Global view of the ELLA bench

On the top part of the picture, we can distinguish electrical power supplies to feed different bench component. The BER tester (grey box on the middle) is used to generate data sequence to drive the modulators and also to analyze the received optical/electrical signal and estimate the BER of the sent sequences after its propagation through the propagation channel part (FSO part). Different configurations of the bench are detailed under schemas to be more understood than the picture in Figure 4-1.

The next part aims to illustrate different configuration that can produced to emulate optical feeder links focusing on the optical power fluctuations coming from time series (Figure 3-15, Figure 3-16 and Figure 3-17).

4.3   OOK optical communication

4.3.1   OOK optical links

The configuration of an NRZ OOK link scenario is shown in Figure 4-2.
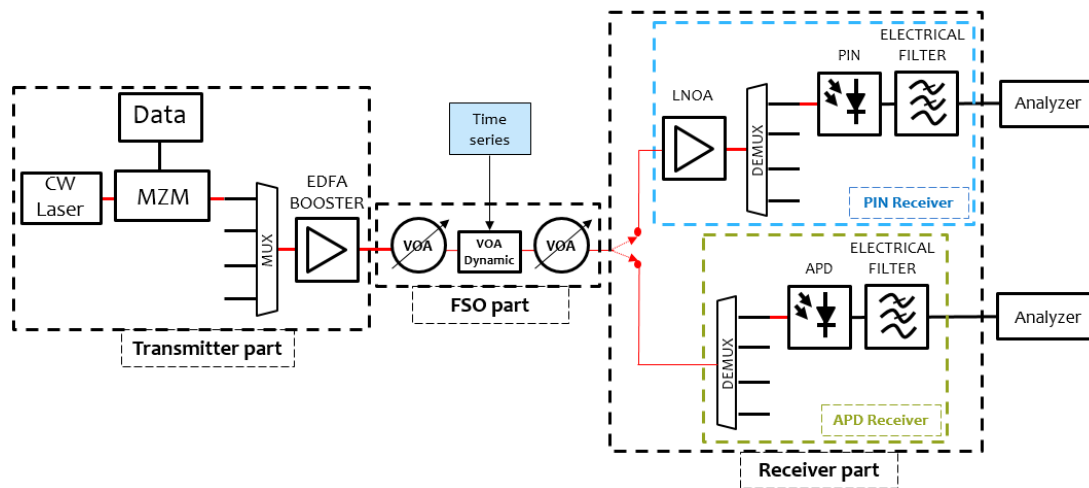
Figure 4-2: NRZ OOK configuration of the ELLA bench with both of receiver possibilities (PIN and APD)

In this configuration, the HPOA may generate an optical power up to 30 dBm that can damage the receiver devices. A VOA is used in order to emulate the first part of static attenuations induced by the atmosphere. The dynamic VOA is not used in the first and only the static attenuation is applied to the optical signal in order to evaluate the receiver sensitivity for different received power levels.

The data signal is generated using a (Bit Error Rate Tester) BERT to a generate Pseudo –Random Binary Sequence (PRBS) of different lengths ($2^7 - 1$, $2^{15} - 1$, $2^{21} - 1$, $2^{31} - 1$) bits with data rate of 10 Gbps. The data stream is amplified using a signal driver and sent to the optical modulator. To follow the optical modulation performances at the transmitter part and through different components, the eye diagrams of the PRBS sent to the modulator, the modulated optical signal and filtered signal using the MUX are shown in Figure 4-3, Figure 4-4 and Figure 4-5.
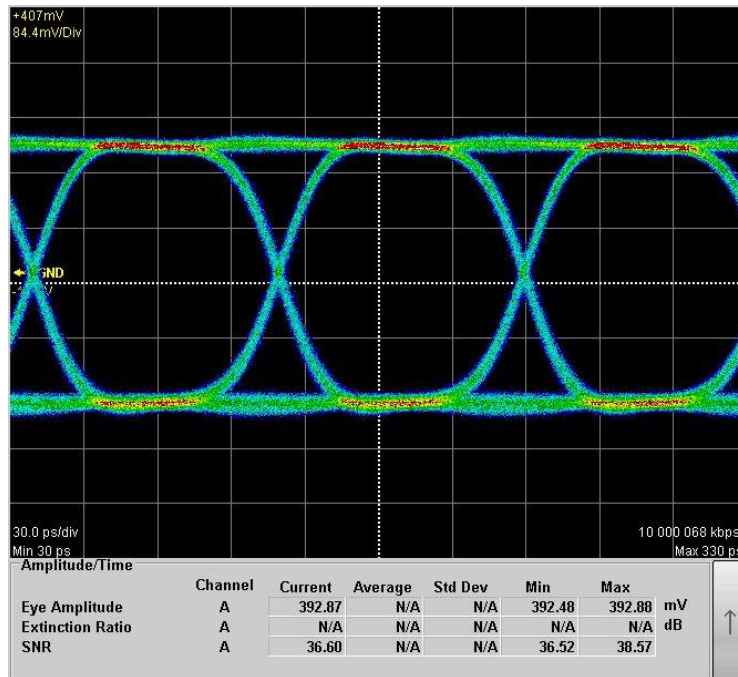
Figure 4-3: Eye diagram for the data signal generated by the BERT for NRZ OOK optical modulation

The data signal used to modulate the optical modulator has a high signal-to-noise ratio (SNR) (more than 36 dB). Its amplitude may be managed in order to ensure a high eye amplitude and guarantee a high performance of optical modulation. This signal is sent to the MZM to realise electro-optic modulation and convert the data into the optical carrier.
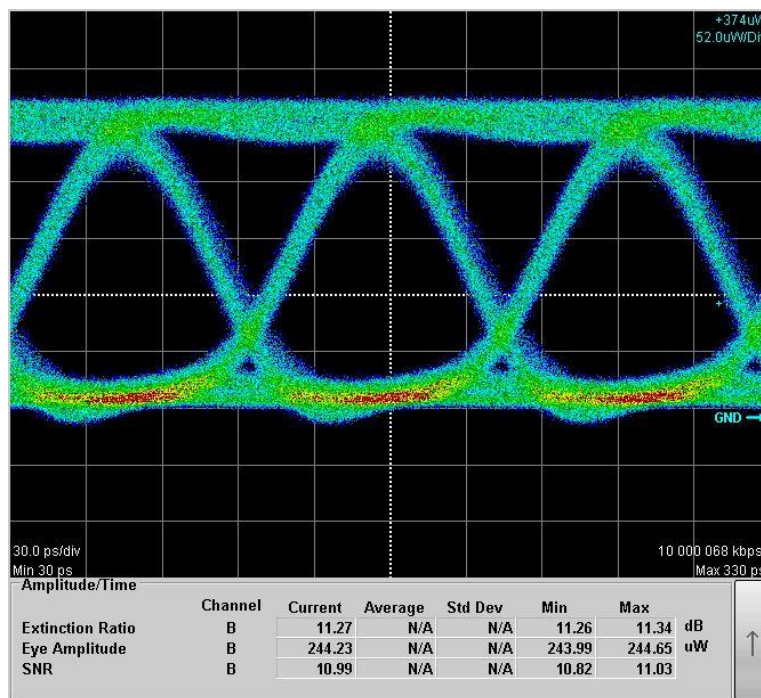
Figure 4-4: Eye diagram for the optical signal after the optical modulator for NRZ OOK optical modulation

106

When the data signal reaches to the modulator, the optical output signal from the modulator presents a low eye amplitude and a very low SNR than the data signal (from 36.6 dB to 12 dB).
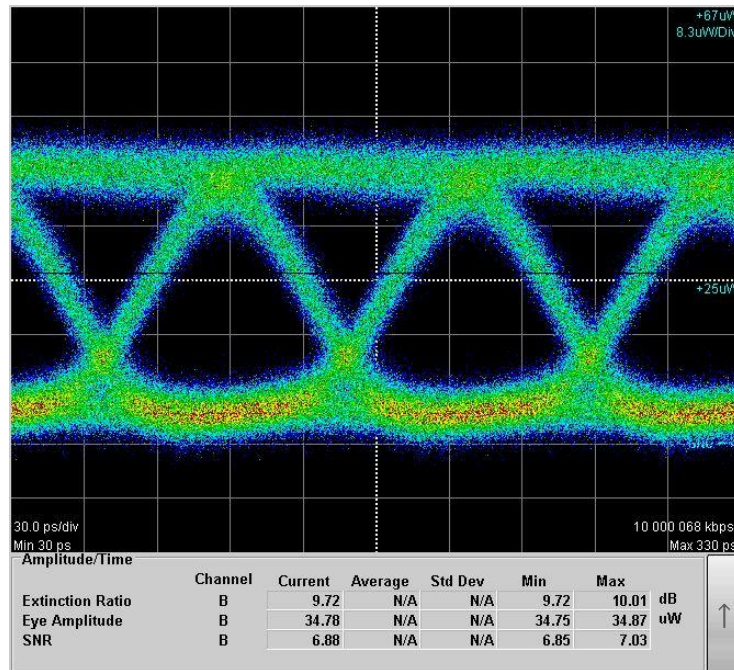
Figure 4-5: Eye diagram for the optical signal after being filtered by the multiplexer.

At this step, the multiplexer degrades the optical signal by cutting the adjacent wavelengths (filtering function) including its insertion loss. It is important to note also that the eye diagram becomes closed (noisy eye) due to insertion loss of the modulator and the dynamic modulator. This signal quality is enough to make a communication OOK link thanks to the HPOA booster that can amplify the optical signal before going through the FSO part. Figure 4-6 gives the evolution of the NRZ OOK optical spectra through different optical component on the bench.
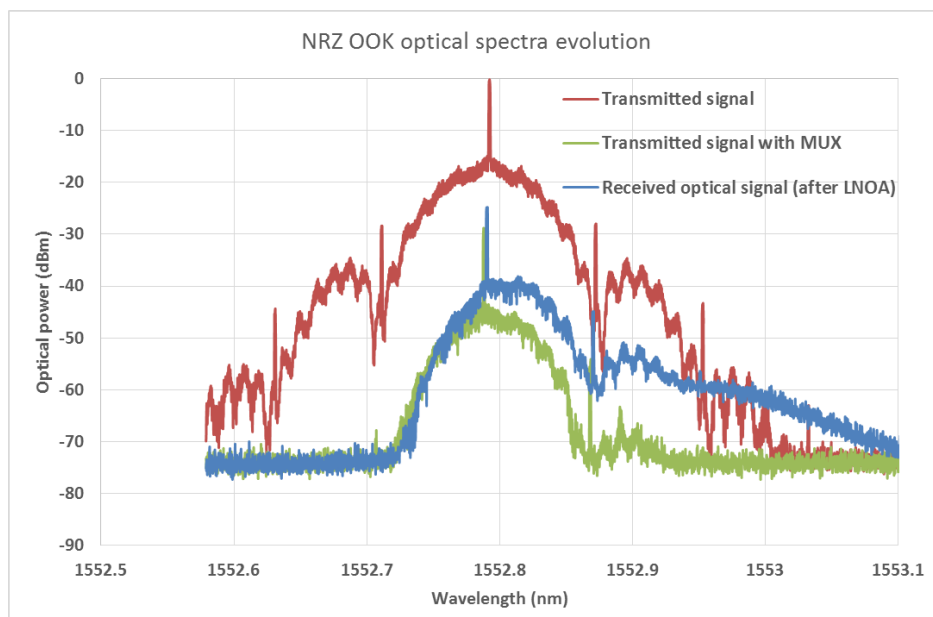
Figure 4-6: Optical spectra evolution from the transmitter to the receiver

From the optical spectra, we can illustrate a symmetric spectrum (red) on the MZM level corresponding to the theoretical spectra of an NRZ OOK transmitter. Then, after going through the MUX, the filtering effect can be shown (green) where the optical spectra is truncated that aims to minimize the transmitted noise and adjacent optical components. The optical signal is sent to the FSO part with only static attenuations and received by the LNOA. It can be remarked that the main optical power of the spectra still focused around the optical carrier (blue).

On the receiver part, two possibilities are offered: the preamplified PIN photodetector or the APD photodetector (without preamplification). A DEMUX is used to decrease the amplified noise generated by the HPOA (Figure 4-6) before detecting the signal with one of the options (PIN or APD). The electrical signal is then sent to the receiver part of the BERT to compare the received stream with the sent stream and estimate the BER of the link. An electrical filter may be used thanks to the BERT that can offer the possibility to filter the detected electrical signal before estimating the BER of the link.

To generate the 50% RZ OOK, the NRZ OOK optical signal is sent to the pulse carver in order to reduce its duty cycle to 50%. The modulator is biased in the middle of its transfer function with an electrical sinusoidal signal having a V_π of the first modulator and frequency of 10 GHz. This transmitter configuration on the ELLA bench is shown in Figure 4-7.
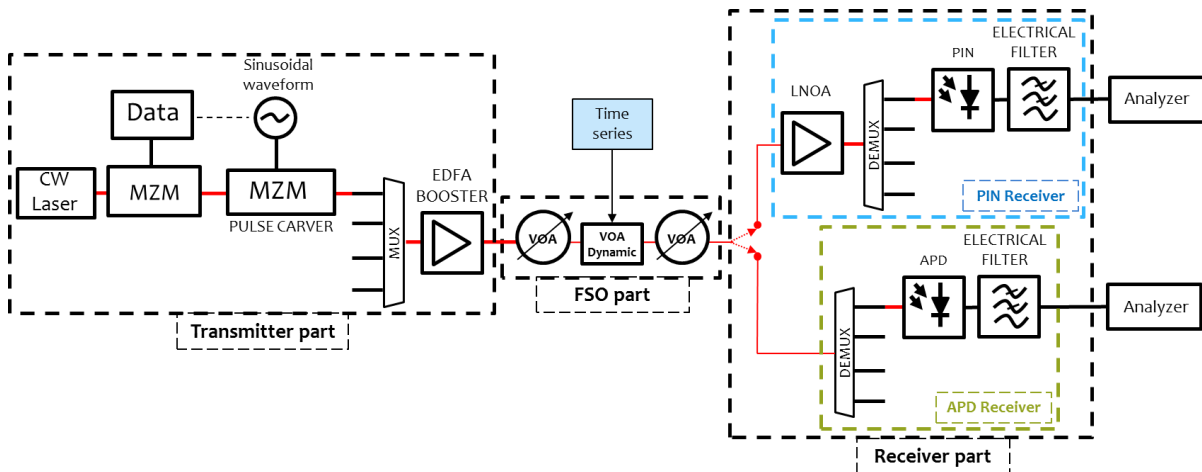
Figure 4-7: 50% RZ OOK configuration of the ELLA bench with both of receiver possibilities (PIN and APD)

At the transmitter (after the EDFA), both of data signal and the clock have to be in phase to insure high quality of the optical signal. Figure 4-8 shows the optical signal after the pulse carver with 50% duty cycle.
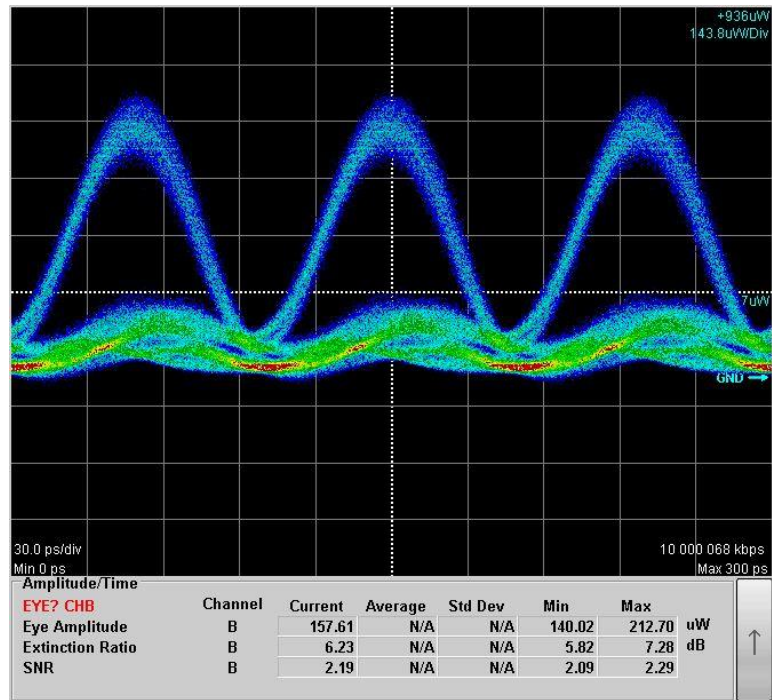
Figure 4-8: 50% RZ OOK optical signal at the transmitter part

The eye diagram presents a very low SNR because of the insertion loss of the second modulator (pulse carver). In addition, the accumulation of both modulators leads to rise the noise in the modulated signal.

Both configurations use the same optical receiver and the first objective of these experimentations is to evaluate the receiver sensitivity and make a comparison with simulation models.

The OOK optical link can now be estimated by giving the BER curves in different configuration.

4.3.2 OOK Link performances

In order to compare the performances achieved using simulation model (summarized in Table 3-5), the BER curves measured as a function of the received average power for NRZ OOK and 50% RZ OOK are given in Figure 4-9. The receiver using APD photo-receiver is only used with the NRZ OOK optical modulation in order to keep the same complexity level between the transmitter and the receiver (the APD receiver needs less component than the PIN receiver and the reduced duty cycle modulation need the pulse carver modulator). Hence, three communication scenarios can be achieved using the ELLA bench with OOK optical modulation.
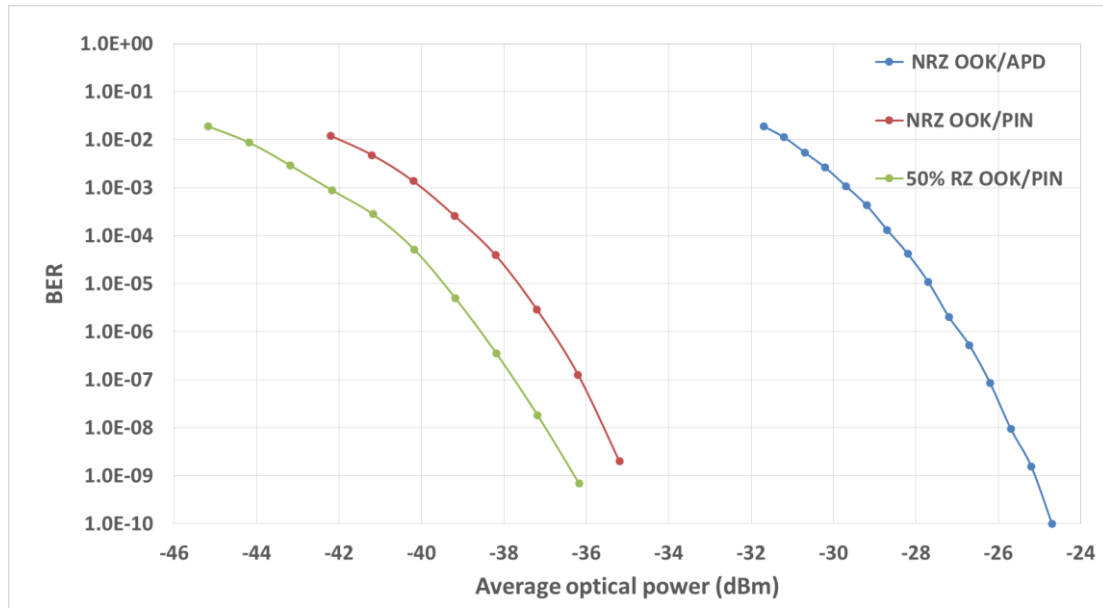
Figure 4-9: BER curves achieved using the optical bench for OOK optical modulation and with PIN and APD photo-receivers

Comparing these curves, the reduced duty cycle leads to improve the receiver sensitivity (illustrated in the simulation model). The APD receiver present high sensitivity penalty for a given BER level that matches with simulated model. The Table 4-2 gives a comparative between the simulated receiver sensitivities and those achieved using the optical bench.

| 10 $Gbps$ | NRZ OOK | | RZ OOK | |
Sensitivity at $BER = 10^{-9}$ (dBm)	PIN	APD	PIN	APD
Simulated model	**-38**	**-27.5**	**-39.5**	-28.8
Experimental results	**-35.5**	**-25.1**	**-36.3**	-------
Difference (dB)	**2.5**	**2.4**	**3.2**	-------

Table 4-2: Comparison between simulation results and experimental results for the receiver sensitivity using OOK optical link

The link dynamic of each scenario is around 10 dB that correspond to the difference between the required optical power values to get a BER of 10^{-3} and 10^{-9}. This dynamic will be recalled when the time series will be used on the ELLA bench.

Before describing these curves, we have to take into account experimental conditions and the temperature deviation of some components which promote to increase the BER value. An error margin of $\pm 1\ dB$ around experimental values has to be considered due to environmental conditions.

From the table, we remark that the simulation results are better than experimentations ($\sim 2\ dB$ for NRZ OOK and 4 dB for 50% RZ OOK). It's important to take into account that noise levels induced by LNOA and HPOA are optimized in the simulation model. In addition, the optical filter used on the bench present a fixed bandwidth value (50 GHz) that the receiver sensitivity depend on this value (cf. 3.2.1.3).

4.3.3   Multiplexing two channels (WDM) using OOK optical modulation

The WDM is a transmission technique that lead to increase the capacity of optical transmission systems. In this section, we will investigate the ELLA bench on the case of multiplexing two wavelengths carriers. The optical modulation to be considered is the NRZ OOK that need only one

optical modulator comparing to the use optical modulation with reduced duty cycle. This part is under experimentation and will be a part of experiments perspectives detailed in 5.2.
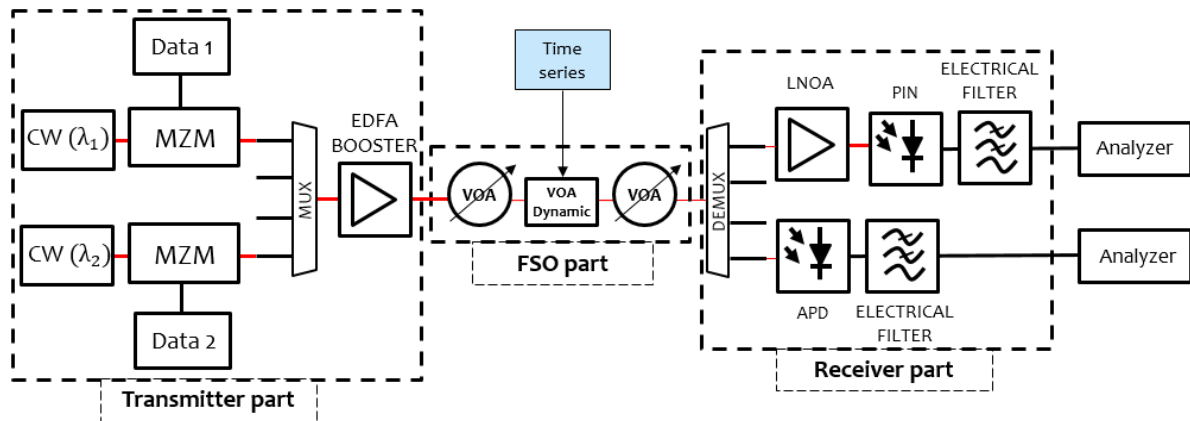
Figure 4-10: ELLA bench configuration used WDM of two optical channels

Two optical carriers, 1552.73 nm and 1553.344 nm, modulated at 10 Gbps each using NRZ OOK modulation are configured. The data PRBS used are decorrelated to insure the incoherence of data multiplexed where the crosstalk may appear between them. Both are multiplexed using the corresponding optical channel and amplified with the EDFA. The FSO part of the bench is still the same as when one channel is used where the optical attenuation is applied for the multiplexed channels. On the receiver part, the two carriers are separated and sent respectively to the preamplified PIN photodetector and the APD photodetector.

This experiment may give the influence of channel multiplexing on the performances of the optical link when only one channel is considered. The main effect that could degrade the receiver performances is the crosstalk where the data of adjacent channel are mixed. We summary in this table the receiver sensitivity of both photo-receivers in the multiplexing case compared the single channel case.

$10\ Gbps$	NRZ OOK	
$Sensitivity\ at\ BER = 10^{-9}\ (dBm)$	PIN	APD
One channel	-35.5	-25.1
Multiplexed channels	---	---

Table 4-3: Comparison of receiver sensitivity between the use of one channel and the use multiplexed channels

By comparing the receiver sensitivities, the multiplexing of two channels lead to introduce the crosstalk that aims to increase the receiver penalty comparing to the use of only a single channel system. The main benefit of the WDM system is an optical communication with a total data rate of 20 Gbps against the rise of the receiver sensitivity. Figure 4-11 illustrates the optical spectra of each channel at the receiver level.
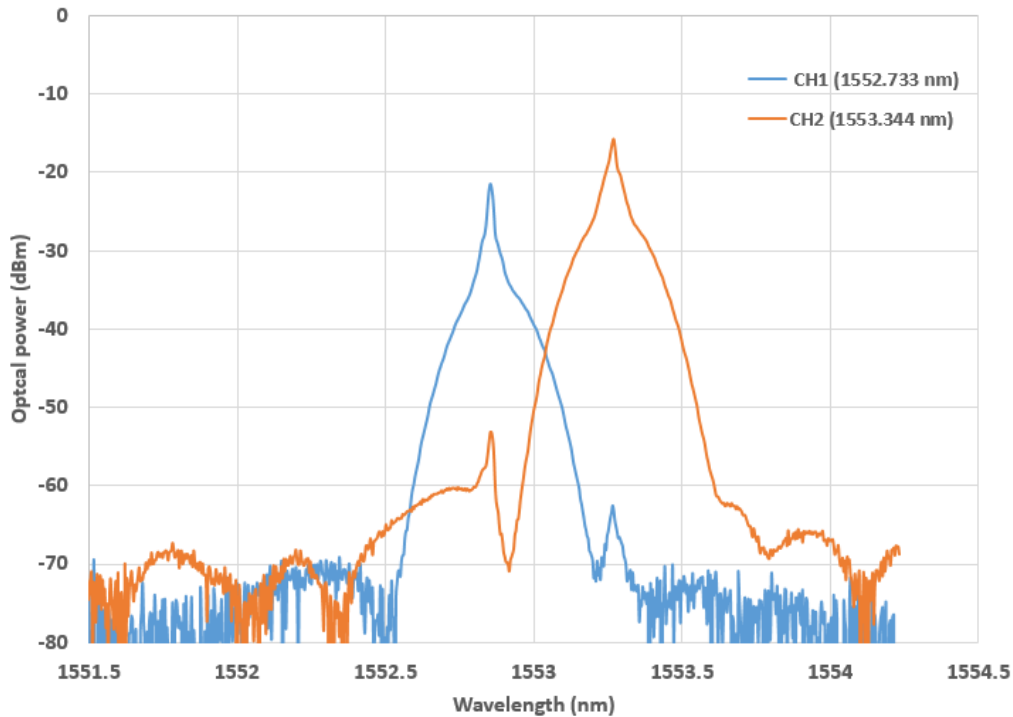
Figure 4-11: Optical spectra of both optical channels at the receiver side. (1552.73 nm and 1553.34 multiplexed)

We will focus in the next part on the dynamic VOA to include times series in order to emulate power fluctuations induced by the atmospheric layers.

4.4   Atmospheric attenuation channel

The communication channel part of the bench contains two different kind of the attenuations:

- Attenuations due to static phenomena that the optical beam meet during its propagation through the atmosphere.
- Attenuation due to random phenomena (turbulence, absorption, diffusion,..).

4.4.1   Static attenuation effect

According to link budget of feeder link optical communication, many static attenuation due the propagation distance or cloud have to be considered. Thereby, the optical bench contains two variable optical attenuators (VOA) on the FSO part whose attenuations will be fixed or slowly varying to represent these static attenuations.

4.4.2   Dynamic attenuation effect

A Dynamic Variable Optical Attenuator (DVOA) whose attenuation will be electrically driven by a signal representative of fading induced by atmospheric turbulences. These input are time series generated by WPLOT shown in Chapter 3.

The device is able to convert an electrical signal to the corresponding attenuation and can work up to 100 kHz variation frequency. Figure 4-12 shows the applied attenuation as a function of input voltage to define limits of attenuations in its voltage domain. It can be shown that the maximum attenuation we can achieve equals 23 dB and the lowest one equals 2 dB (corresponding to insertion loss).
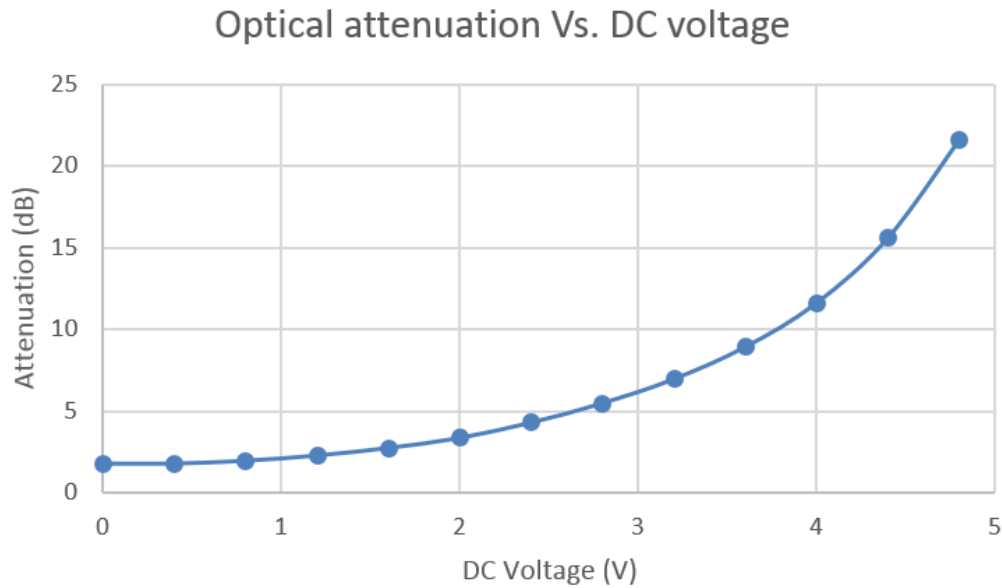
Figure 4-12: Attenuation (dB) vs. input voltage (V) for Nano-speed variable optical attenuator

Then, the time series presenting a sampling frequency of 4000 Samples/s (less than 100 kHz) is injected using a low frequency generator and driven under LabVIEW.

For different cases we plan to study under the optical bench (described on CH3), the attenuation may be low than the maximum offered by the attenuation and two option were considered:

- All attenuation more than 23 dB is considered equals to 23 dB (we conserve the original power fluctuation only for attenuation under 23 dB)
- Times series values are adapted to components attenuation margin.

After exploring both possibilities, we conclude that the second option can note be representative of power fluctuation induced by the atmosphere. If we have a very high value of attenuation on the time series (100 dB for example), it will set at 23 dB and all lowest values will be considered as the same value.

The three time series that are studied in chapter 3 (low turbulences regime, beam wander regime and strong turbulences regime) will be injected in the dynamic VOA on the FSO part of the bench to be compared to the simulation results.

4.5 Emulation of a feeder uplink using OOK communication link

The optical communication is configured to have a BER of 1.10^{-9} before including the time series (in our experiments, this value corresponds to error free). Thereby, the communication still established for low attenuation values (the BER starts to increase) and cut for high attenuation values. The fading time over the time series will be estimated for the three communication link using the OOK modulation and under three different strengths of turbulence. Nine statistic cases will be exposed in this part. Table 4-4 summarizes the fading time estimation obtained with different configuration of the receiver part of the ELLA bench.

NRZ OOK (PIN) NRZ OOK (APD) RZ OOK (PIN)	Without pre-compensation		With pre-compensation	
	Average power (dBm)	Fading time (%)	Average power (dBm)	Fading time (%)
Low turbulence regime	-41.01	86.21%	-37.79	72.14%
	-29.81	77.26%	-26.59	56.25%
	-40.21	79.25%	-36.99	59.46%
Beam wander regime	-44.86	89.20%	-38.61	79.83%
	-33.66	96.25%	-27.41	68.81%
	-44.06	97.10%	-37.81	72.69%
Strong turbulence regime	-54.33	100%	-40.08	98.44%
	-43.13	100%	-28.88	83.10%
	-53.53	100%	-36.28	86.38%

Table 4-4: Estimation of fading time over 2s time series describing the atmospheric fluctuations done with the ELLA bench

In this table, the fading time increases when the turbulence strength increases. The totality of the optical signal over the time series can still under the receiver threshold that corresponds to 100% of the fading time (the case of all optical modulation in the strong turbulence without pre-compensation). Thanks to the pre-compensation effect that permits to recover a small part of the optical (from 100% to 86.38% using RZ OOK optical link).

If we are interested in the received optical power, an improvement going up to 17 dB using the pre-compensation on the case of RZ OOK in strong turbulence however only few dBs have to be noted in low turbulence régime (between 2 and 4 dBs).

In order to illustrate the trend of the BER compared with the BER value without turbulence, we estimated the average BER value over several time series cycles with the receiver biased at $10^{-3}, 10^{-6}, 10^{-9}$ and 10^{-11}. For this experiment, we consider the NRZ OOK configuration.

The accumulation time of the communication is 30 s (versus 2 s of the time series) that make sure to have enough data stream transmitted. The VOA dynamic can offer only up to 23 dB of attention while the time series attenuation value can reach values more than 23 dB. In addition, the receiver power margin to cover the BER values from 10^{-3} and 10^{-11} is only 10 dB. Thereby the time series are normalized to consider both these limitation that lead to cut the communication link. Table 4-5 illustrates the estimated BER values in several turbulence conditions

BER	Low turbulence condition		Beam wander condition		High turbulence condition	
	Without AO	With AO	Without AO	With AO	Without AO	With AO
10^{-3}						
10^{-6}	$1.9 * 10^{-4}$	$1.1 * 10^{-4}$	$2.2 * 10^{-4}$	$8.2 * 10^{-5}$		$3.2 * 10^{-4}$
10^{-9}	$1.1 * 10^{-4}$	$3.1 * 10^{-5}$	$4.2 * 10^{-4}$	$2.2 * 10^{-5}$	$1.0 * 10^{-3}$	$5.0 * 10^{-5}$
10^{-11}	$1.2 * 10^{-5}$	$1.0 * 10^{-5}$	$2.5 * 10^{-5}$	$9.0 * 10^{-7}$	$5.5 * 10^{-5}$	$1.9 * 10^{-6}$

Table 4-5: Average BER values over 30 s of received data accumulation around specifics BER values of the receiver.

We can remark that when the optical receiver is biased to achieve a $BER = 10^{-3}$, the data transmission between the transmitter and the receiver is totally cut and synchronization is lost. The BER value cannot then be estimated at this BER level.

When the receiver is biased to achieve a communication without erroneous received data ($BER = 10^{-11}$), the average BER value is estimated and illustrate an important gain in the beam wander and high turbulence conditions. Figure 4-13, Figure 4-14 and Figure 4-15 give the comparison of the BER curves before and after applying the turbulence conditions.
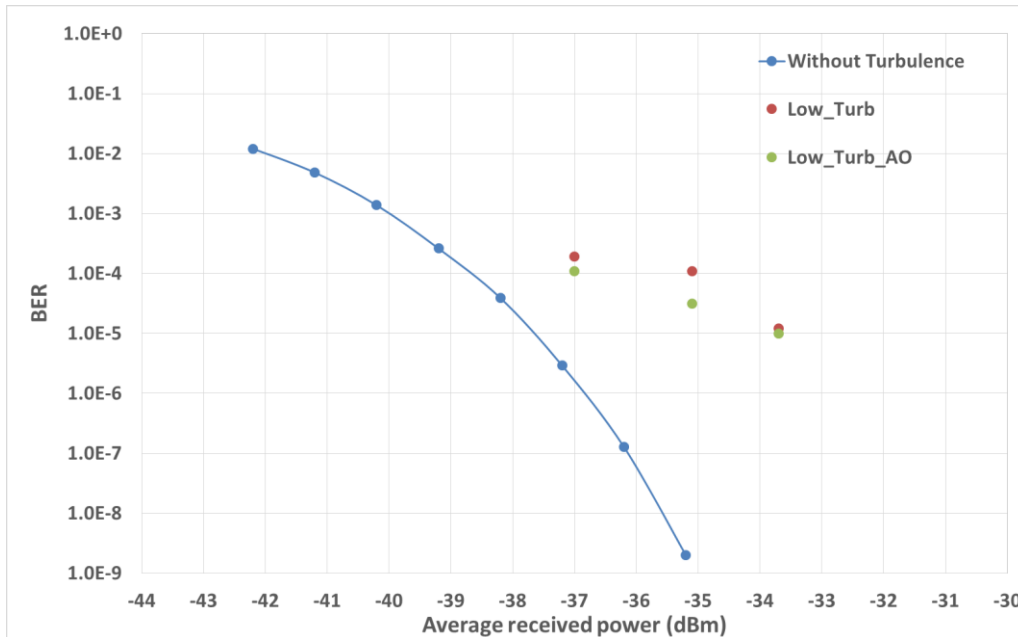
Figure 4-13: BER curves estimated over several time series cycles in the low turbulence condition

In the low turbulence condition, the BER estimation of the optical communication gives approximatively the same trend when the optical power moves. In addition, to achieve highest levels of the BER under turbulence condition, the penalty increases (2 dB for 10^{-4} and 4 dB for 10^{-5}).
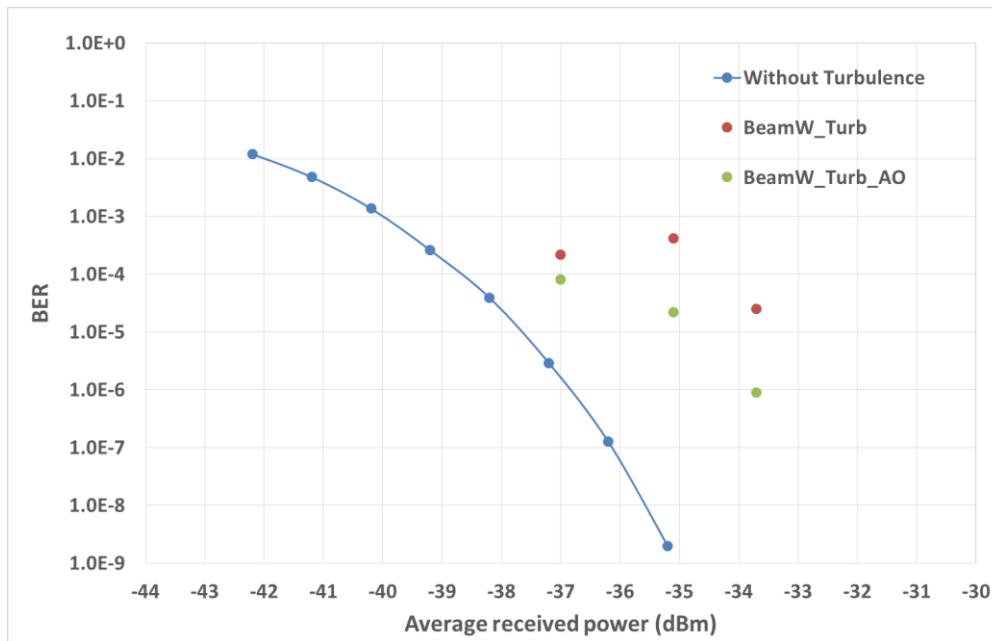
Figure 4-14: BER curves estimated over several time series cycles in the ''beam wander'' condition

In the beam wander conditions, the BER curves present two different saturation ways where we can understand more the benefit of the AO (the penalty moves from 5 dB to 3 dB for the same optical power.
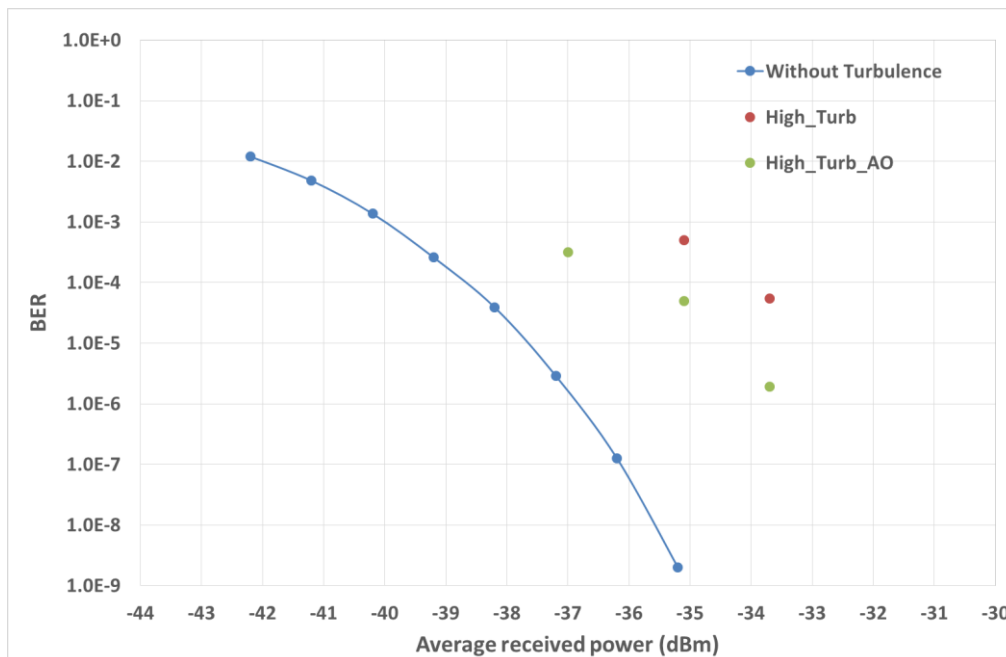
Figure 4-15: BER curves estimated over several time series cycles in the high turbulence condition

This experiment allows to test the robustness of the ELLA optical receiver under different configurations using OOK optical links.

The configuration of the bench is switched on DPSK optical modulation where the same time series will be used to emulate the same atmospheric as the OOK. This will be the subject of the next part.

4.6 DPSK optical communication

4.6.1 DPSK optical links

The optical bench can switched on the DPSK optical modulation by adding a digital coder (detailed in 2.2.5.1.1) in the transmitter part. The data signal is set to have an amplitude of $2V_\pi$ at the minimum of the transfer function of the optical modulator. By the same way as the OOK link at 10 Gbps, a pulse carver may be used to manage the duty cycle of the optical modulated signal. Figure 4-16 gives the configuration of the ELLA bench used to generate a DPSK optical link using the balanced photoreceiver. Both of the booster and the LNOA are used the same way and generate the same power level as the OOK communication link.
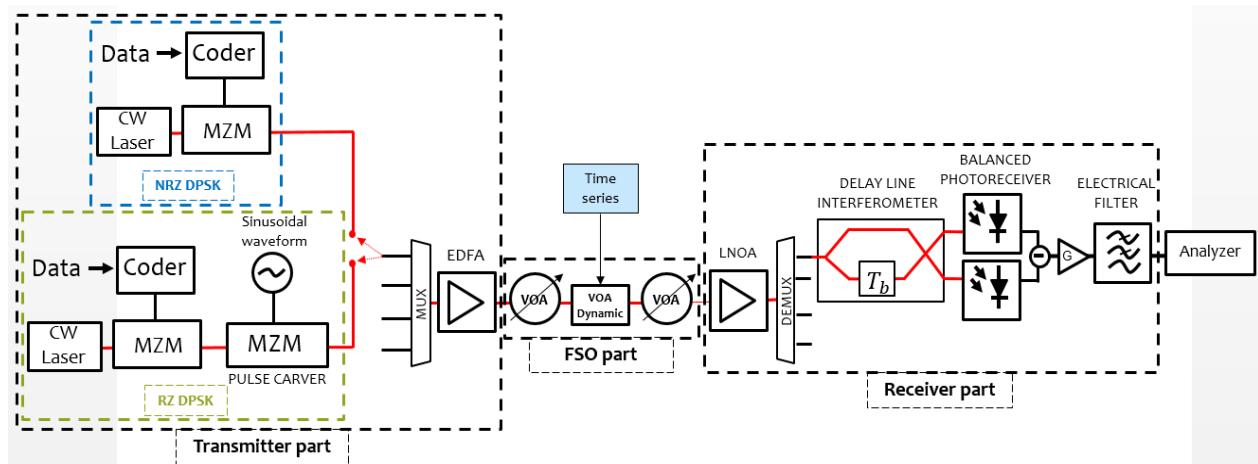
Figure 4-16: 50% RZ DPSK/NRZ DPSK configurations of the ELLA bench with using the balanced photoreceiver.

The FSO part of the optical signal remains the same. On the receiver part, the optical signal goes through the Delay Line Interferometer (DLI) to be demodulated where the phase modulation is converted to the amplitude modulation. The eye diagram of the optical signal at the input of DLI is given in Figure 4-17.
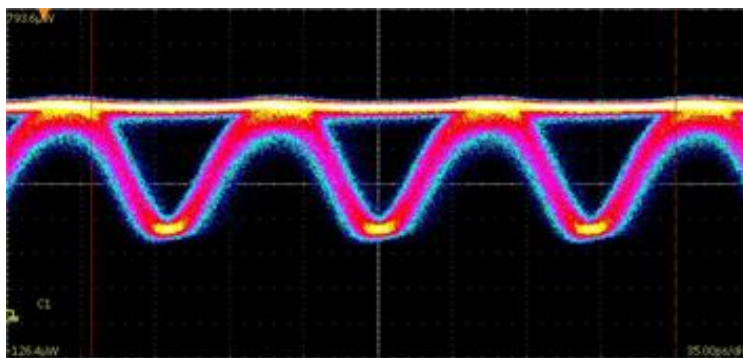
Figure 4-17: Eye diagram at the input of the DLI for NRZ DPSK optical link

The optical signal is then spitted in two parts to be insure the demodulation process using the DLI. It performs the interference between the incoming signal and itself delayed by one bit-time (detailed in 2.2.5.2.1). The DLI is tunable to enable a precise matching of the carrier frequency. A bloc diagram of the used DLI is given in Figure 4-18.
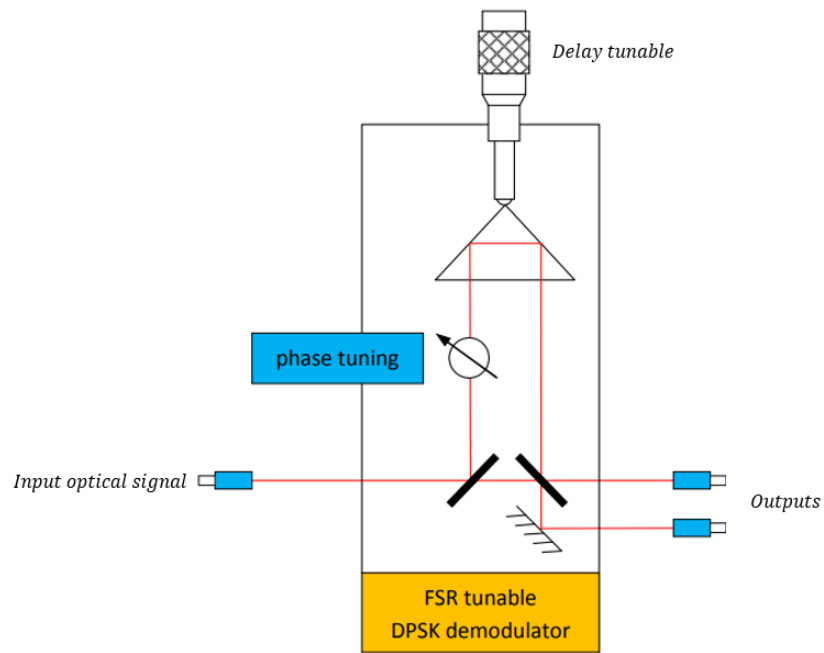
Figure 4-18: Bloc diagram of the DLI used on the ELLA bench [98]

At the output of the DLI, two different type of interferences are shown (constructive and destructive) that are shown in Figure 4-19: Optical eye diagram at the outputs of the DLI, constructive (top) destructive (down)Figure 4-19.
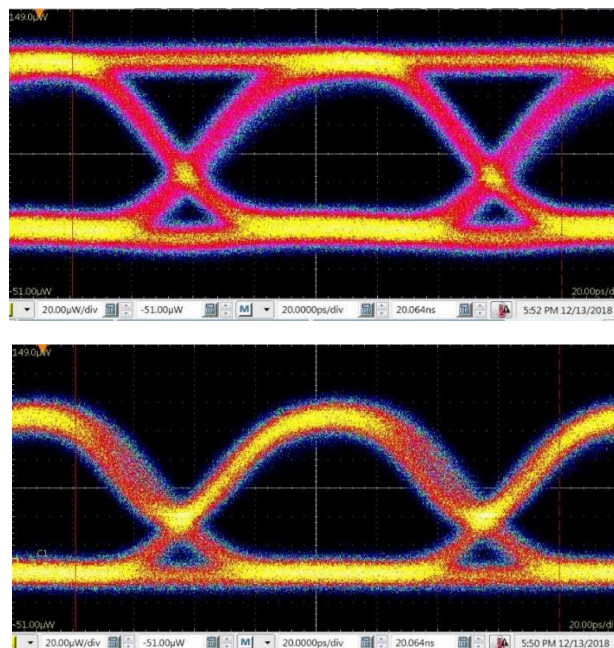
Figure 4-19: Optical eye diagram at the outputs of the DLI, constructive (top) destructive (down)

The DLI presents a high insertion loss ($\sim6dB$) and presents a high sensitivity for vibration. Thereby a cleaning process of the receiver connectors have to be insured in order to limit additional loss. The optical signals are then sent to the balanced photodetector. The detection process consists of two

matched photodiodes that generate an output voltage proportional to the difference between the photocurrents in the two photodiodes.
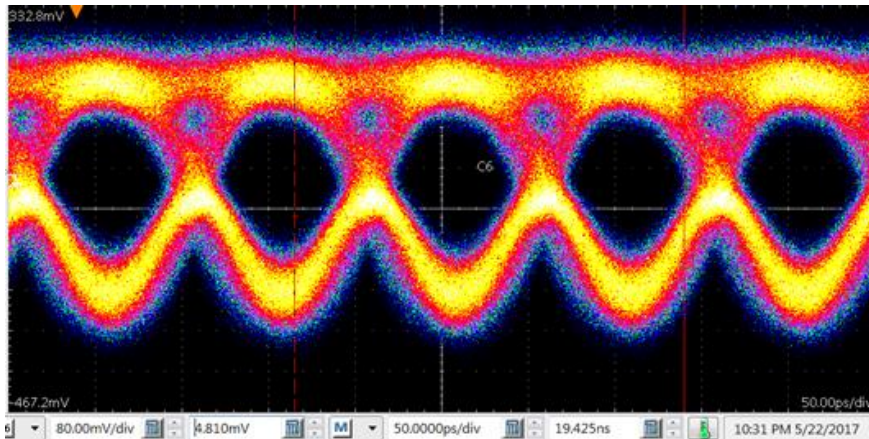
Figure 4-20: Eye diagram of the NRZ DPSK optical signal after the balanced photo receiver.

For the RZ DPSK, the pulse carver is biased at the middle of MZM transmission. The difficulty to build a reduced duty cycle for DPSK optical modulation is the phase shift between the data signal and the signal clock (used for the pulse carver). Both of signals are generated by the same equipment (BER tester) with a time duration shift. In order to avoid this difference, a phase shifter has to be added to control the phase shift and insure no phase on the MZMs level. In addition, for 33% and 67% duty cycles, the data signal has to have an amplitude double of the modulator V_π and half of data rate as the frequency. While 50% RZ DPSK do not need to divide the clock signal and only an amplitude of V_π is enough to carry this duty cycle.

A phase shifter is then used with the clock signal to be synchronized with the data signal. The eye diagram of electrical signal measured after the photodetector is shown in Figure 4-21.
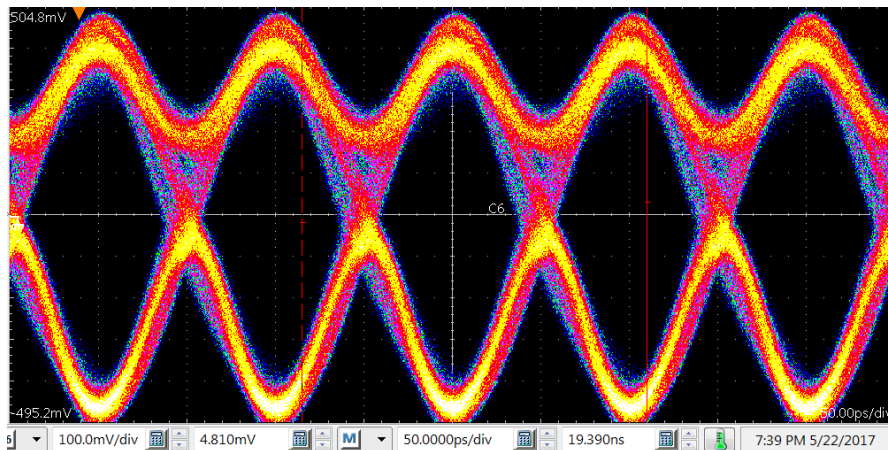
Figure 4-21: Eye diagram of the 50% RZ DPSK optical modulation on the receiver level

By comparing both of eye diagrams (NRZ DPSK and 50%RZ DPSK), the NRZ DPSK modulation presents a low eye amplitude comparing to 50%RZ DPSK in order to conserve the energy per bit. In addition, the eye height increases when the duty cycle is reduced. This benefit may be illustrated when the BER of both communication links is estimated.

The DPSK optical link can now be estimated by giving the BER curves in both of configurations (NRZ DPSK and 50%RZ DPSK).

4.6.2 DPSK link performances

As it is done for the OOK communication link, the average optical power is varied in the FSO part and measured at the input of the receiver. Figure 4-22 illustrates the BER curves for the DPSK optical communication.
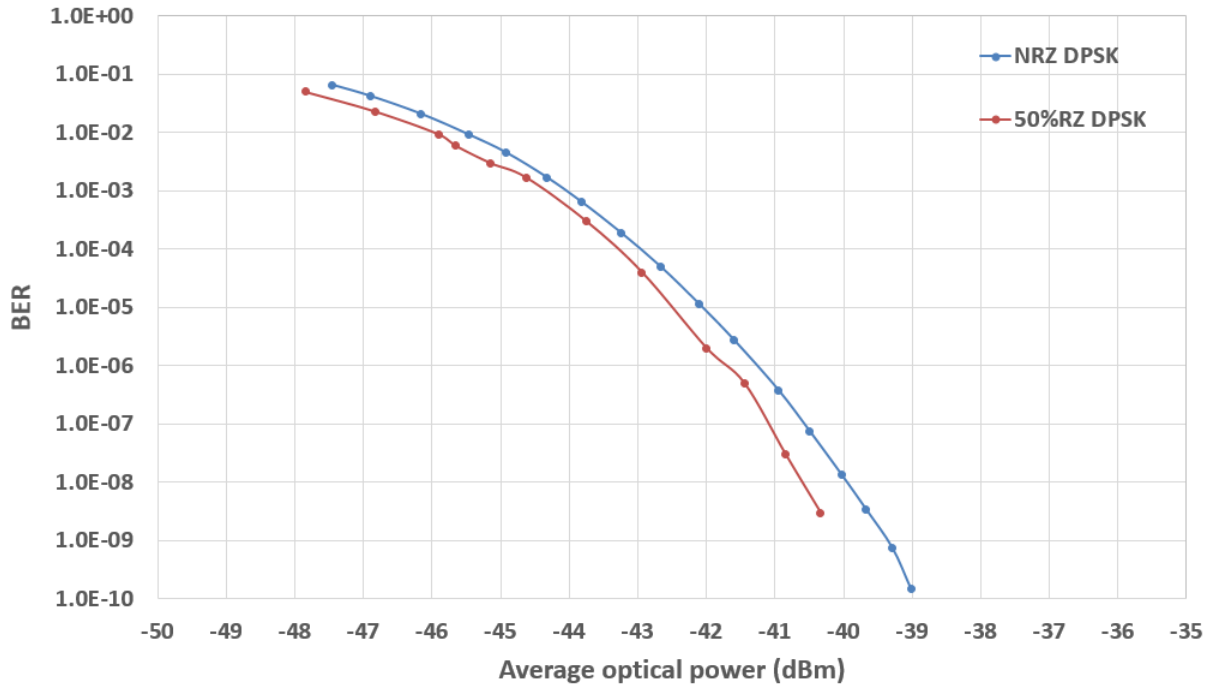
Figure 4-22: BER curves estimated using the ELLA bench for DPSK optical modulation (NRZ DPSK and 50%RZ DPSK)

According to the BER estimation, the reduced duty cycle leads to improve the receiver sensitivity (illustrated in the simulation model and for the OOK communication link). The improvement of the receiver sensitivity equals 0.5 dB (at $BER = 10^{-8}$) and may reach 0.9 dB (at $BER = 10^{-9}$). Table 4-2 gives the simulation results achieved for DPSK communication that it is completed by the experimental values. The Table 4-6 summaries both of OOK and DPSK receiver sensitivities.

$10\ Gbps$ Sensitivity at $BER = 10^{-9}$ (dBm)	NRZ OOK		RZ OOK		NRZ DPSK	RZ DPSK
	PIN	APD	PIN	APD		
Simulated model	-38	-27.5	-39.5	-28.8	**-41.2**	**-42.3**
Experimental results	-35.5	-25.1	-36.3	-------	**-39.3**	**-40.2**

Table 4-6: Comparison between simulation results and experimental results for the receiver sensitivity using OOK and DPSK optical links

As it has been remarked for the OOK communication experiment, we have to take into account experimental conditions and the temperature deviation of some devices which promote to increase the BER value. An error margin of $\pm 1\ dB$ around experimental values has to be considered due environmental conditions.

The receiver sensitivity presents a difference of $\sim 2\,dB$ between the simulation and the experimentation. This decrease is predictable due to the experimental condition and the high noise level introduced by the EDFA.

As a conclusion, the experimental results allow to validate the simulation model and the results obtained despite the difference between BER curves (receiver sensitivity). In order to compare these results with the robustness of the DPSK optical modulation under different turbulence condition, the DPSK link configuration will be considered.

4.7 Phase fluctuation setup Atmospheric perturbation emulation

In communication systems through the atmosphere, the phases and amplitudes of the received optical field is affected by the atmospheric turbulences that reduces the quality of the detected optical power. In order to perform the affected optical signal, FSO systems use adaptive optics (AO) such as deformable mirrors based on digital micro-mirror devices (DMDs) for phase compensation. In our lab experiment, a DMD with high resolution (2560x1600) array presenting 4 million micro-mirrors is used to introduce optical aberrations close to those generated by atmospheric turbulences. Different methods to generate atmospheric aberrations have been proposed, including wind chambers, phase screen, moving plates and spatial light modulators (SLMs) [99][100]–[102].

In this part, an FSO optical bench based on a DMD device is built in order to emulate phase screen deformation and complete the fibred bench presented in the last part.

4.7.1 Digital Micro-mirror Device: characterization

The main advantage of these DMDs is ability to modulate the amplitude of the incoming beam only in two levels (zero one) corresponding to the state of each micro-mirror (''ON'' or ''OFF''). This binary skill of the DMD increases the simplicity of the electronics involved which results in an increased speed to be reconfigured. The DMD of this setup is the Texas Instrument DLP 9000 model that can offer a pattern rate up to 15 kHz [103]. It is controlled by the *LCR6500 LCR9000 GUI* software allowing to set the deflection angle of each individual mirror to either +12 or -12 degrees. Figure 4-23 shows two pixels, one in the ON and one in the OFF.
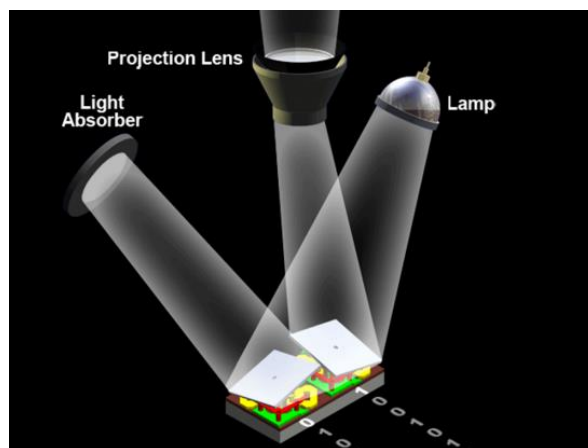
Figure 4-23: Pixels in ON and OFF states [104]

In this figure, the light coming from the lamp can be sent to the lens to follow the optical path or deflected (absorbed) from path. Figure 4-24 illustrate the schematic diagram of the FSO bench built to characterize the DMD device.
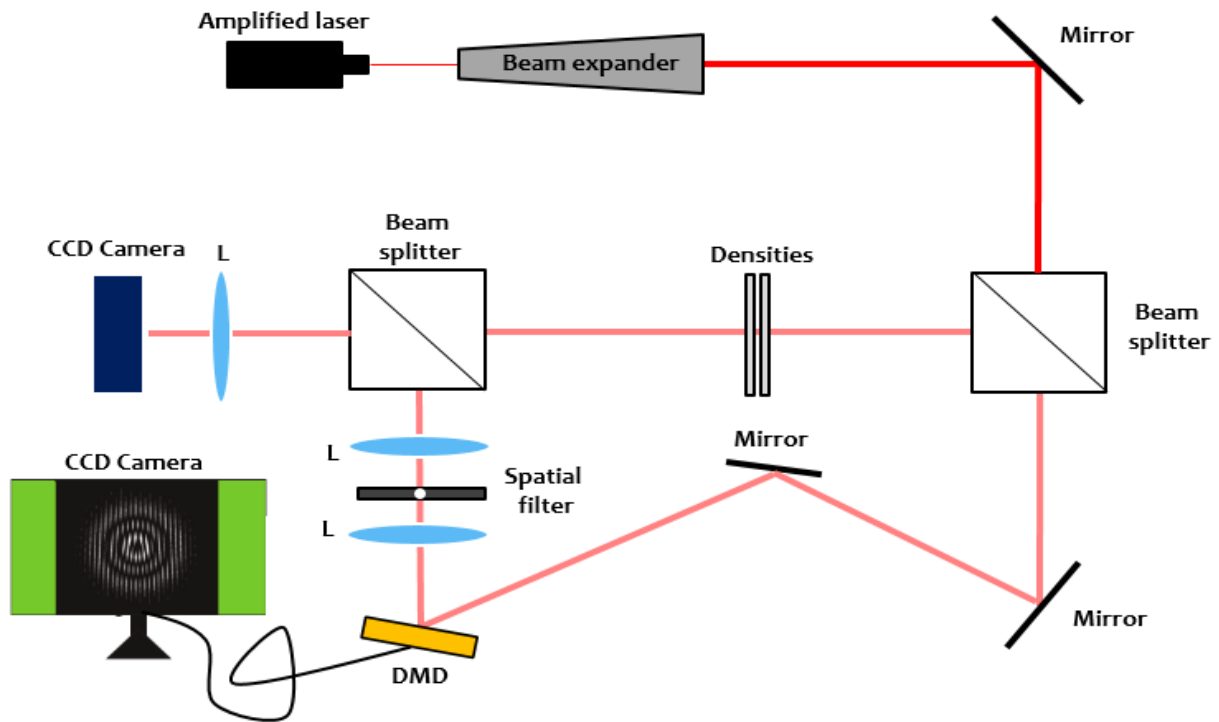
Figure 4-24: Schematic diagram of the experimental setup

At the output of the laser, a collimator is used to avoid the divergence of the beam. Then, a tunable beam expander offering a beam magnifing of 20 in order to manage to beam size and make it compatible with other lens size and especially the DMD size. By expanding the laser beam, the optical density (signal/surface ratio) decreases and to compensate this power density loss, an optical amplifier is used to have enough optical power during its propagation. Then, the optical beam is divided in two parts using a beam splitter. The first part, named the reference beam, is sent directly to the camera after being attenuated optical densities to insure the same power level between interferometry arms. The second part is sent to the DMD which induces an additional phase of the beam wave-front before being recombined with the reference beam. In order to make a comparison with atmospheric turbulence, the interferometry setup allows to compare the extra phase added by the DMD with the reference beam and the influence of the atmosphere can be modeled with just an extra phase added to the original optical beam.

A quite particular 4f-system is used between the DMD and the beam splitter where the first lens is fixed but the aperture, acting as a spatial filter, and the second lens are mobiles. The use of the aperture aims to separate the first order of diffracted light after the DMD.

Finally, the combination of both arms is sent to a charge-coupled-device (CCD) camera for measuring the intensity profile of the generated modes. This Mach-Zehnder interferometer permits to verify the phase patterns and obtain interferograms. In our experiment, we generate a spatial mode by loading computer generated holograms that corresponds to Zernike polynomials.
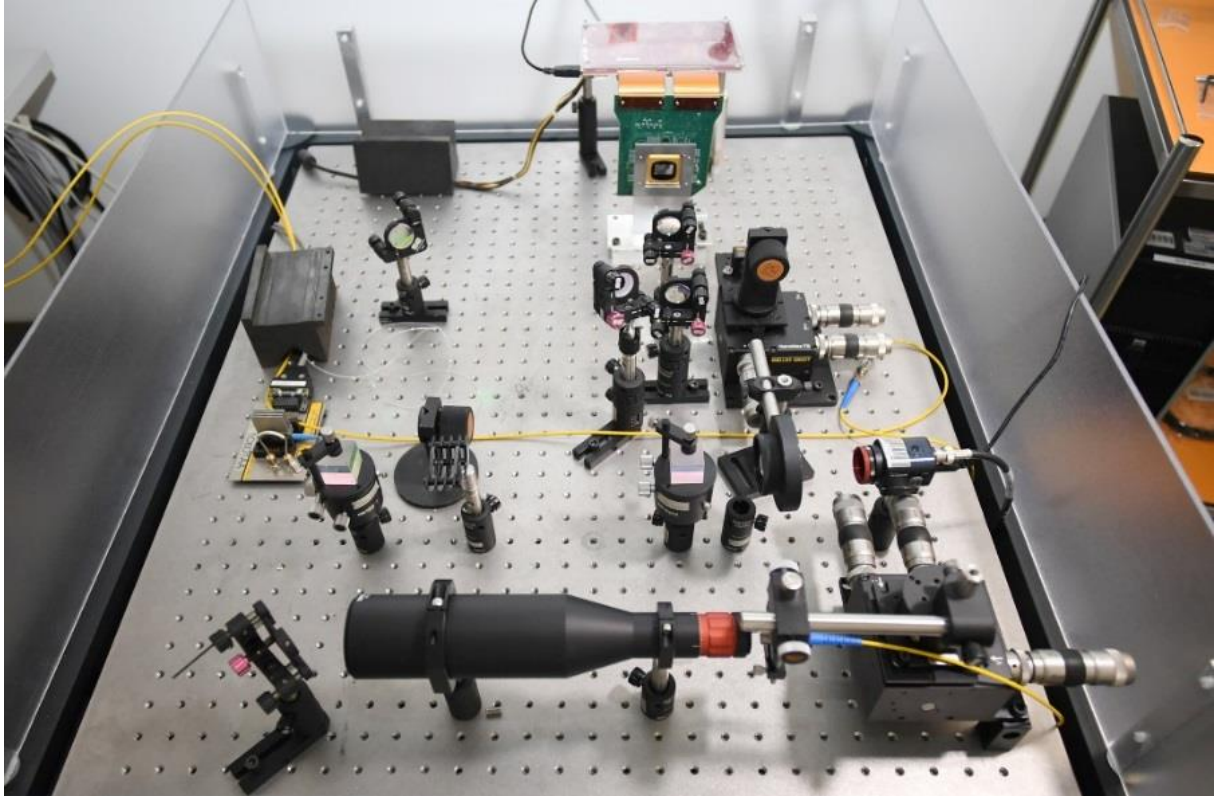
Figure 4-25: Global view of the DMD interferometry system

Two ways to drive the DMD are possible with the same setup that are super-pixel method and holographic methods. Both are described in the following parts.

4.7.1.1 Super-pixel method

The principle of the super-pixel method is to divide the wave front of the signal into squares (super-pixels), shape the amplitude and add different phase each other on the same super-pixel. In addition, the super-pixel state depends on the state of all its pixels (''ON'' or ''OFF'') where not all pixels reflects light. Consequently, this method allows to control both of the amplitude and phase of the optical signal in the DMD surface. Contrariwise, there is a tradeoff to be considered when the size of the super-pixel is chosen where the bigger the number of pixels by super-pixels is, the greater the phase resolution will be. The amplitude/phase resulting from the super-pixel method is the sum of the vectors of the ON pixel corresponding:

$$E = \sum_{i=0}^{m} Re(\pi x_i = 1) + \sum_{i=0}^{m} Im(\pi x_i = 1) \tag{4.1}$$

where m denotes the super-pixel dimension and x_i is the pixel position on the super pixel. Figure 4-26 illustrates an example of a super-pixel with a dimension of $N = 4$ (4x4 = 16 micro-mirrors used for the super-pixel).
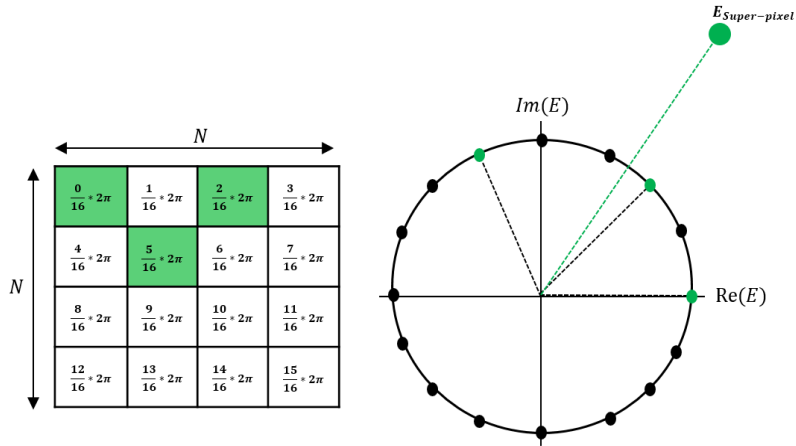
Figure 4-26: Example of a super-pixel containing 16 mirror of the DMD with 3 micro-mirror in the ON state [101]

On the case of all the micro-mirrors are in ON position, the super-pixel becomes a flat mirror. More details about the super-pixel method are detailed in [101]. Another method may be used by the same setup and named holographic method.

4.7.1.2   Holography method

The holographic method consists in considering binary function that will create the DMD's pattern and where the Fourier transform contains the information about the phase deformation. By selecting the first diffracted mode, phase information recorded onto the holographic pattern is collected. Recent optical setups have successfully validated the combination of binary computed-generated holographic methods with DMD [102]. In addition, this method consists on separating of the coming light beam into different spatial modes by interfering it with a holographic pattern composed by a set of binary gratings [100]. The image is reconstructed by illuminating the recorded interference fringes with a coherent course and isolating the first diffracted order. The DMD principle presents a diffractive fringes by reflection and Figure 4-27 illustrates the same principle but with transmission diffraction scheme.
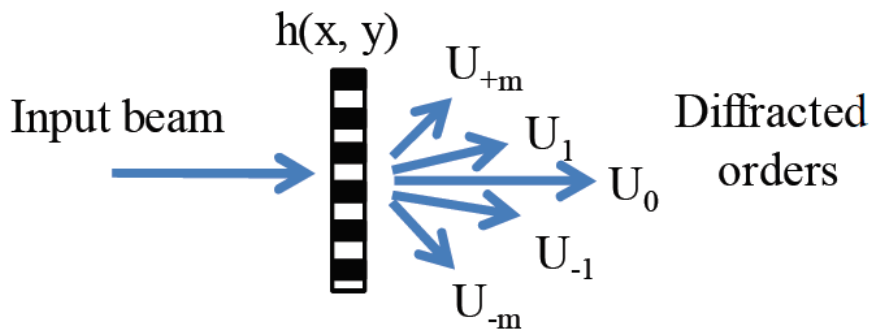
Figure 4-27: Binary holography representing the diffraction of incoming light-wave into multiple orders [99].

A well-known technique to generate binary holograms is to create an interferogram $h(x,y)$ composed by rectangular fringes in which the position and width of each fringe encode the phase and amplitude. For any desired field $(A(x,y)e^{i\phi(x,y)})$ acting over the position and width of the fringes in the interferometer $h(x,y)$ is giving by [105]:

$$h(x,y) = sign\{cos(2\pi\alpha + 2\pi\delta(x,y)) - \cos(\pi q(x,y))\} \qquad (4.2)$$

where the parametric functions $\delta(x,y)$ and $q(x,y)$ correspond to the desired amplitude and phase modulation, are given by:

$$q(x,y) = \frac{arcsin\{A(x,y)\}}{\pi}, \delta(x,y) = \frac{\phi(x,y)}{2\pi} \qquad (4.3)$$

The resulting grating $h(x,y)$ consist of a set of rectangular fringes and by expanding $h(x,y)$ into a spatial Fourier series:

$$h(x,y) = \sum_m U_m = \sum_m \frac{sin\{(\pi m q(x,y))\}}{\pi m} e^{i2\pi m(\alpha + \delta(x,y))} \qquad (4.4)$$

where α denotes the resulting angular separation between modes. In this expression, we observe that the terms $U_{\pm 1}$ (Figure 4-27) corresponds to the desired phase and amplitude modulation titled by an angle corresponding to the diffraction [100].

4.7.1.3   Comparisons of different methods

The two methods are quite similar in the way that they consist in dividing the DMD in small sections to sample the wavefront and recreate the wanted wavefront in the diffracted pattern. The main difficulties in this process is the elaboration of the hologram and filtering out the wanted information. As a result, a tradeoff appears between the spatial resolution and the phase resolution.

The holographic method seems easier to be implemented due to the unique definition of the pattern and the location of wanted information in the light diffraction. Furthermore, the super-pixel method presents some difficulties that need to be highlighted. For the phase modulation, the super-pixel method is not well defined and many patterns on the DMD can achieve same phase modulation. Indeed, there is a choice to be done for how many pixels we need to select for a super-pixel.

For the next part, we will consider the holographic method to drive due to its benefits comparing to the super-pixel method.

4.7.2   Digital Micro-Mirror Device: interference scheme

The first setting to be adjusted is the optical beam size to cover the DMD through the optical system (beam splitter, beam expander, optical densities and spatial filter). The DMD is used as a flat mirror to adjust the interferometer system when the two beams are superposed. In addition, the superposition of both optical beams is not enough to see interference and the angle between their wavefronts need to be as small as is possible. If the 4f-system are correctly placed without misalignments, interference scheme can be shown in the CCD level that can be enlarged by adjusting the position of the beam splitters. Thereby this interferometry system is not robust to any misalignments. Figure 4-28 illustrates the interference scheme obtained after the optimization of alignments.
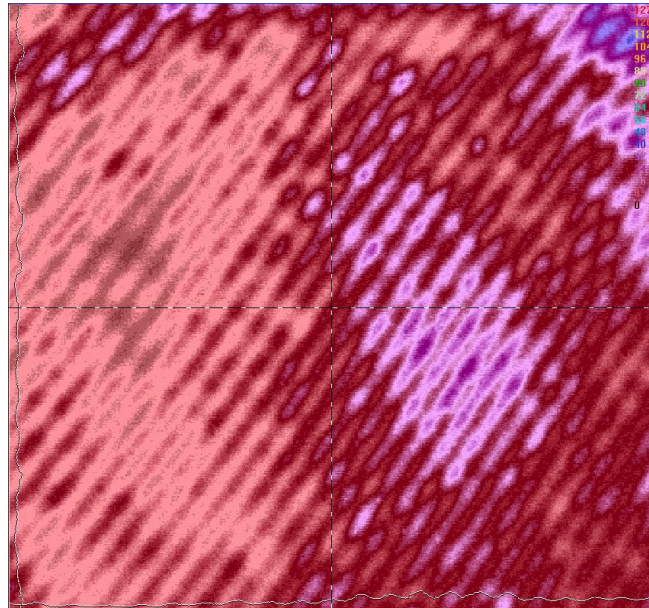
Figure 4-28: Interference scheme between reference beam and the reflected beam from the DMD

This illustration validates that all different components are correctly aligned and the 4f system may be replaced by the spatial filter in order to decrease aberrations in the beam.

The position of the spatial filter have to be calculated to find precisely $(x = 0, y = 0)$ point corresponding to the Fourier plan. The process to find it is to drive the DMD by turning ON half the micro-mirrors in the four directions.
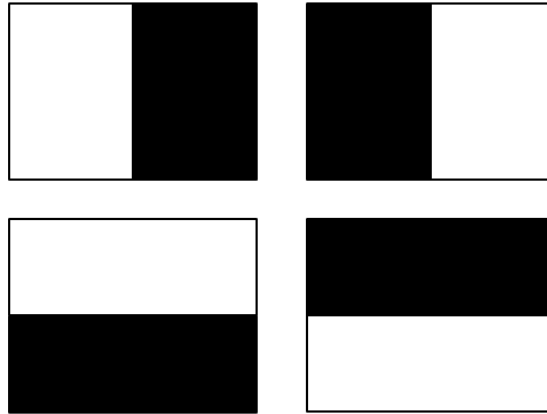
Figure 4-29: Patterns used to drive the DMD in order to find the spatial filter position

The patterns allow to obtain four limits due the junction between ON mirrors and OFF mirrors. By adjusting the beam splitters with maximum of precision, the spatial filter position could be located in the junction of the reflected stains. The filter can then be positioned.

As we consider the holographic method, the desired phase is contained in the first diffraction order. The 4f system can be replaced and the spatial filter have to be moved to the position corresponding to the first diffraction order [106].

The DMD bench is now able to receive the patterns coming from the LOT model and this will be the subject of the next part.

4.7.3   Digital Micro-mirror Device: driving

According to the theory recalled in 2.3.5.2, the atmospheric effects can be modeled using Zernike polynomials. The LOT model take into account the combination of the three first order of these polynomials: Tip/Tilt, Astigmatism and Defocus that are uploaded on the control software to be loaded is the DMD matrix. Firstly, the CCD camera is placed in the optical axis of the DMD in order to study the patterns generated by the DMD. A Matlab program is developed to calculate the first orders of Zernike polynomial that will be used to drive the DMD. Table 4-7 illustrates the generated Zernike polynomials on the DMD by considering holography and super-pixel methods.
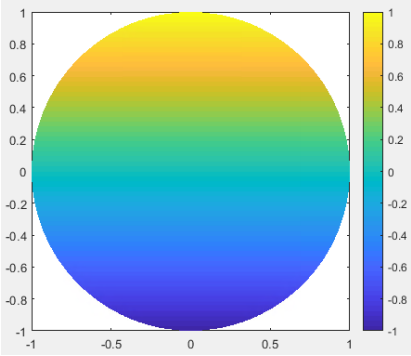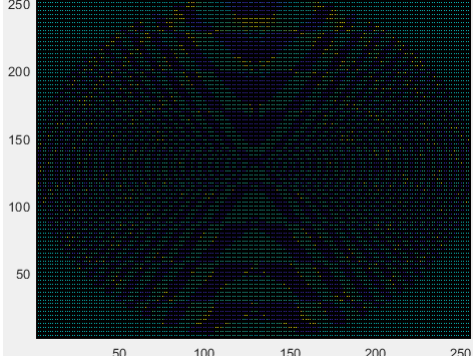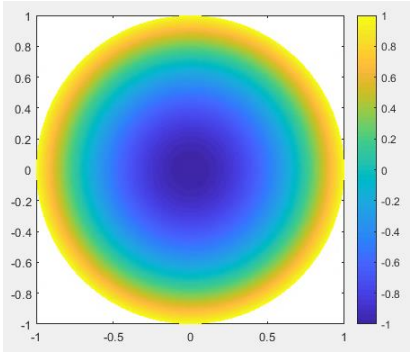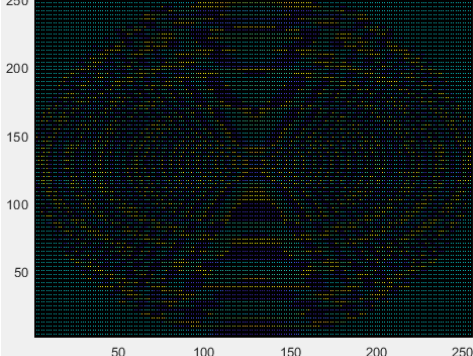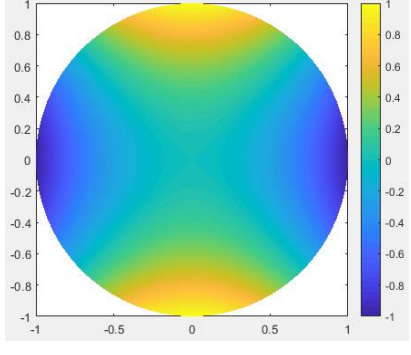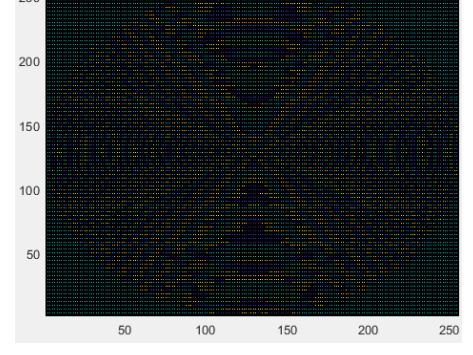
Beam deformation	Zernike polynomial simulated	Holographic method on the DMD
Tip/Tilt		
Defocus		
Primary astigmatism		

Table 4-7: Generation of Zernike low orders polynomials on the DMD matrix

The comparison between the theoretical Zernike order and its effect on the DMD is difficult. We can find some similitude in the global form (i.e. many rings on the defocus effect).

Now, the interferometry system can be modified by removing the reference beam and keeping only the beam deflected by DMD. The optical beam have to be recovered and coupled in a single mode fiber (SMF) to be sent the receiver. For this part, S-340 Piezo Tip/Tilt Stage Mirror Platform allows precision rotation in two orthogonal axes with a fixed pivot point. The parallel-kinematic differential drive enables outstanding angular stability over a wide temperature range. This junction is still under development and may be accomplished as a perspective of this work.

4.8   Conclusion

In this chapter, we introduced different experimentations considered to model an optical feeder link on the laboratory. The fibred ELLA bench allowed to have an optical communication between the transmitter and the receiver using different modulation formats (NRZ OOK, RZ OOK, NRZ DPSK and RZ DPSK). The receiver sensitivity in each configuration of the bench matches well with the theoretical values and the state of the art of such optical systems. In addition, the experimental results are also used to validate the simulation results achieved in chapter 3. The experimental results over different turbulence conditions match well with the simulation results considering the fading time.

For the atmospheric propagation, the times series generated using WPLOT model are used to insure the power fluctuation on the transmitted optical power. Both of BER and the fading time are estimated in different propagation conditions (low turbulence regime, beam wander regime and high turbulence regime). **We illustrate also the gain brought to the communication under atmospheric turbulence goes from 3 dB in low turbulence regime to 15 dB in high turbulence regime**. In order to complete the model, a second optical bench using a DMD device is built to illustrate the phase deformation effect on the optical beam. The LOT is considered where the disturbed beam is compared with the theoretical representation. The junction of these two optical benches is under development and will be a part of the next experimentations.

Conclusion

5 Conclusion and perspectives

5.1 Summary of the main results

Satellites telecommunications must follow the advances of terrestrial network capacities and increase the data rate and performances to remain competitive. In comparison with RF communication systems, space optical communication have advantages such as a large available bandwidth, power efficient, lower size and weight of terminals, no interference with other waves and no frequency regulation. Despite these advantages, these space optical communications suffer from the effects of the atmospheric channel (turbulence and cloud), eye safety issues (due to the highest power needed to establish the communication) and the requirement of accurate pointing system. The technology of the products currently available for terrestrial communication has to be adapted to the requirements of space applications. The need for very high power wide bandwidth optical amplifiers is also a major field of research.

In order to get rid of the signal fading induced by atmospheric turbulence several mitigation techniques are commonly considered. One of the solutions to correct these effects is the adaptive optics (AO) that is a mature technology used in astronomical applications (telescopes and other astronomical instruments). A multiple aperture receiver may be considered to limit atmospheric effects but this method requires many identical optical receivers and apertures that leads to raise the cost of the terminal. In this framework, the main objective of this thesis was to develop optical link architectures (simulations and experimentations) able to be implemented for optical feeder links by considering atmospheric mitigations on the phase of the optical beam.

The first part of this thesis was focused on the development of optical communication architectures (transmitters and receivers) dedicated to the emulation of optical feeder links using OOK and DPSK modulations.

Optical communication link using the OOK modulation has been modeled and presents a receiver sensitivity matching with the literature. For the DPSK optical link, the receiver sensitivity illustrates a benefit of 3 dB comparing to the OOK communication. Different parameters of the transmitter and the receiver components are studied and varied to illustrate their effects on the link performances and especially on the robustness of the optical receiver. The actual performance of DPSK and OOK modulations have been assessed under simulations that can emulate the use cases including GEO feeder links, LEO downlinks and LEO inter-satellite links. The data rate used in 10 Gb/s and a communication link employing two optical channels at 10 Gb/s each one is also assessed.

The WPLOT, developed by A.R CAMBOULIVES, allows emulating the atmospheric effects on the uplink optical beam under different turbulence conditions by emulating three turbulence regimes. The time series generated over few seconds of the atmospheric propagation are generated and used as input on the communication links (OOK and DPSK) to evaluate the transmission performances. Finally, when we consider different turbulence cases, the fading time over the duration of the time series is

measured and the BER is estimated. The results coming from the use of time series on the modeled optical links are encouraging to continue the development of high data rate feeder links. The adaptive optics system modeled in WPLOT illustrates an important improvement of the uplinks communication that can rise up to 15 dB in the worst case of atmospheric turbulences to limit the atmospheric effects on the optical communication.

The second part of this thesis concerned on the development of an optical test bench to emulate an optical feeder link including an atmospheric effect emulator.

The ELLA optical bench is developed using commercial components to achieve OOK and DPSK optical communication. This bench performances are compared to those of the simulation models which present a difference of few dBs (up to 3 dB) due to the experimental conditions and the simplified model of some components used under the simulator. The FSO part of the bench contains a VOA dedicated to receive the same times series used for the simulations study in order to assess the robustness of the optical link. The fading time over the time series duration is around 50 % in the low turbulence cases and may achieve 100% (not enough average power reaching the receiver to insure the optical communication) in the worst case. As for the simulation, the benefit of the pre-compensation stage can be remarked in all cases of atmospheric turbulences (in the worst case for example, the improvement goes from 100% to 86%). In order to compare simulation and experimental results, both curves are summarized in Figure 5-1 :
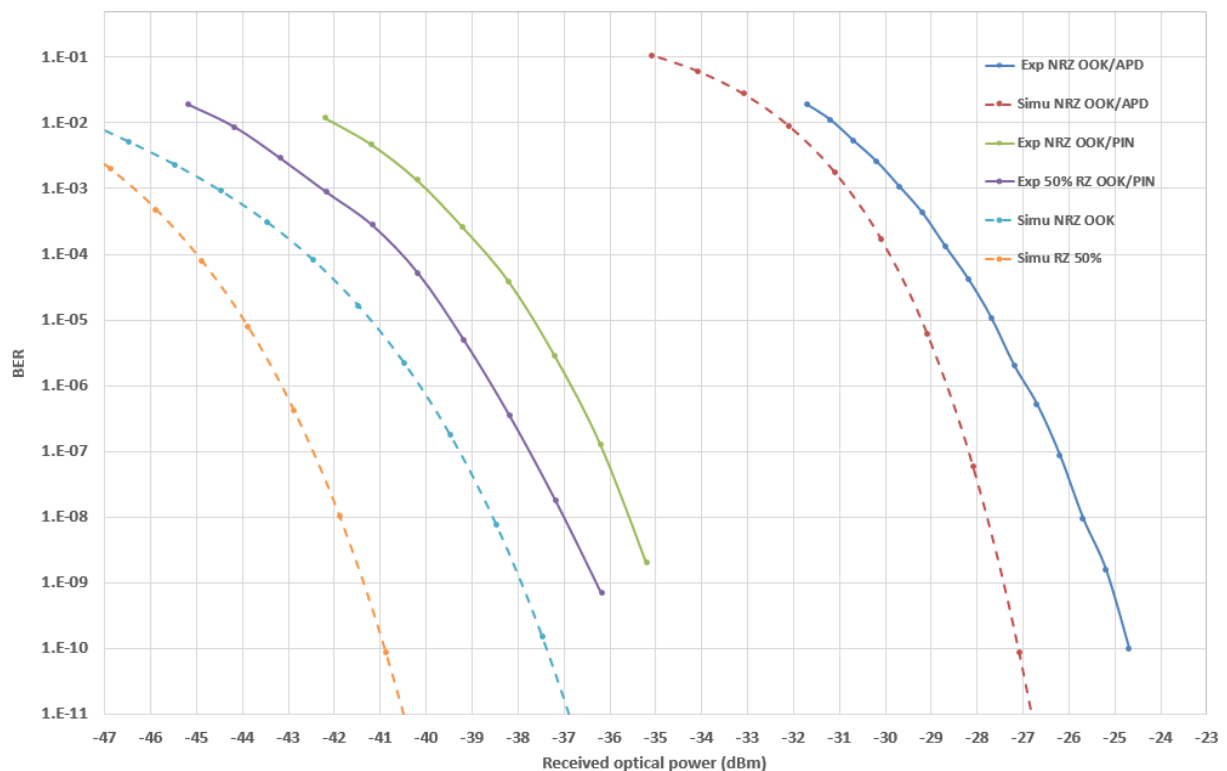
Figure 5-1: Summary of BER curves achieved with simulation models and the ELLA bench for NRZ OOK, NRZ DPSK, 50% RZ OOK and 50% RZ DPSK

For the feeder down links, the ELLA bench may be used as a bidirectional communication depending on the time series attenuations used (WPLOT for the uplink and other time series describing the downlink mitigations).

The DMD dedicated to emulate the phase perturbation of the optical beam caused by the atmosphere is an important asset to complete the optical bench in order to have a more realistic representation of the downlink feeder. To emulate the power fluctuation (amplitude), times series after fiber injection can be used to drive the dynamic VOA. However, the phase deformation could be emulated using the DMD. The use of the DMD is more representative of the downlink feeder because for this link the turbulent atmospheric layers are present at the end of the propagation. For the uplink, the beam goes through the turbulent layers at the beginning of the propagation and then it diverges up to the satellite. The beam size arriving to the satellite is much bigger than the telescope aperture and the phase deformations have been spread out. As a result, the wavefront can be considered as plane. The combination of both optical benches could be the next part of the future work to complete the free space optical communication activities at the IRT.

5.2 Perspectives and scope on the future work

This work allows to have an end-to-end FSO optical link modeling the optical feeder links through the atmosphere under simulation where most of parameters on the link are adjusted to represent a more realistic communication link. Effects of many parameters of the link are studied in order to illustrate which ones may degrades the link performances. These results are validated by developing an optical bench to emulate end-to-end optical link including the atmospheric effects. The AO compensation improves the quality of the received signal after the atmospheric propagation that can goes in this work up to 15 dB and leads to improve the fading time. The experimental work permits to validate the simulation results and to identify many challenges to complete the bench development.

Despite this work achieved on the model of the free space optical communication for satellites application (uplinks and down links), most of challenges discussed in this manuscript need to be more developed. The following points are the main ones that should be investigated to achieve higher data rate links and overcome atmospheric mitigations:

- **Exploring new link architectures using high level optical modulation**

For the simulation part, advanced optical modulations such as direct detection DQPSK or coherent QPSK [107] could be implemented for increasing the spectral efficiency of the link. These modulations have to be studied in order to know if the complexity is compatible with space constraints. In the case of coherent detector the emulation of the spatial phase variation has to be modeled using for example the free space optical bench in order to evaluate the impact on the performances of the demodulation process.

- **Error correcting code on the receiver side to optimize the BER after atmospheric propagation**

The fading estimated of the communication links after the atmospheric propagation may achieve high values aiming to loss the transmitted data information. The received data (in both simulation and experimentation) may be completed by an error code correcting in order to recover the lost packets.

- **New link architectures based on WDM up to 40 channels** [26]

For the experimentation part, one of the next challenges is to complete the optical bench with two additional optical sources and optical modulators to insure the 40 Gb/s. The robustness of optical modulations could be assessed by using different optical modulation on the WDM system.

- **Optical beam recovering into the single mode fiber with a high efficiency injection**

The single mode fiber injection (SMF) part has been explored where the piezo tip/tilt has been positioned. The injection efficiency has to be estimated and optimized before putting this part after the DMD. The recovered signal is then sent to the receiver to estimate the communication performance.

- **The final configuration of the optical bench (ELLA, SMF mechanism and the DMD device)**

The objective of this configuration will be to put together both the fibred bench (ELLA bench) and the DMD device to emulate in the same time the power and phase fluctuations. The main issue to achieve this is to optimize the optical signal injection (coming the DMD) into a single mode fiber to be sent to the receiver and to estimate the link performances. The interferometry setup have to be modified to be adapted to the ELLA bench by removing the reference beam and adding a piezo Tip/Tilt mirror device to optimize the single mode fiber injection.

After generating the optical signal, it is sent to the DMD derived by the Zernike polynomials screens. To recover the optical signal, it is important to manage and optimize the injection from space to fiber. The global final scheme is shown in Figure 5-2.
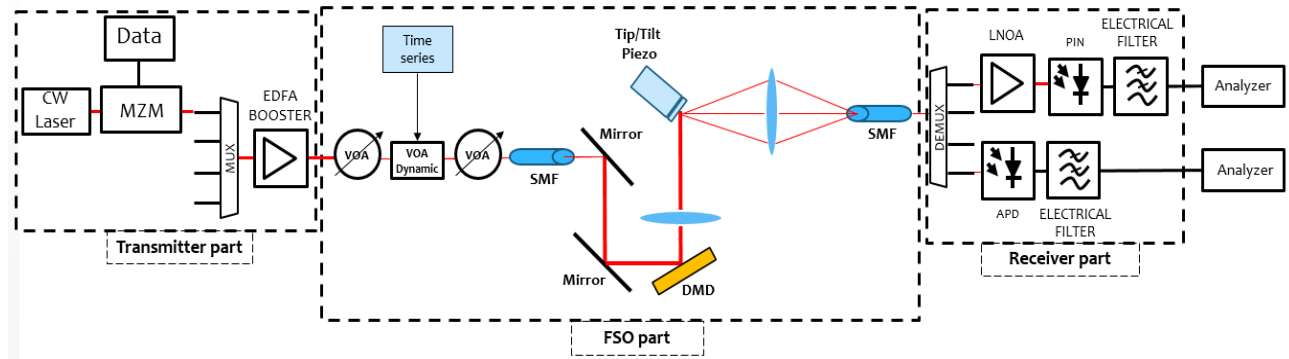
Figure 5-2: Integration of both ELLA bench and DMD device to emulate phase and power fluctuations.

- **Adaptive optics loop to correct the wavefront deformation before the data analyzing**

This system could also be completed by an adaptive optics system to recover the waveform deformation, caused by the atmosphere, by applying the reverse deformation to the optical beam before being sent. This loop could be put at the last part the FSO optical transmission before the SMF injection. In this case the DMD is driven only for generating turbulent perturbed beam. In addition, the multiple aperture receiver could also complete the optical bench where important results of performance optimization are illustrated in [51].

Appendix A

6 Annex A: Zernike polynomials

Zernike polynomials define an orthogonal basis on the unit circle that are used to describe the wavefront in terms of optical aberrations [87]. In 2.3.5.2 section, the first 21 orders of Zernike polynomials are introduced ordered vertically by radial degree and horizontally by azimuthal degree. They are recalled in the following relation [86]:

$$Z_i(\vec{r}, \theta) = R_n^m(\vec{r})\Phi_n^m(\theta)$$

Where i is the Noll's index, n the radial degree and m the azimuthal degree.

Table 6-1 summarizes the first 15 order of Zernike polynomials with their expression and their classical names.

Noll's index (j)	Radial degree (n)	Azimuthal degree (m)	Z_j	Classical name
1	0	0	1	Piston
2	1	1	$2\rho\cos\theta$	Tip
3	1	-1	$2\rho\sin\theta$	Tilt
4	2	0	$\sqrt{3}(2\rho^2 - 1)$	Defocus
5	2	-2	$\sqrt{6}\rho^2\sin 2\theta$	Oblique astigmatism
6	2	2	$\sqrt{6}\rho^2\cos 2\theta$	Vertical astigmatism
7	3	-1	$\sqrt{8}(3\rho^2 - 2\rho)\sin\theta$	Vertical coma
8	3	1	$\sqrt{8}(3\rho^2 - 2\rho)\cos\theta$	Horizontal coma
9	3	-3	$\sqrt{8}\rho^3\sin 3\theta$	Vertical trefoil
10	3	3	$\sqrt{8}\rho^3\cos 3\theta$	Oblique coma
11	4	0	$\sqrt{5}(6\rho^4 - 6\rho^2 + 1)$	Primary spherical
12	4	2	$\sqrt{10}(4\rho^4 - 2\rho^2)\cos 2\theta$	Vertical secondary astigmatism
13	4	-2	$\sqrt{10}(4\rho^4 - 2\rho^2)\sin 2\theta$	Oblique secondary astigmatism
14	4	4	$\sqrt{10}\rho^4\cos 4\theta$	Vertical quadrafoil
15	4	-4	$\sqrt{10}\rho^4\sin 4\theta$	Oblique quadrafoil

Table 6-1: Zernike polynomials with their Noll's index, radial degree, azimuthal degree and classical name

Appendix B

7 Annex B: Publications list

International conference proceedings

K. Elayoubi, A. Rissons, J. Lacan, L. Saint Antonin, M. Sotom, and A. Le Kernec, "RZ-DPSK optical modulation for free space optical communication by satellites," in *IEEE 2017 Opto-Electronics and Communications Conference (OECC) and Photonics Global Conference (PGC)*, 2017, no. 1, pp. 1–2.

C. D. Munoz, K. Elayoubi, A. Rissons, S. Villamizar, and M. Varon, "O-band and C-band VCSEL based optoelectronic oscillator (VBO) for 1.25 Gbit/s pulsed RZ-OOK and RZ-DPSK free space optical transmissions," in *2017 International Topical Meeting on Microwave Photonics (MWP)*, 2017, pp. 1–4.

K. Elayoubi, A. Rissons, and A. Belmonte, "Optical test bench experiments for 1-Tb / s satellite feeder uplinks," *Spie Opt.*, vol. 1077006, no. September, p. August, 2018.

A. Maho, M. Faugeron, A. Le Kernec, K. Elayoubi, and M. Sotom, "Assessment of the effective performance of DPSK vs . OOK in satellite- based optical communications," in *ICSO*, 2018, pp. 2–7.

Appendix C

8 Annex C: WPLOT user guide

Introduction

This technical note aims at describing the code of the WPLOT (With Propagation Low-Order of Turbulence) program. It is intended to help the user to retrieve easily the bibliographic sources and to use correctly the program. This document does not explain the theory behind the formula. For that, the reader shall refer to the bibliographic sources in particular:

- **Adrien-Richard Camboulives,** « Compensation des effets de la turbulence atmosphérique sur un lien optique montant sol-satellite géostationnaire : impact sur l'architecture du terminal sol », École doctorale n°572 Ondes et matières (EDOM), 13 Décembre 2017.
- **François Chassat,** « Propagation optique à travers la turbulence atmosphérique : étude modale de l'anisoplanétisme et application à l'optique adaptative », 1992.
- **Adrien-Richard Camboulives,** « Atmospheric Turbulence on a Ground-to-Satellite Optical Link », IRT ALBS Project, LIV-S-010-L4.2-108-V0, 2016.

Program organization tree

The next figure presents the organization tree of the WPLOT program.
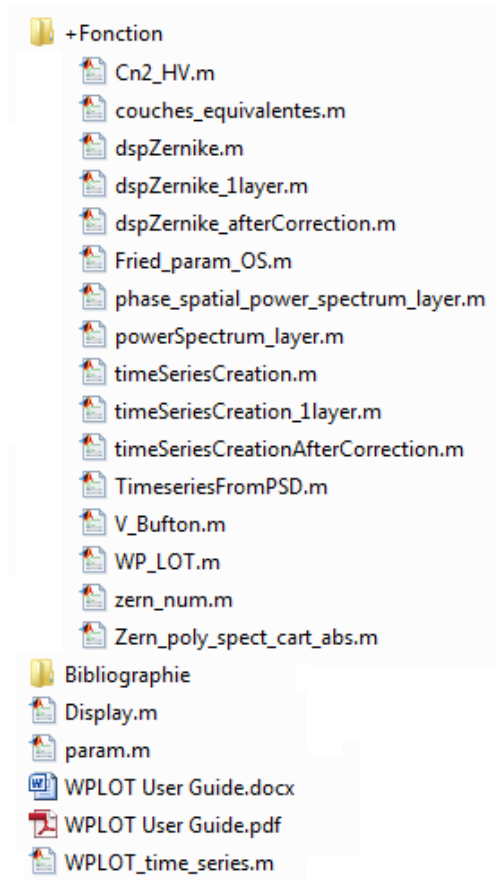
The program is organized as follow:

- [File] **WPLOT User Guide.pdf.** This technical note
- [File] **WPLOT_time_series.m.** The main of the program
- [File] **param.m.** The configuration file for the simulation
- [File] **Display.m.** The script for plotting the results
- [Folder] **+Function.** The set of functions used by the main program file
- [Folder] **Bibliography.** All the references corresponding to the formulae of the program

Using the following notation:

- **Script**
  - Function
    - Sub-function
      - Sub-sub-function
        - Etc.

The dependency tree of the functions of the program can be presented as:

- **param**
  - Fried_param_OS
  - V_Bufton
  - Cn2_HV
- **WPLOT_time_series**
  - timeSeriesCreation
    - TimeseriesFromPSD
    - dspZernike
      - phase_spatial_power_spectrum_layer
      - Zern_poly_spect_cart_abs
        - zern_num
  - timeSeriesCreationAfterCorrection
    - TimeseriesFromPSD
    - dspZernike_afterCorrection
      - phase_spatial_power_spectrum_layer
      - Zern_poly_spect_cart_abs
        - zern_num
  - timeSeriesCreation_1layer
    - TimeseriesFromPSD
    - dspZernike_1layer
      - powerSpectrum_layer
      - Zern_poly_spect_cart_abs
        - zern_num
  - couches_equivalentes
  - timeSeriesCreation_1layer
  - WP_LOT
- **Display**

The following of the technical note describes each function used in the program. A tutorial is also presented at the end of the document for guiding a new user through the simulation process.

Functions

Before going into the details of each function, it is useful to explain the **Matlab Anonymous Functions** because they are widely used in the code.

An anonymous function is like an inline function in traditional programming languages, defined within a single Matlab statement. It is a function that is not stored in a program file, but is associated with a variable whose data type is "function handle". Anonymous functions can accept inputs and return outputs, just as standard functions do. However, they can contain only a single executable statement.

The syntax for creating an anonymous function from an expression is:

```
f = @(arglist)expression
```

For example, you can create a handle to an anonymous function that finds the square of a number as:

```
sqr = @(x) x.^2;
```

Variable `sqr` is the function handle. The @ operator creates the handle, and the parentheses () immediately after the @ operator include the function input arguments. This anonymous function accepts a single input `x` and implicitly returns a single output which is an array of the same size as `x` that contains the squared values.

Now we can find the square of a particular value by passing the value to the function handle, just as we would pass an input argument to a standard function.

```
a = sqr(5)
```

```
a = 25
```

Many Matlab functions accept function handles as inputs so that you can evaluate functions over a range of values. You can create handles either for anonymous functions or for functions in program files. The benefit of using anonymous functions is that you do not have to edit and maintain a file for a function that requires only a brief definition.

For example, we can find the integral of the `sqr` function from 0 to 1 by passing the function handle to the integral function:

```
q = integral(sqr,0,1);
```

We do not need to create a variable in the workspace to store an anonymous function. Instead, we can create a temporary function handle within an expression, such as this call to the integral function:

```
q = integral(@(x) x.^2,0,1);
```

The expression in an anonymous function can include another anonymous function. This is useful for passing different parameters to a function that you are evaluating over a range of values.

In the **param.m** file we can find for example an anonymous function that computes the atmospheric turbulence profile:

```
Cn2 = @(h) Fonction.Cn2_HV(h,V,Cs);
```

The anonymous function `Cn2()` is defined by the function `Cn2_HV()` that is hierarchically called from the **Function** folder. Hence, considering the previous expression, we can say that the function `Cn2()` is an over-definition of the function `Cn2_HV()` with the parameter `V` and `Cs` that are fixed and equal to the corresponding variables defined above in the **param.m** file. The use of `Cn2()` function is as follow:

```
y = Cn2(x);
```

The variable `x` is the altitude array and the variable `y` is the array of Cn2 values.

Nested anonymous functions are used for example in the **couches_equivalentes.m** file. The first anonymous function is defined by:

```
Cn2 = @(h) Fonction.Cn2_HV(h,V,Cs);
```

And the second one is directly used in the integral function:

```
integral(@(h) Cn2(h).*h.^(5/3),h_min,h_max)
```

In other words, we can say that the integral of the function `Cn2_HV(h,V,Cs).*h.^(5/3)` is done over `h` from `h_min` to `h_max` with `V = 21` and `Cs = 5.4e-14`.

WPLOT: description

This function computes the variation of received irradiance as well as the loss due to the turbulence. The figure bellow presents an illustration of some of the geometrical elements that are used hereafter.
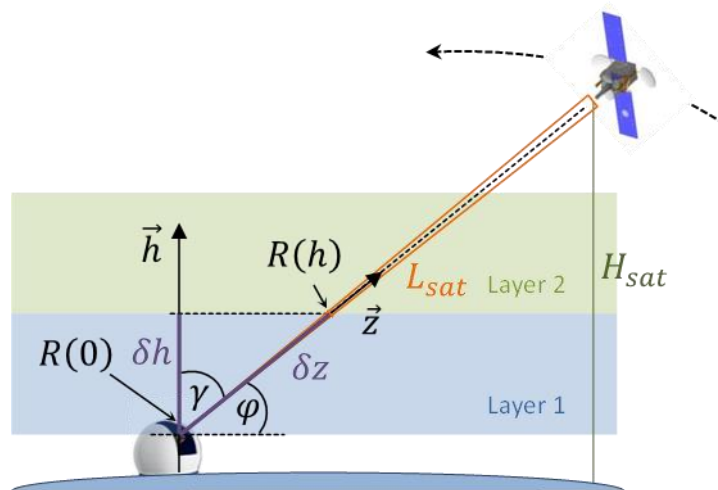
Depending on the size of the waist at the emission, the effects of the atmospheric turbulence on the beam will differ and lead to three distinct irradiance fluctuations regimes:

- $\omega_0 \ll r_0$. When the waist size at emission is much lower than the coherence diameter described by the Fried parameter r_0, the effects of the atmospheric turbulence are limited. At the satellite level, the beam size is therefore very large due to the divergence of the beam, which means that beam wander is negligible compared to the beam spreading.
- $\omega_0 \approx r_0$. When increasing the waist size at emission, the beam divergence is reduced and the beam pointing becomes a key issue. The major impact of atmospheric turbulence on the beam becomes the beam wander. This regime is particularly interesting because beam wander may be compensated using a tilt tracking mirror, which immediately leads to important mitigation

- of irradiance fluctuations. Moreover, in this regime, the beam maintains its coherence and the impact of higher orders is negligible compared to beam wander.
- $\omega_0 \gg r_0$. In this regime, beam coherence is lost and beam breakup occurs. The beam consists of several hot spots and the center of the beam is difficult to position. Beam wander does not have any significance in this case. Mitigation of atmospheric effects becomes more difficult.

We remind that the atmosphere is modeled only up to 20 km altitude in WPLOT. The thickness of the layers of the discretized atmospheric model along the zenithal axis δh [m] is given by:

$$\delta h = \frac{20000}{N_{layer}}$$

With N_{layer} the number of equivalent layers [-]. The default number of layers is 2. Using only two layers is sufficient to make tip/tilt, defocus and astigmatism effects appear.

The equivalent thickness along the propagation axis δz [m] is given by:

$$\delta z = \delta h \times \sec(\gamma)$$

With γ the zenithal angle [rad]

The total length of the propagation path through the modeled atmosphere z_{atm} [m] is given by:

$$z_{atm} = 20000 \times \sec(\gamma)$$

In order to take into account the truncation of the infinite Gaussian beam by the telescope, the effective diameter of the telescope D_{eff} [m] computed. It is given by:

$$D_{eff} = 2w_0 \sqrt{\tanh\left(\frac{D_{tel}^2}{2(2w_0)^2}\right)}$$

With:

- D_{tel} the telescope diameter [m]
- w_0 the waist of the laser beam (half of the pupil diameter) [m]

The equivalent waist in case of no turbulence (diffraction only) w_{eq} [m] is given by:

$$w_{eq} = \frac{D_{eff}}{2} \sqrt{1 + \left(\frac{\lambda \cdot L_{sat}}{\pi \left(\frac{D_{eff}}{2}\right)^2}\right)^2}$$

With:

- L_{sat} the total distance between the satellite and the ground terminals [m]
- D_{eff} the effective diameter of the telescope [m]

The irradiance of the equivalent waist with no turbulence I_0 [W/m²] is given by:

$$I_0 = \frac{2}{\pi w_{eq}^2}$$

Finally the loss due to the turbulence L_{turb} [dB] is given by:

$$L_{turb} = 10 \log\left(\frac{I_{turb}}{I_0}\right)$$

With:

- I_{turb} the irradiance on axis of the optical beam passed through the modelled atmosphere [W/m²]
- I_0 the irradiance on axis of the optical beam passed through the vacuum with no turbulence [W/m²]

All the difficulty is to determine the irradiance after propagation through the atmosphere. For that we have to compute the both the beam spreading and the beam wandering considering hypothesis on the turbulent layer parameters. Several approaches have been considered in the literature and the **Low-Order of Turbulence** (LOT) model of Baker has been selected (and improved) for implementation in WPLOT. In this model, the irradiance fluctuations are described by the deformation of a Gaussian beam using only the first and second order Zernike polynomials, that is the tip-tilt, the defocus and the astigmatism.

In the case of a ground to satellite propagation, the turbulence is in the near field while the satellite is in the far field. According to this model, this means that the turbulence can be integrated in a single phase screen placed at the transmitter prior to the propagation. The phase screen at the transmitter is given by:

$$\Phi_{LOT}(x,y) = k_0 \left(\theta_x x + \theta_y y + \Delta\kappa \frac{1}{2}\left((x^2 + y^2) - \frac{1}{2}w_0^2\right) + c_5 \frac{1}{2}(x^2 - y^2) + c_6 xy \right)$$

With:

$\Phi_{LOT}(x,y)$ the phase screen [rad] versus x and y coordinates [m]

θ_x and θ_y the angular tip-tilt [rad]

$\Delta\kappa$ the defocus curvature [m⁻¹]

c_5 and c_6 the astigmatism curvature [m⁻¹]

Warning: the formulae in the thesis manuscript of Adrien-Richard Camboulives at page 36 and 68 have typo in the term that multiply the $\Delta\kappa$.

The resulting normalized irradiance of a Gaussian beam propagating through atmospheric turbulence up to a satellite at a distance L_{sat} with the phase screen Φ_{LOT} placed at the transmitter is expressed as:

$$I(x,y,L_{sat}) = \frac{2}{\pi} \frac{1}{w_x w_y} e^{-\frac{2}{w_x}((x-\delta x)\cos(\omega) + (y-\delta y)\sin(\omega))^2} e^{-\frac{2}{w_y}((x-\delta x)\sin(\omega) - (y-\delta y)\cos(\omega))^2}$$

The beam wander, partial beam radii, and astigmatism parameters used in the previous equation are respectively given by:

$$\delta_{\{x,y\}} = L_{sat}\theta_{\{x,y\}}$$

$$w_{\{x,y\}} = w_0 \sqrt{\left(1 + L_{sat}\left(\Delta\kappa \pm \sqrt{c_5^2 + c_6^2}\right)\right)^2 + \left(\frac{2L_{sat}}{k_0 w_O^2}\right)^2}$$

$$\omega = \frac{1}{2}\arg(c_5 + ic_6)$$

In the expression of $w_{\{x,y\}}$ the first term under the root square corresponds to the beam broadening induced by defocus and astigmatism and the second term is the broadening induced by the diffraction.

Warning: the model is only valid for $w_0 \leq 1.5r_0$.

The shift from the axis of the centroid of the beam resulting from beam wander is given by δx and δy:

$$\delta x = \frac{2L_{sat}\lambda a_2}{2\pi w_0} \qquad \delta y = \frac{2L_{sat}\lambda a_3}{2\pi w_0}$$

With:

- λ the wavelength of the beam [m]
- L_{sat} the total distance between the satellite and the ground terminals [m]
- w_0 the waist of the laser beam (half of the pupil diameter) [m]
- a_2 the time series of the X-tilt [rad]
- a_3 the time series of the Y-tilt [rad]

The defocus curvature is given by:

$$\Delta\kappa = \frac{8\sqrt{3}}{\pi}\frac{\lambda}{(2w_0)^2}a_4$$

With a_4 the time series of the defocus [rad]

The astigmatism curvature is given by:

$$c_5 = \frac{4\sqrt{6}\lambda a_5}{\pi(2w_0)^2}$$

$$c_6 = \frac{4\sqrt{6}\lambda a_6}{\pi(2w_0)^2}$$

With:

- a_5 the time series of the oblique astigmatism [rad]
- a_6 the time series of the vertical astigmatism [rad]

It has been shown in the thesis of Adrien that the one-layer LOT model does not give an accurate description of the irradiance fluctuation. Thus the LOT model has been improved by getting close to the simulator that uses wave optics propagation through phase screens evenly distributed along the propagation path. In fact, the improved LOT model considers only two atmospheric layers which are enough to take into account tip/tilt, defocus and astigmatism effects. The improved model is referred to **2-Layers Wave Optics simulator** (2L-WO).

In order to take into account the propagation through multiple phase screens, it has been proposed to use the ABCD matrix propagation method, where the ABCD matrix is obtained from:

$$\begin{pmatrix} A & B \\ C & D \end{pmatrix} = \begin{pmatrix} 1 & L_{prop} \\ 0 & 1 \end{pmatrix} \prod_i^{N_{layer}} \begin{pmatrix} 1 & 0 \\ \Delta\kappa_i & 1 \end{pmatrix} \begin{pmatrix} 1 & \Delta z_i \\ 0 & 1 \end{pmatrix}$$

With:

- $\Delta\kappa_i$ the curvature resulting from defocus at the ith layer [m^{-1}]
- Δz_i the distance between two successive phase screens i and $i+1$ [m]
- N_{layer} the total number of considered layers [-]
- L_{prop} the remaining distance to the satellite [m]:

$$L_{prop} = L_{sat} - \sum_i^{N_{layer}} \Delta z_i$$

Considering the following initial complex radius of curvatures:

$$\frac{1}{q_{x_0}} = -\sqrt{c_5^2 + c_6^2} + \frac{\lambda i}{\pi \left(\frac{D_{eff}}{2}\right)^2}$$

$$\frac{1}{q_{y_0}} = \sqrt{c_5^2 + c_6^2} + \frac{\lambda i}{\pi \left(\frac{D_{eff}}{2}\right)^2}$$

With:

- D_{eff} the effective diameter of the telescope [m]
- $i^2 = -1$ the imaginary number [-]

Using the ABCD matrix, the complex radius curvatures after propagation are:

$$q_x = \frac{A q_{x_0} + B}{C q_{x_0} + D} \qquad\qquad q_y = \frac{A q_{y_0} + B}{C q_{y_0} + D}$$

This leads to a modified estimation of the beam radii w_x and w_y compared to Baker's approach:

$$w_x = \sqrt{\frac{\lambda}{\pi \Im\left(\frac{1}{q_x}\right)}} \qquad\qquad w_y = \sqrt{\frac{\lambda}{\pi \Im\left(\frac{1}{q_y}\right)}}$$

With $\Im(\dots)$ the imaginary part.

Warning: the minus sign is putted on the q_{x0} component in the code whereas it is putted on the q_{y0} component in the thesis of Adrien. The code used D_{eff} whereas in the thesis w_0 is used.

Now that all the formulae are presented, we can give some precisions on the process of the computation. In Matlab, most of the above mentioned quantities can be computed using vectorial notation versus the sampled time but others have to be computed for each atmospheric layer at each time sample. This is the case for the defocus effects which involves the a_4 variable and consequently $\Delta\kappa$.

WPLOT: utilization and time series generation

This section is dedicated to the description of the front end scripts which are the **param.m**, the **WPLOT_time_series.m** and the **Display.m**.

The param.m is the configuration file of the simulation. It includes all the parameters that the user can modify and some basic computations. It is recommended to save this configuration script with the simulation results for each completed simulation in order to keep a log of the parameters used to compute the associated results. This file is well commented so we do not provide any additional complement.

After setting all the parameters in the **param.m** file, the user has to execute the **WPLOT_time_series.m** in order to run the simulation. The script computes the angular time series corresponding to each modelled Zernike coefficient:

Variable	Zernike coefficient	Comments
a2_serie	X-tilt	For all the modelled atmosphere
a3_serie	Y-tilt	For all the modelled atmosphere
a4_serie	Defocus	Need to be decomposed for each modelled layer of the atmosphere
a5_serie	Oblique astigmatism	For all the modelled atmosphere
a6_serie	Vertical astigmatism	For all the modelled atmosphere
a2_serie_TC	X-tilt	With pre-compensation
a3_serie_TC	Y-tilt	With pre-compensation

The script also computes the basics of the link budget including:

- Emission telescope gain
- Free space loss
- Reception telescope gain

which seem to be not used by the program.

Finally, the script allows plotting the simulation results:

- Power spectral density of the on-axis irradiance including the turbulence effects without pre-compensation
- Power spectral density of the on-axis irradiance including the turbulence effects with pre-compensation
- Time variation of the loss due to the turbulence without pre-compensation
- Time variation of the loss due to the turbulence with pre-compensation

9 Bibliography

[1]   W. D. Williams, M. Collins, and D. Boroson, "RF and Optical Communications : A Comparison of High Data Rate Returns From Deep Space in the 2020 Timeframe," *Nasa/Tm*, no. March, p. 214459, 2007.

[2]   H. Kaushal and G. Kaddoum, "Optical Communication in Space: Challenges and Mitigation Techniques," *IEEE Commun. Surv. Tutorials*, vol. 19, no. 1, pp. 57–96, Jan. 2015.

[3]   D. Giggenbach, P. E. Lutz, J. Poliak, R. Mata-calvo, and C. Fuchs, "A High-Throughput Satellite System for Serving whole Europe with Fast Internet Service , Employing Optical Feeder Links Ka-band User Links," pp. 49–55, 2015.

[4]   F. Heine, G. Muhlnikel, H. Zech, S. Philipp-May, and R. Meyer, "The European Data Relay System, high speed laser based data links," *2014 7th Adv. Satell. Multimed. Syst. Conf. 13th Signal Process. Sp. Commun. Work.*, pp. 284–286, 2014.

[5]   H. Xuan, Y. Hai-Lin, X. Ping, and W. Wei-Yang, "Point-ahead demonstration of a transmitting antenna for satellite quantum communication," vol. 26, no. 13, pp. 17044–17055, 2018.

[6]   H. Hemmati, A. Biswas, and I. B. Djordjevic, "Deep-space optical communications: Future perspectives and applications," *Proc. IEEE*, vol. 99, no. 11, pp. 2020–2039, 2011.

[7]   R. C. Andrews, Larry & L. Phillips, Ronald & J. Sasiela, Richard & R. Parenti, "Strehl ratio and scintillation theory for uplink Gaussian-beam waves: beam wander effects," *Opt. Eng.*, vol. 45, no. 7, p. 076001, Jul. 2006.

[8]   S. Poulenard, M. Crosnier, and A. Rissons, "Ground Segment Design for Broadband Geostationary Satellite With Optical Feeder Link," *J. Opt. Commun. Netw.*, vol. 7, no. 4, p. 325, Apr. 2015.

[9]   S. Poulenard, M. Ruellan, B. Roy, J. Riédi, F. Parol, and a. Rissons, "High altitude clouds impacts on the design of optical feeder link and optical ground station network for future broadband satellite services," *SPIE Photonics West 2014-LASE Lasers Sources*, vol. 8971, p. 897107, 2014.

[10]   S. Poulenard, B. Roy, M. Hanna, L. Frédéric, H. Le Gléau, and A. Rissons, "Optical Ground Station Network Optimization and Performances for High Data Rate Geosatellite-To-Ground Telemetry," no. September, pp. 10–13, 2013.

[11]   M. Toyoshima, T. Fuse, D. R. Kolev, H. Takenaka, Y. Munemasa, N. Iwakiri, K. Suzuki, Y. Koyama, T. Kubooka, M. Akioka, and H. Kunimori, "Current status of research and development on space laser communications technologies and future plans in NICT," in *2015 IEEE International Conference on Space Optical Systems and Applications (ICSOS)*, 2015, pp. 1–5.

[12]   T. Tolker-Nielsen and J.-C. Guillen, "SILEX : The First European Optical Communication Terminal in Orbit," *ESA Bull.*, vol. 96, no. november, 1998.

[13]   O. Vidal, B. Roy, S. Dimitrov, R. Barrios, D. Giggenbach, and A. Le Kernec, "NEXT GENERATION HIGH THROUHGPUT SATELLITE SYSTEM BASED ON OPTICAL FEEDER LINKS," in *Proceedings of the Ka and Broadband Communications, Navigation and Earth Observation Conference*, 2015.

[14]   M. Toyoshima, "Trends of research and development of optical space," no. Ets Vi, pp. 1–13, 2010.

[15]   Z. Sodnik, B. Furch, and H. Lutz, "Free-Space Laser Communication Activities in Europe: SILEX

and beyond," in *2006 IEEE LEOS Annual Meeting Conference Proceedings*, 2006, pp. 78–79.

[16]   L. Vaillon, G. Planche, V. Chorvalli, and L. Le Hors, "Optical Communications Between an Aircraft and a Geo Relay Satellite : Design & Flight Results of the Lola Demonstrator," *October*, no. 1, 2007.

[17]   M. Sans and Z. Sodnik, "Design of the ESA Optical Ground Station for Participation in LLCD," *ICSOS 2012 Conf. Proc.*, vol. 12, 2012.

[18]   D. Giggenbach, J. Horwath, and M. Knapek, "Optical data downlinks from Earth observation platforms," vol. 719903, no. February 2009, p. 719903, 2009.

[19]   B. S. Robinson, D. M. Boroson, D. A. Burianek, and D. V. Murphy, "The lunar laser communications demonstration," *2011 Int. Conf. Sp. Opt. Syst. Appl. ICSOS'11*, no. Llcd, pp. 54–57, 2011.

[20]   C. Petit, N. Védrenne, V. Michau, G. Artaud, J. L. Issler, E. Samain, M. Toyoshima, M. Akioka, D. Kolev, Y. Munemasa, H. Takenaka, and N. Iwakiri, "Adaptive optics results with SOTA," *2015 IEEE Int. Conf. Sp. Opt. Syst. Appl. ICSOS 2015*, pp. 1–7, 2016.

[21]   E. Luzhanskiy, B. Edwards, D. Israel, D. Cornwell, J. Staren, N. Cummings, T. Roberts, and R. Patschke, "Overview and status of the laser communication relay demonstration," 2016, p. 97390C.

[22]   D. M. Cornwell, "NASA's optical communications program for 2017 and beyond," *IEEE, ICSOS*, no. June, p. 93540E, 2017.

[23]   M. Toyoshima, K. Takizawa, T. Kuri, W. Klaus, M. Toyoda, H. Kunimori, T. Jono, Y. Takayama, N. Kura, K. Ohinata, K. Arai, and K. Shiratama, "Ground-to-OICETS laser communication experiments," 2006, vol. 6304, no. November 2001, p. 63040B.

[24]   T. Jono, Y. Takayama, N. Kura, K. Ohinata, T. Yamawaki, K. Arai, K. Shiratama, and I. Mase, "In-orbit Experiment Result of Inter-satellite Laser communication by OICETS (''Kirari'')," vol. 23, no. 2, pp. 21–29, 2006.

[25]   N. Perlot and B. Nuyen, "Space Optical Communications : Summary of Concept," *CCSDS Collab. Work Environ.*, p. 37, 2014.

[26]   D. Giggenbach, J. Poliak, R. Mata-Calvo, C. Fuchs, N. Perlot, R. Freund, and T. Richter, "Preliminary results of Terabit-per-second long-range free-space optical transmission Experiment THRUST," 2015, p. 96470H.

[27]   F. Moll, H. Weinfurter, M. Rau, C. Schmidt, G. Melén, T. Vogl, S. Nauerth, and C. Fuchs, "Aerospace laser communications technology as enabler for worldwide quantum key distribution," 2016, p. 99000K.

[28]   NASA, "Optical Link Study Group. Final Report," no. June, p. 164, 2012.

[29]   H. Zhang, H. Li, X. Dongya, and C. Chao, "Performance Analysis of Different Modulation Techniques for Free-Space Optical Communication System," *Telkomnika*, vol. 13, no. 3, pp. 1693–6930, 2015.

[30]   T. M. Cover and J. A. Thomas, *Elements of Information Theory 2nd Edition*, Wiley-Inte. 2006.

[31]   P. A. Humblet and M. Azizoglu, "On the Bit Error Rate of Lightwave Systems with Optical

Amplifiers," vol. 9, no. 9102576, pp. 1576–1582, 1991.

[32]   U. M. R. Cnrs, "High Throughput LDPC Decoder for C-RAN Optical Fronthaul Based on Improved Bit-Flipping Algorithm," 2016.

[33]   S. Dimitrov, B. Matuz, G. Liva, R. Barrios, R. Mata-Calvo, and D. Giggenbach, "Digital modulation and coding for satellite optical feeder links," *2014 7th Adv. Satell. Multimed. Syst. Conf. 13th Signal Process. Sp. Commun. Work. ASMS/SPSC 2014*, vol. 2014-Janua, pp. 150–157, 2014.

[34]   W. Atia and R. S. Bondurant, "Demonstration of return-to-zero signaling in both OOK and DPSK formats to improve receiver sensitivity in an optically preamplified receiver," *1999 IEEE LEOS Annu. Meet. Conf. Proceedings. LEOS'99. 12th Annu. Meet. IEEE Lasers Electro-Optics Soc. 1999 Annu. Meet. (Cat. No.99CH37009)*, vol. 1, pp. 226–227, 1999.

[35]   D. O. Caplan and W. A. Atia, "A quantum-limited optically-matched communication link," *Ofc*, vol. 1, p. MM2, 2001.

[36]   J. C. Juarez, D. W. Young, J. E. Sluz, and L. B. Stotts, "High-sensitivity DPSK receiver for high-bandwidth free-space optical communication links," *Opt. Express*, vol. 19, no. 11, p. 10789, 2011.

[37]   M. Pfennigbauer, M. Pauer, P. J. Winzer, and M. M. Strasser, "Performance Optimization of Optically Preamplified Receivers for Return-to-zero and Non Return-to-zero Coding," *AEU - Int. J. Electron. Commun.*, vol. 56, no. 4, pp. 261–267, 2002.

[38]   L. D. Tzeng, O. Mizuhzra, T. V. Nguyen, K. Ogawa, I. Watanabe, K. Makita, M. Tsuji, and K. Taguchi, "A high-sensitivity APD receiver for 10-Gb/s system applications," *IEEE Photonics Technol. Lett.*, vol. 8, no. 9, pp. 1229–1231, 1996.

[39]   N. A. Mohammed, A. S. El-Wakeel, and M. H. Aly, "Performance Evaluation of FSO Link Under NRZ-RZ Line Codes, Different Weather Conditions and Receiver Types in the Presence of Pointing Errors," *Open Electr. Electron. Eng. J.*, vol. 6, no. 1, pp. 28–35, Mar. 2014.

[40]   B. Roy, S. Poulenard, S. Dimitrov, R. Barrios, D. Giggenbach, A. Le Kernec, and M. Sotom, "Optical feeder links for high throughput satellites," in *2015 IEEE International Conference on Space Optical Systems and Applications (ICSOS)*, 2015, pp. 1–6.

[41]   F. Lotse, J.-E. Berg, and R. Bownds, "Indoor propagation measurements at 900 MHz," in *[1992 Proceedings] Vehicular Technology Society 42nd VTS Conference - Frontiers of Technology*, pp. 629–632.

[42]   M. A. Al-Habash, "Mathematical model for the irradiance probability density function of a laser beam propagating through turbulent media," *Opt. Eng.*, vol. 40, no. 8, p. 1554, Aug. 2001.

[43]   G. Liva, E. Paolini, and M. Chiani, "Bounds on the Error Probability of Block Codes over the q-Ary Erasure Channel," *IEEE Trans. Commun.*, vol. 61, no. 6, pp. 2156–2165, Jun. 2013.

[44]   C. Lucien, L. Jerome, V. Nicolas, R. Angelique, and G. Artaud, "Performance evaluation of coded transmission for adaptive-optics corrected satellite-to-ground laser links," *2017 IEEE Int. Conf. Sp. Opt. Syst. Appl. ICSOS 2017*, pp. 71–76, 2018.

[45]   C. Petit, V. Nicolas, C. Petit, and V. Nicolas, "Investigation of adaptive optics performance through propagation channel characterization with the Small Optical TrAnsponder SOTA eraldine Artaud , Etienne Samain , Morio Toyoshima To cite this version :," 2016.

[46]   J. W. Hardy, *Adaptive Optics for Astronomical Telescopes*. Oxford University Press, 1998.

[47]   M. Niu, S. Member, J. Cheng, J. F. Holzman, and R. Schober, "Coherent Free-Space Optical Transmission with Diversity Combining for Gamma-Gamma Atmospheric Turbulence," in *25th Biennial Symposium on Communications Coherent*, 2010, pp. 217–220.

[48]   C. Lao, Z. Lu, Y. Zhou, G. Li, B. Zhang, M. Xu, H. He, G. Zhang, and J. Sun, "Performance of DPSK free-space optical communication with spatial diversity," *Laser Commun. Propag. through Atmos. Ocean. VII*, vol. 1077010, no. September, p. 35, 2018.

[49]   Stuart Shaklan Francois Roddier, "Coupling starlight into single-mode fiber optics," *Appl. Opt.*, vol. 0, no. 1, pp. 87–88, 2008.

[50]   M. Chen, C. Liu, and H. Xian, "Experimental demonstration of single-mode fiber coupling over relatively strong turbulence with adaptive optics," *Appl. Opt.*, vol. 54, no. 29, p. 8722, Oct. 2015.

[51]   A. Belmonte and J. M. Kahn, "Field Conjugation Adaptive Arrays in Free-Space Coherent Laser Communications," *J. Opt. Commun. Netw.*, vol. 3, no. 11, p. 830, Nov. 2011.

[52]   A.-R. Camboulives, "Statistical and temporal irradiance fluctuations modeling for a ground-to-geostationary satellite optical link," vol. 57, no. 4, 2018.

[53]   A.-R. Camboulives, M.-T. Velluet, S. Poulenard, L. Saint-Antonin, and V. Michau, "Optical ground station optimization for future optical geostationary satellite feeder uplinks," in *SPIE LASE*, 2017, vol. 1009608, no. February, p. 1009608.

[54]   A.R. CAMBOULIVES, "Compensation des effets de la turbulence atmosphérique sur un lien optique montant sol-satellite géostationnaire : impact sur l'architecture du terminal sol," Université Paris-Saclay, Thesis, 2017.

[55]   D. M. Cornwell, "NASA's optical communications program for 2015 and beyond," no. March 2015, p. 93540E, 2015.

[56]   J. Essiambre and P. J. Winzer, "Advanced Optical Modulation Formats," in *Proceedings of the IEEE*, 2006, vol. 94, no. 5.

[57]   E. Dirk, *Robust Optical Transmission Systems*. Technische Universiteit Eindhoven, 2008.

[58]   P. Burlamacchi, A. Consortini, L. Ronchi, and G. di Francia, "Laser beam propagation in the atmosphere," *IEEE J. Quantum Electron.*, vol. 3, no. 6, pp. 259–259, Jun. 1967.

[59]   Arun K. Majumdar and Jennifer C. Ricklin, *Free-Space Laser Communications*, vol. 2. 2008.

[60]   F. Moll and M. Knapek, "Wavelength selection criteria and link availability due to cloud coverage statistics and attenuation affecting satellite, aerial, and downlink scenarios," *Proc. SPIE - Int. Soc. Opt. Eng.*, vol. 6709, no. September 2007, pp. 670916–670916–12, 2007.

[61]   G. E. Obarski and J. D. Splett, "Transfer standard for the spectral density of relative intensity noise of optical fiber sources near 1550 nm," *Journal of the Optical Society of America B*, vol. 18, no. 6. p. 750, 2001.

[62]   A. H. Gnauck and P. J. Winzer, "Optical phase-shift-keyed transmission," *J. Light. Technol.*, vol. 23, no. 1, pp. 115–130, Jan. 2005.

[63]   M. Ul Zaman, S. Iqbal, and Isha, "Performance analysis of EDFA amplifier for DWDM system," *2014 Int. Conf. Comput. Sustain. Glob. Dev. INDIACom 2014*, pp. 840–843, 2014.

[64]   D. M. Baney, P. Gallion, and R. S. Tucker, "Theory and measurement techniques for the noise figure of optical amplifiers," *Opt. Fiber Technol.*, vol. 6, no. 2, pp. 122–154, 2000.

[65]   H. Khaleghi, A. Sharaiha, T. Rampone, P. Morel, and M. Guégan, "Semiconductor Optical Amplifiers in Coherent Optical-OFDM Systems," *IEEE Photonics Technol. Lett.*, vol. 24, no. 7, pp. 560–562, 2012.

[66]   N. A. Olsson, "Lightwave systems with optical amplifiers," *J. Light. Technol.*, vol. 7, no. 7, pp. 1071–1082, Jul. 1989.

[67]   E. Desurvire and M. N. Zervas, "Erbium-Doped Fiber Amplifiers: Principles and Applications," *Phys. Today*, vol. 48, no. 2, pp. 56–58, Feb. 1995.

[68]   G. P. Agrawal, *Fiber-Optic Communications Systems, Third Edition.*, vol. 6. 2002.

[69]   L. F. B. Ribeiro, J. R. F. Da Rocha, and O. L. Pinto, "Performance evaluation of EDFA preamplified receivers taking into account intersymbol interference," *J. Light. Technol.*, vol. 13, no. 2, pp. 225–232, 1995.

[70]   P. J. Winzer, M. Pfennigbauer, M. M. Strasser, and W. R. Leeb, "Optimum filter bandwidths for optically preamplified NRZ receivers," *J. Light. Technol.*, vol. 19, no. 9, pp. 1263–1273, 2001.

[71]   P. J. Winzer and A. Kalmár, "Sensitivity Enhancement of Optical Receivers by Impulsive Coding," *J. Light. Technol.*, vol. 17, no. 2, pp. 171–177, 1999.

[72]   Q. Chen and P. Lu, "Fiber Bragg Gratings and Their Applications as Temperature and Humidity Sensors," *At. Mol. Opt. Phys. New Res.*, pp. 235–260, 2008.

[73]   International Telecommunications Union, "Optical Fibres, Cables and Systems," pp. 144–147, 2009.

[74]   P. J. Winzer, A. Kalmar, and W. R. Leeb, "Role of amplified spontaneous emission in optical free-space communication links with optical amplification -- impact on isolation and data transmission; utilization for pointing, acquisition, and tracking," *Proc. SPIE, Free. Laser Commun. Technol. XI*, vol. 3615, 1999.

[75]   Y. K. Lizé, X. Wu, M. Nazarathy, Y. Atzmon, L. Christen, S. Nuccio, M. Faucher, N. Godbout, and A. E. Willner, "Chromatic dispersion tolerance in optimized NRZ-, RZ- and CSRZ-DPSK demodulation.," *Opt. Express*, vol. 16, no. 6, pp. 4228–4236, 2008.

[76]   NIWA Taihoro Nukurangi, "Layers of the atmosphere," 2016. [Online]. Available: https://www.niwa.co.nz/education-and-training/schools/students/layers.

[77]   J. C. Owens, "Optical Refractive Index of Air: Dependence on Pressure, Temperature and Composition," *Appl. Opt.*, vol. 6, no. 1, p. 51, 1967.

[78]   A. N. Kolmogorov, "The local structure of turbulence in incompressible viscous fluid for very large Reynolds numberst," *Society*, vol. 434, no. 1890, pp. 9–13, 2010.

[79]   Richard J. Sasiela, *Electromagnetic Wave Propagation in Turbulence*, Second Edi. The society of Photo-Optical Intrumentation Engineers, 2007.

[80]   D. L. Fried, "Optical Resolution Through a Randomly Inhomogeneous Medium for Very Long and Very Short Exposures," *J. Opt. Soc. Am.*, vol. 56, no. 10, p. 1372, 1966.

[81]   H. T. Yura, "Physical model for strong optical-amplitude fluctuations in a turbulent medium," *J.*

Opt. Soc. Am., vol. 63, no. I, pp. 59–67, 1974.

[82]   V. I. Tatarskii, "Effects of the Turbulent Atmosphere on Wave Propagation," 1971.

[83]   G. J. Baker, "Gaussian beam weak scintillation: low-order turbulence effects and applicability of the Rytov method.," *J. Opt. Soc. Am. A. Opt. Image Sci. Vis.*, vol. 23, no. 2, pp. 395–417, 2006.

[84]   S. F. Clifford, "The classical theory of wave propagation in a turbulent medium," Springer, Berlin, Heidelberg, 1978, pp. 9–43.

[85]   J. W. GOODMAN, *Statistical optics*, 2000th ed., vol. 22, no. 5. Wiley Classics Library Edition, 1986.

[86]   R. J. Noll, "Zernike polynomials and atmospheric turbulence," *J. Opt. Soc. Am.*, vol. 66, no. 3, p. 207, 1976.

[87]   F. Zernike, "Diffraction theory of the knife-edge test and its improved form, the phase-contrast method," *J. Micro/Nanolithography, MEMS, MOEMS*, vol. 1, no. 2, p. 87, 2002.

[88]   V. Sacek, "https://www.telescope-optics.net/zernike_expansion_schemes.htm."

[89]   F. Dios, J. A. Rubio, A. Rodríguez, and A. Comerón, "Scintillation and beam-wander analysis in an optical ground station-satellite uplink," *Appl. Opt.*, vol. 43, no. 19, p. 3866, 2004.

[90]   R. L. Fante, "Electromagnetic beam propagation in turbulent media," *Proc. IEEE*, vol. 63, no. 12, pp. 1669–1692, 1975.

[91]   P. J. Titterton, "Power Reduction and Fluctuations Caused by Narrow Laser Beam Motion in the Far Field," *Appl. Opt.*, vol. 12, no. 2, p. 423, Feb. 1973.

[92]   K. Kiasaleh, "On the probability density function of signal intensity in free-space optical communications systems impaired by pointing jitter and turbulence," *Opt. Eng.*, vol. 33, no. 11, p. 3748, Nov. 1994.

[93]   L. C. Andrews, R. L. Phillips, R. J. Sasiela, and R. Parenti, "PDF models for uplink to space in the presence of beam wander," 2007, p. 655109.

[94]   T. Fusco, V. Michau, F. Mahé, J.-M. Conan, and M. Séchaud, "High resolution imaging through atmospheric turbulence : link between anisoplanatism and intensity fluctuations," 1999, vol. 3866, no. September, pp. 100–109.

[95]   D. Mitic, A. Lebl, and Z. Markov, "Calculating the required number of bits in the function of confidence level and error probability estimation," *Serbian J. Electr. Eng.*, vol. 9, no. 3, pp. 361–375, 2012.

[96]   T. Diallo, A. Pizzinat, F. Saliou, P. Chanclou, and C. Aupetit-berthelemot, "Self-Seeded DWDM Solution for Fronthaul Links in Centralized-Radio Access Network," *J. Light. Technol.*, vol. 34, no. 21, pp. 4965–4971, 2016.

[97]   N. Védrenne, J. M. Conan, M. T. Velluet, M. Sechaud, M. Toyoshima, H. Takenaka, A. Guérin, and F. Lacoste, "Turbulence effects on bi-directional ground-to-satellite laser communication systems," *Proc. Int. Conf. Sp. Opt. Syst. Appl.*, vol. 12, 2012.

[98]   Kylia, "http://kylia.com/kylia/wp-content/uploads/2015/02/datasheet-MINT-V1.2.pdf."

[99]   E. Anzuola and A. Belmonte, "Generation of atmospheric wavefronts using binary micromirror

arrays," *Appl. Opt.*, vol. 55, no. 11, p. 3039, 2016.

[100] S. A. B. Ryder S. Nesbitt, Steven L. Smith, Raymond A. Molnar, "Holographic recording using a digital micromirror device," *Proc. SPIE 3637, Pract. Hologr. XIII,* vol. 3637, no. January, pp. 12–20, 1999.

[101] S. A. Goorden, J. Bertolotti, and A. P. Mosk, "Superpixel-based spatial amplitude and phase modulation using a digital micromirror device," vol. 22, no. 15, pp. 2309–2311, 2014.

[102] M. Chagnon, M. Osman, Q. Zhuge, X. Xu, and D. V. Plant, "Analysis and experimental demonstration of novel 8PolSK-QPSK modulation at 5 bits/symbol for passive mitigation of nonlinear impairments," *Opt. Express*, vol. 21, no. 25, p. 30204, 2013.

[103] Texas Instruments, "DLP9000 Family of 0.9 WQXGA Type A DMDs," 2018. [Online]. Available: http://www.ti.com/lit/ds/symlink/dlp9000.pdf.

[104] A. Report, "DMD 101 : Introduction to Digital Micromirror Device (DMD)," no. October, pp. 1–11, 2013.

[105] B. R. Brown and A. W. Lohmann, "Computer-generated Binary Holograms," *IBM J. Res. Dev.*, 1969.

[106] E. Anzuola and A. Belmonte, "Generation of atmospheric wavefronts using binary micro-mirror arrays," no. Applied Optics, 2016.

[107] L. Lombard, A. Azarian, K. Cadoret, P. Bourdon, D. Goular, G. Canat, V. Jolivet, Y. Jaouën, and O. Vasseur, "Coherent beam combination of narrow-linewidth 15μm fiber amplifiers in a long-pulse regime," *Opt. Lett.*, vol. 36, no. 4, p. 523, 2011.

End of the manuscript